ICQNM 2013

The Seventh International Conference on Quantum, Nano and Micro Technologies

ISBN: 978-1-61208-303-2

August 25-31, 2013

Barcelona, Spain

ICQNM 2013 Editors

Vladimir Privman, Clarkson University - Potsdam, USA

Victor Ovchinnikov, Aalto University, Finland

ICQNM 2013

Foreword

The Seventh International Conference on Quantum, Nano and Micro Technologies [ICQNM 2013], held between August 25-31, 2013 in Barcelona, Spain, continued a series of events covering particularly promising theories and technologies. The conference covered fundamentals on designing, implementing, testing, validating and maintaining various kinds of materials, systems, techniques and mechanisms related to quantum-, nano- and micro-technologies.

Quantum technologies and nano technologies have a great potential to transform communications telecommunications infrastructure and communication protocols, and computers and networking devices. Nanotechnologies and micro-technologies already made their mark on smart materials, nano-medicine, nano-devices, molecular manufacturing, biotechnology, metrology, airspace.

The advancements in material science and computer science have allowed the building, launching and deploying of space exploration systems that continually do more and more as they become smaller and lighter. As an example, carbon nano-tubes have been created that are 250 times stronger than steel, 10 times lighter, and transparent. Similar advances are occurring in glass, plastics and concrete. Spacecraft are being launched, with hulls that are composed of carbon fibers, a light weight high strength material.

Electronic devices, medicine, environment, metrology, aerospace programs, clothes and materials, telecommunications, cryptography, semiconductors, manufacturing, and other domains are impacted by the progress on the areas mentioned above. Particularly, micro imaging, nano-medicine: (drug delivery; nano-particles i.e. viruses; proteins.), bio-nanostructures: (nano-tubes, nano-particles), microsystems, micro fluidics: (including nano-fluidics, modeling; fabrication and application), micro instrumentation / implantable microdevices (miniaturized bio-electronic systems, etc.) and micro sensors benefits from the progress on quantum, nano and micro technologies.

Developing nanoscale-manufactured robots presents fabrication and control challenges. The evolution of mechatronics system and robotic system requires advanced functions for control. Special methods and technologies have been developed to design, analyze, build, controls, and apply micro/nano-robotic systems for biotechnology, medical, information technology, materials, etc. A particular application of nano-robots would be in carrying out projects in hostile environments, utilizing local materials and local energy. Ultra-miniature robotic systems and nano-mechanical devices will be the biomolecular electro-mechanical hardware of future manufacturing and biomedical industry.

Nowadays, there are tremendous attempts to develop new bio-molecular machines, components that can be assembled in nano-devices. Bio-robotics entities are able to manipulate the nano-world components, convey information from the nano/nano to the nano/macro world and navigate at the nano-environment level. Additionally, they are able to self replicate, leading to the bio-robot factory. Protein-based nano-motors and nano-robots, as well as biomolecular components interfaces.

Quantum cryptography uses the uncertainty principle of quantum physics to provide a safe but public means for transmitting vital, secret information. A quantum public key distribution system depends on the uncertainty principle to ensure secrecy. Special protocols correlations and composability algorithms ensure similar functionality as in non-quantum systems. The security related tracks cover a series of events focusing on quantum security aspects. On the quantum protocol side, automated proofs of security and probabilistic model-checking methods have been suggested. Research teams focus on quantum key distribution and aspects related to key composability and correlations. Limitations are mainly related to physical devices and polarization control.

We take here the opportunity to warmly thank all the members of the ICQNM 2013 Technical Program Committee, as well as the numerous reviewers. The creation of such a high quality conference program would not have been possible without their involvement. We also kindly thank all the authors who dedicated much of their time and efforts to contribute to ICQNM 2013. We truly believe that, thanks to all these efforts, the final conference program consisted of top quality contributions.

Also, this event could not have been a reality without the support of many individuals, organizations, and sponsors. We are grateful to the members of the ICQNM 2013 organizing committee for their help in handling the logistics and for their work to make this professional meeting a success.

We hope that ICQNM 2013 was a successful international forum for the exchange of ideas and results between academia and industry and for the promotion of progress in quantum, nano and micro technologies.

We are convinced that the participants found the event useful and communications very open. We hope Barcelona provided a pleasant environment during the conference and everyone saved some time for exploring this beautiful city.

ICQNM 2013 Chairs:

ICQNM Advisory Chairs
Vladimir Privman, Clarkson University - Potsdam, USA
Christian Kollmitzer, AIT Austrian Institute of Technology GmbH, Austria
Wen-Ran Zhang, Georgia Southern University, USA
Victor Ovchinnikov, Aalto University, Finland

ICQNM 2013 Research/Industry Chairs
Marco Genovese, Italian Metrological Institute (INRIM) -Torino, Italy
Keiji Matsumoto, National Institute of Informatics, Japan

ICQNM 2013 Special Area Chairs
QSEC
Masahito Hayashi, Tohoku University, Japan
Fluidics
Alireza Azarbadegan, University College London (UCL), UK

Quantum algorithms and quantum complexity
Francois Le Gall, The University of Tokyo, Japan
Quatum control
Daoyi Dong, University of New South Wales, Australia

ICQNM 2013

Committee

ICQNM Advisory Chairs

Vladimir Privman, Clarkson University - Potsdam, USA
Christian Kollmitzer, AIT Austrian Institute of Technology GmbH, Austria
Wen-Ran Zhang, Georgia Southern University, USA
Victor Ovchinnikov, Aalto University, Finland

ICQNM 2013 Research/Industry Chairs

Marco Genovese, Italian Metrological Institute (INRIM) -Torino, Italy
Keiji Matsumoto, National Institute of Informatics, Japan

ICQNM 2013 Special Area Chairs

QSEC
Masahito Hayashi, Tohoku University, Japan

Fluidics
Alireza Azarbadegan, University College London (UCL), UK

Quantum algorithms and quantum complexity
Francois Le Gall, The University of Tokyo, Japan

Quatum control
Daoyi Dong, University of New South Wales, Australia

ICQNM 2013 Technical Program Committee

Andrew Adamatzky, University of the West of England - Bristol, U.K.
Gerardo Adesso, Quantum Theory Group/Università di Salerno, Italy
Dionys Baeriswyl, University of Fribourg, Switzerland
Irina Buyanova, Linkoping University, Sweden
Weimin M. Chen, Linköping University, Sweden
Taksu Cheon, Kochi University of Technology - Tosa Yamada, Japan
Mihaela Corneanu, Banat's University of Agricultural Sciences and Veterinary Medicine, Romania
Sorin Cotofana, TU Delft, The Netherlands
Sao-Ming Fei, Capital Normal University - Beijing, China
Akihiko Fujiwara, Japan Synchrotron Radiation Research Institute - Hyogo, Japan
Juan Carlos García-Escartín, Universidad de Valladolid, Spain
Yuval Gefen, The Weizmann Institute of Science, Israel
Marco Genovese, Italian Metrological Institute (INRIM) -Torino, Italy

Copyright Information

For your reference, this is the text governing the copyright release for material published by IARIA.

The copyright release is a transfer of publication rights, which allows IARIA and its partners to drive the dissemination of the published material. This allows IARIA to give articles increased visibility via distribution, inclusion in libraries, and arrangements for submission to indexes.

I, the undersigned, declare that the article is original, and that I represent the authors of this article in the copyright release matters. If this work has been done as work-for-hire, I have obtained all necessary clearances to execute a copyright release. I hereby irrevocably transfer exclusive copyright for this material to IARIA. I give IARIA permission or reproduce the work in any media format such as, but not limited to, print, digital, or electronic. I give IARIA permission to distribute the materials without restriction to any institutions or individuals. I give IARIA permission to submit the work for inclusion in article repositories as IARIA sees fit.

I, the undersigned, declare that to the best of my knowledge, the article is does not contain libelous or otherwise unlawful contents or invading the right of privacy or infringing on a proprietary right.

Following the copyright release, any circulated version of the article must bear the copyright notice and any header and footer information that IARIA applies to the published article.

IARIA grants royalty-free permission to the authors to disseminate the work, under the above provisions, for any academic, commercial, or industrial use. IARIA grants royalty-free permission to any individuals or institutions to make the article available electronically, online, or in print.

IARIA acknowledges that rights to any algorithm, process, procedure, apparatus, or articles of manufacture remain with the authors and their employers.

I, the undersigned, understand that IARIA will not be liable, in contract, tort (including, without limitation, negligence), pre-contract or other representations (other than fraudulent misrepresentations) or otherwise in connection with the publication of my work.

Exception to the above is made for work-for-hire performed while employed by the government. In that case, copyright to the material remains with the said government. The rightful owners (authors and government entity) grant unlimited and unrestricted permission to IARIA, IARIA's contractors, and IARIA's partners to further distribute the work.

Table of Contents

Effect of Thermal Radiation during Annealing on Self-organization of Thin Silver Films

Victor Ovchinnikov
Department of Aalto Nanofab
School of Electrical Engineering, Aalto University
Espoo, Finland
e-mail: Victor.Ovchinnikov@aalto.fi

***Abstract*—Fabrication method of self-organized silver nanostructures by annealing of thin films is studied. The method has poor reproducibility and generates different shapes and sizes of nanostructures for identical conditions, but in different furnaces. To clarify the source of instability, the self-organized nanostructures were prepared by annealing of silver films with different strength of thermal radiation. The results demonstrate dependence of morphology and reflectance spectra of the samples on power of thermal radiation. Numerical simulations of heating conditions were performed and confirmed effect of thermal radiation on melting of silver nanostructures. The obtained results can be used to control self-organization of silver nanostructures and to improve reproducibility of the fabrication processes.**

Keywords-self-assembling; silver nanostructure; random array; annealing

I. INTRODUCTION

Metal nanostructures are widely used in different applications ranging from plasmonics [1] and nanopatterning [2,3] to chemical catalyst [4] and metamaterials [5]. The most attractive are silver and gold nanostructures, because they possess plasmon resonances in visible range of wavelength and are used in biosensors [6], surface enhanced Raman spectroscopy (SERS) [2], near field optics [7], etc. Despite of this, industrial application of regular or periodic metal nanostructure arrays is hindered by high cost and complexity of their fabrication. In view of this, significant attention is devoted to study of random or irregular arrays of metal nanostructures and their applications instead of regular arrays. In random arrays, nanostructure shape and space periodicity are varied in the limited range. As a result, random nanostructure arrays still possess resonance features, similar to periodic arrays, but they are not so sharp and strong. It is still suitable for many applications and irregular arrays are widely used in SERS substrate [2] and thin film solar cells [8,9]. Most attractive are random arrays in which one or more parameters are fixed and are not varied, e.g., thickness of all structures is the same or all asymmetric structures are oriented in the same direction or shape of all nanoislands is spherical.

One of the easiest and oldest methods to produce irregular array of metal nanoislands is physical vapor deposition of ultra thin metal film [10-12]. The method works well for film thickness less than 5 nm, when as deposited film consists of isolated nanoislands. At higher thicknesses, when deposited film is lace-like, self-organization of nanoislands can be stimulated by annealing [13,14]. Depending on film material and thickness, annealing cab be done at different temperatures (200 – 800 C), in different ambient (vacuum or gas) and in the time interval from 1 second to several hours. In the resulting nanostructure array, nanoisland size and separation between nanoislands are usually variable, but shape is similar for most of structures on a substrate, e.g., array of ellipsoids or array of peanut-shaped structures [15].

Many papers are devoted to fabrication and study of metal nanospheres, due to potential applications in plasmonics and nanotechonology. The results reported demonstrate broad range of shapes and sizes of nanospheroids for similar fabrication conditions (sample size, film thickness and annealing temperature) [13,14,16]. At the same time, all studies have common features: 1) the diameter of spheres is less than 30 nm or film thickness is less than 8 nm; 2) the sample size is less than 2 x 2 cm^2; 3) there are no details of annealing process and especially no information about relative strength of heating modes (conduction, convection and radiation). Strength of heating modes depends on furnace design, sample holder, position of sample inside of heating volume etc. Any break out of above mentioned limits leads to nanoislands of irregular (non spherical) shape. Due to this, successful reproducing of reported results in other furnace is problematic. In first turn, it concerns preparation of silver and gold nanostructures, which are often formed by annealing.

In this paper, we report on the silver film annealing in controllable conditions with different strength of thermal radiation. At the same time numerical simulations are performed to define variations of heat fluxes through the sample surface. These simulations are compared with corresponding experimental results, to find heating conditions for reproducible formation of silver nanosphere arrays.

The paper is organized as follows. In the subsequent section II, details of sample preparation and measurement procedures are presented. In the section III, the results of work are demonstrated by SEM images and reflectance spectra of the nanostructure arrays and also by heat transfer simulations. The optimal conditions of silver film annealing are discussed in Section IV.

 ISBN: 978-1-61208-303-2

II. EXPERIMENTAL

We have studied 12 nm thick silver films, deposited by electron beam evaporation at rate 0.5 nm/s. As a substrate were used pieces of 4" silicon wafer with 10 nm layer of thermal oxide. Annealing was done in diffusion furnace in nitrogen ambient. To measure temperature of the samples, a copper plate with a hole for thermocouple was used as a holder. The sample had good thermal contact with the holder which was located on the quartz boat during experiment. The furnace tube was opened from one edge to provide manual loading and unloading of the samples at temperature of annealing. The tube temperature was measured by thermocouple and stabilized at 400 C.

Two series of samples were prepared to study effect of thermal radiation on silver self-organization. In the first series the intensity of thermal radiation was controlled by the shield above the sample, in the second series the samples were heated on the holder in loading zone of the furnace. In this case there was only radiation cooling of the sample, because holder was hotter than furnace tube walls.

In the first series (tube annealing), the holder was preheated to 130 C in the central part of the furnace tube and moved to loading zone of the tube. After sample loading the holder was moved in the central zone of the tube. The holder with sample was heated up during 11 minutes and moved out from the central zone to load zone and the sample was taken out. The first sample was opened to heat radiation from the quartz tube walls, because it was not covered by anything. Another two samples were covered by shield (thin plate) to reduce heat radiation. As a material of shield were used silicon and stainless steel (UNS 304) plates with thicknesses 0.7 mm and 1 mm, respectively. The shield had sizes 75 x 85 mm^2 and supported above copper holder on the height 2.5 mm by ceramic posts. The samples were labeled corresponding to tube annealing and protective plate as T, T-Si and T-304 for uncovered, silicon covered and steel covered samples, respectively.

In the second series (hot plate annealing), the holder was heated to target temperature in the central part of the furnace and moved out for sample loading. The sample was loaded on the hot holder and left in the load zone of the furnace for 1 minute. During this time the sample and the copper holder were brought to heat equilibrium. After that the sample was taken out. The samples were labeled corresponding to hot plate annealing and temperature as HP165, HP220, HP295 for annealing at 165 C, 220 C and 295 C, respectively.

The metal films were deposited in e-beam evaporation system IM-9912 (Instrumentti Mattila Oy) at base pressure of 2×10^{-7} Torr and at room temperature of the substrate.

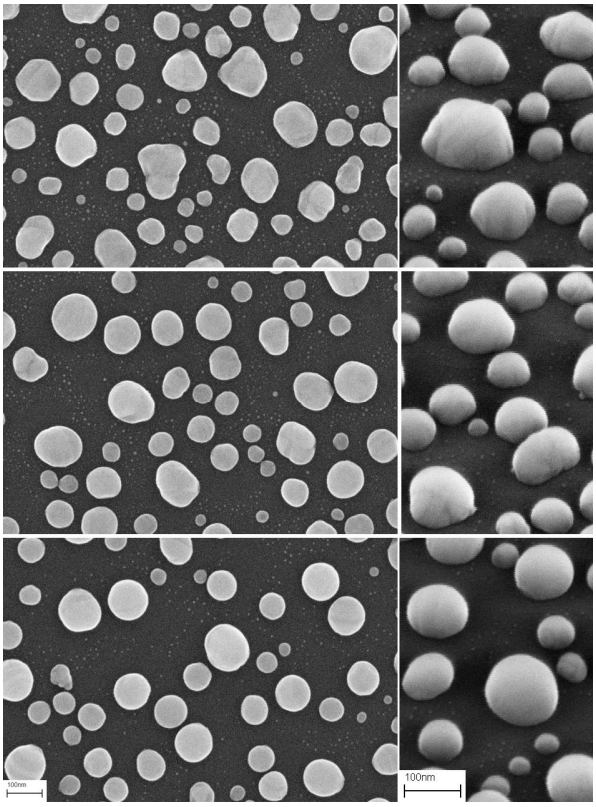

Figure 1. Plan and tilted 45° SEM images of tube annealed samples. From top to bottom T, T-Si and T-304, unprotected and protected by silicon and steel, respectively.Scale bar is 100 nm.

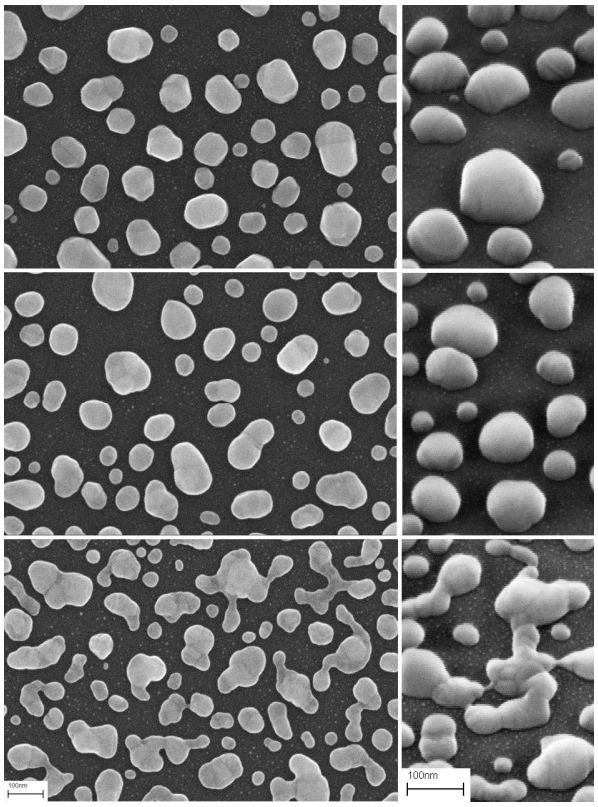

Figure 2. Plan and tilted 45° SEM images of hot plate annealed samples. From top to bottom HP295, HP220 and HP165, annealed at 295 C, 220 C and 165 C, respectively. Scale bar is 100 nm.

 ISBN: 978-1-61208-303-2

Annealing was done in the diffusion furnace THERMCO Mini Brute MB-71. Plan view and tilted at 45^0 SEM images of the samples were observed with Zeiss Supra 40 field emission scanning electron microscope. Reflectance measurements at normal incidence were carried out using FilmTek 2000M reflectometer in the spectral range from 380 to 890 nm.

III. RESULTS

Fig. 1 shows plan view and tilted SEM images of the tube annealed samples. The samples have close values of areal density and nanostructure sizes, but shape of nanoislands depends on annealing conditions. The unprotected sample T demonstrates most irregular islands with straight flats on some of them. The sample with silicon shield T-Si has roundish nanostructures with large shape deviation and the sample with steel shield T-304 shows spherical nanoislands with bi-modal distribution of diameters. It is visible on the tilted images, that nanospheres of the sample T-304 touch substrate at small contact area. In case of samples T and T-Si this contact area is larger and height of nanostructures is less than for sample T-304.

Fig. 2 shows plan view and tilted SEM images of the hot plate annealed samples. In this series shape variations are more significant. It is observed lace like structures for low temperature annealed sample HP165, irregular shapes with rounded corners for the sample HP220 and irregular shapes with flats for high temperature annealed sample HP295. The tilted images demonstrate lowest thickness of nanostructures at the sample HP165 and highest thickness of nanostructures at the sample HP295. The largest contact area with substrate has sample HP220. Tube annealed sample T and hot plate annealed sample HP295 possess flats and look similar. Samples HP220 and T-Si are also similar. The sample HP165 from the second series has no analogue in the first series of samples.

It is need to note that samples have different colours of the surface. The samples T, T-Si and HP295 are green, the sample T-304 is blue, the sample HP220 is grey-blue and the sample HP165 is grey. Colour difference is explained by different reflection spectra which are connected with plasmonic properties of the structures. Fig. 3a demonstrates reflection spectra of the tube annealed samples. According to surface colour, the samples T, T-Si have similar reflection spectra with main peak at wavelength 490 nm and trough at 750 nm. The sample T-304 has main peak at shorter wavelength 450 nm and trough at 640 nm. The coincidence of spectra for samples T and T-Si is unexpected, because they have different SEM images. On the other hand, samples T-Si and T-304 have similar SEM images, but different reflection spectra. Dotted line shows spectrum of the as deposited silver film, i.e., spectrum of the samples before annealing. Fig. 3b demonstrates reflection spectra of the hot plate annealed samples. The low temperature sample HP165 has spectrum similar to as deposited silver film. The sample HP220 has spectrum similar to T-304, but with lower height of peak and wider trough. The spectrum of sample HP295 is close to the spectrum of sample T, only it has wider and weaker peaks.

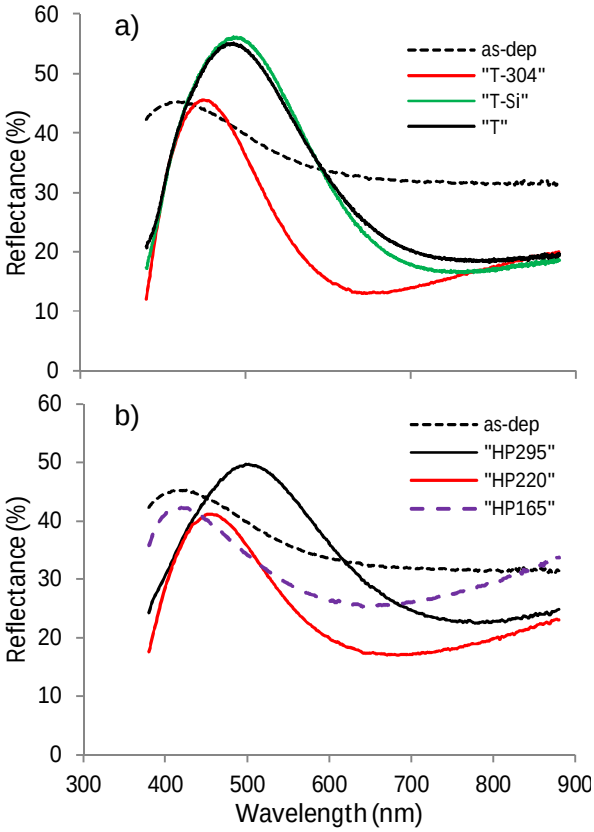

Figure 3. Reflection spectra of tube annealed (top) and hot plate annealed (bottom) samples.

The simulations were done with the help of software COMSOL Multiphysics 3.5a. It was used general heat transfer model for annealing in nitrogen ambient. The effect of heat convection was simulated for laminar nitrogen flow with velocity 0.03 m/s by means of heat transfer coefficients from the COMSOL library. The simulations were verified by

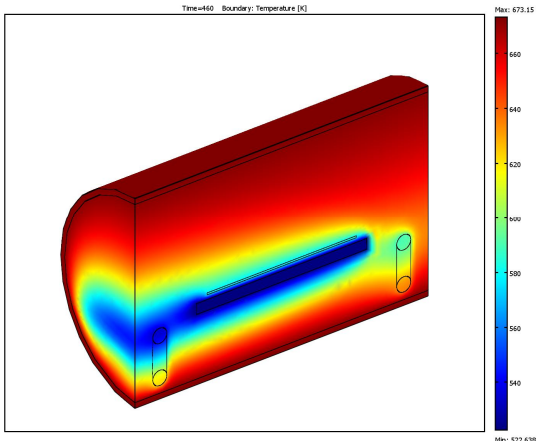

Figure 4. Calculated temperature distribution around quartz boat and copper holder during annealing of steel protected sample T-304. The copper holder has the lowest temperature.

 ISBN: 978-1-61208-303-2

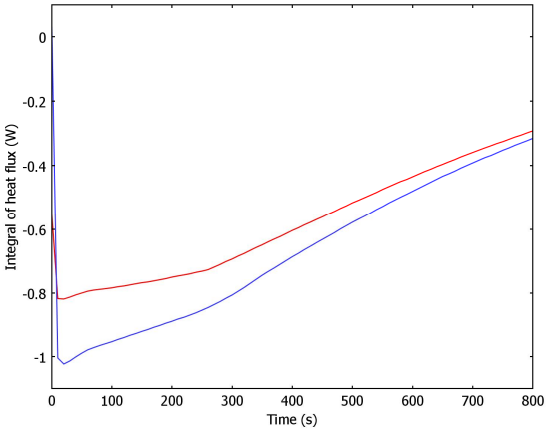

Figure 5. Calculated conductive heat flux (blue) and radiative flux (red) through the upper surface of the copper holder during annealing of uncoverd sample T.

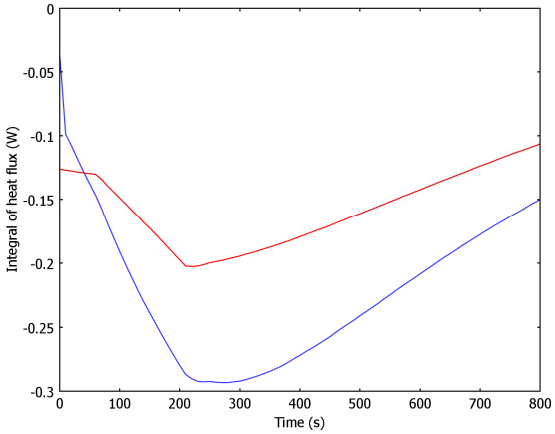

Figure 7. Calculated conductive heat flux (blue) and radiative flux (red) through the upper surface of the copper holder during annealing of sample T-304 with steel shield.

matching of calculated and measured heating curves of the copper holder (not shown). Fig. 4 demonstrates example of temperature distribution in the furnace with steel covered sample T-304. The distribution is given for the holder temperature 250 C, which is close (see below) to the melting point of silver nanostructres. The heat source and the heat sink are furnace walls and the copper holder, respectively. The vertical objects in the left-bottom and right-bottoms corners of the Fig.4 are cross-sections of the quartz boat.

Fig. 5 demonstrates variations of heat fluxes for the uncovered sample T during annealing. The flux is calculated over upper surface of the sample and has positive sign in direction of normal to the surface, i.e., outside of the sample. In this case, the conductive heat flux and the radiative flux have comparable values and decreased during heating of the sample. Fig. 6 shows evolution of holder and steel shield temperatures during annealing of the sample T-304. In the beginning, the shield is heated faster, but in stationary mode

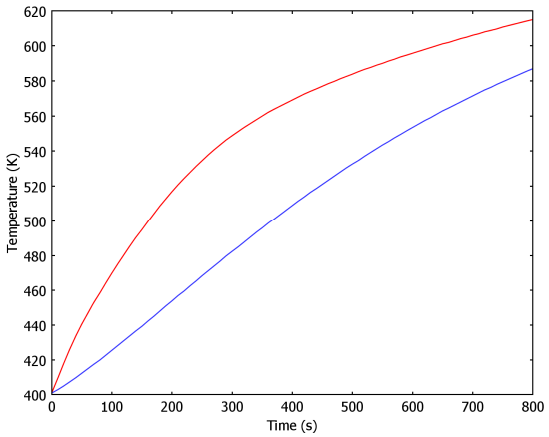

Figure 6. Calculated temperatures of the copper holder (blue) and steel shield (red) during annealing of steel protected sample T-304.

the temperatures of the shield and holder are close to each other. The maximum difference in the holder and shield temperatures (overheating) happens after 250 s of heating. Fig. 7 illustrates effect of shielding of infrared radiation by steel plate. The simulations confirm intuitive feeling that metal shield should decrease the radiation heating of the sample. Indeed, radiation flux of uncovered sample is four times more intensive than for protected one (Fig.5 and Fig.7), when samples have temperature 250 C. The radiation still exists in the shielded sample due to overheating of the shield relatively sample (55 C for the sample T-304), which in turn irradiates the sample. The most attractive in the annealing of the protected sample is three times less conductive flux in comparison with uncovered sample (Fig.5 and Fig.7). It is very important in preventing quenching of melted silver droplets (see below).

IV. DISCUSSION

Melting of silver nanostructures at low temperature annealing has been reported in several studies [14,17,18]. In case of liquid silver, the spherical shape of nanoislands for sample T-304, can be explained by droplet formation on non-wettable surface due to cohesive forces. On other hand, the results of hot plate annealing demonstrate existing of temperature point at which shape of nanoislands is changed. With the help of additional hot plate samples it was found that the point of shape transformation is close to 245 C. The result of annealing at low temperature looks like nanostructures of sample HP220, the annealing at high temperature provides nanostructures similar to sample HP295. The close results were obtained in several studies reported about melting temperature of silver nanostructures in the interval of 250-300 C [17,18]. Therefore, we believe that during our experiments the silver films heated above 245 C were melted, e.g., in samples with flats HP395 and T.

Silver properties modification caused by melting leads to changing of reflection spectra after annealing. It has been already mentioned that areal density and average size of

 ISBN: 978-1-61208-303-2

nanoislands are close to each other in studied samples. However, redshift of dipolar resonance in melted samples is relatively large and cannot be only explained by changing of island geometry. Resonance wavelength shift can be provided by changing of dielectric environment or dielectric function of silver in melted samples. Due to identical environment in the studies samples, it can be concluded that spectrum variations are connected with dielectric function of silver. Moreover, from spectral peak and trough broadening follows that not only real, but imaginary part of silver dielectric function was changed. One of the possible explanations is increased defect concentration in melted samples, how it was reported earlier [19].

It cost to note that additionally to bulk melting (discussed above) in nanostructures exists also surface melting or pre-melting. Pre-melting happens at lower temperature [17] and is responsible for shape variation between samples HP165 and HP220. But surface melting is not connected with increasing of defect concentration in resulting nanoislands (Fig. 3b).

Reflection spectra (Fig.3) demonstrate plasmon properties of silver nanostructres. The troughs in the range 650 – 750 nm correspond to dipole plasmon resonance and peaks at 450 – 500 nm correspond to quadrupole resonance. The different appearance in the reflection is connected with different radiation patterns of dipole and quadrupole [13]. These resonances are valid for annealed samples. Non annealed samples possess very broad range of infrared radiation (see spectrum of as deposited sample). During annealing silver temperature is higher than temperature of the substrate due additional radiation heating [20-22]. After melting liquid silver nanoislands are divided in smaller ones due to Rayleigh instability [14]. Geometry change causes blueshift of plasmon resonance, observed in the measured spectra and interruption of infrared heating, because radiation with new resonance wavelength does not exist. The cold substrate (Fig. 4) cools down silver nanostructures and causes their solidification. Our estimation for 100 nm sphere gives transition time to thermal equilibration with substrate in the range of 10^{-8} s. So fast quenching happens without proper crystallization and generates defects in silver lattice.

In case of tube annealing of protected samples melting happens at higher holder temperature. Depending on conductive and radiative heat fluxes the melted silver is cooled with much lower rate (sample T-Si) or does not solidify at all (sample T-304). For the hot plate annealing there is also quenching mechanism, despite of absence of radiation. Silver nanostructure is heated by substrate and cooled by nitrogen. In other words, there is heat flow from the substrate to ambient through nanostructure. This heat flow creates temperature drop on the interfacial thermal resistance between substrate and silver droplet, what in turn leads to decreasing of silver temperature and quenching.

V. CONCLUSIONS

We have demonstrated the effect of thermal radiation on furnace annealing of thin silver films. Due to plasmon resonance in infrared, the radiation heating of silver films can be very strong and provides overheating of the silver nanostructures relatively substrate. This overheating is self-limited owing to size dependence of resonance wavelength. After melting and fragmentation of silver nanostructures to smaller nanoislands, plasmon resonance is shifted to visible range and does not support any more heating of silver nanoislands. As a result, they are quenched to solid state with irregular shape and high defect concentration. The minimization of radiation heating supports nanostructures in liquid state after melting, providing spherical shape of nanoislands after solidification. This opens new approaches to fabrication of self-assembled silver nanostructures.

ACKNOWLEDGMENT

This research was undertaken at the Micronova Nanofabrication Centre, supported by Aalto University.

REFERENCES

[1] M. A. Garcia, “Surface plasmons in metallic nanoparticles: fundamentals and applications”, J. Phys. D: Appl. Phys., vol. 44, 2011, p. 283001, (20pp.).

[2] A. Shevchenko, V. Ovchinnikov, and A. Shevchenko, ”Large-area nanostructured substrates for surface enhanced Raman spectroscopy”, Appl. Phys. Lett., vol. 100, 2012, p. 171913 (4pp.).

[3] V. Ovchinnikov and A. Shevchenko, “Self-organization-based fabrication of stable noble-metal nanostructures on large-area dielectric substrates”, Journal of Chemistry, vol. 2013, 2013, Article ID 158431, 10pp., http://dx.doi.org/10.1155/2013/158431.

[4] Y. F. Guan, A. V. Melechko, A. J. Pedraza, M. L. Simpson, and P. D. Rack, “Non-lithographic organization of nickel catalyst for carbon nanofiber synthesis on laser-induced periodic surface structures,” Nanotechnology, vol. 18, 2007, pp. 335306 – 335312.

[5] E. Cortes, L. Mochán, B. S. Mendoza, and G. P. Ortiz, “Optical properties of nanostructured metamaterials”, Phys. Status Solidi B, vol. 247, 2010, pp. 2102 – 2107.

[6] J. N. Anker et al., “Biosensing with plasmonic nanosensors”, Nature Materials, vol. 7, 2008, pp. 442 – 453.

[7] X. Zhang and Z. Liu, “Superlenses to overcome the diffraction limit”, Nature Materials, vol. 7, 2008, pp. 435 – 441.

[8] X. Sheng et al., “Design and non-lithographic fabrication of light trapping structures for thin film silicon solar cells”, Adv. Mater. vol. 23, 2011, pp. 843 – 847.

[9] C. Eminian, F.-J. Haug, O. Cubero, X. Niquille, and C. Ballif, “Photocurrent enhancement in thin film amorphous silicon solar cells with silver nanoparticles”, Progress in Photovoltaics: Research and Applications, vol. 19, 2011, pp. 260 – 265.

[10] J. Maa and T. E. Hutchinson, “Early growth of thin films deposited by ion beam sputtering”, J. Vac. Sci. Technol., vol.14, 1977, pp. 116-121.

[11] M. Gnanavel, D.B. Mohan, and C.S. Sunandana, “Optics of quasi-particle phase transitions in nanostructured Ag thin films”, Thin Solid Films, vol. 517, 2008, pp. 1058 – 1062.

[12] G. Xu, M. Tazawa, P. Jin, and S. Nakao, “Sufrace plasmon resonance of sputtered Ag films: substrate and mass thickness denepndence”, Appl. Phys. A, vol. 80, 2005, pp. 1535-1540.

[13] J.W. Little, T.A. Callcott and T.L. Ferrell, “Sufrace-plasmon radiation from ellipsoidal silver spheroids”, Phys. Rev. B, vol. 29, 1984, pp.1606-1615.

 ISBN: 978-1-61208-303-2

[14] S.R. Bhattacharyya et al., “Growth and melting of silicon supported silver nanocluster films”, J. Phys. D: Appl. Phys., vol. 42, 2009, p. 035306 (9pp.).

[15] S. Karim et al., “Morphological evolution of Au nanowires controlled by Rayleigh instability”, Nanotechnology, vol. 17, 2006, pp. 5954-5959.

[16] P. Royer, J.P. Goudonnet, R.J. Warmack and T.L. Ferell, “Substrate effects on surface-plasmon spectra in metal-island films”, Phys. Rev. B, vol. 35, 1987, pp.3753-3759.

[17] O.A. Yeshchenko, I.M. Dmitruk, A.A. Alexeenko and A.V. Kotko, “Surface Plasmon as a probe for melting of silver nanoparticles”, Nanotechnology, vol. 21, 2010, p. 045203 (6pp.).

[18] M. Khan et al., “Structural and thermal studies of silver nanoparticles and electrical transport study of their thin films”, Nanoscale Research Letters, vol. 6, 2011, p. 434 (8pp.), doi:10.1186/1556-276X-6-434.

[19] S.A. Little, T. Begou, R. E. Collins and S. Marsillac, “Optical detection of melting point depression for silver nanoparticles via in situ real time spectroscopic ellipsometry”, Appl. Phys. Lett., vol. 100, 2012, p. 051107 (4pp.).

[20] E.C. Garnett et al., “Self-limited plasmonic welding of silver nanowire junctions”, Nature Materials, vol.11, 2012, pp.241-249.

[21] G. Baffou, R. Quidant and C. Girard, “Heat generation in plasmonic nanostructures: Influence of morphology”, App. Phys. Lett., vol. 94, 2009, p. 153109 (3pp.).

[22] A. O. Govorov and H.H. Richardson, “Generating heat with metal nanoparticles”, Nanotoday, vol. 2, 2007, pp. 30- 38.

 ISBN: 978-1-61208-303-2

Monte Carlo Studies of Particle Diffusion on a Patchwise Bivariate Surface

Alexander Tarasenko and Lubomir Jastrabik
Institute of Physics, v.v.i.
Academy of Sciences CR
Prague, Czech Republic
Email: taras@fzu.cz, jastrab@fzu.cz

***Abstract*—The diffusion of particles adsorbed on a patchwise surface with two non equivalent sites is investigated in the framework of a lattice-gas model. We derived the analytical expressions for the diffusion coefficients. Using the kinetic Monte Carlo simulations we calculate the coverage dependencies of the diffusion coefficients in the wide region of the lateral interaction between the particles. The theoretical dependencies are compared with the numerical data. The good coincidence of the data obtained by the two different methods corroborates the validity of the approach developed for the description of the particle migration over such complex heterogeneous lattices.**

***Index Terms*—surface diffusion; kinetic Monte Carlo simulations; patchwise lattice.**

I. Introduction

The diffusive mass transfer controls the rates of a multitude of physical, chemical, and biological processes. The theoretical investigations of these processes attract much attention, but the complexity of the real systems also makes their study extremely difficult. The majority of the widely used systems are strongly heterogeneous. Crystals and thin films consist of small nanocrystals, domains, and other heterogeneities. The surfaces have random potential reliefs with broad distributions of energetic parameters like adsorption energies and potential barriers.

A theoretical model has been developed by Ross and Olivier to describe the particle (atoms, molecules) adsorption on such heterogeneous surfaces [1]. In this model the surface is composed of a number of randomly distributed or ordered patches with different adsorption sites. The model is widely used in experimental and theoretical investigations of effects of the heterogeneity on a variety of surface processes like adsorption, desorption, diffusion and catalysis [2]. Due to the great versatility and complexities of the patchy surfaces, it seems impossible to do some definitive conclusions about the transport of particles over such surfaces. Nevertheless, it occurs that in some simple cases one can obtain a rather satisfactory description of the particle diffusion over the heterogeneous surfaces.

We study the influence of the heterogeneity on the surface diffusion of adsorbed particles in the framework of the lattice-gas formalism. In particular, we consider a special case of the surface with only two different types of the adsorption sites, grouped into small square clusters of a given size, and given energy of adsorption. This simple model includes the most important features that are expected to influence the transport over such surfaces. The general and universal approach developed for the investigation of the migration of particles adsorbed on the strongly heterogeneous lattices is applied here for the description of the particle migration on the patchwise bivariate lattices [3].

We rederive the analytical expressions for the diffusion coefficients for the patchwise lattice. The coefficients are also evaluated by the kinetic Monte Carlo (kMC) simulations [4] of the particle migration over the patchwise lattice mentioned above. The theoretical dependencies are compared with the numerical data. It occurs that the coincidence between the data, obtained by the two independent qualitatively different methods, is rather good.

The paper is organized as follows. In Section II, we describe the model and give the definitions of the diffusion coefficients and other necessary quantities. In Section III, we analyze the peculiarities of the particle migration over the lattice. Some details of the kMC method are presented in Section IV. The results are discussed in Section V. Finally, we present the summary of our results and conclusions in Section VI.

II. The Lattice-Gas Model and Diffusion Coefficients

We consider the migration of particles adsorbed on a square lattice of N adsorption sites with a regular and periodic heterogeneity. The lattice is composed of the deep, d, and

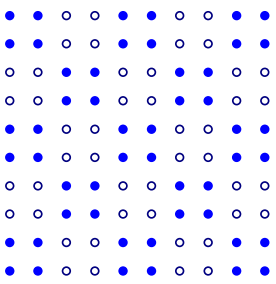

Fig. 1. Schematic view of the square patchwise bivariate lattice. The open and filled circles denote the shallow and deep adsorption sites.

 ISBN: 978-1-61208-303-2

shallow, s, sites arranged in the square 2×2 patches, as shown in Figure 1. The corresponding adsorption energies, ε_d and ε_s, are large relative to the thermal energy, $k_B T$. The N_a particles populate the sites, jumping occasionally to the nearest neighbor (NN) empty adsorption sites. When the duration of the jumps is much shorter than the particle sojourn in the sites, the state of the particle system is completely described by a set of the occupation numbers n_i with

$$n_i = \begin{cases} 1, & \text{if the } i\text{th site is occupied,} \\ 0, & \text{if the } i\text{th site is empty.} \end{cases} \quad (1)$$

The double occupancy is forbidden. The particle concentration, or surface coverage θ, equals to N_a/N. There is also a lateral interaction φ between the NN particles.

The particle migration is described by some diffusion coefficients. Conceptually, the simplest diffusion coefficient is a single particle, or tracer diffusion coefficient, D_t. It addresses the random walks of the individual tagged particles

$$D_t = \lim_{t\to\infty} \frac{1}{4tN_a} \left\langle \sum_{k=1}^{N_a} \vec{r}_k^{\,2}(t) \right\rangle. \quad (2)$$

The jump, or center-of-mass diffusion coefficient, D_j, describes the asymptotic behavior of the center of mass of the system of adsorbed particles

$$D_j = \lim_{t\to\infty} \frac{1}{4tN_a} \left\langle \left[\sum_{k=1}^{N_a} \vec{r}_k(t) \right]^2 \right\rangle. \quad (3)$$

Here $\vec{r}_k(t)$ is the displacement of the kth particle after the time t; the brackets $\langle \cdots \rangle$ denote the average over the particle configurations. The coefficients are well-suited for the kMC simulations, as they are expressed in terms of the directly accessible quantities $\vec{r}_k(t)$.

The Fickian (also chemical, collective, transport) diffusion coefficient D_c, describing the mass transfer over the lattice, is determined by the Fick's first law which constitutes the relationship between the flux of the particles, $\vec{J}(\vec{r}, t)$, and the gradient of their concentration, $\theta(\vec{r}, t)$

$$\vec{J}(\vec{r}, t) = -D_c \vec{\nabla} \theta(\vec{r}, t). \quad (4)$$

III. Diffusion of particles over the patchwise lattice

In the following we consider the case of a strongly heterogeneous lattice, i.e., $\exp(\varepsilon_d) \gg \exp(\varepsilon_s)$. The heterogeneity results in the striking difference between the s and d sites. The particles tend to occupy the deep sites. Therefore, in the low coverage region, $\theta < 1/2$, almost all s sites are empty, and the overwhelming majority of the particles occupy the d sites. In the high coverage region, $\theta > 1/2$, almost all d sites are filled and the rest $N_a - N/2$ particles occupy the shallow sites.

Also, the inhomogeneity implies the much higher jump rate ν_s for the fast $s \to d$ and $s \to s$ jumps than for the slow $d \to s$ and $d \to d$ jumps with the jump rate ν_d. We call them fast and slow jumps, that means not the duration of a jump itself, but the fact that the averaged time of a particle sojourn in the d sites, ν_d^{-1}, is considerably longer than the corresponding time for the s sites, ν_s^{-1}. There is an important difference between fast and slow jumps. The slow and fast jumps take place on the largely different time scale as $\nu_s \gg \nu_d$. The particles do not stay long in the s sites. Any jump to a shallow site gives rise to the fast jump, which occurs almost immediately after the previous slow jump. In the time scale determined by the slow jumps the fast jump cannot be separated from the precedent slow jump. They should be considered together like a single elementary act of the particle migration. The characteristic coverage, $\theta = 1/2$, separates concentration regions where the particle migration has qualitatively different behavior. In the following Subsections, we consider the specific properties of the diffusion in these regions.

A. Low coverage region

At low coverages, the d patches are partially filled and the s patches are empty. Any migration act starts with a slow jump from an initial d site. There are two possibilities for the activated particle. It can jump to some d or s empty NN site. The $d \to d$ jumps correspond to the ordinary diffusion over the homogeneous lattice of d sites. But the jumps to the shallow sites are more effective. In this case, the particle can perform $1, 2, \ldots$ fast jumps until it finds an empty d site. The particle migrates performing sequence of jumps: the first slow jump and some fast jumps. The final fast jump to the d site finishes the succession. These jump successions, performed by single particles, give the main contribution to the total particle displacement in the low coverage region.

The probability to find an empty final d site decreases as $\theta \to 1/2$. At the stoichiometric coverage $\theta = 1/2$ the system of particles is strongly ordered: almost all d sites are occupied and almost all s sites are empty. Many activated particles cannot find the empty d sites and return to their initial sites. The tracer and jump diffusion coefficients have minimum at this coverage. An interesting consequence of the fact that the particle migration proceeds by the jump sequences performed by single particles is the similar behavior of the tracer and jump diffusion coefficients: they are practically equal in the wide coverage region $0 \le \theta < 1/2$.

The probabilities of the jump successions are determined by the particle configurations on the perimeter d sites surrounding the s patch. There are $z = 4l$ sites surrounding the $l \times l$ patch, which we label by the index $i = 1, 2, \ldots, z$. The particle configuration on the perimeter sites is determined by the occupation numbers of these sites: for particles n_i and for vacancies $h_i \equiv 1 - n_i$. For example, $h_1 n_2 \cdots h_z$ denotes the configuration when the 1st site is empty, the second is filled,..., the zth is empty. The probabilities of the particle configurations are the average values of the product $\langle h_1 n_2 \cdots h_z \rangle$.

Let us suppose that the probability to occupy an empty perimeter d site is the same for all these sites. It is a rather simple approximation. The sites located closer to the initial site have higher probabilities to be occupied than the

 ISBN: 978-1-61208-303-2

further located ones. To obtain the correct probabilities one should calculate, in principle, the infinite series of jumps for every configuration. But, our aim is to demonstrate only the applicability of the approach to the description of the particle diffusion over the patchwise lattice. This approximation permits to derive the analytical expressions for the diffusion coefficients, which are rather simple, but, nevertheless, give quite satisfactory results.

B. High coverage region

At high coverages all d sites are occupied. The $N/2$ particles are trapped in the deep patches and the rest $N_a - N/2$ particles occupy the s sites. The weakly adsorbed particles perform a lot of the fast jumps in the s patches. But it is easy to see that these fast jumps do not give noticeable contribution to the total displacement. The particles are confined in the s patches and cannot migrate over the surface jumping between the s sites only.

It is a specific feature of the patchwise lattices, that there is no infinite connected cluster of the s sites spanning over the whole lattice. The migration over the whole lattice should include slow jumps. The non-zero contribution to the diffusion is produced by successions of slow and fast jumps. But these successions are different from the previous low coverage case.

Again, the first jump of the succession is a slow one. A particle jumps from a d site to some empty s site. And the vacancy in the d patch is filled very fast by the other mobile particle. If the fast jump is performed by a particle from another s patch, these succession of the slow and fast jumps performed by different particles transfers particle between the s patches (over the occupied d patch). Such jump successions, performed by different particles, give the main contribution to the diffusion in the high coverage region $\theta > 1/2$. These jump successions considerably reduce the tracer diffusion coefficient as compared with the jump diffusion coefficient: $D_j \gg D_t$, if $1/2 < \theta < 1$.

The probabilities of the jump successions are determined by the particle configurations in the two s patches (denoted as 1st and 2nd), which are the NNs of the initial d site. There are $z' = 2l^2$ s sites, which we label by the index $i = 1, 2, \ldots, z'$. The particle configurations in the patches are determined by the occupation numbers of the s sites. After the slow jump from the initial d site to the 2nd patch, the particles from the 1st and the 2nd patches try to occupy the vacancy in the initial site. The jump succession ends when some particle fills the vacancy. If the particle jumps from the 1st patch, the total particle displacement changes. The jump succession transfers one particle from the 1st patch to the 2nd patch. This concerted jumps of different particles are equivalent to a single jump of a particle between the NN s patches. In the case, when the vacancy is filled by a particle from the 2nd patch, the total particle displacement remains the same. There is no particle transfer between the s patches.

As in the previous case, we supposed that the probability for any particle in the 1st and 2nd s patches to occupy the vacancy in the initial site is the same. To justify this approximation it may be useful to consider the ideas developed in the method of the real-space renormalization group [5]. Analogously with this approach, the patches should be considered as the block sites, deep or shallow, depending on the type of lattice sites composing the block site. The lattice is transformed to the ordinary heterogeneous square lattice of d and s block sites arranged in the alternating order. The particle diffusion is a sequence of jumps between the NN sites. As the migration path for any particle includes many jumps between the block sites, the details of the particle migration inside the blocks (patches) should be smoothed out in some sense, averaged. The migration proceeds by the jump pairs between the blocks. And the jumps will be characterized by some renormalized jump rates and the jump length only. The similar character of the particle migration results in the similar expressions for the diffusion coefficients. The analytical expressions derived for the case of the patchwise lattice are the modified expressions obtained for the heterogeneous square lattice [3]. These expressions relate the kinetic quantities D_j and D_c with the equilibrium thermodynamic quantities as follows:

$$\begin{aligned} D_j &= \nu_d L_z^2 P_{00} P_z^{<} e^{\mu}/\theta, \\ D_c &= \nu_d L_z^2 P_{00} P_z^{<} e^{\mu}/\chi_T, \quad \theta < 1/2, \end{aligned}$$

and

$$\begin{aligned} D_j &= \nu_d L_{z'}^2 P_{00} P_{z'}^{>} e^{\mu}/\theta, \\ D_c &= \nu_d L_{z'}^2 P_{00} P_{z'}^{>} e^{\mu}/\chi_T, \quad \theta > 1/2. \end{aligned} \tag{5}$$

Here

$$P_z^{<} = \frac{1}{z-1}\left(z - 1 - n_d - n_d^2 - n_d^3 - \cdots - n_d^{z-1}\right)$$

$$P_{z'}^{>} = \frac{1}{z'-1}\left(z' - 1 - h_s - h_s^2 - h_s^3 - \cdots - h_s^{z'-1}\right)$$

$P_{00} = \langle h_i h_j \rangle$ is the probability to find a pair of empty s and d NN sites; $z = 4l = 8$ is the number of d sites surrounding an s patch, and $z' = 2l^2 = 8$ is the number of s sites in two s patches; n_d, n_s are the average occupancies of the d and s sites; L_z^2 and $L_{z'}^2$ stand for the mean square displacements and $h_d = 1 - n_d$, $h_s = 1 - n_s$.

It should be noted the following. The analytical expressions derived for the inhomogeneous lattices work perfectly because all NN sites for the d and s sites are equivalent. The jumping particles occupy them with equal probabilities. In the patchwise lattice, the NN sites are not equivalent, and particles occupy these sites with different probabilities. The probabilities depend on the distance between the initial and final sites. The more distant sites give smaller contribution to the total displacement. Really, the quantities L_z, $L_{z'}$, z, and z' should be considered as the fitting parameters of the approach.

IV. Monte Carlo simulations

For the kMC simulations, we used a 2D square arrangement of $M = 4096$ sites with periodic boundary conditions. The initial particle configurations are generated by placing $M\theta$ particles on the randomly chosen sites. The initial configurations $\{n_i\}$ are equilibrated by the first idle kMC run.

 ISBN: 978-1-61208-303-2

To simulate the particle diffusion one should define the rate of particle jumps, the so-called transition algorithm. We assume that the particles perform thermally activated jumps to their NN empty adsorption sites. A particle should surmount the potential barrier separating the initial and final sites. The activation energy is given by the difference between the saddle point energy $\varepsilon_{sp}(=0)$ and the initial state energy ε_i. Usually, the interaction between the activated particle at the saddle point and its NNs is neglected. We select the well established expression for the jump rate derived in the transition state theory [6], [7]

$$\nu_{if} = \nu_0 \exp\left(-\varepsilon_i + \varphi \sum_{k=1}^{4} n_k\right). \quad (6)$$

Here ν_{if} is the jump rate from the initial ith site to the NN final fth site; the summation is carried out over the NNs of the initial site and $\varepsilon_i = \varepsilon_{d,s}$ depending on the type of the initial site. Here and henceforth we use the system of units with $k_B T = 1$.

The jump rate is the same for all possible jumps from the ith site. The repulsive interaction increases and the attractive one decreases the particle energy and the jump rate.

For the kMC simulations we use the BKL algorithm [4]. The algorithm operates in a space of possible events. In contrast to the standard technique, where we consider fixed time intervals at which a jump may occur with a certain probability, the BKL algorithm randomly selects a jump out of all possible events and subsequently associates the number of clock ticks that must be passed for the event to take place. There are no rejected attempts, which results in a higher efficiency of the kMC simulations. We used the kMC simulations for the calculations of the tracer and jump diffusion coefficients, adsorption isotherms, the pair NN correlation function P_{00}, and the isothermal susceptibility

$$\chi_T = N^{-1} \sum_{ij} \langle (n_i - \theta)(n_j - \theta) \rangle. \quad (7)$$

The Fickian diffusion coefficient D_c is calculated via the Kubo–Green equation [8]

$$D_c = \theta D_j / \chi_T. \quad (8)$$

The values of the energetic parameters used for the kMC simulations are the same for all dependencies: $\varepsilon_d - \varepsilon_s = 6$, $\varphi = -2.5, -2, \ldots, 2.5$. In order to obtain accurate values of the necessary quantities, runs of 10^6 kMC steps for up to 5×10^5 different initial configurations were performed.

V. Results and Discussion

The coverage dependencies for the tracer diffusion coefficient $D_t(\theta)$ are plotted in Figures 2 and 3 for the repulsive and attractive lateral interaction, respectively. As it was mentioned above, the tracer diffusion coefficient describes the behavior of the tagged particles. For the homogeneous systems D_t is a monotone decreasing convex function of the surface coverage θ. In the heterogeneous lattices, the dependencies

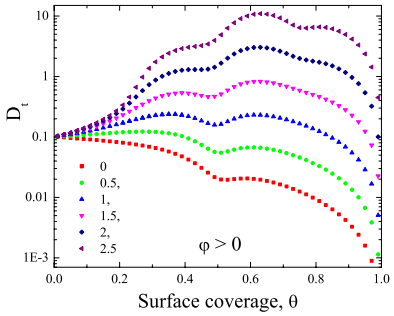

Fig. 2. The coverage dependencies of the tracer diffusion coefficient, D_t, for the repulsive interaction $0 \le \varphi \le 2.5$. Symbols denote the kMC data.

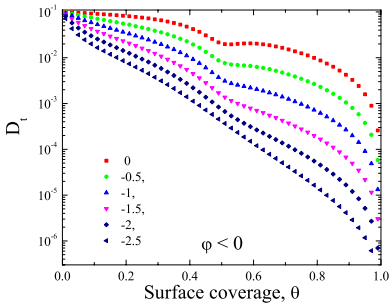

Fig. 3. The coverage dependencies of the tracer diffusion coefficient, D_t, for the attractive interaction $-2.5 \le \varphi \le 0$. The notations are the same as in the previous Figure 2.

$D_t(\theta)$ have minimum at the stoichiometric coverage $\theta = 1/2$. The nature of this minimum can be explained as follows. At this coverage, all d sites are filled and the overwhelming majority of the jump sequences are unsuccessful. Particles jump to the shallow sites and return back. The minimum is a characteristic feature for the tracer and jump diffusion coefficients for many heterogeneous lattices of different geometries and dimensions. We have two independent sets of data for the jump diffusion coefficient: the kMC data and the analytical dependencies 5. They are plotted as symbols and solid lines, respectively, in Figures 4 and 5. The coverage dependencies have qualitatively the same behavior as the corresponding dependencies for the tracer diffusion coefficient. As in the previous case, the dependencies $D_j(\theta)$ have minimum at the stoichiometric coverage $\theta = 1/2$.

There is a good coincidence of the kMC data with the analytical dependencies 5. The expressions give a qualitatively correct description of the coverage dependencies in the whole coverage region for the wide region of the lateral interaction.

In Figures 6 and 7, we present the coverage dependencies for the Fickian diffusion coefficient $D_c(\theta)$. The dependencies have maximum at the half coverage $\theta = 1/2$ for the weak lateral interaction. The dependence $D_c(\theta)$ is symmetrical for the Langmuir lattice gas, i.e. $\varphi = 0$. But the lateral interaction spoils the symmetry. The limiting values of the

 ISBN: 978-1-61208-303-2

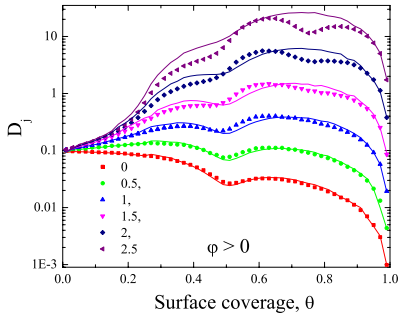

Fig. 4. The coverage dependencies of the jump diffusion coefficient, D_j, for the repulsive interaction $0 \leq \varphi \leq 2.5$ as indicated. Symbols denote the kMC data. The solid lines are analytical dependencies 5.

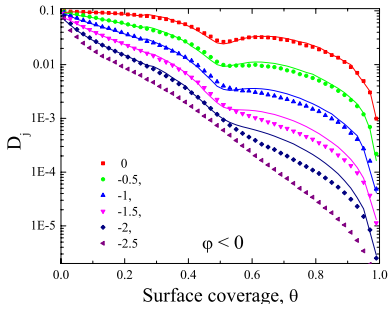

Fig. 5. The coverage dependencies of the jump diffusion coefficient, D_j, for the attractive interaction $-2.5 \leq \varphi \leq 0$. The notations are the same as in previous Figure 4.

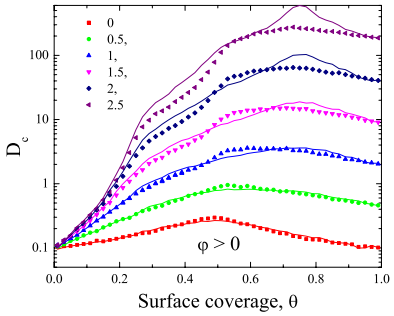

Fig. 6. The coverage dependencies of the Fickian diffusion coefficient, D_c, for the repulsive lateral interaction $0 \leq \varphi \leq 2.5$ as indicated. The notations are the same as in previous Figure 4.

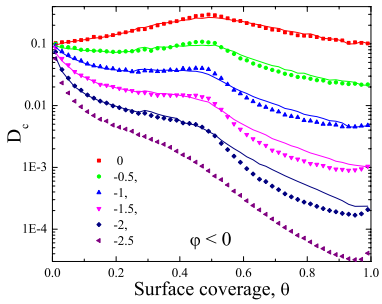

Fig. 7. The coverage dependencies of the Fickian diffusion coefficient, D_c, for the attractive lateral interaction $-2.5 \leq \varphi \leq 0$ as indicated. The notations are the same as in previous Figure 4.

Fickian diffusion coefficient for the empty and filled lattices are different. On the empty lattice jumping particles do not have NN particles. If $\theta \to 1$, every jumping particle has 3 NNs, which change its jump rate. The ordering in the particle system at the stoichiometric coverages $\theta = 1/4$ and $\theta = 3/4$ produces the additional fine structure and weak maxima on the coverage dependencies of the Fickian diffusion coefficient.

As it was mentioned above, the sites in the patches are located at different distances from the initial site. Then, their participation in the jump successions will be also different. The simplest way to account this difference is to fit the numerical data with the analytical dependencies calculated for the different z and z'. The dependencies D_j and D_c are smooth, slowly varying functions of z and z'. The best coincidence between the kMC and analytical data is achieved for $z = 5$ and $z' = 4$. One can consider them as the effective numbers of the NN sites participating in the particle migration. They are significantly reduced as compared with the exact geometrical values $z = z' = 8$.

VI. Summary

We have investigated the diffusion of particles over the inhomogeneous patchwise lattice with two kinds of the adsorption sites. Such lattices have specific features qualitatively influencing the particle diffusion. The lattice inhomogeneity governs the migration of particles. It imposes a very specific correlation on the particle jumps. The slow and fast jumps collect in the jump successions. The approach developed for the investigations of the particle diffusion in the heterogeneous lattices gives simple analytical expressions for the diffusion coefficients, which describe perfectly the particle migration in many heterogeneous lattices of different symmetry and dimensionality [3]. These expressions perfectly describe the particle diffusion in many heterogeneous lattices with two types of adsorption sites: 1D chain, square, honeycomb, dice, cubic, anisotropic, triangular (see, for example, [9]).

The successions of the correlated slow and fast jumps, performed by single particles, are the main migration acts in the low coverage region $\theta < 1/2$. The successions transfer particles between the d patches. They describe quite well the particle diffusion in this region.

Another type of the jump successions, performed by the two particles, dominates in the high coverage region $\theta > 1/2$. Such jump successions transfer particles between the s patches.

The coverage dependencies of the tracer, center-of-mass and Fickian diffusion coefficients are calculated using the kMC simulations of the particle migration and the theoretical approach based on the conception of jump successions. It should be noted the almost perfect coincidence between the analytical

 ISBN: 978-1-61208-303-2

dependencies and the kMC data in the rather wide region of the lateral interaction $-1.5 < \varphi < 1.5$. The noticeable discrepancies appear for the very strong lateral attractions $|\varphi| > 1.5$. The strong attraction results in the non-uniform distribution of the particles, i.e., the formation of islands of the dense phase with $\theta \to 1$ surrounded by a rarefied LG phase with $\theta \to 0$. The strong lateral repulsion tends to arrange particles in the ordered structures with alternating empty and filled sites. These correlations in the particle distribution should be accounted for the better coincidence of the theory with the kMC simulations.

The analytical expressions 5 can be used for the estimations of the diffusion coefficients for such lattices. The good coincidence demonstrates the correctness of the used approach based on the conception of the correlated jump successions.

The long jump successions control the particle diffusion over different heterogeneous lattices [11], [12]. But, it is salient to emphasize an important difference between the lattices mentioned above and the lattice considered here. The common feature of these quite different heterogeneous lattices (disordered square and triangular lattice) is the existence of an infinite connected cluster of shallow sites. The particles can migrate over the lattices jumping exclusively over the s sites. They perform long sequences of jumps and the diffusion is described by the simple law D_t, $D_j \sim (1 - n_d)^{-1}$. The percolation determines the character of the particle migration on these lattices. These lattices are equivalent for the particle diffusion, and the diffusion coefficients are the same. There is no such infinite connected cluster on the patchwise lattices. The particles perform long jump successions, but the effective length of these succession does not grow with the concentration of the particles trapped in the deep sites n_d. The coefficients D_t and D_j have a minimum at the stoichiometric coverage. The long jump successions transfer particles like ordinary pairs of slow and fast jumps. Only the first slow jump and the final fast jump are really effective. Many fast jumps over the s patches do not give any contribution to the migration. Therefore, the diffusion is described by the corresponding analytical expressions derived for the ordinary jump pairs [3]. It is rather interesting that almost the same expressions with some minor modifications describe the particle diffusion in the patchwise lattice, which looks very different from the above mentioned heterogeneous lattices.

It should be noted that the analysis and conclusions have a general character. One should expect that the results obtained for this lattice can be applied for a wide class of the patchwise surfaces. The specific character of the particle migration by the sequences of the jump pairs should not change considerably on the lattices with patches of the irregular forms and different sizes. The cardinal properties of the lattices, as the lattice symmetry and dimensionality, play a minor role when diffusion is determined by the long jump successions.

The main advantage of the proposed approach is the unified description of the particle diffusion in different heterogeneous lattices. The theoretical expressions for the diffusion coefficients give good description of the particle diffusion in the different heterogeneous structures. The coincidence between the analytical and numerical data is really satisfactory despite the numerous approximations made during the derivation of the expressions.

ACKNOWLEDGMENT

This work has been supported in part by the grants P108/12/1941 of the GACR and TA01010517 of the TACR.

REFERENCES

[1] S. R. Ross and J. R. Olivier, “On physical adsorption. XII. The adsorption isotherm and the adsorptive energy distribution of solids,” J. Phys. Chem., vol. 65, April 1961, pp. 608-615, doi: 10.1021/j100822a005.

[2] “Equilibria and dynamics of gas adsorption on heterogeneous solid surfaces”, W. W. Rudzinski, W. A. Steele, and G. Zgrablich, Eds., Amsterdam: Elsevier 1997.

[3] A. Tarasenko, L. Jastrabik, and T. Muller, “Modeling diffusion on heterogeneous lattices: Derivation of general analytical expressions and verification for a two-dimensional square lattice,” Phys. Rev. B, vol. 75, April 2007 pp. 085401(11), doi: 10.1103/PhysRevB.75.085401.

[4] A. B. Bortz, M.H. Kalos, and J.L. Lebowitz, ”A new algorithm for Monte Carlo simulations of Ising spin systems”, J. Comput. Phys., vol. 17, Jan. 1975, pp. 10-18, doi: 10.1016/0021-9991(75)90060-1.

[5] Th. Niemeyer and J. M. J. van Leeuwen, “Wilson theory for 2-dimensional Ising spin systems”, Physica, vol. 71, Jan. 1974, pp. 17-40, doi: 10.1016/0031-8914(74)90044-5.

[6] M. G. Evans and M. Polanyi, “Some applications of the transition state method to the calculation of reaction velocities, especially in solutions”, Trans. Faraday Soc., vol. 31, March 1935, pp. 875-894, doi: 10.1039/TF9353100875.

[7] H. Eyring, “The activated complex in chemical reactions”, J. Chem. Phys., vol. 3, Feb. 1935, pp. 107-115, doi: 10.1063/1.1749604.

[8] D. Forster, “Hydrodynamic Fluctuations, Broken Symmetry and Correlation Functions”, London: Benjamin 1975.

[9] A. Tarasenko and L. Jastrabik, ”Diffusion in heterogeneous lattices”, Appl. Surf. Sci., vol. 256, June 2010, pp.5137-5144, doi: 10.1016/j.apsusc.2009.12.076.

[10] A. Tarasenko and L. Jastrabik, “Diffusion of particles over anisotropic heterogeneous lattices”, Physica A, vol. 391, April 2012, pp. 1048-1061, doi: 10.1016/j.physa.2011.11.006.

[11] A. Tarasenko and L. Jastrabik, “Diffusion of particles on an inhomogeneous disordered square lattice with two non-equivalent sites”, Surf. Sci., vol. 602, Aug. 2008, pp. 2975-2982, doi: 10.1016/j.susc.2008.07.037.

[12] A. Tarasenko and L. Jastrabik, “Diffusion of particles over triangular inhomogeneous lattice with two non-equivalent sites”, Physica A, vol. 388, Feb. 2009, pp. 2109-2121, doi: 10.1016/j.physa.2009.02.009.

 ISBN: 978-1-61208-303-2

On Electronic Photoemission from Irradiated C_{60}

P.-G. Reinhard
Institut für Theoretische Physik 2
Universität Erlangen-Nürnberg
Erlangen, Germany

P. Wopperer, P. M. Dinh, E. Suraud
Laboratoire de Physique Théorique
Université Paul Sabatier
Toulouse, France
e-mail: suraud@irsamc.ups-tlse.fr

***Abstract*—We analyze the angular distribution of photoemission (PAD) from irradiated C_{60} clusters focusing on the impact of resonances on emission properties. We make a prospective investigation in terms of a widely used jellium approach, developing an improved version thereof. The jellium allows a simple access in terms of reduced dimension, which is a priori justified by the high degree of symmetry of C_{60}. We show that the PAD is strongly affected by optical resonances, an effect, which would be certainly even enhanced if using a more realistic description of the ionic background.**

Keywords*—C_{60}, *optical resonances, photoemission, jellium model, time-dependent density-functional theory.

I. INTRODUCTION

Photo-induced reactions constitute a key tool to explore the properties of molecules and clusters. Detailed measurements of the emitted electrons provide useful data for analyzing irradiation dynamics. We think here, in particular, of their kinetic energies and angular distributions, coined Photo-electron Angular Distributions (PAD) [1], [2]. Such measurements have a long history in cluster physics [3], [4], [5], [6]. The steady upgrades of light sources and target setups now allow to gather such data with high precision in a large variety of systems [7], [8], [9], and even to analyze dynamical features [9]. Amongst these many studied systems is also the much celebrated fullerene C_{60} [10], which can be viewed as a particularly symmetric large molecule or as a cluster. This interesting system has also been analyzed with respect to photo-emission properties [9]. Although it is rather convenient to handle in experiments, C_{60} remains a demanding object for a theoretical description, particularly if one aims to analyze its dynamics in full detail. However, the increasing number of experimental results calls for more systematic theoretical analysis of the dynamical response to irradiation, especially in terms of the properties of emitted electrons.

In this contribution, we consider, in particular, the PAD on C_{60} and analyze it as a function of laser frequency. The aim is to investigate the relation between PAD and the optical excitation spectrum, especially its resonances. The optical response is the first important observable because it provides the entrance door for the coupling of a system to light pulses. The detailed analysis of the structure of the optical response is thus the crucial first step. In particular, its resonances strongly influence ionization dynamics [11]. For a first exploration, we choose as simple approach a spherical jellium profile as model for the ionic background. This can be justified by the fact that the highly regular shape of C_{60} is close to spherical symmetry and because we restrict ourselves to rather short laser pulses during which ionic motion can be neglected. Moreover, we remind that experiments in gas phase deal with an isotropic ensemble of cluster orientations. This, in turn, requires involved orientation averaging when dealing with detailed ionic background [12]. Spherical jellium represents as such an isotropic system and so provides a simple way to account for the necessary orientation averaging. As a further technical advantage, the spherical jellium background allows us to use a cylindrically symmetric approximation for describing electronic wavefunctions, which represents enormous computational savings and so allows systematic studies. The theoretical description of electrons relies here on Time-Dependent Density-Functional Theory (TDDFT) [13] at the level of Time-Dependent Local-Density Approximation (TDLDA) with the xc-functional of [14] and LDA augmented by an average Self-Interaction Correction [15]. Electronic wavefunctions are discretized on a cylindrical grid and absorbing boundary conditions are used to remove gently the escaping electrons [16], [17], which also provides a simple estimate of the PAD [18].

The paper is outlined as follows: Section II introduces a spherical jellium model for C_{60} with soft jellium boundaries. The obtained values for the Ionization Potential (IP) and the HOMO-LUMO gap are discussed as a function of the model parameters and compared to experimental results. The following section, Section III, discusses the structure of the absorption spectrum determined within the TDLDA approach for the presented jellium model and points out the main features in the spectrum such as resonances and the collective Mie surface plasmon. Section IV analyzes in detail the impact of optical resonances on photoemission observables, e.g., on total ionization and angular distribution of emitted electrons. Thereby, the molecule is irradiated by a femtosecond laser pulse with frequencies tuned around the resonances above the IP.

II. THE JELLIUM BACKGROUND

The spherical jellium model for C_{60} has been used since long because it is an efficient approach for many principle studies, for often used parametrizations see [19], [20]. A slight disadvantage of these jellium models is that they deliver an electronic shell closure at electron number $N_{\rm el} = 260$, rather far away from the experimental $N_{\rm el} = 240$. (The latter comes from the fact that each carbon atom provides 4 valence electrons taking part in binding which altogether make 240 active electrons.) Not only this, the steep jellium boundaries are not well suited for computations using a grid representation as we do.

In order to have a robust jellium model usable on finite size meshs, the model should display a smooth transition from the homogeneous bulk density to zero. This can be achieved

 ISBN: 978-1-61208-303-2

TABLE I. POTENTIAL PARAMETER v_0, IP AND HOMO-LUMO GAP FOR THE THREE DIFFERENT SURFACE WIDTHS σ UNDER CONSIDERATION. THE LAST LINE INDICATES THE EXPERIMENTAL VALUES FOR IP AND GAP.

σ [a_0]	v_0 [Ry]	IP [Ry]	gap [Ry]
0.5	1.5	0.56	0.16
0.6	1.9	0.56	0.12
0.7	2.38	0.56	0.07
exp.		0.57	0.13

by smoothing the step functions in the steep jellium model to Woods-Saxon profiles leading to the following ansatz for the pseudo-density $\rho_{\rm jel}$ and the pseudo-potential $V_{\rm shift}$ of the jellium model:

$$\rho_{\rm jel}(r) = \frac{3}{4\pi r_s^3}\frac{1}{1+\exp((r-R_0)/\sigma)}\frac{1}{1+\exp((R_i-r)/\sigma)} \quad , \tag{1}$$

$$V_{\rm shift}(r) = v_0\frac{1}{1+\exp((r-R_0)/\sigma)}\frac{1}{1+\exp((R_i-r)/\sigma)} \quad , \tag{2}$$

$$R_0 = R+\frac{\Delta R}{2} \quad , \quad R_i = R-\frac{\Delta R}{2} \quad . \tag{3}$$

The pseudo-density $\rho_{\rm jel}$ is the positively charged counterpart of the electron density forming both together a neutral system. In addition to the Coulomb potential of $\rho_{\rm jel}$, we also consider a pseudo-potential $V_{\rm shift}$, which consists in a localized potential shift to put energetic relations right. Similar as for the previous steep jellium models, we choose $R = 6.7\,a_0$ and $r_s = 1.15236\,a_0$. New is the parameter for the surface width σ. It allows some further fine tuning. But it should also be chosen sufficiently large for numerical convenience. We will consider a series of σ. The jellium width ΔR is to be chosen such that the total charge fits N, i.e.

$$4\pi\int dr\, r^2\,\rho_{\rm jel}(r) = N \quad . \tag{4}$$

Actually, we find with the soft jellium model a shell closure at $N_{\rm el} = 238$, thus very close to the expected value of $N_{\rm el} = 240$. Thus we choose for the background $N = N_{\rm el} = 238$. Altogether we have the model parameters

$$N = 238\ ,\ r_s = 1.15236\,a_0\ ,\ R = 6.7\,a_0 \quad \sigma = 0.5,\ 0.6,\ 0.7\,a_0 \quad . \tag{5}$$

The radius width ΔR is adjusted according to condition (4). We consider three models with surface widths $\sigma = 0.5$, 0.6, and $0.7\,a_0$. The strength v_0 of the potential shift depends on σ. The v_0 is listed in Table I together with IP and HOMO-LUMO gap. The table shows that the IP is robust and already well tuned by the choices for r_s, R and v_0. The HOMO-LUMO gap is extremely sensitive to the softness parameter σ. The experimental data are also found in Table I for comparison. It indicates that $\sigma = 0.6\,a_0$ is the preferred choice concerning the HOMO-LUMO gap.

III. DIPOLE SPECTRA

As a first step, we will look at the optical absorption spectrum of C_{60} in terms of the dipole strength. To this end, we use TDDFT with the techniques of spectral analysis as outlined in [21]. We compare the results for the three values for σ under consideration.

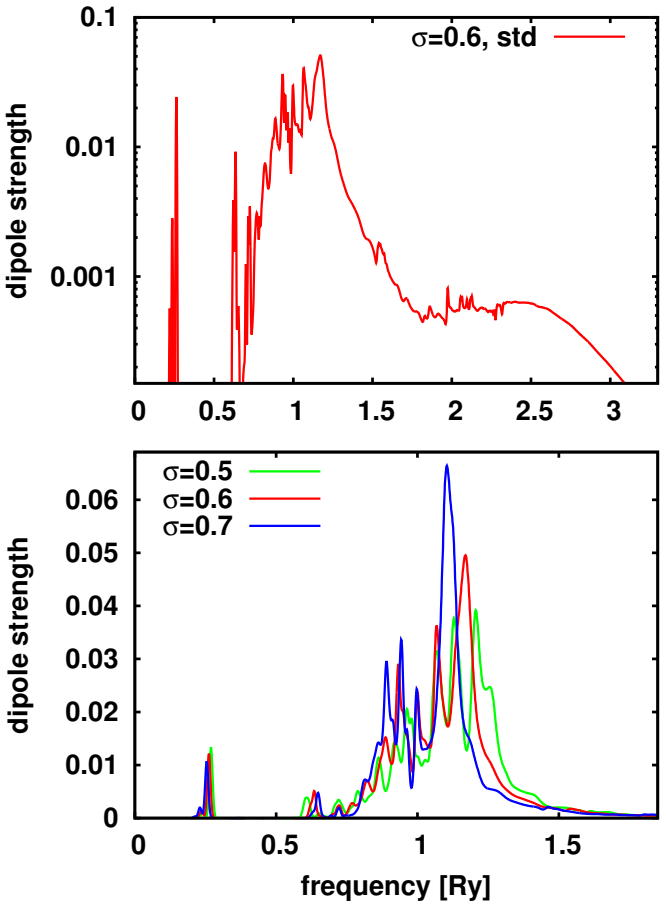

Fig. 1. Dipole strength for C_{60} in the soft jellium model under varying conditions. The lower panel shows the strength on a linear scale and compares the three cases with different surface width σ. The upper panel shows the spectrum for the standard case ($0.6\,a_0$) on logarithmic scale and for a broader frequency range.

Figure 1 shows the results. The low energy peak at about 0.3 Ry is surprisingly robust against variation of σ in spite of the fact that the HOMO-LUMO gap is strongly dependent on σ. This indicates that this low energy peak is of collective nature. The Mie surface plasmon peak resides around 1 Ry. It is strongly fragmented and broadened. The largest dependence on σ is seen in the upper branch of the surface plasmon peak. There is some down shift with increasing σ and a strong change of fragmentation. Only the case $\sigma = 0.7\,a_0$ displays one clean upper peak while the two other σ produce double and triple peaks. We have also checked the impact of box size and number of absorbing points. Comparing with results from a 50% larger box and another case with twice as much absorbing points (32 instead of 16 points). The spectral structures are practically independent of the box. Thus we have to conclude that they are a physical feature of the given jellium model. As these structures appear in the particle continuum, they correspond to scattering resonances. The upper panel shows the spectrum in logarithmic scale and over a larger frequency band. This points out even better the dominance of the Mie surface plasmon and it indicates furthermore a broad resonance

 ISBN: 978-1-61208-303-2

at about 2.5 Ry, probably a volume plasmon.

IV. Trend of anisotropy and emission time with laser frequency

The full angular distributions $d\sigma/d\Omega$ are functions of the angles θ and ϕ for each laser frequency $\omega_{\rm las}$. Spherical symmetry reduces this to a function of θ only. Even then, it is extremely hard to study systematic trends with such bulky observables. Fortunately, it turns out that the most characteristic pattern in the regime of weak laser excitations (one photon processes) is the anisotropy β_2. Indeed, the PAD cross section $d\sigma/d\Omega$ can be shown to be proportional to $1 + \beta_2 P_2(\theta)$, where P_2 is the second Legendre polynomial and θ the angle with respect to the laser polarization axis [12]. We will now investigate the anisotropy β_2 as function of laser frequency. For reasons of numerical convenience, we use here the softest model with $\sigma = 0.7\,{\rm a}_0$. The laser frequencies used here are all in a range above the IP of C_{60} and the intensities are moderate such that we deal with one-photon processes throughout. The PAD can thus be simply analyzed by means of the anisotropy parameter β_2.

Figure 2 shows observables from electron emission computed with the soft jellium model with surface width $\sigma = 0.7\,{\rm a}_0$. The intensity was kept constant throughout all frequencies. The upper panel repeats the dipole strength from TDLDA and compares it with the strength of the pure one-particle-one-hole ($1ph$) states as deduced from the static calculations. This shows that the Mie surface plasmon peak resides in a vacuum of $1ph$ states. A bunch of fragmented strength below the resonance is caused by the coupling to the many $1ph$ states there. The middle panel shows the total ionization $N_{\rm esc}(\omega_{\rm las})$. It follows nicely the trends of the dipole strength.

The lower panel finally shows the anisotropy $\beta_2(\omega_{\rm las})$. Large fluctuations are seen at the lower frequency side where we have the $1ph$ dominated states in the spectrum (see upper panel) and also the values are generally larger in this region. Above that $1ph$ region, the values drop to lower level and remain rather constant over a broad range of $\omega_{\rm las}$. The first three vertical dashed lines mark two minima and one maximum of β_2 while the fourth vertical line goes through the resonance peak. It is interesting to note that the minima of β_2 are related to the position of strongest slope upwards wings of the dipole strength before a peak. The maximum in β_2 seems to be related to a minimum in the dipole strength. Nothing special for β_2 can be spotted at the resonance frequency and along the right wing of the resonance.

It is known that the time profile of dipole oscillations and ionization depends on the laser frequency in relation to system resonances, see e.g. [22]. In order to allow tracking a frequency dependence, we reduce the time profile of ionization $N_{\rm esc}(t)$ to three key values: maximum slope $\partial_t N_{\rm esc}$, the time $t_{\rm max}$ at which maximum slope is reached, and the "final slope" $\partial_t N_{\rm esc}\big|_{t=t_{\rm fin}}$ at the end of the simulation time. The definition is illustrated in Figure 3. We see that the off-resonant case shows significant emission only during the laser pulse of 500/Ry while the resonant case is accompanied by long persisting dipole oscillations, which lead to emission after the pulse has died out. This feature is characterized by the final slope. Zero final slope indicates an off-resonant excitation. The figure also

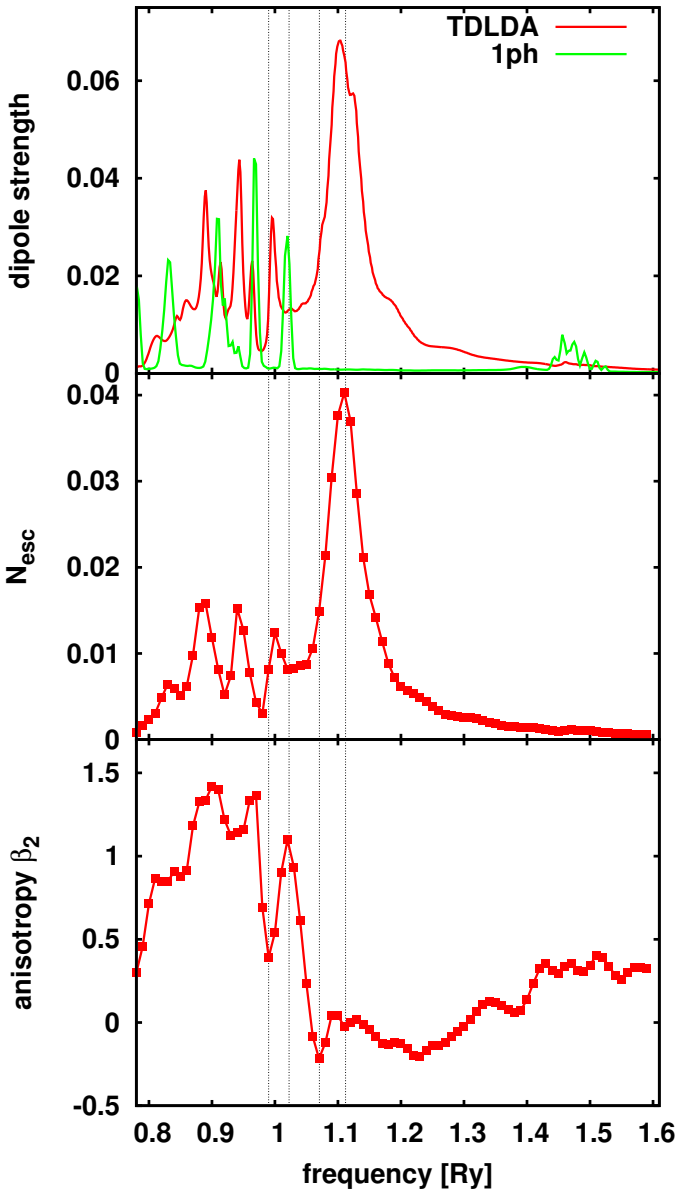

Fig. 2. Properties of electron emission after laser excitation as function of laser frequency $\omega_{\rm las}$. The soft jellium model with $\sigma = 0.7$ a_0 is used. The laser pulse had field strength $E_0 = 0.00034\,{\rm Ry/a_0}$ and pulse length $500/$ Ry. Lower: anisotropy β_2. Middle: ionization. Upper: dipole strength for full TDLDA and for pure $1ph$ excitations.

indicates that resonant emission is associated with some delay leading to later $t_{\rm max}$.

Figure 4 shows the three key values of ionization as function of laser frequency. The upper panel shows the time $t_{\rm max}$ where $N_{\rm esc}(t)$ has maximum slope. Peaks in dipole strength (resonances) are clearly related to delay in emission thus larger $t_{\rm max}$. However, the small peaks in the $1ph$ region make a much larger effect than the broad Mie surface plasmon peak. A similar behavior is seen in the maximum (relative) slopes as such, which are shown in the middle panel. It is plausible that large $t_{\rm max}$ correlate with low maximum slopes and vice versa. Large fluctuations reside in the region of $1ph$ strength. The lower panel shows the final slopes, evaluated at

 ISBN: 978-1-61208-303-2

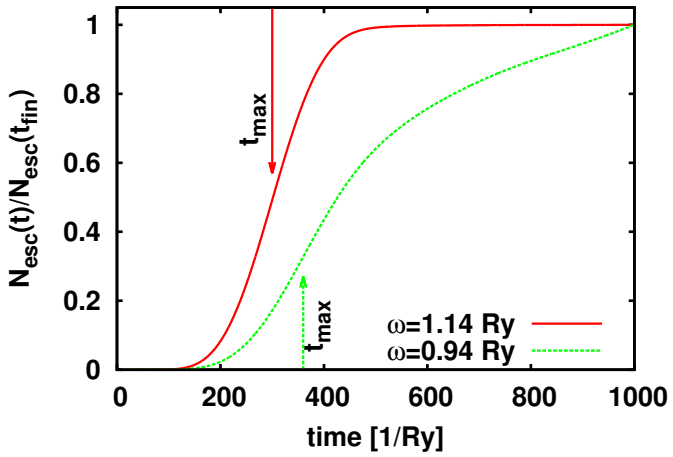

Fig. 3. Time evolution of ionization $N_{\rm esc}$ for one resonant ($\omega_{\rm las} = 0.94\,$Ry) and one off-resonant ($\omega_{\rm las} = 1.14\,$Ry) case. The time $t_{\rm max}$ at which maximum slope occurs is indicated for each case. The maximum and the final slope can be read off visually.

the end of the computation ($t_{\rm final} = 1000$/Ry). It indicates the amount of post-oscillations, which persist after the laser pulse is over. And again, we see large effects in the $1ph$ region, none at all at Mie plasmon resonance.

We have seen in the above discussion that the position of $1ph$ states relative to the resonance peak may have a decisive impact on the pattern of β_2 and slopes. We check this by comparing the soft jellium model used above ($\sigma = 0.7\,{\rm a}_0$) with the steep jellium model from Bauer et al [20]. The results are shown in Figure 5. The resonance position for the steep jellium is a bit higher. This is due to the fact that we use here 260 electrons, instead of 238 in the soft jellium. The important point is the relative position between $1ph$ strength and the resonance. And here it is clear that the steep jellium produces a much larger overlap between resonance and $1ph$ band. Moreover, the $1ph$ spectra of steep jellium are less bunched than those of soft jellium. (This may be a result from the coarse numerical reproduction of steep jellium on a finite grid.) The resonance is thus more strongly fragmented and more fuzzy for steep jellium. The anisotropy seems to yield at first glance different pattern. But the qualitative findings are the same: we see high β_2 with large fluctuations in the energy range of the $1ph$ bands but a smaller and more constant β_2 above the band. The final slope (right lower panel) confirms this sensitivity to the $1ph$ region. This also holds for the maximum slope and time thereof where fluctuations are correlated with the $1ph$ band and constant trends above. However, in these latter two observables we see much smaller fluctuations for the steep jellium. Altogether, this comparison shows the extreme sensitivity of the results to the detailed spectral fragmentation. The effects may be now understood qualitatively. But a quantitative prediction will require a very reliable model of C_{60}.

V. Conclusion

This first investigation, although preliminary, already provided several interesting conclusions. The soft jellium model delivers an acceptable description of C_{60} with $N_{\rm el} = 238$ electrons while allowing conveniently large grid spacings.

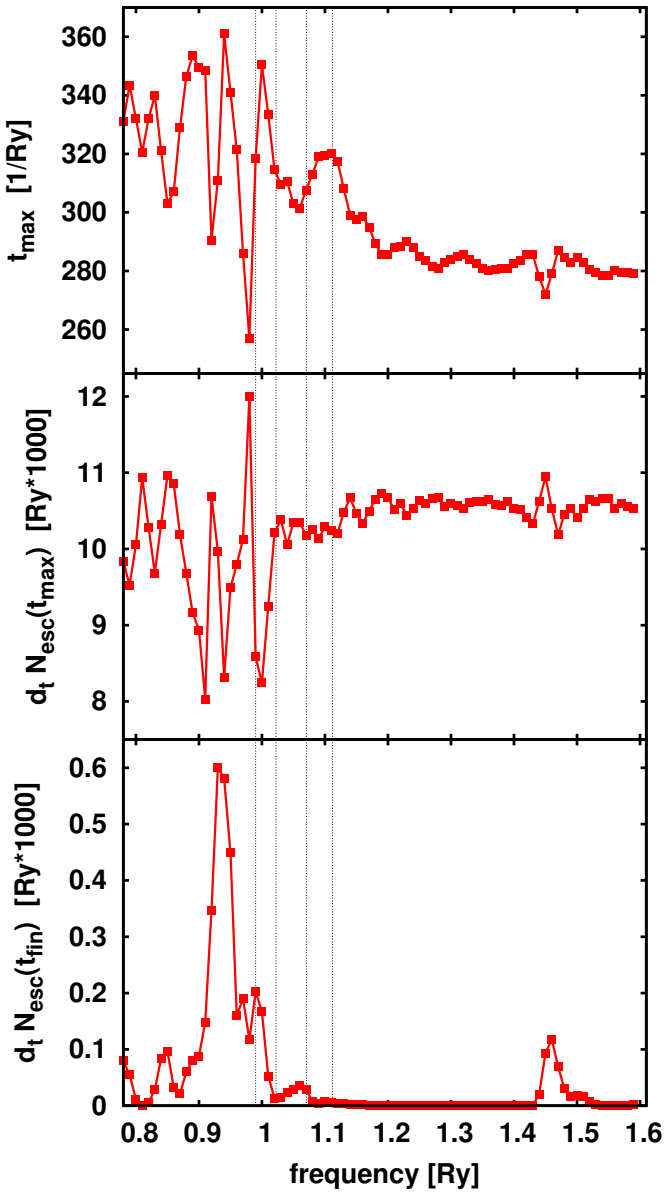

Fig. 4. Properties of the time profile of ionization as function of laser frequency $\omega_{\rm las}$. Jellium model and laser conditions were the same as in Figure 2. Lower: Final slope of $\partial_t N_{\rm esc}\big|_{t=t_{\rm fin}}$. Middle: maximum slope $\partial_t N_{\rm esc}$. Upper: time of maximum slope $t_{\rm max}$. The vertical lines are placed at the same frequencies as in Figure 2 to allow better comparison.

There is a significant fragmentation (depending on model parameters) of the surface plasmon resonance, which is caused by a high density of $1ph$ resonances in the continuum. A possible weakness is that the spherical model leads to a too pronounced structure due to the bunching of s.p. levels into degenerated angular momentum blocks. The lower symmetry of the actual fullerene structure may deliver a more diffuse sequence of resonances, which, in turn, could allow the surface plasmon to look more like one broad resonance peak. The question is what effect the bunching may have on the trends of the anisotropy parameter β_2. Comparison of results from steep with soft jellium indicates that more diffuse $1ph$ spectra reduce the amplitude of the fast fluctuations in anisotropy

 ISBN: 978-1-61208-303-2

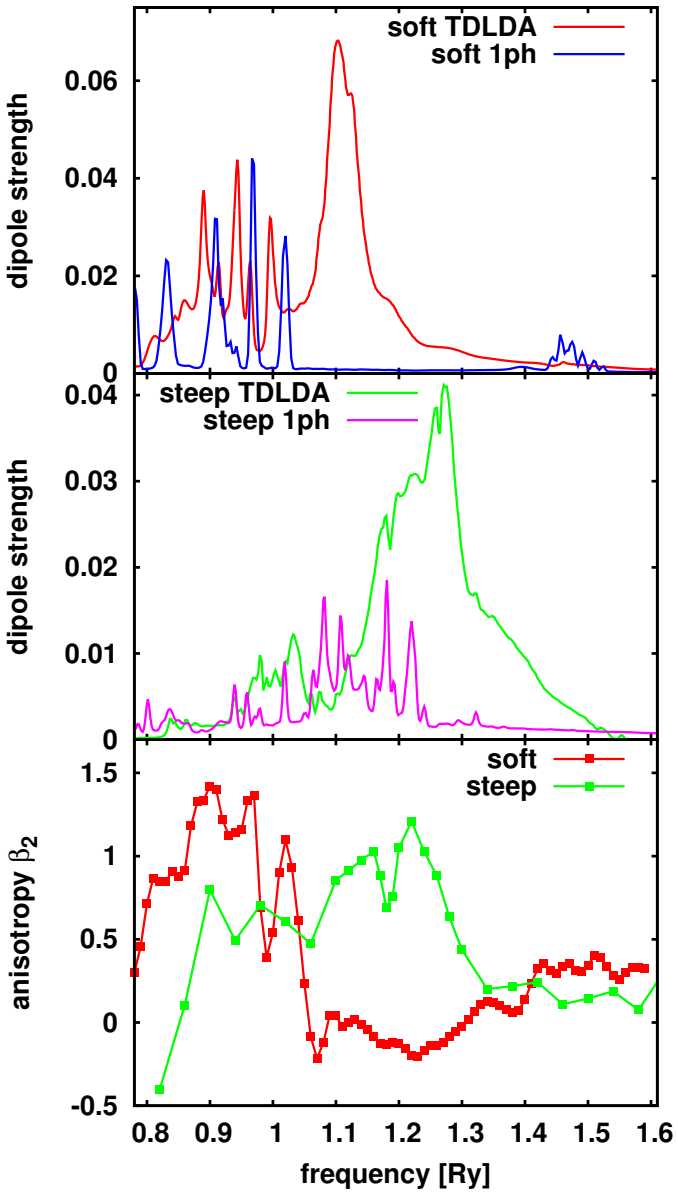

Fig. 5. Similar as Figure 2, but here comparing the soft jellium model $\sigma = 0.7a_0$ (red lines) with the steep jellium model of [20] (green lines). The dipole spectra for the two cases are shown in separate panels each one comparing full TDLDA with pure $1ph$ spectra. The lowest panel compares the anisotropies β_2 between steep and soft jellium.

and slopes. The soft jellium model allows robust and stable calculations of basic emission properties as anisotropy and emission time. The results confirm a relation between dipole strength and minima or maxima in the anisotropy as function of laser frequency. These effects are, however, much more pronounced in the regime of $1ph$ fragmentation than in the surface plasmon resonance. This qualitative result seems to be confirmed by calculations in the steep jellium model. The next step is certainly to explore these trends in a more detailed manner using a full ionic background and thus a full 3D description of the system. The first results of such more complete computations are presently being produced.

ACKNOWLEDGMENT

The authors thank Institut Universitaire de France and Humboldt foundation for support.

REFERENCES

[1] D. Turner, *Molecular Photoelectron Spectroscopy*. Wiley, New York, 1970.

[2] P. Ghosh, *Introduction to photoelectron spectroscopy*. John Wiley and Sons, New York, 1983.

[3] D. G. Leopold and W. C. Lineberger, "A study of the low-lying electronic states of Fe_2 and Co_2 by negative ion photoelectron spectroscopy," *J. Chem. Phys.*, vol. 85, pp. 51–55, 1986.

[4] D. G. Leopold, J. Ho, and W. C. Lineberger, "Photoelectron spectroscopy of mass-selected metal cluster anions. i. Cu_n^-, $n = 1 - 10$," *J. Chem. Phys.*, vol. 86, pp. 1715–1726, 1987.

[5] G. Ganteför, K. H. Meiwes-Broer, and H. O. Lutz, "Photodetachment spectroscopy of cold aluminum cluster anions," *Phys. Rev. A*, vol. 37, pp. 2716–2718, 1988.

[6] K. M. McHugh, J. G. Eaton, G. H. Lee, H. W. Sarkas, L. H. Kidder, J. T. Snodgrass, M. R. Manaa, and K. H. Bowen, "Photoelectron spectra of the alkali metal cluster anions: $Na^-_{n=2-5}$, $K^-_{n=2-7}$, $Rb^-_{n=2-3}$, and $Cs^-_{n=2-3}$," *J. Chem. Phys.*, vol. 91, pp. 3792–3793, 1989.

[7] J. C. Pinaré, B. Baguenard, C. Bordas, and M. Broyer, "Angular distributions in photoelectron spectroscopy of small tungsten clusters: competition between direct and thermionic emission," *Eur. Phys. J. D*, vol. 9, pp. 21–24, 1999.

[8] C. Bartels, C. Hock, J. Huwer, R. Kuhnen, J. Schwöbel, and B. v. Issendorff, "Probing the angular momentum character of the valence orbitals of free sodium nanoclusters," vol. 323, pp. 1323–1327, 2009.

[9] M. Kjellberg, O. Johansson, F. Jonsson, A. V. Bulgakov, C. Bordas, E. E. B. Campbell, and K. Hansen, "Momentum-map-imaging photoelectron spectroscopy of fullerenes with femtosecond laser pulses," vol. 81, p. 023202, 2010.

[10] H. Kroto, "Symmetry, space, stars and C_{60}," *Rev. Mod. Phys.*, vol. 69, pp. 703–722, 1997.

[11] P.-G. Reinhard and E. Suraud, *Introdcution to cluster dynamics*. Wiley-VCH, Berlin, 2003.

[12] P. Wopperer, B. Faber, P. M. Dinh, P.-G. Reinhard, and E. Suraud, "Orientation averaged angular distributions of photo-electrons from free na clusters," vol. 375, pp. 39–42, 2010.

[13] M. Marques, C. Ullrich, F. Nogueira, A. Rubio, K. Burke, and E. Gross, *Time Dependent Density Functional Theory*. Springer Berlin, 2006.

[14] J. P. Perdew and Y. Wang, "Accurate and simple analytic representation of the electron-gas correlation energy," *Phys. Rev. B*, vol. 45, pp. 13 244–13 249, 1992.

[15] C. Legrand, E. Suraud, and P.-G. Reinhard, "Comparison of self-interaction-corrections for metal clusters," *J. Phys. B: At. Mol. Opt. Phys.*, vol. 35, pp. 1115–1128, 2002.

[16] C. A. Ullrich, *J. Mol. Struct. (THEOCHEM)*, vol. 501-502, p. 315, 2000.

[17] P.-G. Reinhard, P. D. Stevenson, D. Almehed, J. A. Maruhn, and M. R. Strayer, "Role of boundary conditions in dynamic studies of nuclear giant resonances and collisions," vol. 73, p. 036709, 2006.

[18] A. Pohl, P.-G. Reinhard, and E. Suraud, "Angular distributions of electrons emitted from Na clusters," vol. 70, p. 023202, 2004.

[19] M. J. Puska and R. M. Nieminen, "Photoabsorption of atoms inside C_{60}," vol. 47, p. 1181, 1993.

[20] D. Bauer, F. Ceccherini, A. Macchi, and F. Cornolti, "C_{60} in intense femtosecond laser pulses: Nonlinear dipole response and ionization," vol. 64, p. 063203, 2001.

[21] F. Calvayrac, P.-G. Reinhard, and E. Suraud, "Spectral signals from electronic dynamics in sodium clusters," *Ann. Phys. (N.Y.)*, vol. 255, pp. 125–162, 1997.

[22] F. Calvayrac, P.-G. Reinhard, E. Suraud, and C. A. Ullrich, "Nonlinear electron dynamics in metal clusters," vol. 337, pp. 493–578, 2000.

 ISBN: 978-1-61208-303-2

Study of Protein Conjugation with Different Types of CdTe Quantum Dots

Jana Chomoucka, Jana Drbohlavova, Petra Businova, Jan Prasek, Jan Pekarek, Jaromir Hubalek
Department of Microelectronics
Brno University of Technology
Brno, Czech Republic
chomoucka@feec.vutbr.cz

Jana Chomoucka, Jana Drbohlavova, Marketa Vaculovicova, Petra Businova, Jan Prasek, Jan Pekarek, Jaromir Hubalek
Central European Institute of Technology
Brno University of Technology
Brno, Czech Republic

Abstract— **In this paper, the interaction between bovine serum albumin (BSA) and water soluble CdTe quantum dots (QDs) modified with different ligands (3-mercaptoacetic acid, thioglycolic acid and glutathione) was studied using the fluorescence spectroscopy. It was found that the presence of QDs led to a strong quenching effect of BSA, which could be explained by a covalent interaction between the protein and the quencher, demonstrating the formation of QDs-BSA bioconjugates.**

Keywords-quantum dots; conjugation; protein; bovine serum albumin; glutathione; 3-mercaptoacetic acid; thioglycolic acid.

I. INTRODUCTION

Semiconductor nanocrystals, also known as quantum dots (QDs), are nano-scaled inorganic particles in the size range of 1–10 nm [1]. Due to their quantum confinement, QDs show unique and fascinating optical properties, such as sharp and symmetrical emission spectra, high quantum yield (QY), good chemical and photo-stability and size dependent emission [2]. So far, QDs have been linked with bio-recognition molecules such as proteins, peptides and nucleic acids, and have been successfully used in biological and medical fields such as immunoassay, DNA hybridization, cell imaging and potential photodynamic therapy [3]. In general, reported QD bioconjugation approaches are mainly based on bifunctional linkage (such as 1-ethyl-3-(3-dimethylaminopropyl) carbodiimide hydro-chloride, EDC hydro-chloride), electrostatic attraction, and biotin–avidin interaction. However, no matter what conjugation approach is used, QDs bioconjugates need to be purified and characterized. The adsorption of protein molecules on nanoparticles (NPs) surface changes their surface functionality, which influences their behavior in biological systems. Moreover, the formation of NP–protein conjugates provides NPs stability over the broad range of pH and ionic strengths. Smaller NPs favor native-like protein structure more strongly, whereas larger NPs provide larger surface area of contact for adsorbed proteins resulting in stronger interactions between proteins and NPs [4]. The efficiency of this interaction can be a decisive factor for the fate of a NP within the biological system. But at the same time, the interaction between QDs bioconjugation is of great importance in biological applications [5].

BSA has been one of the most extensively studied proteins, particularly because of its structural homology with human serum albumin. It was often used as coating reagent to modify the surface of NPs due to its strong affinity to the variety of NPs, such as gold NPs, silica NPs, and QDs. Serum albumins play an important role in the transport of many exogenous and endogenous ligands, binding covalently and reversibly to these ligands and increasing the tumor selectivity of the ligands by enhanced permeation and retention effect. Up to now, QDs modified by BSA have been applied as ion sensors, fluorescence resonance energy transfer, and chemiluminescence resonance energy transfer. Moreover, due to the increasing extension of nanotechnology in biological sciences, it is imperative to develop a detailed understanding how biological entities, especially proteins, may interact with nanoscale particles [6].

In this paper, the interaction between bovine serum albumin (BSA) and water soluble CdTe quantum dots modified with different ligands (3-mercatoacetic acid, thioglycolic acid and glutathione) was studied using fluorescence spectroscopy. It was found that the presence of QDs led to a strong quenching of fluorescence emission, which could be explained by covalent interaction between the protein and the quencher, demonstrating the formation of QDs-BSA bioconjugates [7].

This paper is structured as follows: Section I describes properties of QDs and their bioconjugation approach. Section II represents the synthesis of water soluble CdTe QDs modified with different ligands (3-mercatoacetic acid, thioglycolic acid and glutathione) and their bioconjugation with BSA. The interaction between BSA and CdTe QDs is discussed in Section III, Section IV concludes the paper.

II. MATERIAL AND METHOD

A. Chemicals

All chemicals were purchased by Sigma Aldrich (Czech Republic) in ACS purity unless otherwise stated. Aqueous solutions were prepared using MilliQ water.

B. Synthesis of CdTe QDs

The procedure for synthesis of glutathione (GSH)-capped CdTe QDs was adapted from the work of Duan et al. [8] with slight modifications. The synthesis of 3-mercaptopropionic acid (MPA)-capped CdTe QDs and thioglycolic acid (TGA)-capped CdTe QDs were adapted from the work of Wang et al. [9]. Sodium telluride was used as Te source. Due to the

 ISBN: 978-1-61208-303-2

fact that sodium telluride is air stable, all of the operations were performed in the air avoiding the need for inert atmosphere. The synthesis of CdTe QDs and their subsequent coating were as follows: 114 mg of the $CdCl_2$.2.5 H_2O was diluted with 25 mL of water. During the constant stirring, 65 µL MPA (56 µl TGA or 150 mg GSH), 25 mg of sodium citrate, 2 mL of Na_2TeO_3 solution (c = 0.01 mol/L), and 10 mg of $NaBH_4$ were added into cadmium(II) aqueous solution. 1 M NaOH was then used to adjust the pH to 10 under vigorous stirring. The mixture was kept at 95 °C under the reflux cooling for 3 hours.

C. Bioconjugation of CdTe QDs

1) Electrostatic attraction

BSA can easily conjugate with CdTe QDs by electrostatic attraction. 250 µL of QDs were added to a mixture of 137.5 µL BSA and 92.5 µL phosphate buffered saline (0.01 M, pH 7.4), and the solution stood at room temperature for 2 h. The reaction solution was stored in the refrigerator at 4 °C [10]. The final concentration of QDs was set to 0, 0.5, 1, 1.5, 2 and 5 mg/mL and final concentration of BSA was calculated to be 15 mg/mL.

2) Covalent conjugation

For the conjugation of BSA with CdTe QDs (final concentration 0; 0.5; 1; 1.5; 2 and 5 mg/mL), 100 µL of 0.05 M EDC and 100 µL of 5 mM N-hydroxysuccinimide (NHS) were added to 500 µL of QDs redispersed in 20 mM phosphate buffer (PB) of pH 7.4 and incubated at 32 ºC for 30 min under slight shaking conditions. 200 µL of BSA in 20 mM PB were added to the reaction mixture and further incubated at 32 ºC for 3 h under slight shaking conditions. The solution was kept at 4 ºC overnight to deactivate the remaining EDC-NHS. The unbound protein was removed by centrifugation at 10,000 rpm for 20 min [11]. The final concentration of QDs was set to 0, 0.5, 1, 1.5, 2 and 5 mg/mL and the final concentration of BSA was calculated to be 15 mg/mL.

D. Characterization of CdTe QDs

Photoluminescence spectra were measured at room temperature with Fluorolog, HORIBA Jobin Yvon and quantum yield was calculated with Quanta φ, HORIBA Jobin Yvon.

III. Results and Discussion

A. CdTe QDs characterization

To investigate the behavior of QDs in the presence of BSA, water soluble CdTe QDs were synthesized. We selected three kinds of mercaptan ligands such as MPA, TGA, GSH for the preparation of QDs. The emission spectra of typical CdTe QDs used in this study were measured at excitation wavelength of 380 nm. The emission spectrum is displayed by one emission peak at 620 nm in the case of MPA-capped CdTe QDs, one peak at 506 nm in the case of GSH-capped CdTe QDs and one peak at 540 nm in the case TGA-capped CdTe QDs. All peaks in characterized spectra showed a good symmetry and a narrow spectral width (see Figure 1). The quantum yield of CdTe QDs was evaluated to be 11.5 % in the case of CdTe-MPA, 16.5 % in the case of CdTe-GSH and 7% for CdTe-TGA.

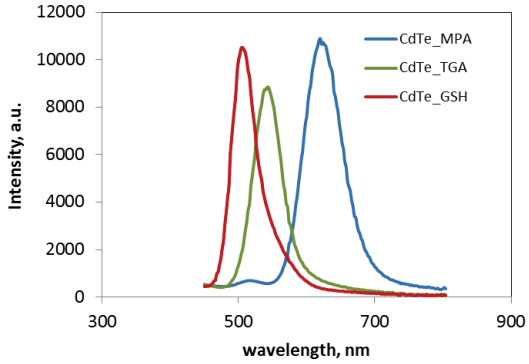

Figure 1. Fluorescence spectra of CdTe QDs capped with MPA, GSH and TGA.

B. The effect of QDs on BSA fluorescence spectra

Fluorescence (FL) quenching efficiency and the aspect of quenching mechanism of the BSA by QDs were studied by FL spectroscopy. CdTe QDs were prepared in aqueous phase using MPA, GSH or TGA as a stabilizer, resulting in the linkage of the thiol groups to the surface of CdTe QDs by SH-Cd coordination, while the functional carboxylic group is free, which can be easily coupled to biomolecules with amino groups, such as proteins, peptides or amino acids. BSA absorption spectrum shows absorption peak in UV region at 280 nm, and FL peak at 328 nm. It was found that the emission of CdTe QDs decreases progressively with increasing concentration of BSA.

1) Electrostatic attraction

The fluorescence intensity of BSA was quenched accompanied by a slight blue shift of the maximum emission wavelength with increasing concentration of CdTe QDs as can be seen in Figure 2 – Figure 4. These figures represent the emission spectra of MPA-QDs conjugation (GSH-QDs, TGA-QDs, respectively) with BSA via electrostatic interaction. The blue shift here indicated that tryptophan residue (BSA component) was in more hydrophobic environment due to the tertiary structural change of albumin. The intrinsic reason for this change might lie in the more flexible conformation of albumin adsorbed on the NPs surface, which favored the access of tryptophan residues to the bulk surface of QDs [12]. The FL quenching is known to occur due to excited state reactions, energy transfer, collisional quenching (dynamic quenching) and complex formation (static quenching). The last two processes are mainly considered. Both dynamic quenching and static quenching reveal the connection of linearity between relative FL intensity (F_0/F) and QDs concentration [13]. The quenching of BSA FL by QDs can be described by Stern-Volmer equation:

$$\frac{F_0}{F} = 1 + K_{SV}[Q] \quad (1)$$

where F_0 and F are FL intensity of BSA in the absence and presence of QDs, respectively, [Q] is QDs concentration and K_{SV} is the Stern-Volmer quenching constant. The F_0/F ratios were calculated and plotted against quencher concentration according to (1). After linear fit, K_{SV} were calculated from the slope of the plots [14]. The results show that the quenching constant K_{SV} is variant with different type of QDs and the higher K_{SV} is, the higher is the quenching effect [15]. The FL intensity decreased more significantly in the case of BSA-QDs than in the case of MPA-QDs or TGA-QDs. The ratios of MPA-QDs bonded with BSA exhibited a quite good linearity with determination coefficient R^2 of 0.9782 (see Figure 5). The Stern-Volmer plot of GSH-QDs quenching properties exhibited linear trend with coefficient of determination R^2 to be 0.9953 and in the case of TGA-QDs the coefficient of determination R^2 was 0.8717. The results suggest that QDs can effectively quench the FL of BSA in a ligand dependent manner.

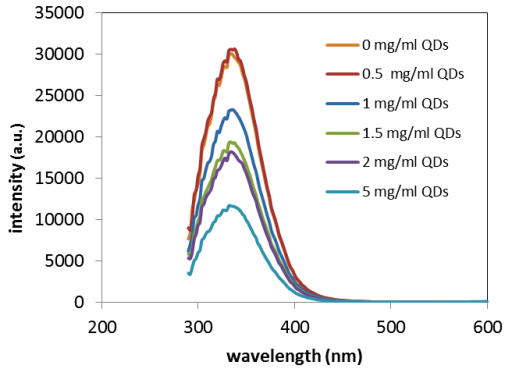

Figure 2. Emission spectra of BSA capped with MPA-CdTe QDs via electrostatic interaction at various QDs concentration.

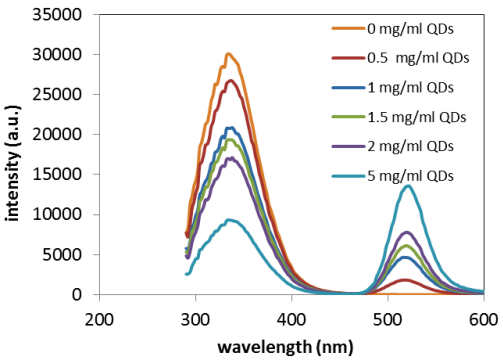

Figure 3. Emission spectra of BSA capped with GSH-CdTe QDs via electrostatic interaction at various QDs concentration.

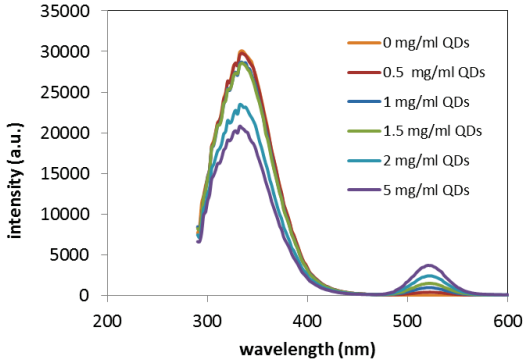

Figure 4. Emission spectra of BSA capped with TGA-CdTe QDs via electrostatic interaction at various QDs concentration.

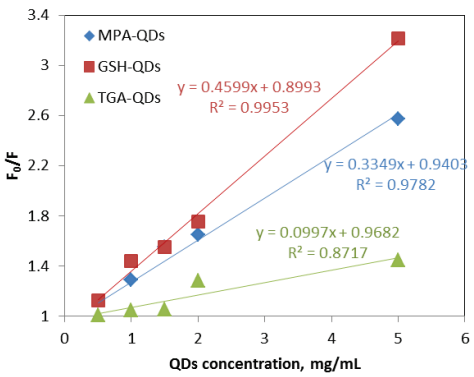

Figure 5. Stern-Volmer plot of BSA FL quenching effect caused by CdTe QDs electrostatic conjugation with BSA.

These results indicated that QDs can effectively quench the FL of BSA in a ligand-dependent manner. Structurally, this is due to the presence of NH_2 and COOH groups in the QDs capping agent, namely MPA (1 × COOH group); GSH (3 × NH_2 and 2 × COOH groups) and TGA (1 × COOH group). Therefore hydrogen bonds can be easily formed between GSH-QDs and BSA. In other words, the number of amino-groups can strongly influence the interactions between BSA and QDs capped with GSH. Therefore, the order of interactions between BSA and QDs is as follows: TGA-QDs < MPA-QDs < GSH-QDs.

2) Covalent conjugation

In the case of QDs covalently bonded with BSA, EDC and NHS were used as coupling agents. Figure 6 – Figure 8 represent the emission spectra of BSA with various concentrations of MPA-QDs, GSH-QDs and TGA-QDs. The FL intensity was quenched by the addition of various types of QDs (the most significantly in the case of GSH-QDs) with BSA concentration of 15 mg/mL.

 ISBN: 978-1-61208-303-2

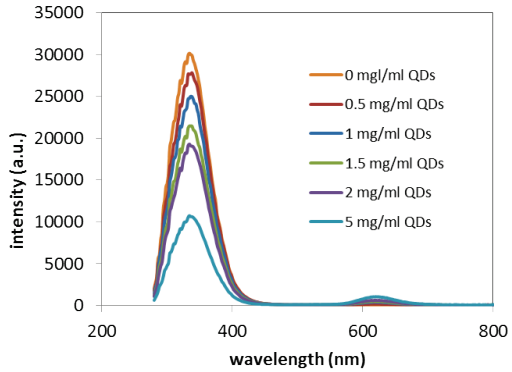

Figure 6. Emission spectra of BSA capped MPA-CdTe QDs via covalent interaction at various QDs concentration.

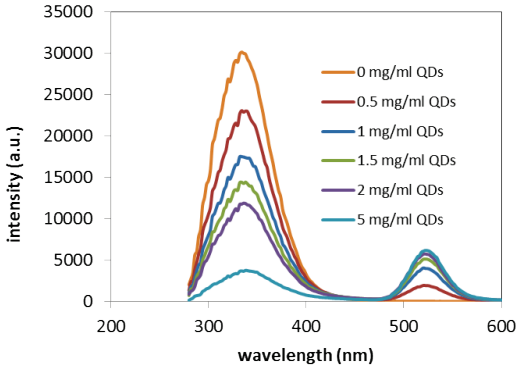

Figure 7. Emission spectra of BSA capped with GSH-CdTe QDs via covalent interaction at various QDs concentration.

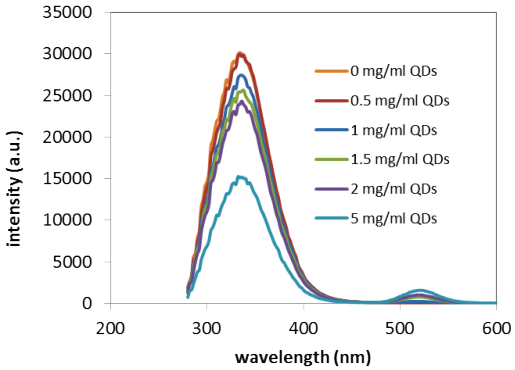

Figure 8. Emission spectra of BSA capped with TGA-CdTe QDs via covalent interaction at various QDs concentration.

The results suggest the interaction between BSA and QDs occurs and the quenching effect of QDs on the FL emission of BSA is found to be concentration dependent, thus QDs can bind to the BSA. In the case of MPA-QDs bonded with BSA, results exhibited a very good linearity with coefficient of determination R^2 of 0.9998 (see Figure 9). The Stern-Volmer plot of GSH-QDs quenching properties exhibited linear trend with coefficient of determination R^2 to be 0.9965 and in the case of TGA-QDs the coefficient of determination R^2 was 0.9904. This behavior suggests that only statistic quenching is taking place. The highest K constant was observed in the case of GSH-QDs, which is due to the presence of higher number of NH_2 groups in GSH (3 groups) compared to MPA and TGA. The K_{SV} constants of BSA covalently bonded to QDs are much higher compared to the electrostatic interactions between QDs and BSA.

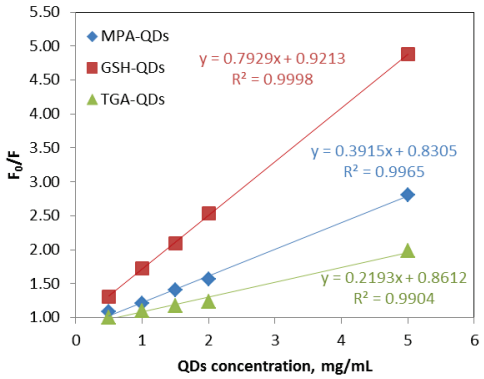

Figure 9. Stern-Volmer plot of BSA FL quenching effect caused by CdTe QDs covalently conjugated with BSA.

IV. CONCLUSION

Water soluble CdTe QDs modified with different ligands (MPA, TGA and GSH) were prepared by a simple one step method using Na_2TeO_3 and $CdCl_2$. The emission spectra display that the emission peak lies at 620 nm in the case of MPA-capped CdTe QDs, at 506 nm in the case of GSH-capped CdTe QDs and at 540 nm in the case of TGA-capped CdTe QDs. In the next stage, QDs were covalently and electrostatically conjugated to BSA. It was found that the presence of QDs led to a strong quenching of the FL emission, which could be explained by a covalent interaction between the protein and the quencher, demonstrating the formation of QDs-BSA bioconjugates.

ACKNOWLEDGMENT

This work has been supported by Grant Agency of the Czech Republic under the contract GACR 102/13-20303P, the operational program Research and Development for Innovation, by the project "CEITEC - Central European Institute of Technology" CZ.1.05/1.1.00/02.0068 from European Regional Development Fund and by the project NANOE CZ.1.07/2.3.00/20.0027 from European Social Fund.

 ISBN: 978-1-61208-303-2

REFERENCES

[1] J. Chomoucka, J. Drbohlavova, V. Adam, R. Kizek, and J. Hubalek, "Synthesis of Glutathione-coated Quantum Dots", 32nd International Spring Seminar on Electronics Technology, IEEE, 2009, pp 653-657.

[2] G. P. C. Drummen, "Quantum Dots-From Synthesis to Applications in Biomedicine and Life Sciences", Int. J. Mol. Sci., vol. 11 (1), Jan. 2010, pp. 154-163.

[3] M. Ryvolova, et al., "Glutathione modified CdTe quantum dots as a label for studying DNA interactions with platinum based cytostatics", Electrophoresis, vol. 34 (6), Mar. 2013, pp. 801-808.

[4] S. Singh, et al., "Conjugation of nano and quantum materials with bovine serum albumin (BSA) to study their biological potential", Journal of Luminescence, vol. 141, 2013, pp. 53-59.

[5] M. Ryvolova, et al., "Biotin-modified glutathione as a functionalized coating for bioconjugation of CdTe-based quantum dots", Electrophoresis, vol. 32 (13), Jun. 2011, pp. 1619-1622.

[6] J. Liang, Y. Cheng, and H. Han, "Study on the interaction between bovine serum albumin and CdTe quantum dots with spectroscopic techniques", Journal of Molecular Structure, vol. 892 (1–3), 2008, pp. 116-120.

[7] J. Drbohlavova, et al., "Effect of Nucleic Acid and Albumin on Luminescence Properties of Deposited TiO2 Quantum Dots", Int. J. Electrochem. Sci., vol. 7 (2), Feb. 2012, pp. 1424-1432.

[8] J. L. Duan, L. X. Song, and J. H. Zhan, "One-Pot Synthesis of Highly Luminescent CdTe Quantum Dots by Microwave Irradiation Reduction and Their Hg2+-Sensitive Properties", Nano Res., vol. 2 (1), Jan. 2009, pp. 61-68.

[9] J. Wang, and H. Han, "Hydrothermal synthesis of high-quality type-II CdTe/CdSe quantum dots with near-infrared fluorescence", Journal of Colloid and Interface Science, vol. 351 (1), 2010, pp. 83-87.

[10] X. Huang, et al., "Characterization of quantum dot bioconjugates by capillary electrophoresis with laser-induced fluorescent detection", Journal of Chromatography A, vol. 1113 (1–2), 2006, pp. 251-254.

[11] A. Chopra, et al., "CdTe nanobioprobe based optoelectrochemical immunodetection of diabetic marker HbA1c", Biosensors and Bioelectronics, vol. 44, 2013, pp. 132-135.

[12] P. Liu, Y. S. Liu, and Q. S. Wang, "Studies on the interaction of CdTe QDs with bovine serum albumin", J. Chem. Technol. Biotechnol., vol. 87 (12), Dec. 2012, pp. 1670-1675.

[13] Q. Wang, et al., "Interaction of different thiol-capped CdTe quantum dots with bovine serum albumin", Journal of Luminescence, vol. 132 (7), 2012, pp. 1695-1700.

[14] L. Ding, et al., "Spectroscopic Studies on the Thermodynamics of L-Cysteine Capped CdSe/CdS Quantum Dots-BSA Interactions", J. Fluoresc., vol. 21 (1), Jan. 2011, pp. 17-24.

[15] A. Baride, D. Engebretson, M. T. Berry, and P. Stanley May, "Quenching of coumarin emission by CdSe and CdSe/ZnS quantum dots: Implications for fluorescence reporting", Journal of Luminescence, vol. 141, 2013, pp. 99-105.

 ISBN: 978-1-61208-303-2

Effects of Noise on the Security of Entanglement Swapping Based QKD Protocols

Stefan Schauer and Martin Suda
Department Safety and Security
AIT Austrian Institute of Technology GmbH
Vienna, Austria
stefan.schauer@ait.ac.at, martin.suda.fl@ait.ac.at

***Abstract*—In this article, we discuss the effects of noise in a quantum channel on the security of quantum key distribution protocols based on entanglement swapping. Therefore, we look at two different models of quantum noise, the depolarization channel and the decoherence channel. Based on these models, we examine at first the effects on entanglement swapping and further the implications on the security parameters in quantum cryptography. We are able to show that a fidelity of at least 0.9428 is necessary to guarantee the security of the protocol. Additionally, we take the exponential decrease of entanglement over the distance between the communication parties into account. Using the photonic channel with coherence lengths from 10 km to 50 km as a reference model, we find that in this scenario the maximum length of a quantum channel for secure communication based on entanglement swapping lies between 1.19 km and 6.12 km.**

***Keywords*—quantum key distribution; entanglement swapping; noisy channels; security analysis.**

I. INTRODUCTION

Quantum key distribution (QKD) is an important application of quantum mechanics and QKD protocols have been studied at length in theory and in practical implementations [1], [2], [3], [4], [5], [6], [7], [8]. Most of these protocols focus on prepare and measure schemes, where single qubits are in transit between the communication parties Alice and Bob. The security of these protocols has been discussed in depth and security proofs have been given for example in [9], [10], [11]. In addition to these prepare and measure protocols, several protocols based on the phenomenon of entanglement swapping have been introduced [12], [13], [14], [15], [16]. In these protocols, entanglement swapping is used to obtain correlated measurement results between the legitimate communication parties, Alice and Bob. In other words, each party performs a Bell state measurement and due to entanglement swapping their results are correlated and further on used to establish a secret key.

Entanglement swapping has been introduced by Bennett et al. [17], Zukowski et al. [18] as well as Yurke and Stolen [19], respectively. It provides the unique possibility to generate entanglement from particles that never interacted in the past. In detail, Alice and Bob share two Bell states of the form $|\Phi^+\rangle_{12}$ and $|\Phi^+\rangle_{34}$ such that afterwards Alice is in possession of qubits 1 and 3 and Bob of qubits 2 and 4 (cf. (2) in Figure 1). The overall state can now be written as

$$|\Phi^+\rangle_{12} \otimes |\Phi^+\rangle_{34} = \frac{1}{2}\Big(|\Phi^+\rangle|\Phi^+\rangle + |\Phi^-\rangle|\Phi^-\rangle + |\Psi^+\rangle|\Psi^+\rangle + |\Psi^-\rangle|\Psi^-\rangle\Big)_{1324} \quad (1)$$

Then, Alice performs a complete Bell state measurement on the two qubits 1 and 3 in her possession, and at the same time the qubits 2 and 4 at Bob's side collapse into a Bell state although they originated at completely different sources. Moreover, the state of Bob's qubits depends on Alice's measurement result (cf. (4) in Figure 1). As presented in eq. (1) Bob always obtains the same result as Alice when performing a Bell state measurement on his qubits.

The effects of noise on entangled states have already been discussed in detail in literature. It has been pointed out that the fidelity is reduced due to the noise in a quantum channel and entanglement purification methods have been developed to overcome this problem [20], [21], [22], [23]. In principle, entanglement purification can be used to bring a tempered entangled state arbitrarily close to a pure stated given the required resources. This is one of the reasons why the security of QKD protocols based on entanglement swapping has been discussed on the surface so far. They have only been analyzed using pure states in an idealistic environment (loss-free quantum channels, perfect devices, etc.) not considering the noise in a real-world environment. In this article, we are going to look at the security of QKD protocols based on entanglement swapping in a noisy environment. Using the *depolarizing channel* as well as the *dephasing channel* as reference models, the effect of the natural noise on entanglement swapping is described. Further, threshold values on the fidelity of the entanglement of the initial states are given, below which a secure communication is possible. Additionally, we look at the impact of the distance between Alice and Bob on the fidelity of entanglement and also estimate threshold values for the security of entanglement swapping QKD protocols in connection with the length of a quantum channel.

In the following section, we are going to shortly review the two most common noisy channel models, the depolarizing channel and the dephasing channel. In Section III, the effect of the noisy channels on entanglement swapping are described. In detail, the probabilities for uncorrelated results coming from entanglement swapping are computed. In the following Sections IV and V, we discuss the effects of noise on the security parameters and the maximal channel length for secure communication using these models. Here, we are relating the

 ISBN: 978-1-61208-303-2

fidelity of the initial states as well as the length of the quantum channel to upper bounds coming from current QKD protocols. In the end, we summarize the results and give a short outlook on the next steps into this topic.

II. Noisy Channel Models

In a classical communication, the only type of errors that occur are bit flip errors, i.e., a change from 0 to 1 and vice versa. Since qubits are more sophisticated systems than classical bits, two major types of errors can occur: bit flip and phase flip errors. Further, any linear combination of these two errors is possible. A bit flip and phase flip of a qubit is described by the Pauli operations σ_x and σ_z, respectively. Consequently, if both errors occur at the same time this can be described by the Pauli operation σ_y.

A very common way to characterize a noisy quantum channel is to use the *depolarizing channel* [24], [25]. This model takes both bit flip and phase flip errors on the qubit in transit into account and is therefore described by the application of all three Pauli operations σ_x, σ_y and σ_z. If the qubit transmitted over the noisy channel is part of an entangled state, the whole system is affected by the noisy channel. In case of a Bell state, e.g., $|\Phi^+\rangle$, the system of the two qubits after the effect of the depolarizing channel can be described by a Werner state [26]

$$\begin{aligned} W_F &= \mathrm{F}|\Phi^+\rangle\langle\Phi^+| \\ &+\frac{1-\mathrm{F}}{3}\Big(|\Phi^-\rangle\langle\Phi^-| + |\Psi^+\rangle\langle\Psi^+| + |\Psi^-\rangle\langle\Psi^-|\Big) \end{aligned} \tag{2}$$

with fidelity $\langle\Phi^+|W_F|\Phi^+\rangle = F$. A more common way to look at the Werner state is to describe it in connection with white noise, i.e.,

$$\rho = (1-p)|\Phi^+\rangle\langle\Phi^+| + p\frac{\mathbb{1}}{4} \tag{3}$$

where p is the error probability. In this case the fidelity can be easily computed as $\mathrm{F} = 1 - 3p/4$.

A more specialized model for a noisy quantum channel is the phase damping or also called *dephasing channel* [27]. This is a phase scrambling and energy preserving mechanism described by the two operators

$$\sqrt{\frac{1+e^{-p}}{2}}\mathbb{1} \qquad \text{and} \qquad \sqrt{\frac{1-e^{-p}}{2}}\sigma_z \tag{4}$$

with p again the probability that an error is introduced by the quantum channel. Looking at the scenario where one qubit of the Bell state $|\Phi^+\rangle$ is transmitted over the noisy channel, the resulting state can be described as

$$\chi = \frac{1+e^{-p}}{2}|\Phi^+\rangle\langle\Phi^+| + \frac{1-e^{-p}}{2}|\Phi^-\rangle\langle\Phi^-| \tag{5}$$

III. Entanglement Swapping in a Noisy Environment

As a consequence of the transmission of qubits over a noisy channel the operations on those qubits are affected, too. In the protocols we are dealing with in this article the most interesting operation is entanglement swapping. Following eq. (1) and Figure 1 we assume Alice prepares the Bell state $|\Phi^+\rangle\langle\Phi^+|_{12}$ and Bob prepares $|\Phi^+\rangle\langle\Phi^+|_{34}$ in their respective laboratories.

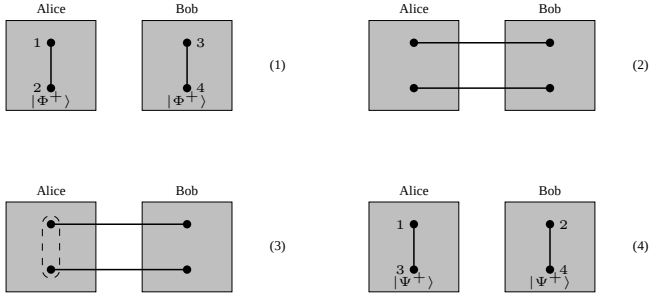

Fig. 1. Illustration of a standard setup for an entanglement swapping based QKD protocol.

They send qubits 2 and 3 to the other party over a depolarizing channel such that the overall system is described by $\rho \otimes \rho$. After Alice's Bell state measurement on qubits 1 and 3 in her possession the system of qubits 2 and 4 is (assuming Alice obtains $|\Phi^+\rangle\langle\Phi^+|_{13}$)

$$\begin{aligned} \rho_{24} =& \frac{4-6p+3p^2}{4}|\Phi^+\rangle\langle\Phi^+|_{24} \\ &+\frac{2p-p^2}{4}\Big(|\Phi^-\rangle\langle\Phi^-| + |\Psi^+\rangle\langle\Psi^+| + |\Psi^-\rangle\langle\Psi^-|\Big)_{24} \end{aligned} \tag{6}$$

which is again a Werner state (cf. eq. (2) above). Comparing this equation with eq. (1) describing entanglement swapping with pure states we directly see that Alice and Bob obtain correlated results only with probability

$$P_{corr} = \frac{4-6p+3p^2}{4} \tag{7}$$

and Bob's measurement yields an arbitrary state not correlated to Alice's measurement with probability

$$P_{err} = \frac{6p-3p^2}{4} \tag{8}$$

For QKD protocols based on entanglement swapping this means that an error is detected during the communication between Alice and Bob. Considering Figure 2 we see that performing entanglement swapping over a noisy channel gives reasonable results, i.e., it is more likely to obtain correlated results than uncorrelated, only if $P_{err} < P_{corr}$. The maximum error probability to achieve that is $(3-\sqrt{3})/3$, which is the point where $P_{err} = P_{corr}$, corresponding to a fidelity of the initial states of at least $F = 0.683$. This value indicates a lower bound on the initial states to make entanglement swapping possible.

Taking at a dephasing channel instead of a depolarizing channel into account, we obtain a different error rate. If Alice and Bob again prepare the states $|\Phi^+\rangle\langle\Phi^+|_{12}$ and $|\Phi^+\rangle\langle\Phi^+|_{34}$, the overall system after they sent their qubits over the quantum channel is described by $\chi \otimes \chi$. Alice performs a Bell state measurement on qubits 1 and 3 in her possession, which leads to the state (assuming again that Alice's result is $|\Phi^+\rangle\langle\Phi^+|_{13}$)

$$\begin{aligned} \chi_{24} =& \frac{1+e^{-2p}}{2}|\Phi^+\rangle\langle\Phi^+|_{24} \\ &+\frac{1-e^{-2p}}{2}|\Phi^-\rangle\langle\Phi^-|_{24} \end{aligned} \tag{9}$$

 ISBN: 978-1-61208-303-2

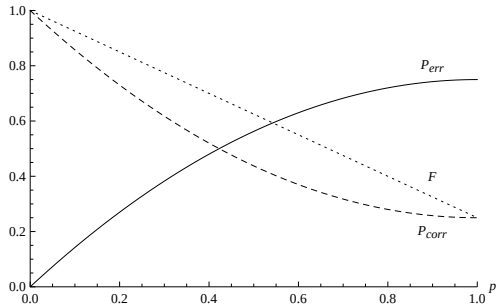

Fig. 2. The probabilities P_{corr} (dashed line) and P_{err} (solid line) from entanglement swapping in a depolarizing channel.

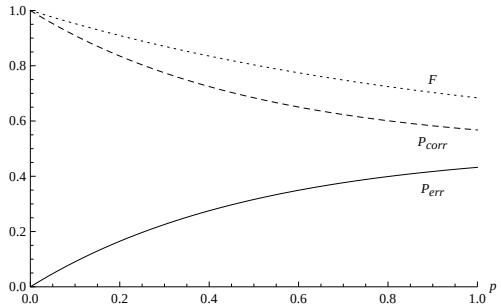

Fig. 3. The probabilities P_{corr} (dashed line) and P_{err} (solid line) from entanglement swapping in a dephasing channel.

Analogous to the depolarizing channel, Alice and Bob obtain correlated results only with probability

$$P_{corr} = \frac{1 + e^{-2p}}{2} \tag{10}$$

and they obtain different results with probability

$$P_{err} = \frac{1 - e^{-2p}}{2} \tag{11}$$

In contrary to the depolarizing channel, we see from Figure 3 that P_{corr} and P_{err} never intersect, i.e., it is always $P_{err} < P_{corr}$. This is a huge advantage, since the maximum probability that Alice and Bob obtain uncorrelated results is $P_{err} = 0.4323$ for $p = 1$, which is much smaller compared to the the error probability for the depolarizing channel defined in eq. (8) above. Nevertheless, this leads to almost the same minimal fidelity $\mathrm{F} = 0.6839$ compared to the required fidelity in the depolarizing channel described above, indicating that the dephasing channel has a much higher error tolerance.

IV. Effects on Security Parameters

To guarantee perfect security in quantum cryptography all noise – introduced naturally or by an adversary – is treated as it is caused by an eavesdropper. In particular, this leads to the rather paranoid but very useful assumption that Eve is able to exchange the noisy channel between Alice and Bob by a perfect quantum channel, i.e., a lossless channel where the polarization and phase are preserved. Hence, Eve can use the error Alice and Bob expect to come from their noisy channel to disguise her eavesdropping attempt. Additionally, in a realistic environment errors can also occur from the physical apparatus itself, affecting, e.g., the detector efficiency [28]. Since we are dealing with a theoretical model of the noisy quantum channel in this article, we are excluding the physical apparatus from our discussions limiting ourselves solely to errors coming from the noisy channel.

The first direct consequence for Alice and Bob when using noisy channels is that they can not allow an error rate larger than the error usually introduced by an adversary. For example, as it is described in most of the protocols based on entanglement swapping [12], [13], [14], [15], [16], the error rate due to Eve's intervention is 25%. If the natural error caused by a noisy channel is equal or larger than 25%, Alice and Bob will not detect Eve's presence. From eq. (8) we know that in case of a depolarizing channel Alice and Bob expect an error rate $P_{err} = 3(2 - p^2)/4$ from entanglement swapping such that $p < 0.1835$. This means, for a fidelity of the initial states $\mathrm{F} > 0.8624$ the natural error introduced by the depolarizing channel is always smaller than 25%, i.e., the error introduced by Eve. Similarly, due to the higher error tolerance of the dephasing channel Alice and Bob can handle a higher error probability compared to the depolarizing channel (cf. eq. (11) and eq. (8)). In this case $p < 0.3466$ and, accordingly, the fidelity of the initial states has to satisfy $\mathrm{F} > 0.8535$ such that the natural error introduced by dephasing is always smaller than 25%.

As discussed in detail in the following paragraphs, Eve has the opportunity to attack only a fraction of all qubits in transit between Alice and Bob. This reduces the error rate coming from her intervention but leaves Eve also with a smaller amount of information about the sifted key. To react on this threat, Alice and Bob perform error correction (EC) and privacy amplification (PA). A basic idea on how these two building blocks of quantum cryptography work and which methods are involved therein is given in [29] and [30]. We just want to stress that using these two primitives Eve's information about the key can be reduced to an arbitrary small amount. Furthermore, as pointed out in [31], to successfully perform error correction and privacy amplification based on one-way classical communication the error rate is bounded above by

$$P_{EC} = \frac{1 - \frac{1}{\sqrt{2}}}{2} \simeq 0.1465 \tag{12}$$

to be achievable [28]. Since the error correction still leaks some information to an adversary, privacy amplification is applied to the key to lower Eve's information to an arbitrary small amount. For a maximum error rate of $P_{PA} \simeq 0.11$ Eve's information can be reduced to at most one bit of the whole key (cf. [11], [32]). Therefore, in the following paragraphs, we define lower bounds on the fidelity of the initial states to achieve these two thresholds P_{EC} and P_{PA}.

Considering entanglement swapping in a noisy channel, we obtain the corresponding lower bounds p_{EC} and F_{EC} for an error rate $P_{err} \simeq 0.1465$ using eq. (8) from above (cf. also Figure 2)

$$p_{EC} \simeq 0.1029 \qquad \mathrm{F}_{EC} \simeq 0.9228. \tag{13}$$

Hence, the fidelity of the initial states has to be over 92% to make one-way error correction feasible. The final bounds p_{PA} and F_{PA} to achieve a maximum error rate of $\simeq 0.11$ and thus secure communication are then

$$p_{PA} \simeq 0.0762 \qquad \mathrm{F}_{PA} \simeq 0.9428, \tag{14}$$

 ISBN: 978-1-61208-303-2

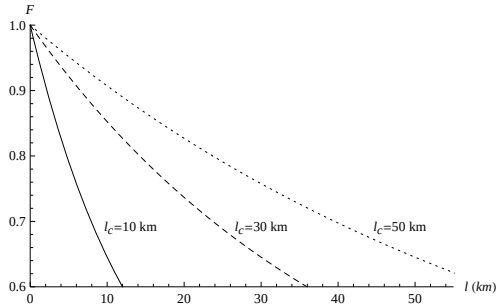

Fig. 4. Correlation between the fidelity F and the length l of a noisy quantum channel.

i.e., the fidelity has to be an additional 2% higher compared to eq. (13) to achieve the maximal tolerable error rate of $\simeq 11\%$.

Analogous to the computations above, the threshold values for the dephasing channel can be computed. By inserting into eq. (11) above we obtain

$$p_{EC} \simeq 0.1733 \qquad \mathrm{F}_{EC} \simeq 0.9204. \tag{15}$$

In this case, the error probability P_{EC} can be almost twice as high compared to the depolarizing channel resulting in almost the same fidelity for the initial states. Furthermore, the final bounds p_{PA} and F_{PA} are then

$$p_{PA} \simeq 0.1242 \qquad \mathrm{F}_{PA} \simeq 0.9415. \tag{16}$$

Again, the fidelity of the initial states is almost the same compared to the depolarizing channel, whereas the error probability can be almost twice as high.

V. Effects on the Channel Length

In a realistic environment we also have to take into account that the fidelity F of the entanglement decreases exponentially with the length l of the channel. Modeling our quantum channel as a *photonic channel* [33] it has been shown in [34] that the fidelity is given by

$$\mathrm{F} \simeq \left| \frac{1 + e^{-l/2l_c}}{2} \right|^2 \tag{17}$$

where l_c is the coherence length of an optical fiber. Therefore, we see from Figure 4 that the fidelity of the initial state is below 0.68 for a channel longer than 8.64 km and a coherence length $l_c = 10$ km, which means that entanglement swapping is no longer possible at this distance. For a higher coherence length, the maximum distance is increased accordingly to 25.91 km with $l_c = 30$ km or 43.19 km with $l_c = 50$ km. The decrease of the fidelity of entanglement has a huge impact on the security of quantum cryptography based on entanglement swapping as discussed above. In Figure 4, we used three different values for the coherence length l_c: 10 km, 30 km and 50 km. As we can directly see from Figure 4, a higher coherence length results in a smaller decrease of the fidelity. As shown in Section III, using a depolarization channel Alice and Bob need a fidelity of at least $\mathrm{F}_{EC} = 0.9228$ to perform error correction and a fidelity $\mathrm{F}_{PA} = 0.9428$ to reduce the error rate to 0.11. Furthermore, when using a dephasing channel the respective fidelities do not differ very much from these result, i.e., $\mathrm{F}_{EC} = 0.9204$ and $\mathrm{F}_{PA} = 0.9415$.

TABLE I. Comparison of minimal fidelity and maximal channel length in the depolarizing and dephasing channel.

Channel	**Coherence Length**		
Depolarizing	$l_c = 10$ km	$l_c = 30$ km	$l_c = 50$ km
$\mathrm{F}_{EC} \simeq 0.9228$	1.64 km	4.92 km	8.20 km
$\mathrm{F}_{PA} \simeq 0.9428$	1.19 km	3.59 km	5.98 km
Dephasing	$l_c = 10$ km	$l_c = 30$ km	$l_c = 50$ km
$\mathrm{F}_{EC} \simeq 0.9204$	1.69 km	5.08 km	8.47 km
$\mathrm{F}_{PA} \simeq 0.9415$	1.22 km	3.67 km	6.12 km

Combining our results from the previous section with eq. (17) we can directly see that in a quantum channel with coherence length $l_c = 10$ km F_{EC} limits the length of the quantum channel to 1.64 km when using a depolarizing channel. Moreover, to guarantee a fidelity F_{PA}, the length of the channel has to be at most 1.19 km (cf. Table I). Taking a higher coherence length of $l_c = 30$ km, the distance over which error correction is still possible increases to 4.92 km and the distance for secure communication increases to 3.59 km. In the third scenario where we take $l_c = 50$ km, we still get the fidelity F_{EC} at a distance of 8.20 km and the fidelity F_{PA} at a distance of 5.98 km. Using the dephasing channel the maximal distances do not differ very much from these values (cf. Table I).

These distances are still very low and of minor practical value for quantum communication since, for example, physical implementations of prepare and measure QKD protocols work over larger distances [5], [6], [7], [8]. Hence, Alice and Bob have to increase the fidelity of their entangled states before they can perform entanglement swapping, i.e., start the actual protocol. As already pointed out above, this is achieved using entanglement purification and nested purification protocols [20], [21], [22], [23]. Nevertheless, the fidelity can only be brought to its maximum in theory, since too many resources would be required. Hence, there will always be a certain error coming from entanglement swapping, which Alice and Bob have to deal with.

VI. Conclusion

In this article, we discussed the effect of noise on the security parameters of QKD protocols based on entanglement swapping. Therefore, we used two reference models for a noisy channel, the depolarizing channel and the more specific dephasing channel. Taking these two models into account, we showed that the fidelity of the initial states of a QKD protocol has to be at least $\mathrm{F} \simeq 0.68$ to obtain reasonable results from entanglement swapping. Regarding the security of QKD protocols, we looked at two threshold values often referred to in literature: P_{EC}, which describes the maximum error rate to make one-way classical error correction possible, and P_{PA}, which denotes the maximum error rate such that privacy amplification can be used to reduce the information of an adversary to a minimum. Based on these threshold values the minimal fidelity of the initial states was computed. Here, we showed that a minimal fidelity $\mathrm{F} \simeq 0.9428$ is required to obtain a maximum error rate of 0.11 in a depolarizing channel. Accordingly, in a dephasing channel the fidelity is slightly lower with $\mathrm{F} \simeq 0.9415$ (cf. also Table I).

 ISBN: 978-1-61208-303-2

Additionally, we discussed the exponential decrease of the fidelity when transmitted through a noisy channel. In this case, we looked in detail at the photonic channel as reference model and calculated the maximum length of a channel to achieve the minimal fidelities described above. For different coherence lengths of 10 km, 30 km, and 50 km we obtained maximum distances between 1.19 km and 6.12 km for a fidelity $F \simeq 0.94$.

As pointed out, these values are rather low compared to physical implementations of prepare and measure QKD protocols. Hence, one of our next steps is to refine the model for the decrease of entanglement over distance to a more practical scenario. Further, we want to investigate entanglement purification protocols in context with entanglement swapping based QKD protocols and their respective impacts on the security.

ACKNOWLEDGMENTS

We would like to thank Christian Kollmitzer, Oliver Maurhart as well as Beatrix Hiesmayr and Marcus Huber for fruitful discussions and interesting comments.

REFERENCES

[1] C. H. Bennett and G. Brassard, "Public Key Distribution and Coin Tossing," in *Proceedings of the IEEE International Conference on Computers, Systems, and Signal Processing*. IEEE Press, 1984, pp. 175–179.

[2] A. Ekert, "Quantum Cryptography Based on Bell's Theorem," *Phys. Rev. Lett.*, vol. 67, no. 6, pp. 661–663, 1991.

[3] C. H. Bennett, G. Brassard, and N. D. Mermin, "Quantum Cryptography without Bell's Theorem," *Phys. Rev. Lett.*, vol. 68, no. 5, pp. 557–559, 1992.

[4] D. Bruss, "Optimal Eavesdropping in Quantum Cryptography with Six States," *Phys. Rev. Lett*, vol. 81, no. 14, pp. 3018–3021, 1998.

[5] A. Muller, H. Zbinden, and N. Gisin, "Quantum Cryptography over 23 km in Installed Under-Lake Telecom Fibre," *Europhys. Lett.*, vol. 33, no. 5, pp. 335–339, 1996.

[6] A. Poppe, A. Fedrizzi, R. Usin, H. R. Böhm, T. Lorünser, O. Maurhardt, M. Peev, M. Suda, C. Kurtsiefer, H. Weinfurter, T. Jennewein, and A. Zeilinger, "Practical Quantum Key Distribution with Polarization Entangled Photons," *Optics Express*, vol. 12, no. 16, pp. 3865–3871, 2004.

[7] A. Poppe, M. Peev, and O. Maurhart, "Outline of the SECOQC Quantum-Key-Distribution Network in Vienna," *Int. J. of Quant. Inf.*, vol. 6, no. 2, pp. 209–218, 2008.

[8] M. Peev, C. Pacher, R. Alléaume, C. Barreiro, J. Bouda, W. Boxleitner, T. Debuisschert, E. Diamanti, M. Dianati, J. F. Dynes, S. Fasel, S. Fossier, M. Fürst, J.-D. Gautier, O. Gay, N. Gisin, P. Grangier, A. Happe, Y. Hasani, M. Hentschel, H. Hübel, G. Humer, T. Länger, M. Legré, R. Lieger, J. Lodewyck, T. Lorünser, N. Lütkenhaus, A. Marhold, T. Matyus, O. Maurhart, L. Monat, S. Nauerth, J.-B. Page, A. Poppe, E. Querasser, G. Ribordy, S. Robyr, L. Salvail, A. W. Sharpe, A. J. Shields, D. Stucki, M. Suda, C. Tamas, T. Themel, R. T. Thew, Y. Thoma, A. Treiber, P. Trinkler, R. Tualle-Brouri, F. Vannel, N. Walenta, H. Weier, H. Weinfurter, I. Wimberger, Z. L. Yuan, H. Zbinden, and A. Zeilinger, "The SECOQC Quantum Key Distribution Network in Vienna," *New Journal of Physics*, vol. 11, no. 7, p. 075001, 2009.

[9] N. Lütkenhaus, "Security Against Eavesdropping Attacks in Quantum Cryptography," *Phys. Rev. A*, vol. 54, no. 1, pp. 97–111, 1996.

[10] ——, "Security Against Individual Attacks for Realistic Quantum Key Distribution," *Phys. Rev. A*, vol. 61, no. 5, p. 052304, 2000.

[11] P. Shor and J. Preskill, "Simple Proof of Security of the BB84 Quantum Key Distribution Protocol," *Phys. Rev. Lett.*, vol. 85, no. 2, pp. 441–444, 2000.

[12] A. Cabello, "Quantum Key Distribution without Alternative Measurements," *Phys. Rev. A*, vol. 61, no. 5, p. 052312, 2000.

[13] ——, "Reply to "Comment on "Quantum Key Distribution without Alternative Measurements"","," *Phys. Rev. A*, vol. 63, no. 3, p. 036302, 2001.

[14] ——, "Multiparty Key Distribution and Secret Sharing Based on Entanglement Swapping," *quant-ph/0009025 v1*, 2000.

[15] D. Song, "Secure Key Distribution by Swapping Quantum Entanglement," *Phys. Rev. A*, vol. 69, no. 3, p. 034301, 2004.

[16] C. Li, Z. Wang, C.-F. Wu, H.-S. Song, and L. Zhou, "Certain Quantum Key Distribution achieved by using Bell States," *International Journal of Quantum Information*, vol. 4, no. 6, pp. 899–906, 2006.

[17] C. H. Bennett, G. Brassard, C. Crepeau, R. Jozsa, A. Peres, and W. K. Wootters, "Teleporting an Unknown Quantum State via Dual Classical and EPR Channels," *Phys. Rev. Lett.*, vol. 70, no. 13, pp. 1895–1899, 1993.

[18] M. Zukowski, A. Zeilinger, M. A. Horne, and A. K. Ekert, ""Event-Ready-Detectors" Bell State Measurement via Entanglement Swapping," *Phys. Rev. Lett.*, vol. 71, no. 26, pp. 4287–4290, 1993.

[19] B. Yurke and D. Stolen, "Einstein-Podolsky-Rosen Effects from Independent Particle Sources," *Phys. Rev. Lett.*, vol. 68, no. 9, pp. 1251–1254, 1992.

[20] C. H. Bennett, G. Brassard, S. Popescu, B. Schumacher, J. Smolin, and W. K. Wootters, "Purification of Noisy Entanglement and Faithful Teleportation via Noisy Channels," *Phys. Rev. Lett.*, vol. 76, no. 5, pp. 722–725, 1996.

[21] D. Deutsch, A. Ekert, R. Josza, C. Machiavello, S. Popescu, and A. Sanpera, "Quantum Privacy Amplification and the Security of Quantum Cryptography over Noisy Channels," *Phys. Rev. Lett.*, vol. 77, no. 13, pp. 2818–2821, 1996.

[22] C. H. Bennett, D. P. DiVincenzo, J. A. Smolin, and W. K. Wootters, "Mixed-state Entanglement and Quantum Error Correction," *Phys. Rev. A*, vol. 54, no. 5, pp. 3824–3851, 1996.

[23] W. Dür, H.-J. Briegel, J. I. Cirac, and P. Zoller, "Quantum Repeaters Based on Entanglement Purification," *Phys. Rev. A*, vol. 59, no. 1, pp. 169–181, 1999.

[24] C. H. Bennett, C. A. Fuchs, and J. A. Smolin, "Entanglement-Enhanced Classical Communication on a Noisy Quantum Channel," *quant-ph/9611006 v1*, 1996.

[25] D. G. Fischer, M. Mack, M. A. Cirone, and M. Freyberger, "Enhanced Estimation of a Noisy Quantum Channel Using Entanglement," *Phys. Rev. A*, vol. 64, no. 2, p. 022309, 2001.

[26] R. F. Werner, "Quantum States with Einstein-Podolsky-Rosen Correlations Admitting a Hidden-Variable Model," *Phys. Rev. A*, vol. 40, no. 8, p. 4277, 1989.

[27] I. Devetak and P. Shor, "The Capacity of a Quantum Channel for Simultaneous Transmission of Classical and Quantum Information," *Comm. Math. Phys*, vol. 256, no. 2, pp. 287–303, 2005.

[28] V. Scarani, H. Bechmann-Pasquinucci, N. J. Cerf, M. Dušek, N. Lütkenhaus, and M. Peev, "The Security of Practical Quantum Key Distribution," *Rev. Mod. Phys.*, vol. 81, no. 3, pp. 1301–1350, 2009.

[29] C. H. Bennett, F. Bessette, G. Brassard, L. Salvail, and J. Smolin, "Experimental Quantum Cryptography," *J. Crypt.*, vol. 5, no. 1, pp. 3–28, 1992.

[30] B. Huttner and A. Ekert, "Information Gain in Quantum Eavesdropping," *J. Mod. Opt.*, vol. 41, no. 12, pp. 2455–2466, 1994.

[31] N. Gisin, G. Ribordy, W. Tittel, and H. Zbinden, "Quantum Cryptography," *Rev. Mod. Phys.*, vol. 74, no. 1, p. 145, 2002.

[32] B. Kraus, N. Gisin, and R. Renner, "Lower and Upper Bounds on the Secret-Key Rate for Quantum Key Distribution Protocols Using One-Way Classical Communication," *Phys. Rev. Lett.*, vol. 95, no. 8, p. 080501, 2005.

[33] S. J. van Enk, J. I. Cirac, and P. Zoller, "Photonic Channels for Quantum Communication," *Science*, vol. 279, no. 5348, pp. 205–208, 1998.

[34] D. Bouwmeester, A. Ekert, and A. Zeilinger, *The Physics of Quantum Information: Quantum Cryptography, Quantum Teleportation, Quantum Computation*, 3rd ed. Springer, 2001.

 ISBN: 978-1-61208-303-2

QKD on a Board Limited by Detector Rates in a Free-Space Environment

Alan Mink and Joshua C Bienfang
National Institute of Standards and Technology (NIST),
Gaithersburg, MD, USA
amink@nist.gov, joshua.bienfang@nist.gov

***Abstract*—We discuss a high-speed quantum key distribution (QKD) system with the protocol infrastructure implemented on a printed circuit board that can operate with various photonic subsystems. We achieve sub-nanosecond resolution with serial data receivers operating up to 2.5 Gb/s. Data processing bottlenecks are avoided with pipelined algorithms and controlled data flow implemented in a field-programmable gate array. This eliminates processing on the attached computer and frees CPU cycles for related activities, such as key management and system monitoring. Operating in a laboratory setting, we tested the QKD boards up to their maximum 2.5 GHz transmission rate, and found that under low-link-loss, high-count-rate conditions, timing jitter in the single-photon detectors imposed critical limitations to the maximum achievable throughput.**

Key words: quantum communication, QKD, programmable instrumentation, gigahertz signals

I. INTRODUCTION

The current generation of quantum key distribution (QKD) [1] systems has achieved Mb/s of privacy amplified (PA) key [5,17]. This has been accomplished with Gb/s quantum channels sustained by hardware for data handling and time binning of quantum-channel signals and associated sifting operations. As researchers pursue the next generation of QKD systems that can sustain Gb/s of PA key [4], highly optimized and parallel implementations will be required to handle QKD post-processing as well. While it may not be productive to further increase the quantum channel transmission rate, progress is being made in multiplexing and other photonic configurations [12,18] to achieve Gb/s sifting rates.

Our QKD research focus has been speed. Our initial testbed [2] was designed around a free-space system using a 1.25 GHz transmission rate, which resolves to 800 ps time bins. Although we were able to attempt to send a single photon in each of those time bins, setting our attenuated-laser sources at a mean photon number of 0.1 yields, on average, actual photons in one of every 10 time bins, an average photon emission rate of 125 MHz. Shortly following this free-space testbed, we developed a similar fiber based testbed [16] operating at the same speeds. Anticipating multiple photonic subsystems and quantum channels, we originally planned a common infrastructure for timing, framing, sifting and post-processing (reconciliation [13] and privacy amplification). To handle 800 ps time bins, we designed hardware to manage timing, framing and sifting. This reduces the GHz data rates to MHz data rates for post-processing, which we originally thought could be handled in a sustained fashion by software on a computer. We found that this approach worked for data rates up to about 1 Mb/s for PA data. Because our hardware had a capacity of greater than 30 Mb/s of sifted key and our QKD systems were producing up to 4 Mb/s of sifted keys [17], we developed an enhanced version of our hardware that would also implement post-processing, and thereby increase the PA key rate. The result was a hardware implementation able to operate at 2.5 GHz, using 400 ps time bins, with an output capacity of up to 12 Mb/s of PA key. We note that although it is feasible to distribute post-processing over multiple software instances, this approach was deemed to be too cumbersome for practical deployment and the compact hardware approach was more appealing.

Here we report [20] on experiments with this 2nd generation hardware infrastructure. We attempted to determine some of our QKD system limitations in a laboratory testing environment. In so doing, we discovered that in our implementation, faster transmission rates did not result in significantly faster PA key rates, primarily due to jitter in our single-photon detectors. The remainder of this paper will outline our hardware designs followed by our experimental free-space QKD configuration and the performance we observed.

II. HARDWARE INFRASTRUCTURE

Our 1st generation hardware to manage the timing, framing and sifting was a pair of custom designed printed circuit boards (PCBs), see Fig. 1, that included a field programmable gate array (FPGA) for processing, GHz serializer/deserializer (SERDES) chips for communication and a PCI interface to exchange data with the computer. FPGAs have about an order of magnitude slower clock rate than CPUs, but allow a designer to define arbitrary complex logical operations with an extensive level of parallelism that can make up for the lower clock rate. Furthermore, FPGAs are not hobbled by random operating system interrupts and other background processing tasks that make guaranteeing a fixed number of compute cycles in a given time interval impossible. SERDES are the foundation of high-speed transceivers. They convert between a parallel data stream at a lower data rate and a serial data stream at a higher data rate. For example, between a 10-bit parallel data stream at 125 MHz and a serial data stream at 1.25 GHz. The higher speed serial data stream is for transmission, while the lower speed parallel data stream is for processing on the FPGA. SERDES also provide an important clock-recovery function

 ISBN: 978-1-61208-303-2

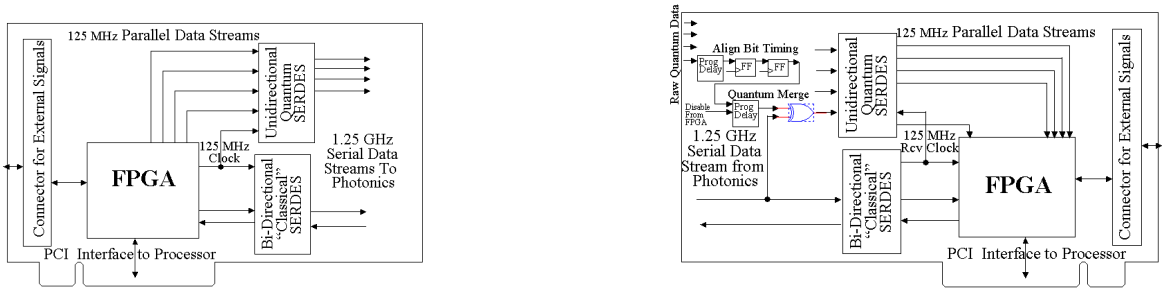

Figure 1. 1st generation PCB Functional Block Diagrams of Alice (left) and Bob (right), four quantum channels and one classical channel.

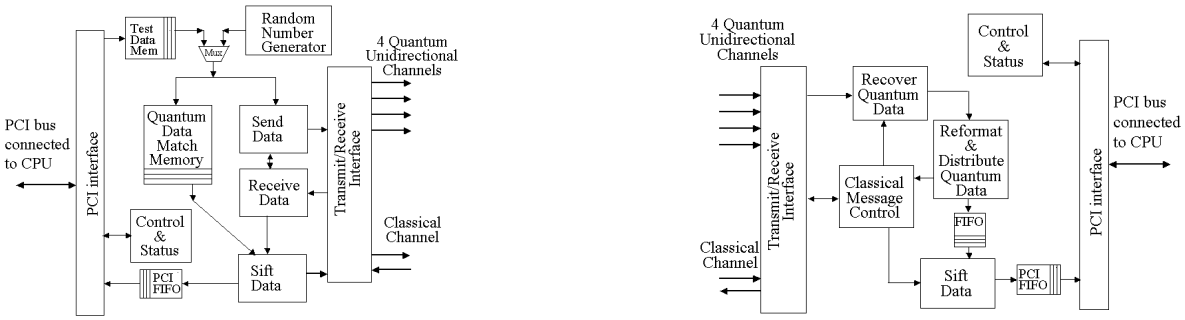

Figure 2. 1st generation PCB Logical Modules of Alice (left) and Bob (right).

that allows the receiver to synchronize to the clock of the transmitter.

To explain the operation of the FPGA firmware, we walk through the flow of the logical modules shown in Fig. 2. The Random Number Generator module on Alice's FPGA generates two bit-streams of pseudo random data, each at up to 1.25 Gbit/s; one stream for the bit value and the other for the basis. Their 2-bit combinations define the four polarization states transmitted on the quantum channel. These streams are temporarily stored in the Match Memory as well as passed to the Send Data modules where each 2048 bit pairs are grouped into a packet. Each packet is then passed to the Transmit/Receive module where they are synchronously used to control the photonics that send signals to Bob on the quantum channel and a "Sync" message on the classical channel. These electrical signals are sent from the PCB to the photonics, where they are shaped and converted to optical signals for the classical and quantum channels.

When a "Sync" message is received by the Transmit/Receive module in Bob's FPGA, it begins the capture of one packet's worth of data from the Quantum channel detectors. At this point the photonics have separated the photon arrival stream into four separate electrical signals, corresponding to the four possible measurement outcomes. Although the first transmission event leaves Alice at the same time as the first bit of the "Sync" message, it can arrive sometime later than the "Sync" message because quantum-channel signals follow a different path than the classical-channel signals. We measure this channel delay and specify its value, via the PCI interface, to the FPGA to provide the necessary compensation. For each detector, a packet's worth of time-bin samples are captured and are passed to the Recover Quantum Data module where they are aligned and then searched for rising edges that denote a detection event. The location within the quantum packet and the associated detector (i.e., tagged time bin, basis and value) are passed to the Reformat & Distribute Quantum Data module. This module reformats the data into a set of triples consisting of time bin, basis and bit value. For each packet, this set is temporarily stored in a FIFO and also passed to the Classical Message Control module where time bin and basis information, a detection pair, is sent back to Alice for sifting.

When Alice's Receive Data module gets a packet's detection pairs, which could be empty, it passes that information to the Sift module. The Sift module compares the basis value of each pair against the stored value in the Quantum Data Match Memory. If they match, then the bit value stored in the Match Memory is placed in the PCI FIFO forming Alice's stream of ordered Sifted bits. The associated state stream is then deleted from Alice's temporary database and a copy of the matching detection pair is also sent back to Bob as an acknowledgement. When Bob's Classical Message Control module receives the acknowledge list, Bob passes that list to its Sift module, which compares it against the list in its Temp FIFO and discards all entries that are not on the acknowledge list (i.e., those with incorrect basis). For those items that are on the list, the bit value is placed in the PCI FIFO forming Bob's stream of ordered Sifted bits. These Sifted bits are passed to an application program running on the CPU via a device driver in the operating system through a DMA (Direct Memory Access) transfer. DMA is a fast memory transfer that does not require CPU intervention, thus allowing the CPU to continue computation during the transfer.

As mentioned above, this initial design was hampered by the software post-processing speed, limited on-chip memory

 ISBN: 978-1-61208-303-2

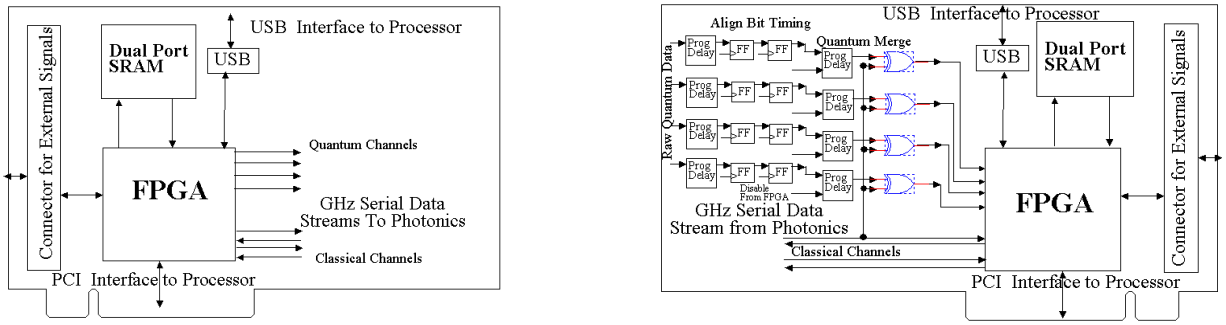

Figure 3. 2nd Generation PCB Functional Block Diagrams of Alice (left) and Bob (right), four quantum channels and two classical channels.

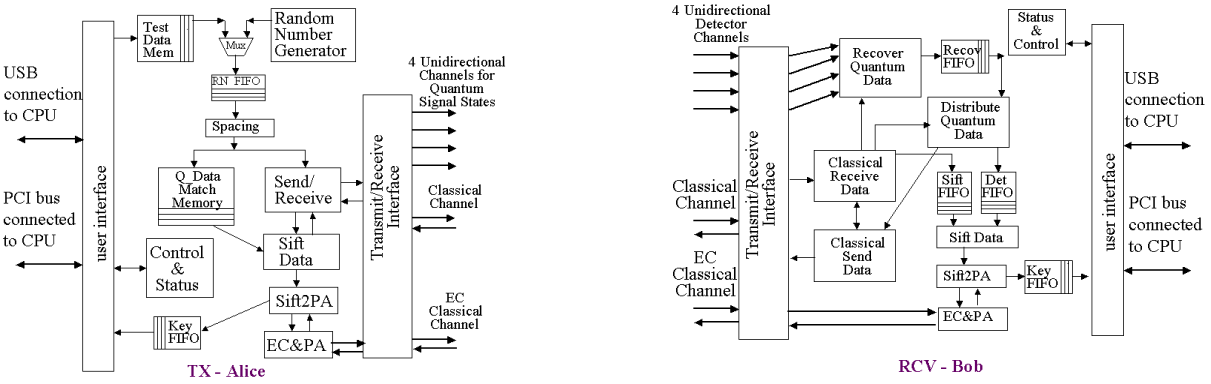

Figure 4. 2nd Generation PCB Logical Modules of Alice (left) and Bob (right).

that degraded performance as the distance between Alice and Bob increased, and the inability to increase the transmission rate that controls the time-bin temporal resolution. Our 2nd generation hardware, see Fig. 3, incorporated all the functionality of our 1st generation as well as functionality to overcome these limitations [10]. To include the post-processing algorithms we upgraded to a newer FPGA, ten times larger. This upgrade also provided a set of on-chip SERDESs, whose transmission speeds were faster and programmable, thus offering a higher transmission rate and better time-bin resolution. By eliminating the separate SERDES chips, we had space on the PCB for an additional memory chip to buffer data for longer round trip times between Alice and Bob.

Although the post-processing logical block, "EC&PA", in Fig. 4 seems like a small addition to Fig. 2, it represents the vast majority of the new FPGA implementation. For error correction, we are using a variant of the Cascade reconciliation algorithm [13]. We have also implemented the low density parity check (LDPC) error correction algorithm [14,11]. Cascade is an interactive algorithm that requires multiple round trips to refine information on the data to be corrected. LDPC is a one-way algorithm that requires a single transmission of correction data, but different error correction structures are required for different error rates and changing these structures in hardware is slow and inconvenient. Cascade requires about 1 to 2 bytes of memory per bit of data to be corrected, whereas LDPC requires about 20 to 30 bytes of memory – an order of magnitude more. Our FPGA implementation of Cascade was about twice as fast as our LDPC FPGA implementation. Even accounting for the latency associated with a link length of 200 km between Bob and Alice, Cascade was still faster. Because of the FPGA memory limitations, we were able to install four parallel tasks (threads) of Cascade, but only two threads of LDPC. Thus we chose Cascade because of the speed advantage.

The sifting process presents the reconciliation algorithms with a set of ordered bits that do not need any identification with either Alice or Bob. The peer reconciliation algorithms are asymmetrical, but are independent of Alice and Bob, and we designate them as Active and Passive. As in our software implementation, we use multiple parallel threads. The memory requirement of Active is more than that of Passive. To conserve the limited memory of the FPGA, we allocate an equal number of both Passive and Active threads on Alice and the opposite combination of threads on Bob.

Each Active and Passive pair implements reconciliation in three phases. Each phase requires at least one round trip communication to exchange information. Phase 1 and 3 are executed once, while phase 2 may be repeated. A summary follows:

1. Active and Passive identically randomize their bits, divide them into many disjoint groups and compute parity for each group. A group is less than 100 bits and

 ISBN: 978-1-61208-303-2

greater than 5 bits. Passive sends its set of parity to Active, who uses it to estimate the error rate and to identify groups that need correction. If the estimate is too high, Active and Passive discard the data, wait for new data and restart **phase 1**. If the estimate is low enough to process, Active computes a Hamming code on each group to be corrected and sends that set of Hamming codes to Passive. Passive decodes each Hamming code and affects correction where possible. Then go to **phase 2**.

2. Active and Passive identically randomize their bits, divide them into many disjoint groups and compute parity for each group. As the remaining error rate decreases, the size of a group increases. Passive sends its set of parity to Active, who uses it to estimate the remaining error rate and to identify groups that need correction. If the estimate is below a threshold, Active and Passive go to **phase 3**. Otherwise if the probability is above the threshold, Active computes a Hamming code on each group to be corrected and sends that set of Hamming codes to Passive. Passive decodes each Hamming code and affects correction where possible. Repeat **phase 2** until the remaining error probability drops below the threshold. If the maximum repetitions have been exceeded, discard the data and, wait for new data and restart at **phase 1**.
3. Execute a special final correction pass. Active computes a Hamming code on each group to be corrected and sends that set of Hamming codes to Passive. Passive decodes each Hamming code and affects correction where possible. Where not possible, discard that group and send a list of discarded groups to Active. Active and Passive send their bits to the next stage for verification and PA. Then they wait for new data and restart at **phase 1**.

This implementation of Cascade repeatedly executes a few operations that can reuse the same memory and the same logic resources. This results in a compact and efficient FPGA implementation. Since keeping the Active and Passive set of bits aligned is essential, randomizing those bits must be done exactly the same by both. This is accomplished by using a pseudo-random generator with Active and Passive using the same seed. Since the randomization is used to mix up the bits and expose errors, there is no need to keep that seed secret, although one can. The information exposed during Cascade is the sum of the sets of parity bits plus the sum of the sets of Hamming codes. Thus we keep track of this total, 1 bit for each parity bit and $\log_2(n)$ for each n-bit Hamming code. This total represents the reduction due to error correction during PA.

The bulk of the parallelism comes from multiple Cascade threads. Because of the interactive nature of Cascade, there is not much parallelism within a thread, although the communication latency can be mitigated by overlapping the waiting time with computations.

The now corrected data is accumulated for PA, but first a hash code signature of that data is computed and exchanged for comparison. These bits contribute an additional reduction during PA. If the hash signatures differ, the data is discarded. If the signatures are the same, the PA algorithm is invoked and the resulting PA bits are passed to the CPU.

The resulting capacity performance of this 2nd generation infrastructure is about 12 Mb/s for a QBER of 1 % and about 10 Mb/s for a QBER of 2 %. This is an order of magnitude faster than our 1st generation hardware. These rates were obtained using simulated QKD data, since our QKD photonic systems could not produce high enough data rates to stress this infrastructure, as we discuss below.

III. EXPERIMENTAL TESTS

To test the performance of the 2nd generation QKD hardware infrastructure in conjunction with an actual quantum-channel physical layer, we use the BB84 system described in [15]. To minimize link loss and allow the fullest range of throughputs for testing the hardware, the system is setup in a laboratory setting with a 1 m free-space path between Alice and Bob. The classical channel for timing and sifting operates at 2.5 Gb/s and the classical channel for post-processing operates at 1.25 Gb/s, both are at 1550 nm over 15 m of optical fiber, and the quantum channel operates at transmission rates up to 2.5 GHz at 851.4 nm with attenuated gain-switched vertical-cavity surface-emitting lasers (VCSELs) producing < 50 ps optical pulses. The narrow-band interference filters used to block background solar photons described in [15] were removed from Bob's receive aperture. Opaque enclosures and high-transmissivity 10 nm bandpass filters at the single-photon detectors were used to suppress background light in the lab below the dark count level of the detectors. As described in [15], the four silicon single-photon avalanche diode detectors were modified for improved timing resolution, and exhibit a full-width at half-maximum of roughly 200 ps for count rates up to about 1 MHz. Link losses up to -27 dB are simulated by inserting neutral density filters in the 1 m path between Alice and Bob. The protocol implemented in the hardware infrastructure is not yet configured for decoy-state QKD [9], meaning that the high link losses investigated in this experimental test exceed the operational range of the current configuration. Nonetheless, it was deemed valuable to test the hardware's data-processing capabilities over a wide range of throughputs, particularly those at the lowest link losses and highest count rates.

The quantum channel SERDES operate at 2.5 GHz, providing 400 ps detection time bins. To operate at lower transmission rates, we simply spaced transmission events by 1, 2, or 4 clock cycles. At the lower transmission rates, the hardware's timing resolution allowed us to operate in either a gated mode, in which only detection events that occur in the transmission time bin are retained for sifting, or an ungated mode, in which events that occur at any time during a transmission period of 2 or 4 time bins are retained. For example, at 625 MHz there would be one 400 ps transmission time bin as well as three additional 400 ps time bins before the next possible transmission time bin. Gated mode retains events in only the transmission time bin while ungated mode retains events occurring in any of the four time bins.

 ISBN: 978-1-61208-303-2

The results of the experimental trials are shown in Figs. 5-7. In all cases, higher transmission rates resulted in higher sifted-bit rates, as expected. However, as shown in Fig. 6, lower link attenuations caused the QBER to rise significantly, particularly for a transmission rate of 2.5 GHz. The resulting error corrected and PA throughput is shown in Fig. 7, where it is clear that, for this system, transmission rates of 1.25 GHz or 625 MHz outperform 2.5 GHz at most attenuations. This is because the QBER detriment induced by detector jitter at high average count rates outweighs any benefit in additional sifted bit rates that may be gained by operating at 2.5 GHz transmission rates.

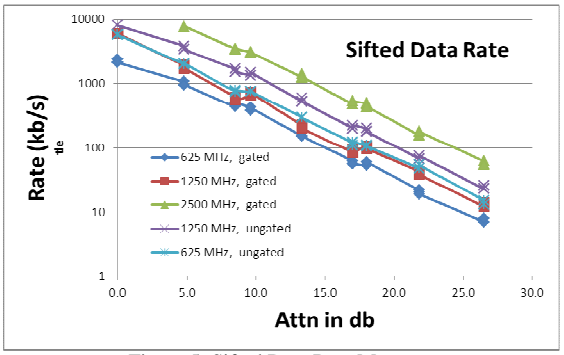

Figure 5. Sifted Data Rate Measurements.

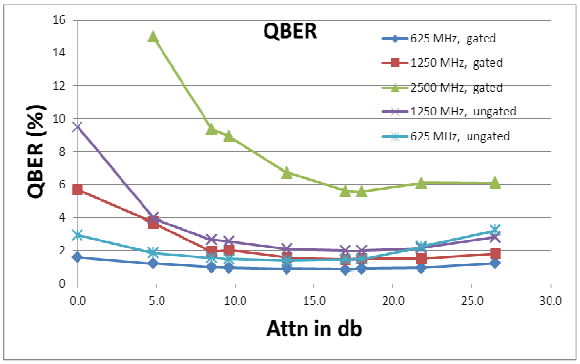

Figure 6. QBER Measurements.

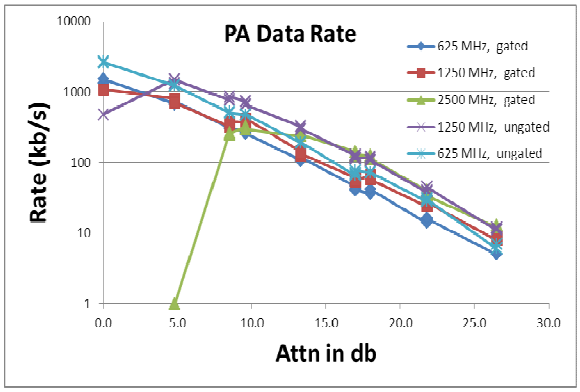

Figure 7. Privacy Amplified Data Rate Measurements.

The rise in QBER at attenuations below 10 dB reflects the increase in detector jitter with count rate, even with the detector modifications described in [15]. At these low link losses and high transmission rates, each detector is counting at rates well into the MHz range, and the timing resolution of the detectors is significantly degraded. At these high count rates and sifted bit rates, the detector jitter become so great that there is a significant probability that a detection event will occur in a clock cycle later than the one in which it was transmitted, driving up the QBER. Above a QBER of 11 %, the post-processing algorithm cannot distill bits from the sifted string.

The highest PA throughput was achieved at the more moderate transmission rate of 625 MHz. With about 5.7 Mb/s of sifted key and a QBER close to 3 %, the PA rate was about 2.6 Mb/s. The highest sifting rate of about 8 Mb/s was achieved at a transmission rate of 1.25 GHz, but because of a QBER of about 9.5 %, the PA rate was about 480 Kb/s. Unfortunately these bit rates are well within the performance range of the hardware, and the physical layer was not able to produce data at rates sufficient to stress the hardware beyond its capabilities. With a detector dead time, τ, of 50 ns, our secure sifting limit [3] is about 10 Mbits/s = $1/(2*\tau)$. Even within our laboratory environment we were not able to achieve that rate.

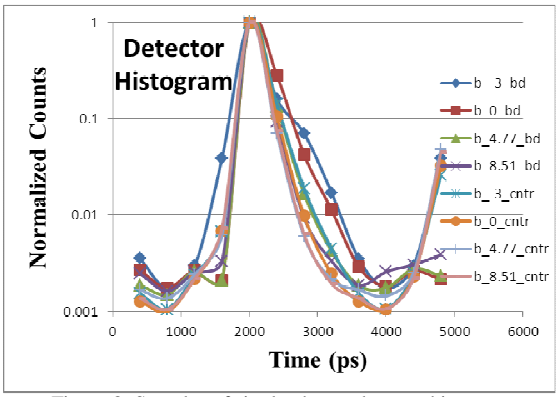

Figure 8. Samples of single photon detector histogram.

Our PCB can also capture detection histogram data with a 400 ps time-bin resolution and we compared that to a commercial time-correlate single-photon counting system (TCSPC) with 4 ps time-bin resolution. While transmitting at 312.5 MHz, we measured each detector separately to determine the jitter effects in the time bins other than the one in which we transmitted. For 312.5 MHz, we are transmitting in every 8th 400 ps time-bin. Theoretically we should only see detection events in every 8th time-bin, but it is well known that these detection histograms have a long tail caused by jitter, as can be seen in the example shown in Fig. 8. Although the TCSPC yielded cleaner measurements with deeper lows, our board measurements were reasonably close, but neither was able to predict the QBERs we measured.

IV. GB/S QKD

As researchers pursue the next QKD level of Gb/s PA key [4], highly optimized and parallel implementations will be required to handle QKD post-processing. The current replacement for Cascade seems to be LDPC that can asymptotically approach the Shannon limit. LDPC and

 ISBN: 978-1-61208-303-2

PA are one-way post-processing algorithms that are coarse grained computations in the sense that a given data set does not need to communicate until a solution is obtained. Thus, each data set can be assigned to a separate independent computation engine and each result could be collected sequentially at completion to maintain their order. Maintaining synchronization between Alice and Bob's bits is required throughout these operations. Up to 100 Mb/s of LDPC error correction performance [6] has been reported for a graphics processing unit (GPU) implementation. Thus 5 computers with 2 GPUs each could error correct at a Gb/s rate. LDPC performance of 47 Gb/s [19] has been reported for a custom chip implementation. It is not clear whether this chip could operate with structures appropriate for QKD, but that chip indicates that such designs are possible.

Similar implementation characteristics apply to PA along with a rather large data set requirement for efficient PA key generation ratios [8]. Brute force algorithms are of $O(n^2)$ complexity, while efficient algorithms based on FFTs are of O(n*log(n)) complexity. FFT performance of about 100 GFlops [7] for 2^{20} elements has been reported for a GPU implementation, which we estimate to be about 1/8 to 1/4 Gb/s privacy amplification rate. Thus 2-4 computers with 2 GPUs each could privacy amplify at a Gb/s rate.

V. CONCLUSION

We have discussed two generations of hardware infrastructure supporting QKD photonic operations. Our newest infrastructure is capable of producing 12 Mbits/s of PA key at 1 % QBER, but because of limitations in our detectors and increased jitter at high data rates we were not able to approach that limit. Furthermore, moving to higher photon transmission rates did not provide for higher PA key rates, because of higher QBERs due to jitter. Attaining Gb/s QKD rates will require specially crafted hardware with high levels of parallelism.

REFERENCES

[1] C. H. Bennet and G. Brassard, "Quantum Cryptography: Public key distribution and coin tossing", Proc of the IEEE Intern'l Conf on Computers, Systems, and Signal Processing, Bangalore, India, Dec. 1984, pp 175-179.

[2] J.C. Bienfang, et al. "Quantum key distribution with 1.25 Gbps clock synchronization", Optics Express. Vol. 12 (9), May 3, 2004, pp 2011-2016.

[3] V. Burenkov, B. Qi, B. Fortescue, and H.-K. Lo, "Security of high speed quantum key distribution with finite detector dead time", arXiv.org:arXiv:1005.0272, 3 May 2010.

[4] DARPA-BAA-12-42, "Quiness: Macroscopic Quantum Communications", May 15, 2012. <https://www.fbo.gov/index?s=opportunity&mode=form&id=6a3a61d577305f71d9be268925c4b201&tab=core&_cview=0> (accessed 5/29/2013)

[5] A. R. Dixon, Z. L. Yuan, J. F. Dynes, A. W. Sharpe, and A. J. Shields, "Continuous operation of high bit rate quantum key distribution", Appl. Phys. Ltr. **96**, 161102, Apr 19, 2010; <http://dx.doi.org/10.1063/1.3385293> (accessed 5/29/2013)

[6] G. Falcao, V. Silva, and L. Sousa, "How GPUs can outperform ASICs for fast LDPC decoding". Proc. of the 23rd Intern'l Conf on Supercomputing, ACM, 2009, pp 390–399.

[7] N. K. Govindaraju, B. Lloyd, Y. Dotsenko, B. Smith, and J. Manferdelli, "High Performance Discrete Fourier Transforms on Graphics Processors", Proc. ACM/IEEE Conf on Supercomputing, Austin, TX, Nov. 2008, pp 1-12.

[8] M.Hayashi and T.Tsurumaru, "Concise and tight security analysis of the Bennett-Brassard 1984 protocol with finite key length", *New Journal of Physics* **14,** 093014, Sept. 2012. <http://iopscience.iop.org/1367-2630/14/9/093014/> (accessed 5/29/2013)

[9] H.K. Lo, X.F. Ma, and K. Chen, "Decoy state quantum key distribution", Phys. Rev. Lett. 94, 230504 , June 2005.

[10] A. Mink, "Custom hardware to eliminate bottlenecks in QKD throughput performance", Proc. SPIE: Optics East 07, 6780, 678014-1, Boston, MA, Sept. 2007.

[11] A. Mink and A. Nakassis,"LDPC for QKD Reconciliation", The Computing Science and Technology International Journal, Vol. 2, No. 2, June, 2012, ISSN (Print) 2162-0660, ISSN (Online) 2162-0687, June, 2012, <http://www.researchpub.org/journal/cstij/number/vol2-no2/vol2-no2-1.pdf> (accessed 5/29/2013)

[12] J. Mora, W. Amaya, A. Ruiz-Alba, A. Martinez, D. Calvo, V. Muñoz, and J. Capmany, "Simultaneous transmission of 20x2 WDM/SCM-QKD and 4 bidirectional classical channels over a PON", Opt. Express 20, 16358-16365, July 2012.

[13] A. Nakassis, J. Bienfang, and C. Williams, "Expeditious reconciliation for practical quantum key distribution", Proc. SPIE: Quantum Information and Computation II, Proc. SPIE 5436, Aug. 2004, pp 28-35.

[14] A. Nakassis and A. Mink, "LDPC error correction in the context of Quantum Key Distribution", Proc. SPIE: Defense Security & Sensing, Balt., MD, Apr. 2012.

[15] A. Restelli, J.C. Bienfang, C.W. Clark, I. Rech, I. Labanca, M. Ghioni, S. Cova, "Improved Timing Resolution Single-Photon Detectors in Daytime Free-Space Quantum Key Distribution With 1.25 GHz Transmission Rate", IEEE J. Sel. Top. Quantum Electron. 16, Sept. 2010, pp 1084–1090.

[16] X. Tang, L. Ma, A. Mink, A. Nakassis, B. Hershman, J. Bienfang, R. F. Boisvert, C. Clark, and C. Williams, "High Speed Fiber-Based Quantum Key Distribution using Polarization Encoding", Proc. of SPIE Optics and Photonics Conf, San Diego, CA, Vol. 5893, July 2005.

[17] X. Tang, L. Ma, A. Mink, T. Nakassis, H. Xu, B. Hershman, J. Bienfang, D. Su, R. Boisvert, C. Clark, and C. Williams, "Quantum Key Distibution System Operating at Sifted-key Rate Over 4 Mbits/s," SPIE Defense & Security Symp, Orlando, FL, Vol. 6244-25, Apr 2006, pp. 62440P-1 -7.

[18] N. Walenta, A. Burg, J. Constantin, N. Gisin, O. Guinnard, R. Houlmann, C. Ci Wen Lim, T. Lunghi, and H. Zbinden, "1 Mbps coherent one-way QKD with dense wavelength division multiplexing and hardware key distillation", QCRYPTO2012, Singapore, Sept 2012.

[19] Z. Zhang, V. Anantharam, M. Wainwright, and B. Nikolic. "A 47 Gb/s LDPC Decoder with Improved Low Error Rate Performance". Symp on VLSI Circuits, June, 2009, pp 22-23.

[20] The identification of any commercial product or trade name does not imply endorsement or recommendation by the National Institute of Standards and Technology.

 ISBN: 978-1-61208-303-2

General Quantum Hilbert Space Modeling Scheme for Entanglement

Diederik Aerts, Sandro Sozzo
Center Leo Apostel for Interdisciplinary Studies
Brussels Free University
diraerts@vub.ac.be, ssozzo@vub.ac.be

***Abstract*—We work out a classification scheme for quantum modeling in Hilbert space of any kind of composite entity violating Bell's inequalities and exhibiting entanglement. Our framework includes situations with entangled states and product measurements, and also situations with both entangled states and entangled measurements. We show that entanglement is structurally a joint property of states and measurements, and that entangled measurements enable quantum modeling of situations that are usually believed to be 'beyond quantum'. Our results are extended from pure states to quantum mixtures. Entanglement classification has potentially an impact on quantum technologies and quantum cryptography, where entanglement is employed as a fundamental resource.**

Keywords-quantum modeling; Bell inequalities; entanglement; marginal law; Tsirelson bound.

I. INTRODUCTION

Entanglement is one of the most intriguing aspects of quantum physics. Entailing the violation of 'Bell's inequalities', it is responsible for a number of non-classical and far from well understood phenomena, such as quantum nonlocality [1] and quantum non-Kolmogorovness [2], [3], [4]. Several powerful potential applications of entanglement have been identified, which make it one of the most important study objects in quantum information theory and quantum technology. Otherwise impossible tasks, such as 'superdense coding' and 'teleportation', the 'quantum key distribution' and other protocols in quantum cryptography, the basic algorithms in quantum computation, exploit entanglement and its basic features. And, more, advanced experimental techniques, such as ion trapping and some fundamental processes in quantum interferometry, need entanglement and its purification, characterization and detection.

What was additionally very amazing is that entanglement appears, together with some other quantum features (contextuality, emergence, indeterminism, interference, superposition, etc.), also outside the microscopic domain of quantum theory, in the dynamics of concepts and decision processes within human thought, in computer science, in biological interactions, etc. These results constituted the beginning of a systematic and promising search for quantum structures and the use of quantum-based models in domains where classical structures show to be problematical [5], [6], [7], [8], [9], [10], [11]. Coming to our research, many years ago we already identified situations in macroscopic physics which violate Bell's inequalities [12], [13]. More recently, we have performed a cognitive test showing that a specific combination of concepts violates Bell's inequalities [14], [15], [16]. These two situations explicitly exhibit entanglement and present deep structural and conceptual analogies [17], [18], [19]. Resting on these findings, in the present paper, we put forward a general analysis and elaborate a global framework for the mathematical description of (not necessarily physical) composite entities violating Bell's inequalities. The entanglement in these situations is detected, represented and classified within explicit quantum models, where states, measurements and probabilities are expressed in the typical Hilbert space formalism. Our quantum-theoretic approach identifies different types of situations according to the quantum description that is required for their modeling.

(i) Bell's inequalities are violated within 'Tsirelson's bound' [20] and the marginal distribution law holds ('customary quantum situation'). In this case, entangled states and product measurements are present.

(ii) Bell's inequalities are violated within Tsirelson's bound and the marginal distribution law is violated ('nonlocal non-marginal box situation 1'). In this case, both entangled states and entangled measurements are present.

(iii) Bell's inequalities are violated beyond Tsirelson's bound and the marginal distribution law is violated ('nonlocal non-marginal box situation 2'). In this case, both entangled states and entangled measurements are present.

(iv) Bell's inequalities are violated beyond Tsirelson's bound and the marginal distribution law holds ('nonlocal box situation'). In this case, both entangled states and entangled measurements are present.

Technical aspects, definitions and results will be introduced in Sections II-A (pure states) and II-B (mixtures). We will show that entanglement is generally a joint feature of states and measurements. If only one measurement is at play and the situation of a pure state is considered, entanglement is identified by factorization of probabilities and can be distributed between state and measurement. If more measurements are at play, the violation of Bell's inequalities is sufficient to reveal entanglement in both the pure and the mixed case. But, in both cases the marginal distribution law imposes serious contraints in the ways this entanglement can be distributed.

Cases (i) are the customary situations considered in Bell-type experiments on microscopic quantum particles, but

 ISBN: 978-1-61208-303-2

they are very special in our analysis and approach. They correspond to situations where the symmetry of the entity is such that all the entanglement of the situation can be pushed into the state, allowing a model with only product measurements, where the marginal distribution law is satisfied. Cases (ii) instead seem to be present in situations of real quantum spin experiments (a mention of the 'experimental anomaly' indicating in our opinion the presence of entangled measurements occurs already in Alain Aspect PhD thesis [21], and was identified more explicitly in [22]). Case (iii) will be studied in Section III, where we observe that a quantum model can be worked out also for situations beyond Tsirelson's bound, contrary to widespread beliefs. Finally, in Section IV we put forward an example of case (iv), namely, the so-called 'nonlocal box', which is studied as a purely theoretical construct – no physical realizations have been found prior than the ones we present here – in the foundations of quantum theory [23].

II. Experiments on composite entities

In this section, we introduce the experimental setup we aim to represent in our formalism. Let S be a composite entity made up of the sub-entities S_A and S_B, and let S be prepared in the state p. A 'Bell-type experimental setting' can be described as follows.

We denote the single (dichotomic) measurements on S_A and S_B by e_A, $e_{A'}$, respectively, e_B, $e_{B'}$, with outcomes λ_{A_1}, λ_{A_2}, $\lambda_{A'_1}$, $\lambda_{A'_2}$, λ_{B_1}, λ_{B_2} and $\lambda_{B'_1}$, $\lambda_{B'_2}$, respectively. Let us consider e_A. If the outcome λ_{A_1} (λ_{A_2}) is obtained for e_A, then the state p changes into a state p_{A_1} (p_{A_2}). Analogously, we can associate final states with the other measurements.

We denote the coincidence measurements on S by e_{AB}, $e_{AB'}$, $e_{A'B}$ and $e_{A'B'}$, which involve both S_A and S_B (e_{AB} can, e.g., be performed by performing e_A on S_A and e_B on S_B, but it can be a more general measurement). The measurement e_{AB} has four outcomes $\lambda_{A_1B_1}$, $\lambda_{A_1B_2}$, $\lambda_{A_2B_1}$ and $\lambda_{A_2B_2}$, and four final states $p_{A_1B_1}$, $p_{A_1B_2}$, $p_{A_2B_1}$ and $p_{A_2B_2}$. The measurement $e_{AB'}$ has four outcomes $\lambda_{A_1B'_1}$, $\lambda_{A_1B'_2}$, $\lambda_{A_2B'_1}$ and $\lambda_{A_2B'_2}$, and four final states $p_{A_1B'_1}$, $p_{A_1B'_2}$, $p_{A_2B'_1}$ and $p_{A_2B'_2}$. The measurement $e_{A'B}$ has four outcomes $\lambda_{A'_1B_1}$, $\lambda_{A'_1B_2}$, $\lambda_{A'_2B_1}$ and $\lambda_{A'_2B_2}$, and four final states $p_{A'_1B_1}$, $p_{A'_1B_2}$, $p_{A'_2B_1}$ and $p_{A'_2B_2}$. Finally, the measurement $e_{A'B'}$ has four outcomes $\lambda_{A'_1B'_1}$, $\lambda_{A'_1B'_2}$, $\lambda_{A'_2B'_1}$ and $\lambda_{A'_2B'_2}$, and four final states $p_{A'_1B'_1}$, $p_{A'_1B'_2}$, $p_{A'_2B'_1}$ and $p_{A'_2B'_2}$.

Let us now consider the coincidence measurement e_{AB}. In it, the outcomes $\lambda_{A_1B_1}$, $\lambda_{A_1B_2}$, $\lambda_{A_2B_1}$ and $\lambda_{A_2B_2}$ are respectively associated with the probabilities $p(\lambda_{A_1B_1})$, $p(\lambda_{A_1B_2})$, $p(\lambda_{A_2B_1})$ and $p(\lambda_{A_2B_2})$ in the state p. We define in a standard way the expectation value $E(A,B)$ for the measurement e_{AB} as $E(A,B) = p(\lambda_{A_1B_1}) + p(\lambda_{A_2B_2}) - p(\lambda_{A_1B_2}) - p(\lambda_{A_2B_1})$, hence considering $\lambda_{A_1B_1} = \lambda_{A_2B_2} = +1$ and $\lambda_{A_1B_2} = \lambda_{A_2B_1} = -1$. Similarly, we define the expectation values $E(A,B')$, $E(A',B)$ and $E(A',B')$ in the state p for the coincidence measurements $e_{AB'}$, $e_{A'B}$ and $e_{A'B'}$, respectively.

Finally, we introduce the quantity $\Delta = E(A',B') + E(A,B') + E(A',B) - E(A,B)$, and the Clauser-Horne-Shimony-Holt (CHSH) version of Bell's inequalities, that is, $-2 \leq \Delta \leq 2$ [24]. If $\mathcal{S}_p$ is a set of experimental data on the entity S in the state p for the measurements e_{AB}, $e_{AB'}$, $e_{A'B}$ and $e_{A'B'}$ and the CHSH inequality is satisfied, then a single probability space exists for $\mathcal{S}_p$, which satisfies the axioms of Kolmogorov (classical, or 'Kolmogorovian', probability). If the CHSH inequality is violated, we say that entanglement occurs between S_A and S_B, since such a classical space does not exist in this case [2], [3], [4].

A. Entanglement and pure states

Let us now come to a quantum-mechanical representation of the situation in Section II in the Hilbert space $\mathbb{C}^2 \otimes \mathbb{C}^2$, canonically isomorphic to $\mathbb{C}^4$ by means of the correspondence $|1,0,0,0\rangle \leftrightarrow |1,0\rangle \otimes |1,0\rangle$, $|0,1,0,0\rangle \leftrightarrow |1,0\rangle \otimes |0,1\rangle$, $|0,0,1,0\rangle \leftrightarrow |0,1\rangle \otimes |1,0\rangle$, $|0,0,0,1\rangle \leftrightarrow |0,1\rangle \otimes |0,1\rangle$, where $\{|1,0\rangle, |0,1\rangle\}$ and $\{|1,0,0,0\rangle, |0,1,0,0\rangle, |0,0,1,0\rangle, |0,0,0,1\rangle\}$ are the canonical bases of $\mathbb{C}^2$ and $\mathbb{C}^4$, respectively. Let us also recall that the vector space $\mathcal{L}(\mathbb{C}^4)$ of all linear operators on $\mathbb{C}^4$ is isomorphic to the vector space $\mathcal{L}(\mathbb{C}^2) \otimes \mathcal{L}(\mathbb{C}^2)$, where $\mathcal{L}(\mathbb{C}^2)$ is the vector space of all linear operators on $\mathbb{C}^2$. The canonical isomorphism above introduces hence a corresponding canonical isomorphism between $\mathcal{L}(\mathbb{C}^4)$ and $\mathcal{L}(\mathbb{C}^2) \otimes \mathcal{L}(\mathbb{C}^2)$. Both these isomorphisms will be denoted by $\leftrightarrow$ in the following, and we will work in both spaces $\mathbb{C}^4$ and $\mathbb{C}^2 \otimes \mathbb{C}^2$ interchangeable.

Let us put forward a completely general quantum representation, where the state p is represented by the unit vector $|p\rangle \in \mathbb{C}^4$, and the measurement e_{AB} by the spectral family constructed on the ON basis $\{|p_{A_1B_1}\rangle, |p_{A_1B_2}\rangle, |p_{A_2B_1}\rangle, |p_{A_2B_2}\rangle\}$, where the unit vector $|p_{A_iB_j}\rangle$ represents the state $p_{A_iB_j}$, $i,j = 1,2$. Hence, e_{AB} is represented by the self-adjoint operator $\mathcal{E}_{AB} = \sum_{i,j=1}^{2} \lambda_{A_iB_j} |p_{A_iB_j}\rangle\langle p_{A_iB_j}|$. Analogously, we can construct the self-adjoint operators $\mathcal{E}_{AB'}, \mathcal{E}_{A'B}, \mathcal{E}_{A'B'}$ respectively representing $e_{AB'}$, $e_{A'B}$ and $e_{A'B'}$.

The probabilities of the outcomes of e_{AB}, $e_{AB'}$, $e_{A'B}$ and $e_{A'B'}$ in the state p are respectively given by $p(\lambda_{A_iB_j}) = |\langle p_{A_iB_j}|p\rangle|^2$, $p(\lambda_{A_iB'_j}) = |\langle p_{A_iB'_j}|p\rangle|^2$, $p(\lambda_{A'_iB_j}) = |\langle p_{A'_iB_j}|p\rangle|^2$ and $p(\lambda_{A'_iB'_j}) = |\langle p_{A'_iB'_j}|p\rangle|^2$.

Moreover, if we put $\lambda_{X_iY_i} = +1$, $\lambda_{X_iY_j} = -1$, $i,j = 1,2$, $j \neq i$, $X = A, A'$, $Y = B, B'$, we can write the expectation value in the state p as $E(X,Y) = \langle p|\mathcal{E}_{XY}|p\rangle$ and the Bell operator by $B = \mathcal{E}_{AB'} + \mathcal{E}_{A'B} + \mathcal{E}_{AB'} - \mathcal{E}_{AB}$. Thus, the CHSH inequality can be written as $-2 \leq \langle p|B|p\rangle \leq +2$.

Let us now introduce the notions of 'product state' and 'product measurement'.

 ISBN: 978-1-61208-303-2

Definition 1. *A state p, represented by the unit vector $|p\rangle \in \mathbb{C}^4$, is a 'product state' if there exists two states p_A and p_B, represented by the unit vectors $|p_A\rangle \in \mathbb{C}^2$ and $|p_B\rangle \in \mathbb{C}^2$, respectively, such that $|p\rangle \leftrightarrow |p_A\rangle \otimes |p_B\rangle$. Otherwise, p is an 'entangled state'.*

Definition 2. *A measurement e, represented by a self-adjoint operator $\mathcal{E}$ in $\mathbb{C}^4$, is a 'product measurement' if there exists measurements e_A and e_B, represented by the self-adjoint operators $\mathcal{E}_A$ and $\mathcal{E}_B$, respectively, in $\mathbb{C}^2$, such that $\mathcal{E} \leftrightarrow \mathcal{E}_A \otimes \mathcal{E}_B$. Otherwise, e is an 'entangled measurement'.*

Let now p be a product state, represented by $|p_A\rangle \otimes |p_B\rangle$, where $|p_A\rangle$ and $|p_B\rangle$ represent the states p_A and p_B, respectively. And let e be a product measurement, represented by $\mathcal{E}_A \otimes \mathcal{E}_B$, where $\mathcal{E}_A$ and $\mathcal{E}_B$ represent the measurements e_A and e_B, respectively. The following theorems, that are proved in [17], establish a connection between product states, measurements and the marginal law, and they will be used repeatedly in the following sections.

Theorem 1. *The spectral family of the self-adjoint operator $\mathcal{E}_A \otimes \mathcal{E}_B$ representing the product measurement e has the form $|p_{A1}\rangle\langle p_{A1}| \otimes |p_{B1}\rangle\langle p_{B1}|$, $|p_{A1}\rangle\langle p_{A1}| \otimes |p_{B2}\rangle\langle p_{B2}|$, $|p_{A2}\rangle\langle p_{A2}|\otimes|p_{B1}\rangle\langle p_{B1}|$ and $|p_{A2}\rangle\langle p_{A2}|\otimes|p_{B2}\rangle\langle p_{B2}|$, where $|p_{A1}\rangle\langle p_{A1}|$ and $|p_{A2}\rangle\langle p_{A2}|$ is a spectral family of $\mathcal{E}_A$ and $|p_{B1}\rangle\langle p_{B1}|$ and $|p_{B2}\rangle\langle p_{B2}|$ is a spectral family of $\mathcal{E}_B$.*

Theorem 1 states that the spectral family of a product measurement is constructed on an ON basis of product states.

Theorem 2. *Let p be a product state represented by $|p_A\rangle \otimes |p_B\rangle$, and e a product measurement represented by $\mathcal{E}_A \otimes \mathcal{E}_B$. Then, there exists probabilities $p(\lambda_{A_1})$, $p(\lambda_{B_1})$, $p(\lambda_{A_2})$ and $p(\lambda_{B_2})$, where $p(\lambda_{A_i})$ ($p(\lambda_{B_i})$) is the probability for the outcome λ_{A_i} (λ_{B_i}) of e_A (e_B) in the state p_A (p_B), $i = 1, 2$, such that $p(\lambda_{A_1}) + p(\lambda_{A_2}) = p(\lambda_{B_1}) + p(\lambda_{B_2}) = 1$, and $p(\lambda_{A_iB_j}) = p(\lambda_{A_i})p(\lambda_{B_j})$, where $\lambda_{A_iB_j}$, $i, j = 1, 2$ are the outcomes of e in the state p.*

From Th. 2 follows that, if the probabilities $p(\lambda_{A_iB_j})$ do not factorize, then only three possibilities exist: (i) the state p is not a product state; (ii) the measurement e is not a product measurement; (iii) both p is not a product state, and e is not a product measurement.

Let us consider the coincidence measurements e_{AB}, $e_{AB'}$, $e_{A'B}$ and $e_{A'B'}$ introduced above, together with their outcomes and probabilities in the state p.

Definition 3. *We say that a set of experimental data $\mathcal{S}_p(AB)$ collected on the measurement e_{AB} satisfies the 'marginal distribution law' if, for every $i = 1, 2$,*

$$\sum_{j=1,2} p(\lambda_{A_iB_j}) = \sum_{j=1,2} p(\lambda_{A_iB'_j}) \quad (1)$$

$$\sum_{j=1,2} p(\lambda_{A_jB_i}) = \sum_{j=1,2} p(\lambda_{A'_jB_1}) \quad (2)$$

We say that the marginal distribution law is satisfied in a Bell test if it is satisfied by all measurements e_{AB}, $e_{AB'}$, $e_{A'B}$ and $e_{A'B'}$.

Theorem 3. *Let e be a product measurement. Then, the marginal distribution law is satisfied by e.*

Theorem 4. *If no measurement among e_{AB}, $e_{AB'}$, $e_{A'B}$ and $e_{A'B'}$ satisfy the marginal distribution law, then at least two measurements are entangled.*

The latter provide a sharp and complete description of the structural situation: 'entanglement is a relational property of states and measurements'. If Th. 2 is not satisfied by a set of data collected in a single measurement, then one can transfer all the entanglement in the state, or in the measurement, or in both. Theorem 4 then shows that, if the marginal distribution law is violated, no more than two measurements can be products. The main consequence is that, if a set of experimental data violate both Bell's inequalities and the marginal distribution law, then a quantum-mechanical representation in the Hilbert space $\mathbb{C}^2 \otimes \mathbb{C}^2$ cannot be worked out, which satisfies the data and where only the initial state is entangled while all measurements are products.

Finally, we remind a technical result on the violation of the CHSH inequalitiy with product measurements. The standard quantum inequality $\Delta \leq 2\sqrt{2}$ holds for product measurements and is called 'Tsirelson's bound' [20]. This is typically considered the maximal violation of Bell's inequalities that is allowed by quantum theory, and will be discussed in the following sections.

B. Entanglement and mixtures

We have proved in Section II-A, Th. 2, that entanglement in a state-measurement situation can be traced by investigating whether the probabilities factorize, in the case of pure states. We show in this section that this does not hold any longer in the case of mixtures and provide a criterion for the identification of entanglement in the latter case. To this end, let us consider an entity S prepared in the mixture m of the pure product states r_1, r_2, ..., represented by the unit vectors $|r_{A_1}\rangle \otimes |r_{B_1}\rangle$, $|r_{A_2}\rangle \otimes |r_{B_2}\rangle$, ..., with weights w_1, w_2, ..., respectively ($w_i \geq 0$, $\sum_i w_i = 1$). The mixture m is thus represented by the density operator $\rho = \sum_i w_i |r_{A_i}\rangle\langle r_{A_i}| \otimes |r_{B_i}\rangle\langle r_{B_i}|$. Suppose that the measurement e_{AB} is a product measurement, represented by the self-adjoint operator $\mathcal{E}_{AB} = \mathcal{E}_A \otimes \mathcal{E}_B$, with spectral family on the ON basis $\{|p_{A_1B_1}\rangle, |p_{A_1B_2}\rangle, |p_{A_2B_1}\rangle, |p_{A_2B_2}\rangle\}$, where $|p_{A_iB_j}\rangle = |p_{A_i}\rangle \otimes |p_{B_j}\rangle$, $i, j = 1, 2$, while the spectral families of $\mathcal{E}_A$ and $\mathcal{E}_B$ are constructued on the ON bases $\{|p_{A_i}\rangle\}_{i=1,2}$ and $\{|p_{B_j}\rangle\}_{j=1,2}$, respectively. The probability $p_m(\lambda_{A_1B_1})$ that the outcome $\lambda_{A_1B_1}$ is obtained when e_{AB}

is performed on S in the mixture m is

$$\begin{aligned} p_m(\lambda_{A_1B_1}) &= Tr[\rho|p_{A_1B_1}\rangle\langle p_{A_1B_1}|] \\ &= \sum_i w_i p_i(\lambda_{A_1}) p_i(\lambda_{B_1}) \end{aligned} \quad (3)$$

where $p_i(\lambda_{A_1})$ and $p_i(\lambda_{B_1})$ are the probabilities for the sub-measurements e_A and e_B, respectively. Analogous formulas hold for the other outcomes, as follows

$$p_m(\lambda_{A_1B_2}) = \sum_i w_i p_i(\lambda_{A_1}) p_i(\lambda_{B_2}) \quad (4)$$

$$p_m(\lambda_{A_2B_1}) = \sum_i w_i p_i(\lambda_{A_2}) p_i(\lambda_{B_1}) \quad (5)$$

$$p_m(\lambda_{A_2B_2}) = \sum_i w_i p_i(\lambda_{A_2}) p_i(\lambda_{B_2}) \quad (6)$$

Hence, if we start with the numbers $p_m(\lambda_{A_iB_j})$, $i,j=1,2$, then it is not possible in general to prove that no mixture of product states that exist that gives rise to these numbers.

The violation of the marginal distribution law remains however a criterion for the presence of genuine entanglement. Indeed, let m be a mixture represented by the density operator ρ, and let us suppose that, e.g., the measurement e_{AB}, is a product measurement, represented by the self-adjoint operator $\mathcal{E}_A \otimes \mathcal{E}_B$, with spectral family on the ON basis $\{|p_{A_1B_1}\rangle, |p_{A_1B_2}\rangle, |p_{A_2B_1}\rangle, |p_{A_2B_2}\rangle\}$, where $|p_{A_iB_j}\rangle = |p_{A_i}\rangle \otimes |p_{B_j}\rangle$, $i,j=1,2$. We have

$$\begin{aligned} & p_m(\lambda_{A_1B_1}) + p_m(\lambda_{A_1B_2}) \\ &= Tr[\rho|p_{A_1B_1}\rangle\langle p_{A_1B_1}|] + Tr[\rho|p_{A_1B_2}\rangle\langle p_{A_1B_2}|] \\ &= p_m(\lambda_{A_1}) = p_m(\lambda_{A_1B_1'}) + p_m(\lambda_{A_1B_2'}) \end{aligned} \quad (7)$$

This means that the identification of a violation of the marginal law remains an indication of the presence of genuine entanglement.

Let us now consider Bell's inequalities in case of a mixture of product states and product measurements e_{AB}, $e_{AB'}$, $e_{A'B}$ and $e_{A'B'}$. They are respectively represented by the 'expectation value operators' $\mathcal{E}_{AB} = \mathcal{E}_A \otimes \mathcal{E}_B$, $\mathcal{E}_{AB'} = \mathcal{E}_A \otimes \mathcal{E}_{B'}$, $\mathcal{E}_{A'B} = \mathcal{E}_{A'} \otimes \mathcal{E}_B$ and $\mathcal{E}_{A'B'} = \mathcal{E}_{A'} \otimes \mathcal{E}_{B'}$, where $\mathcal{E}_A = |p_{A_1}\rangle\langle p_{A_1}| - |p_{A_2}\rangle\langle p_{A_2}|$, ..., $\mathcal{E}_{B'} = |p_{B_1'}\rangle\langle p_{B_1'}| - |p_{B_2'}\rangle\langle p_{B_2'}|$. We have

$$\mathcal{E}_{AB'} + \mathcal{E}_{A'B'} = (\mathcal{E}_A + \mathcal{E}_{A'}) \otimes \mathcal{E}_{B'} \quad (8)$$

$$\mathcal{E}_{A'B} - \mathcal{E}_{AB} = (\mathcal{E}_{A'} - \mathcal{E}_A) \otimes \mathcal{E}_B \quad (9)$$

Hence, one of the Bell operators is given by

$$\begin{aligned} B &= \mathcal{E}_{AB'} + \mathcal{E}_{A'B'} + \mathcal{E}_{A'B} - \mathcal{E}_{AB} \\ &= (\mathcal{E}_A + \mathcal{E}_{A'}) \otimes \mathcal{E}_{B'} + (\mathcal{E}_{A'} - \mathcal{E}_A) \otimes \mathcal{E}_B \end{aligned} \quad (10)$$

Suppose we consider a product state p represented by the unit vector $|p\rangle = |r_A\rangle \otimes |r_B\rangle$. The factor Δ in the CHSH inequality is, in this case,

$$\begin{aligned} \Delta = \langle p|B|p\rangle &= \langle r_A|\mathcal{E}_A|r_A\rangle\langle r_B|\mathcal{E}_{B'}|r_B\rangle \\ &+\langle r_A|\mathcal{E}_{A'}|r_A\rangle\langle r_B|\mathcal{E}_{B'}|r_B\rangle + \langle r_A|\mathcal{E}_{A'}|r_A\rangle\langle r_B|\mathcal{E}_B|r_B\rangle \\ &-\langle r_A|\mathcal{E}_A|r_A\rangle\langle r_B|\mathcal{E}_B|r_B\rangle \end{aligned} \quad (11)$$

Let us consider the following mathematical result.

Lemma 1. *If x, x', y and y' are real numbers such that $-1 \leq x, x', y, y \leq +1$ and $\Delta = x'y' + x'y + xy' - xy$, then $-2 \leq \Delta \leq +2$.*

Proof: Since Δ is linear in all the variables x, x', y, y', it must take on its maximum and minimum values at the corners of the domain of this quadruple of variables, that is, where each of x, x', y, y' is +1 or -1. Hence at these corners Δ can only be an integer between -4 and +4. But Δ can be rewritten as $(x+x')(y+y') - 2xy$, and the two quantities in parentheses can only be 0, 2, or -2, while the last term can only be -2 or +2, so that Δ cannot equal -3, +3, -4, or +4 at the corners. ■

One can verify at once that Eq. (11) satisfies Lemma 1, i.e., $-2 \leq \langle p|B|p\rangle \leq +2$. Hence, the CHSH inequality holds whenever p is a product state.

Let us investigate whether we can prove that Bell's inequalities are satisfied also when p is a mixture of product states. Hence, let m be a mixture of the pure product states r_1, r_2, ..., represented by the unit vectors $|r_{A_1}\rangle \otimes |r_{B_1}\rangle$, $|r_{A_2}\rangle \otimes |r_{B_2}\rangle$, ..., with weights w_1, w_2, ..., respectively, so that m is represented by the density operator $\rho = \sum_i w_i |r_{A_i}\rangle\langle r_{A_i}| \otimes |r_{B_i}\rangle\langle r_{B_i}|$. We have, by using Eq. (11),

$$\begin{aligned} \Delta = Tr[\rho B] = \sum_i w_i \Big(& \langle r_{A_i}|\mathcal{E}_A|r_{A_i}\rangle\langle r_{B_i}|\mathcal{E}_{B'}|r_{B_i}\rangle \\ & +\langle r_{A_i}|\mathcal{E}_{A'}|r_{A_i}\rangle\langle r_{B_i}|\mathcal{E}_{B'}|r_{B_i}\rangle \\ & +\langle r_{A_i}|\mathcal{E}_{A'}|r_{A_i}\rangle\langle r_{B_i}|\mathcal{E}_B|r_{B_i}\rangle \\ & -\langle r_{A_i}|\mathcal{E}_A|r_{A_i}\rangle\langle r_{B_i}|\mathcal{E}_B|r_{B_i}\rangle \Big) \end{aligned} \quad (12)$$

If we now put, for every i,

$$\begin{aligned} \delta_i = & \langle r_{A_i}|\mathcal{E}_A|r_{A_i}\rangle\langle r_{B_i}|\mathcal{E}_{B'}|r_{B_i}\rangle \\ & +\langle r_{A_i}|\mathcal{E}_{A'}|r_{A_i}\rangle\langle r_{B_i}|\mathcal{E}_{B'}|r_{B_i}\rangle \\ & +\langle r_{A_i}|\mathcal{E}_{A'}|r_{A_i}\rangle\langle r_{B_i}|\mathcal{E}_B|r_{B_i}\rangle \\ & -\langle r_{A_i}|\mathcal{E}_A|r_{A_i}\rangle\langle r_{B_i}|\mathcal{E}_B|r_{B_i}\rangle \end{aligned} \quad (13)$$

we get from Lemma 1 that, for every i, $-2 \leq \delta_i \leq +2$. Then, we can prove that $-2 \leq \Delta = \sum_i w_i \delta_i \leq +2$. Indeed, if, for every i, $\delta_i = +2$, we have $\sum_i w_i \delta_i = 2\sum_i w_i = +2$. Analogously, if, for every i, $\delta_i = -2$, we have $\sum_i w_i \delta_i = -2\sum_i w_i = -2$. Since now $\sum_i w_i \delta_i$ is a convex combination of δ_i, with weights w_i, its value lies in the convex set of numbers with extremal points -2 and +2, hence in the interval $[-2, +2]$, as maintained above. This proves that the CHSH inequality is satisfied when the situation is such that we have product measurements and a mixture of product states.

Summing up the results obtained in this section, we can say that the structural situation is the following.

(i) If product measurements are performed, the marginal distribution law holds whenever the state is a pure product state or a mixture of product states. This entails that there

 ISBN: 978-1-61208-303-2

is genuine entanglement when the marginal distribution law is violated, independent of the state of the entity.

(ii) When the marginal distribution law is satisfied and Bell's inequalities are violated, we have genuine entanglement. Indeed, Bell's inequalities hold also for a mixture of product states. In this case, the validiy of the marginal distribution law entails that all the entanglement can be pushed into the state.

(iii) When the marginal distribution law is satisfied, and the state is pure, we have genuine entanglement when the probabilities do not factorize. Indeed, for a pure product state and the marginal law satisfied, hence product measurements, the probabilities factorize.

It remains to investigate whether we can find more direct criteria for genuine entanglement allowing states to be mixtures, without the need to recur to the violation of Bell's inequalities. Indeed, entanglement exists which does not violate Bell's inequalities, hence the latter violation is only a sufficient condition.

III. Quantum realization of a nonlocal non-marginal box

In this section, we elaborate a quantum model in Hilbert space for an entity violating both Tsirelson's bound and the marginal distribution law. This case study manifestly reveals that the costruction of a quantum model is allowed by entangled measurements. Experimental realizations of this situation in physical and cognitive situations can be found in [18], [19].

Let S be an entity prepared in the pure entangled state p. Bell-type measurements are defined as usual. The measurement e_{AB} has the outcomes $\lambda_{A_1B_1}$, $\lambda_{A_1B_2}$, $\lambda_{A_2B_1}$ and $\lambda_{A_2B_2}$, and the final states, $p_{A_1B_1}$, $p_{A_1B_2}$, $p_{A_2B_1}$ and $p_{A_2B_2}$. The measurement $e_{AB'}$ has the outcomes $\lambda_{A_1B'_1}$, $\lambda_{A_1B'_2}$, $\lambda_{A_2B'_1}$ and $\lambda_{A_2B'_2}$, and the final states, $p_{A_1B'_1}$, $p_{A_1B'_2}$, $p_{A_2B'_1}$ and $p_{A_2B'_2}$. The measurement $e_{A'B}$ has four outcomes $\lambda_{A'_1B_1}$, $\lambda_{A'_1B_2}$, $\lambda_{A'_2B_1}$ and $\lambda_{A'_2B_2}$, and the final states $p_{A'_1B_1}$, $p_{A'_1B_2}$, $p_{A'_2B_1}$ and $p_{A'_2B_2}$. The measurement $e_{A'B'}$ has the outcomes $\lambda_{A'_1B'_1}$, $\lambda_{A'_1B'_2}$, $\lambda_{A'_2B'_1}$ and $\lambda_{A'_2B'_2}$, and the final states $p_{A'_1B'_1}$, $p_{A'_1B'_2}$, $p_{A'_2B'_1}$ and $p_{A'_2B'_2}$.

To work out a quantum-mechanical model for the latter situation in the Hilbert space $\mathbb{C}^2 \otimes \mathbb{C}^2$, considering it canonical isomorphic with $\mathbb{C}^4$, we represent the entangled state p by the unit vector $|p\rangle = |0, \sqrt{0.5}e^{i\alpha}, \sqrt{0.5}e^{i\beta}, 0\rangle$. The measurement e_{AB} is represented by the ON (canonical) basis $|p_{A_1B_1}\rangle = |1,0,0,0\rangle$, $|p_{A_1B_2}\rangle = |0,1,0,0\rangle$, $|p_{A_2B_1}\rangle = |0,0,1,0\rangle$, $|p_{A_2B_2}\rangle = |0,0,0,1\rangle$, and hence the probabilities of the outcomes $\lambda_{A_iB_j}$ of e_{AB} in the state p are given by $p(\lambda_{A_1B_1}) = |\langle p_{A_1B_1}|p\rangle|^2 = 0$, $p(\lambda_{A_1B_2}) = |\langle p_{A_1B_2}|p\rangle|^2 = 0.5$, $p(\lambda_{A_2B_1}) = |\langle p_{A_2B_1}|p\rangle|^2 = 0.5$, $p(\lambda_{A_2B_2}) = |\langle p_{A_2B_2}|p\rangle|^2 = 0$.

The measurement $e_{AB'}$ is represented by the ON basis $|p_{A_1B'_1}\rangle = |0, \sqrt{0.5}e^{i\alpha}, \sqrt{0.5}e^{i\beta}, 0\rangle$, $|p_{A_1B'_2}\rangle = |0, \sqrt{0.5}e^{i\alpha}, -\sqrt{0.5}e^{i\beta}, 0\rangle$, $|p_{A_2B'_1}\rangle = |1,0,0,0\rangle$, $|p_{A_2B'_2}\rangle = |0,0,0,1\rangle$, and the probabilities of the outcomes $\lambda_{A_iB'_j}$ of $e_{AB'}$ in the state p are given by $p(\lambda_{A_1B'_1}) = |\langle p_{A_1B'_1}|p\rangle|^2 = 1$, $p(\lambda_{A_1B'_2}) = |\langle p_{A_1B'_2}|p\rangle|^2 = 0$, $p(\lambda_{A_2B'_1}) = |\langle p_{A_2B'_1}|p\rangle|^2 = 0$, $p(\lambda_{A_2B'_2}) = |\langle p_{A_2B'_2}|p\rangle|^2 = 0$.

The measurement $e_{A'B}$ is represented by the ON basis $|p_{A'_1B_1}\rangle = |0, \sqrt{0.5}e^{i\alpha}, \sqrt{0.5}e^{i\beta}, 0\rangle$, $|p_{A'_1B_2}\rangle = |1,0,0,0\rangle$, $|p_{A'_2B_1}\rangle = |0, \sqrt{0.5}e^{i\alpha}, -\sqrt{0.5}e^{i\beta}, 0\rangle$, $|p_{A'_2B_2}\rangle = |0,0,0,1\rangle$, which entails probability 1 for the outcome $\lambda_{A'_1B_1}$ in the state p.

Finally, the measurement $e_{A'B'}$ is represented by the ON basis $|p_{A'_1B'_1}\rangle = |0, \sqrt{0.5}e^{i\alpha}, \sqrt{0.5}e^{i\beta}, 0\rangle$, $|p_{A'_1B'_2}\rangle = |1,0,0,0\rangle$, $|p_{A'_2B'_1}\rangle = |0,0,0,1\rangle$, $|p_{A'_2B'_2}\rangle = |0, \sqrt{0.5}e^{i\alpha}, -\sqrt{0.5}e^{i\beta}, 0\rangle$, which entails probability 1 for the outcome $\lambda_{A'_1B'_1}$ in the state p.

Let us now explicitly construct the self-adjoint operators representing the measurements e_{AB}, $e_{AB'}$, $e_{A'B}$ and $e_{A'B'}$. They are respectively given by

$$\mathcal{E}_{AB} = \sum_{i,j=1}^{2} \lambda_{A_iB_j} |p_{A_iB_j}\rangle\langle p_{A_iB_j}| \tag{14}$$

$$\mathcal{E}_{AB'} = \sum_{i,j=1}^{2} \lambda_{A_iB'_j} |p_{A_iB'_j}\rangle\langle p_{A_iB'_j}| \tag{15}$$

$$\mathcal{E}_{A'B} = \sum_{i,j=1}^{2} \lambda_{A'_iB_j} |p_{A'_iB_j}\rangle\langle p_{A'_iB_j}| \tag{16}$$

$$\mathcal{E}_{A'B'} = \sum_{i,j=1}^{2} \lambda_{A'_iB'_j} |p_{A'_iB'_j}\rangle\langle p_{A'_iB'_j}| \tag{17}$$

The self-adjoint operators corresponding to measuring the expectation values are obtained by putting $\lambda_{A_iB_i} = \lambda_{A_iB'_i} = \lambda_{A'_iB_i} = \lambda_{A'_iB'_i} = +1$, $i = 1,2$ and $\lambda_{A_iB_j} = \lambda_{A_iB'_j} = \lambda_{A'_iB_j} = \lambda_{A'_iB'_j} = -1$, $i,j = 1,2; i \neq j$. If we now insert these values into Eqs. (14)–(17) and define one of the 'Bell operators' as

$$\begin{aligned} B &= \mathcal{E}_{AB'} + \mathcal{E}_{A'B} + \mathcal{E}_{AB'} - \mathcal{E}_{AB} \\ &= \begin{pmatrix} 0 & 0 & 0 & 0 \\ 0 & 2 & 2e^{i(\alpha-\beta)} & 0 \\ 0 & 2e^{-i(\alpha-\beta)} & 2 & 0 \\ 0 & 0 & 0 & 0 \end{pmatrix} \end{aligned} \tag{18}$$

and its expectation value in the entangled state p, we get $\Delta = \langle p|B|p\rangle = 4$ in the CHSH inequality.

We add some conclusive remarks that are discussed in detail in [18], [19]. The measurement e_{AB} is a product measurement, since it has the product states represented by the vectors in the canonical basis of $\mathbb{C}^4$ as final states. Hence, e_{AB} 'destroys' the initial entanglement to arrive at a situation of a product state. The measurements $e_{AB'}$, $e_{A'B}$ and $e_{A'B'}$ are instead entangled measurements, since they are represented by spectral families constructed on entangled states (Th. 1). We finally observe that the marginal ditribution law is violated. Indeed, we have, e.g., $0.5 = p(\lambda_{A_1B_1}) + p(\lambda_{A_1B_2}) \neq p(\lambda_{A_1B'_1}) + p(\lambda_{A_1B'_2}) = 1$. Since then the situation above violates Bell's inequalities beyond Tsirelson's bound, we can say that we have an example of a 'nonlocal non-marginal box situation 2', if we follow

 ISBN: 978-1-61208-303-2

the classification in Section I. The locution 'nonlocal non-marginal box situation 1' has instead been used to denote a situation violating the marginal distribution law, but not Tsirelson's bound [17], [18], [19]. It seems that situations of this kind have been observed in Bell-type experiments on microscopic quantum particles, where they have been classified as 'anomalies' [21], [22]. We are elaborating an explanation of these anomalies in terms of entangled measurements within our quantum-theoretic framework. From a quantum foundational point of view, such an explanation would (i) constitute a breakthrough toward understanding the mechanism of entanglement, (ii) shed new light into the so-called 'no-signaling problem'.

The mathematical description presented here, modeling physical and cognitive experimental examples and in other papers [18], [19] are relevant, in our opinion, because they explictly show that a quantum model in Hilbert space can be elaborated also for a situation going beyond Tsirelson's bound, if one introduces entangled measurements. This reveals that the violation of Bell's inequalities is 'not limited by Tsirelson's bound' and can even be maximal, as we will see in the next section, too.

IV. Quantum realization of a nonlocal box

In this section, we provide a quantum Hilbert space modeling for an entity which maximally violate Bell's inequalities, i.e., with value 4, but satisfies the marginal distribution law. In physics, a system that behaves in this way is called a 'nonlocal box' [23]. We will see that such a system exhibits the typical symmetry which gives rise to the marginal distribution law being valid in quantum theory. Concrete experimental realizations of this situation can be found in [18].

We consider four measurements f_{AB}, $f_{AB'}$, $f_{A'B}$ and $f_{A'B'}$, with outcomes $\mu_{A_iB_j}$, ..., and $\mu_{A'_iB'_j}$, $i,j=1,2$, respectively, and a composite entity S in the mixture m of the pure entangled states p and q, represented by the unit vectors $|p\rangle = |0,\sqrt{0.5}e^{i\alpha},0.5e^{i\beta},0\rangle$ and $|q\rangle = |0,\sqrt{0.5}e^{i\alpha},-0.5e^{i\beta},0\rangle$, respectively, with equal weights. Thus, m is represented by the density operator $\rho = 0.5|p\rangle\langle p| + 0.5|q\rangle\langle q|$.

The first measurement f_{AB} is represented by the ON basis $|r_{A_1B_1}\rangle = |1,0,0,0\rangle$, $|r_{A_1B_2}\rangle = |0,1,0,0\rangle$, $|r_{A_2B_1}\rangle = |0,0,1,0\rangle$, $|r_{A_2B_2}\rangle = |0,0,0,1\rangle$, which gives rise to the self-adjoint operator

$$\mathcal{F}_{AB} = \sum_{i,j} \mu_{A_iB_j} |r_{A_iB_j}\rangle\langle r_{A_iB_j}| \tag{19}$$

By applying Lüders' rule, we can now calculate the density operator representing the final state of the entity S after the measurement f_{AB}. This gives

$$\rho_{AB} = \sum_{i,j=1}^{2} |r_{A_iB_j}\rangle\langle r_{A_iB_j}|\rho|r_{A_iB_j}\rangle\langle r_{A_iB_j}| = \rho \tag{20}$$

as one can easily verify. This means that the nonselective measurement f_{AB} leaves the state m unchanged or, equivalently, the marginal distribution law holds, in this case.

The second measurement $f_{AB'}$ is represented by the ON basis $|r_{A_1B'_1}\rangle = |0,\sqrt{0.5}e^{i\alpha},\sqrt{0.5}e^{i\beta},0\rangle$, $|r_{A_1B'_2}\rangle = |1,0,0,0\rangle$, $|r_{A_2B'_1}\rangle = |0,0,0,1\rangle$, $|r_{A_2B'_2}\rangle = |0,\sqrt{0.5}e^{i\alpha},-\sqrt{0.5}e^{i\beta},0\rangle$, which gives rise to a self-adjoint operator

$$\mathcal{F}_{AB'} = \sum_{i,j} \mu_{A_iB'_j} |r_{A_iB'_j}\rangle\langle r_{A_iB'_j}| \tag{21}$$

By applying Lüders' rule, we can again calculate the density operator representing the final state of the vessels of water after $f_{AB'}$. This gives

$$\rho_{AB'} = \sum_{i,j=1}^{2} |r_{A_iB'_j}\rangle\langle r_{A_iB'_j}|\rho|r_{A_iB'_j}\rangle\langle r_{A_iB'_j}| = \rho \tag{22}$$

Also in this case, the nonselective measurement $f_{AB'}$ leaves the state m unchanged. If we consider the experimental realization in [18] of the nonlocal box situation, we can see that we can represent the measurements $f_{A'B}$ and $f_{A'B'}$ by the same self–adjoint operators as the one representing $f_{AB'}$. Also in these cases we obviously get that the density operators after applying Lüders' rule remain the same. This implies that the marginal distribution law is always satisfied.

Let us now evaluate the expectation values corresponding to the four measurements above in the mixed state m and insert them into the CHSH inequality. The expectation value operators for this version are given by

$$\mathcal{F}_{AB} = \begin{pmatrix} 1 & 0 & 0 & 0 \\ 0 & -1 & 0 & 0 \\ 0 & 0 & -1 & 0 \\ 0 & 0 & 0 & 1 \end{pmatrix} \tag{23}$$

$$\mathcal{F}_{AB'} = \mathcal{F}_{A'B} = \mathcal{F}_{A'B'} = \begin{pmatrix} -1 & 0 & 0 & 0 \\ 0 & 1 & 0 & 0 \\ 0 & 0 & 1 & 0 \\ 0 & 0 & 0 & -1 \end{pmatrix} \tag{24}$$

Hence, our Bell operator is given by

$$B = \mathcal{F}_{AB'} + \mathcal{F}_{A'B} + \mathcal{F}_{A'B'} - \mathcal{F}_{AB} = \begin{pmatrix} -4 & 0 & 0 & 0 \\ 0 & 4 & 0 & 0 \\ 0 & 0 & 4 & 0 \\ 0 & 0 & 0 & -4 \end{pmatrix} \tag{25}$$

This gives $\Delta = Tr\rho B = 4$ in the CHSH inequality, which shows that Bell's inequalities are maximally violated in the mixture m. Following our classification scheme in Section I, we can can regard our quantum model for the nonlocal box above as an example of a 'nonlocal box situation'.

In quantum theory, the possibility of constructing a quantum representation for a nonlocal box is usually maintained to be forbidden by quantum laws, i.e., Tsirelson's bound. We have shown here that such a quantum representation

 ISBN: 978-1-61208-303-2

can indeed be elaborated, once entangled measurements are taken into account.

V. Conclusions

We have presented a quantum-theoretic modeling in Hilbert space for the description of the entanglement that characterizes situations experimentally violating Bell's inequalities. We have shown that different types of quantum models can be constructed, in addition to the 'customary quantum situation', depending on the behavior with respect to (i) the marginal distribution law, (ii) Tsirelson's bound. Moreover, entangled measurements provide an operational and technical resource for dealing with situations that are typically considered 'beyond the customary quantum situation'. This scheme has been extended to quantum mixtures, attaining some nontrivial conclusions.

The perspective above is completely general, for it enables detection and representation of the entanglement that is present in any kind of composite entity, once experimental tests are defined giving rise to the scheme necessary to formulate Bell's inequalities. We also believe our scheme to be valuable for the study of quantum foundational problems in a more general way. Indeed, the introduction of entangled measurements reveals a new understanding of the entanglement dynamics in Bell-type experiments, also on microscopic quantum particles and nonlocal boxes. The realization of an experimental nonlocal box may have a deep impact on the technologies employed in quantum information to detect, measure and preserve entanglement.

References

[1] J. S. Bell, "On the Einstein-Podolsky-Rosen paradox," Physics, vol. 1, 1964, pp. 195–200.

[2] L. Accardi and A. Fedullo, "On the statistical meaning of complex numbers in quantum theory," Lett. Nuovo Cim., vol. 34, 1982, pp. 161–172.

[3] D. Aerts, "A possible explanation for the probabilities of quantum mechanics," J. Math. Phys., vol. 27, 1986, pp. 202–210.

[4] I. Pitowsky, Quantum Probability, Quantum Logic, Berlin: Springer, 1989.

[5] D. Aerts and S. Aerts, "Applications of quantum statistics in psychological studies of decision processes," Found. Sci., vol. 1, 1995, pp. 85–97.

[6] D. Aerts and L. Gabora, "A theory of concepts and their combinations I: The structure of the sets of contexts and properties," Kybernetes, vol. 34, 2005, pp. 167–191.

[7] D. Aerts and L. Gabora, "A theory of concepts and their combinations II: A Hilbert space representation," Kybernetes, vol. 34, 2005, pp. 192–221.

[8] D. Aerts, "Quantum structure in cognition," J. Math. Psychol., vol. 53, 2009, pp. 314–348.

[9] E. M. Pothos and J. R. Busemeyer, "A quantum probability model explanation for violations of 'rational' decision theory," Proc. Roy. Soc. B, vol. 276, 2009, pp. 2171–2178.

[10] A. Y. Khrennikov, Ubiquitous Quantum Structure, Berlin: Springer, 2010.

[11] J. R. Busemeyer and P. D. Bruza, Quantum Models of Cognition and Decision, Cambridge: Cambridge University Press, 2012.

[12] D. Aerts, "Example of a macroscopical situation that violates Bell inequalities", Lett. Nuovo Cim., vol. 34, 1982, pp. 107–111.

[13] D. Aerts, S. Aerts, J. Broekaert, and L. Gabora, "The violation of Bell inequalities in the macroworld," Found. Phys., vol. 30, 2000, pp. 1387–1414.

[14] D. Aerts and S. Sozzo, "Quantum structure in cognition: Why and how concepts are entangled," LNCS, vol. 7052, Berlin: Springer, 2011, pp. 118–129.

[15] D. Aerts, L. Gabora, and S. Sozzo, "Concepts and their dynamics: A quantum–theoretic modeling of human thought," Top. Cogn. Sci. (in print). ArXiv: 1206.1069 [cs.AI].

[16] D. Aerts, J. Broekaert, L. Gabora, and S. Sozzo, "Quantum structure and human thought," Behav. Bra. Sci., vol. 36, 2013, pp. 274–276.

[17] D. Aerts and S. Sozzo, "Quantum entanglement in concept combinations," accepted in Int. J. Theor. Phys., ArXiv:1302.3831 [cs.AI], 2013.

[18] D. Aerts and S. Sozzo, "Entanglement zoo I. Foundational and structural aspects, accepted in LNCS, 2013.

[19] D. Aerts and S. Sozzo, "Entanglement zoo II. Applications in physics and cognition, accepted in LNCS, 2013.

[20] B. S. Tsirelson, "Quantum generalizations of Bell's inequality," Lett. Math. Phys., vol. 4, 1980, pp. 93–100.

[21] A. Aspect, "Bell's inequality test: More ideal than ever," Nature, vol. 398, 1982, pp. 189–190.

[22] G. Adenier and A. Y. Khrennikov, "Is the fair sampling assumption supported by EPR experiments?," J. Phys. A, vol. 40, 2007, pp. 131–141.

[23] S. Popescu and D. Rohrlich, "Nonlocality as an axiom," Found. Phys., vol. 24, 1994, pp. 379–385.

[24] J. F. Clauser, M. A. Horne, A. Shimony, and R. A. Holt, "Proposed experiment to test local hidden-variable theories," Phys. Rev. Lett., vol. 23, 1969, pp. 880–884.

 ISBN: 978-1-61208-303-2

Electrical and Structural Analysis of CNT-Metal Contacts in Via Interconnects

Patrick Wilhite, Anshul Vyas, Jason Tan, and Cary. Y. Yang
Santa Clara University, Center for Nanostructures
Santa Clara, USA
pwilhite@scu.edu; avyas@scu.edu; jttan@scu.edu; cyang@scu.edu

Phillip Wang, Jeongwon Park, Hua Ai, and Murali Narasimhan
Applied Materials
Santa Clara, USA
phillip_wang@amat.com; jeongwon_park@amat.com; hua_ai@amat.com; murali_narasimhan@amat.com

***Abstract*- Vertically aligned carbon nanotubes grown by plasma-enhanced chemical vapor deposition offer a potentially suitable material for via interconnects in next-generation integrated circuits. Key performance-limiting factors include high contact resistance and low carbon nanotube packing density, which fall short of meeting the requirements delineated in the ITRS roadmap for interconnects. For individual carbon nanotube s, contact resistance is a major performance hurdle since it is the dominant component of carbon nanotube interconnect resistance, even in the case of vertically aligned carbon nanotube arrays. In this study, we correlate the carbon nanotube-metal interface nanostructure to their electrical properties in order to elucidate growth parameters that can lead to high density and low contact resistance and resistivity.**

Keywords-carbon nanotube; via; resistance; contact resistance.

I. INTRODUCTION

Nanocarbons, in general, and Carbon Nanotubes (CNTs) in particular are expected to be implemented in next-generation integrated circuit (IC) technologies, due to their high tolerance to electromigration and high current-carrying capacity [1-3]. Moreover, with resistivities reported in the range of 10^{-6} Ωcm for single-walled CNTs [3], they are indeed viable materials to replace copper (Cu) in vias and interconnects for ICs with sub-20 nm feature sizes. Attaining a CNT resistivity of 10^{-6} Ωcm for functional devices or simply meeting the industry requirement for interconnect resistance [1] is a daunting challenge for researchers, but its superior current capacity over Cu is already a distinct advantage, as the current capacity of Cu in the sub-20 nm regime is expected to be significantly less than half of its bulk value of 10^6 A/cm^2 [4]. Aside from resistivity, the greatest challenge to overcome is minimization of the resistance between CNT and metal contact, which critically depends on CNT growth and subsequent device fabrication processes.

Recently, we reported individual CNT resistances of about 1 kΩ in a vertically aligned CNT array with average diameter ~100 nm and length ~1.5 μm [4]. Of such resistance, about 800 Ω is attributed to the contact between the CNT and metal electrodes. These results are consistent with prior reports using similar techniques [5,6]. High-resolution transmission electron microscopy (HRTEM) images revealed a clean interface between CNT and the underlayer metal, albeit with significant surface asperity and large metal grains [4].

Further, energy-dispersive x-ray spectroscopy (EDS) showed significant amounts of oxygen and nitrogen present in the interfacial region, which could negatively impact the contact resistance.

Currently, we have succeeded in reducing the average diameter of the PECVD-grown CNTs to about 15 nm, while increasing the packing densities to >10^{11} cm^{-2}. This result is comparable to recent work reported for CNT vias [5] and is closer to values delineated by the current ITRS roadmap [1]. However, initial current-voltage (*I-V)* measurements suggest that the underlayer metal surface graininess is the primary cause for high contact resistance. To improve CNT electrical behavior, we have made changes to the CNT growth process to improve the as-grown CNT-metal contact with the primary objective of reducing the contact resistance, thus yielding a total CNT via resistance closer to that of Cu.

In this paper, the CNT-metal interface is studied extensively using HRTEM to gain a better understanding of the physical origin of contact resistance, and to provide the needed feedback for process improvement. *I-V* characteristics of individual CNTs are measured to allow extraction of electrode contact resistance and CNT resistivity. Correlation of these electrical performance parameters for CNTs grown under different conditions with their respective HRTEM images provides the needed insight that will lead to the eventual functionalization of CNT via interconnects.

In the next sections, we will elaborate on the device fabrication, followed by the characterization of these devices using HRTEM and electrical measurements.

II. CNT GROWTH AND DEVICE FABRICATION

Titanium (Ti) is an excellent underlayer metal due to its compatibility with current IC technology.

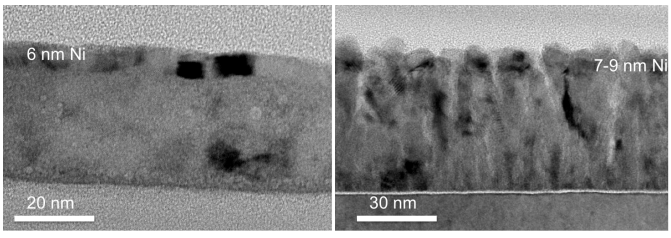

Fig. 1. Cross-sectional SEM images of substrates consisting of Ni catalyst film on Ti underlayer. Smooth or continuous films (a) results in lower contact resistance compared with grainy substrate (b).

 ISBN: 978-1-61208-303-2

High-density CNT growth is observed on Ti film with significant surface roughness, where the Ti grains serve as templates for the nickel (Ni) catalyst film deposition, as shown in Fig. 1. CNTs appear to grow on the grain boundaries, and smaller grains result in higher density. Different film deposition conditions can be used to study the effect of graininess on CNT packing density and diameter distribution, as well as contact resistance.

The starting wafer consists of a thin silicon dioxide layer that serves as a diffusion barrier to subsequent film deposition. The Ti underlayer and Ni catalyst films are deposited using magnetron sputtering. This underlayer serves as the base electrode, and provides a clean interface to the as-grown CNTs. CNTs are then grown using a plasma-enhanced chemical vapor deposition (PECVD) reactor, with acetylene as the carbon source and ammonia as reducing agent. PECVD growth parameters are optimized for the Ni/Ti layers to yield the highest CNT packing density. Smooth Ti substrates with 6 nm of Ni yield higher CNT array density (1.9 x 10^{10} cm^{-2}), than grainy substrates (1.2 x 10^{10} cm^{-2}) with ~8 nm of Ni. Scanning Electron Microscope (SEM) images of as-grown CNT arrays are shown in Fig. 2.

After CNT growth, the exposed surface is encapsulated in a polymer matrix to fill the interstitial spacing within the CNT arrays. This provides electrical isolation among the CNTs, while providing the structural rigidity necessary to land the nanoprober tips for electrical measurements. The CNT surface is then planarized using ion-beam sputtering and mechanical polishing. Sections of the same substrate are further polished to different lengths for electrical probing, as described below.

III. DEVICE CHARACTERIZATION

A. Electrical Measurements

Due to the geometry of the vertically-aligned CNT array, a four-point-probe measurement is not feasible to directly determine the CNT resistivity and contact resistance. To extract these values, a linear fit of the CNT total resistance, R_T, versus CNT length, L_{CNT}, behavior is used with the assumption that each CNT and its contacts are ohmic resistors. Because the contact resistance R_C is diameter-dependent, all measurements are performed on CNTs with similar diameters. Thus, R_C and CNT resistivity ρ can be extracted using

$$R_T = R_C + R_{CNT} = R_C + \frac{4\rho}{\pi D_{CNT}^2} L_{CNT} \,. \qquad (1)$$

R_C is simply the resistance intercept of the R_T *vs.* L_{CNT} line as shown in Fig. 3, while L_{CNT} and diameter (D_{CNT}) are determined from SEM images. The CNT resistivity is then determined from the slope of the line and using Eq. (1).

For these measurements, the nanoprober-CNT contact resistance is minimized with Joule heating from current stressing. This improves R_C by several orders of magnitude [4-6]. Despite such improvement, R_C is still the dominant factor governing CNT device performance, as apparent from Fig. 3(a) for CNTs grown on a grainy substrate. With a smooth substrate, we are able to grow CNTs with individual contact resistance below 400 Ω, as shown in Fig. 3(b). And contact resistance around 300 Ω and CNT resistivity in the 10^{-4} - 10^{-5} Ωcm range as given in Table I are now achievable.

B. High-Resolution Transmission Electron Microscopy

HRTEM images of the CNT-Ti interface reveal two significant differences in CNTs grown on the smooth Ti substrate compared with those on the grainy substrate, as

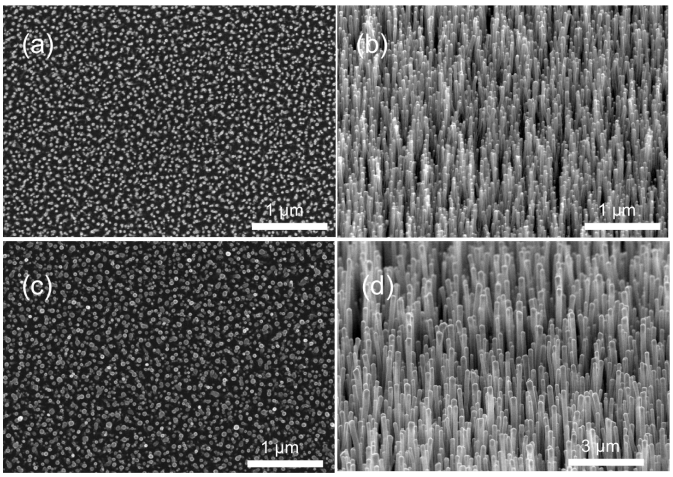

Fig. 2. Top-view (a) and (b) tilted-view SEM images of as-grown CNT arrays on smooth Ti underlayer with density ~ 1.9 x 10^{10} cm^{-2}. (c) Top-view and (d) tilted-view of as-grown CNT on grainy substrate with density ~ 1.2 x 10^{10} cm^{-2}. Growth on smooth Ti substrate shows smaller average diameter and narrower diameter distribution.

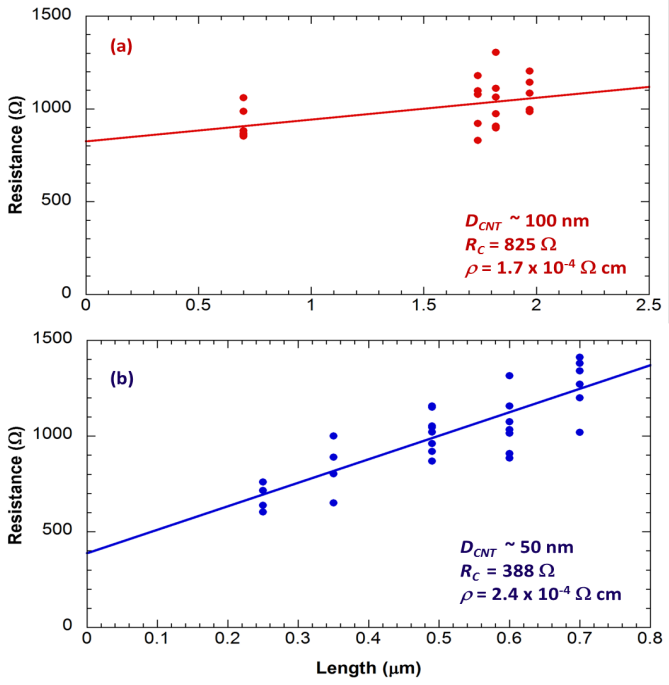

Fig. 3. Total resistance R_T versus CNT length L_{CNT} for grainy substrate (a) and smooth substrate (b). Each data point corresponds to an individual CNT measurement.

TABLE I. PROJECTIONS OF 30 nm-CNT VIA RESISTANCE BASED ON PRESENT RESULTS FROM US AND OTHERS [10], AND COMPARED WITH THAT OF CU. CALCULATED RESULTS ARE BASED ON 120 nm-LONG VIA AND CNT DENSITY OF 4.4 X 10^{11} cm^{-2}.

Via	R_C	ρ (Ω cm)	D_{CNT} (nm)	R_{CNT}	30 nm Via resistance
AIST	N/A	~ 1 x 10^{-4}	~ 4	9.55 kΩ (calc.)	190 Ω [1] (calc.)
SCU	300 Ω	~5 x 10^{-5}	15	340 Ω	160 Ω [2] (projected)
Cu	~15 Ω	5 x 10^{-6}			~25 Ω

shown in Fig. 4. CNTs on the smooth substrate show parallel graphitic planes perpendicular to the metal underlayer, while those on the grainy substrate have structures resembling stacked cups. The latter structure is generally called carbon nanofiber (CNF) [7,8]. These distinct nanostructures near the metal interface appear to be dictated by the catalyst particle shape and size, and defined in the early stages of CNT growth [9]. While both structures appear to have a clean interface with Ti, the smoother substrate shows less grain boundaries and provides a more effective conduction path across the interface. Further, the HRTEM images confirm that a smooth underlayer results in more uniform CNT growth and higher density. And the multi-wall structure near the interface is clearly the primary reason for a lower contact resistance. Such findings are valuable for the eventual optimization of the CNT growth process to yield functional via interconnects.

IV. CONCLUSION

Using a PECVD reactor, we have grown CNTs on Ni/Ti substrates with different degrees of graininess to elucidate the growth parameters that can eventually lead to via fabrication

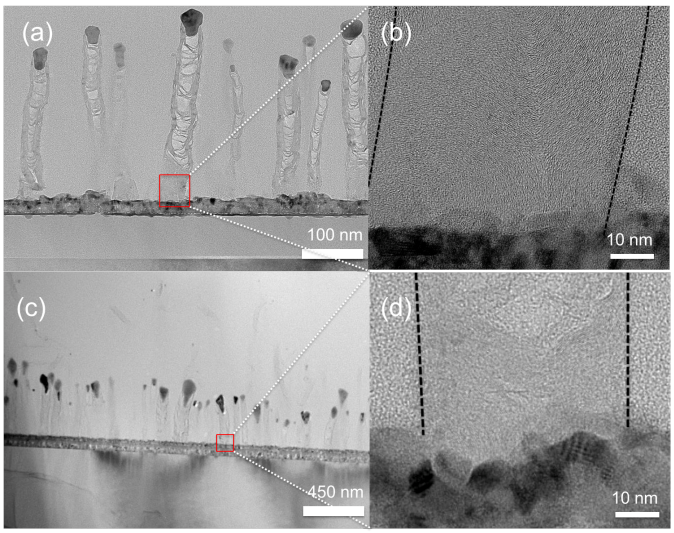

Fig. 4. (a) TEM cross-sectional image of as-grown CNTs on (a) smooth Ti substrate, and (b) HRTEM image of an individual CNT-metal interface as indicated in (a). (c) & (d) Corresponding images for a grainy Ti substrate. Both sets of interface images display a clean interface between CNT and underlayer metal.

process optimization. For a functional CNT via, maximal CNT density, minimal average CNT diameter, very low CNT-metal contact resistance, and parallel multi-wall CNT structure are needed. This study provides the basis to define the growth and fabrication tasks to achieve such targets. To quantify these targets based on our present results, simple projections of resistance for a 30 nm via are given in Table I, where comparison with Cu is also shown.

It is clear from such comparison that the key in "matching" Cu via resistance lies in minimizing the CNT-metal contact resistance and to a lesser extent, maximizing the CNT density. Efforts on CNT growth and device fabrication are underway to achieve densities >10^{11} cm^{-2}, while further improving the CNT-metal interface.

REFERENCES

[1] 2011 International Technology Roadmap for Semiconductors, http://www.itrs.net/Links/2012ITRS/Home2012.htm.

[2] T. Saito, T. Yamada, D. Fabris, H. Kitsuki, P. Wilhite, M. Suzuki, and C.Y. Yang, "Improved contact for thermal and electrical transport in carbon nanofiber interconnects," Applied Physics Letters 93, 102108 (1-3) (2008).

[3] M. S. Dresselhaus, G. Dresselhaus, and P. Avouris, "Carbon nanotubes: synthesis, structure, properties, and applications," Berlin, New York, Springer, 2001.

[4] P. Wilhite, A. Vyas, J. Tan, P. Wang, J. Park, M. Jackson, and C.Y .Yang, "Nanostructure Characterization of Carbon Nanotube/Metal Interfaces," MRS Spring Meeting, San Francisco, 2012.

[5] W. Wu, S. Krishnan, T. Yamada, X. Sun, P. Wilhite, R. Wu, K. Li, and C.Y. Yang, "Contact resistance in carbon nanostructure via interconnects," Applied Physics Letters 94, 2009, 163113 (1-3).

[6] K. Li, R. Wu, P. Wilhite, V. Khera, S. Krishnan, X. Sun, and C.Y. Yang, "Extraction of contact resistance in carbon nanofiber via interconnects with varying lengths," Applied Physics Letters 97, 2010, 253109 (1-3).

[7] Q. Ngo, A.M. Cassell, V. Radmilovic, J. Li, S. Krishnan, M. Meyyappan, and C.Y. Yang, "Palladium catalyzed formation of carbon nanofibers by plasma enhanced chemical vapor deposition," Carbon 45, 2007, 424-428.

[8] A. V. Melechko, V. I. Merkulov, T. E. McKnight, M. A. Guillorn, K. L. Klein, D. H. Lowndes, and M. L. Simpson, "Vertically aligned carbon nanofibers and related structures: Controlled synthesis and directed assembly," J. Appl. Phys. 97, 2005, 041301 (1-7).

[9] A. V. Melechko, K. L. Klein, J. D. Fowlkes, D. K. Hensley, I. A. Merkulov, T. E. McKnight, P. D. Rack, J. A. Horton, and M. L. Simpson, "Control of carbon nanostructure: From nanofiber toward nanotube and back," J. Appl. Phys. 102, 2007, 074314 (1-7).

[10] M. Nihei, "CNT/Graphene Technologies for Advanced Interconnects," IITC Short Course, San Jose, 2012.

 ISBN: 978-1-61208-303-2

Determination of the Structure of a 1-D Nano-Particle by Means of an Electric Field

Guillermo Monsivais
Instituto de Física, Universidad Nacional Autónoma de México
México, D.F., Mexico
e-mail: monsi@fisica.unam.mx

María T. Pérez-Maldonado
Facultad de Física, Universidad de La Habana
Havana, Cuba
e-mail: mtperez@fisica.uh.cu

Víctor Velasco
Instituto de Ciencia de Materiales de Madrid, CSIC
Madrid, Spain
e-mail: vrvr@icmm.csic.es

***Abstract*— In this paper, a method to determine the configurational structure of a chain of atoms, based in the application of an electric field is proposed. This method gives the possibility to detect the existence and localization of dislocations and the presence of impurities inside the particle. This is a simple example of the so-called inverse problems, which consist in specifying the configuration of a system from the knowledge of the spectrum. On the other hand, in the so-called direct problems, which are studied much more frequently in the literature, one must obtain the spectrum from the knowledge of the characteristics of the system.**

Keywords-quasiperiodic systems; electron states; Stark ladders.

I. INTRODUCTION

The study of the electronic properties of materials that do not have translational symmetry has been a very active field in the last years. Among the important properties of these structures are: the Anderson localization, the fractal properties of the spectrum of the quasi crystals, etc. In particular, the discovery of the Anderson localization phenomenon of quantum mechanics [1] gave origin to one of the most important subjects in condensed matter physics. On the other hand, the systems whose structural order is described by means of deterministic sequences like those of Fibonacci [2], Thue-Morse [3], Godreche-Luck [4], etc. can be seen as an intermediate case between periodic and disordered 1-D systems. It has been observed that the electronic spectra of some of these systems are self-similar, and the energy bands divide into several sub-bands, each of which further subdivides into more sub-bands and so on [5-7].

Most of these studies have been direct problems in the sense that they begin with a given system, and then the eigenvalues and eigenfunctions are obtained. Here, we consider a particular case of an inverse problem [8]. We follow here the same path at the beginning, but then, we return to the characteristics of the systems and we establish a correlation between the configuration of the system and the characteristics of the spectrum. We show that the configuration of the systems considered here can be deduced from the knowledge of the spectra. The main idea is to employ the capability of the electric field to produce well-separated eigenvalues. In particular, if the systems are periodic, the electric field produces the well-known Wannier-Stark Ladders (WSL), which consists of a series of equally spaced energy levels appearing in the spectrum [9]. The distance between the neighboring energies is proportional to the field intensity. This property of the electric field allows the prediction of the approximate configuration of the imperfect crystal, in spite of the chaotic appearance of the spectrum at first view.

The article is organized as follows: In Section II the model for a deformed crystal is described. The properties of the calculated spectra are discussed in Section III. Section IV is devoted to explain the main conclusions derived from this work.

II. MODEL FOR THE DEFORMED CRYSTAL

In order to show how an electric field can be used for the aforementioned objectives, we consider a one-dimensional crystal that has suffered a deformation under control. Then, the structure of the spectrum is analyzed and a correlation between the structure of the particle and the spectrum is established. The electrified imperfect crystal is modeled as follows. Let us suppose that the potential for one electron in a 1-D system can be described by means of the following expression (see Fig. 1).

$$V(x)=\sum_{i=1}^{N-1}\beta_i\delta(x-x_i)+\sum_{i=1}^{N-1}h_i\theta(x-x_i) \quad 0<x<x_N \tag{1}$$

 ISBN: 978-1-61208-303-2

with $x_i \in [0, x_N]$, $i = 0,...,N$. The values of the potential at the ends of the interval $(0, x_N)$ are equal to infinite, in order to confine the movement of the electron inside this interval. Here, $\delta(x - x_i)$ and $\theta(x - x_i)$ are the Dirac delta function and the Heaviside step function, respectively [10]. The length of the interval (x_1, x_{i+1}) will be denoted as l_i. We note that when the lengths l_i and the intensities β_i of the delta potentials are set equal to constants l_0 and $\beta_1 \ \forall i$, respectively, the potential (1) can be seen as the superposition of a periodic potential, plus a linear term $f x$ due to a uniform applied electric field of intensity f. The relation between the parameters h_i and the intensity of the electric field is $h_i = l_i f = (x_{i+1} - x_i) f$.

The specific form of the potential $V(x)$ will be a superposition of blocks of type A_i and blocks of type B_i. The block A_i is a flat interval of height $V_i \equiv \sum_{m=1}^{i} h_m$ and length l_A independent of i. The block B_i is a delta potential of intensity β_i. When $f = 0$, we have $V_i = 0 \ \forall i$, and all the blocks A_i are equal to a given block A. In this case, we can obtain periodic structures, if we take, for example, all the blocks B_i equal to a given block B and we take the configuration $AB\,AB\,AB\,AB\,AB\ldots$.

We will study the evolution of the electronic spectrum when the potential (1) becomes disordered by changing the distribution of the blocks. We will start from perfect periodic structures and then we will gradually perturb them to obtain a quasi-periodic structure. Here, we will only consider the Fibonacci sequences [2] S_8. However, the use of this sequence is not restrictive and one can use the electric field to analyze any other type of imperfect crystals. For the case $f = 0$, we built these sequences using the blocks A and B defined above and using the Fibonacci rule $S_{j+1} = \{S_j, S_{j-1}\}$ [2], with the initial conditions $S_1 = A$ and $S_2 = AB$, being j the generation number. The eighth generation is

S_8=ABAABABAABAABABAABABAABAABABAABAAB. (2)

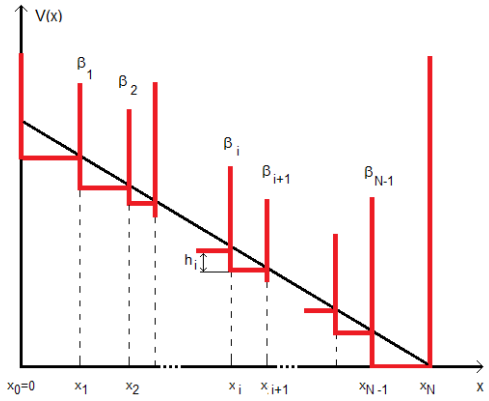

Figure 1. Potential $V(x)$ given by (1).

III. PROPERTIES OF THE SPECTRUM

Briefly, in the following, we use the phrase "periodic system" or "locally periodic system" to denote a section of a periodic system inside the potential well of Fig. 1. For future reference, we start by discussing the well-known effect of an electric field on the spectrum of a periodic system. By means of the transfer matrix method, we have calculated the energies and the results which are shown in Fig. 2. The figure shows the evolution of the energy levels as a function of the electric field intensity f. Each line corresponds with an energy level. The characteristics of a similar spectrum were discussed many years ago in [11]. On the left of these figures, we see that all the levels are grouped in bands, as must be for $f = 0$, since in this case, the system is periodic. Each band in Fig. 2 has 8 levels, because the potential considered in the figure has exactly 8 cells.

It is easy to prove that the upper limit of the $n-$th band of a finite periodic sequence is equal to the upper limit E_n of the $n-$th band of the infinite Kronig-Penney model [12]. Furthermore, it is also equal to the $n-$th level of an infinite well of length p, which is given by $E_n = n^2\pi^2/2p^2$.

 ISBN: 978-1-61208-303-2

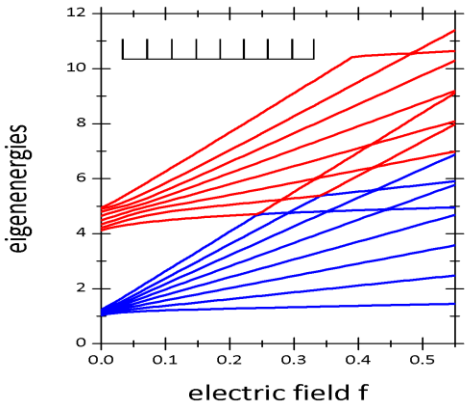

Figure 2. First and second bands of the electronic spectrum of a finite periodic structure with 8 cells (see inset) as functions of the electric field intensity.

For the lower level of the $n-$th band, there is not a closed expression, but it can be proved [13] that it is very close to the lower limit e_n of the $n-$th band of the infinite Kronig-Penney model, which satisfies the following expression [12]

$$\cos\left(\sqrt{2e_n}\,p\right)+\beta\frac{\sin\left(\sqrt{2e_n}\,p\right)}{\sqrt{2e_n}}=\pm 1. \qquad (3)$$

We have verified that E_1, E_2, e_1 and e_2 obtained from these formulas are in agreement with the plotted values on the left sides of Fig. 2, where we have used $p=2.$ On the right of this figure (corresponding with the value $f=0.55$), the levels appear separated due to the presence of the electric field. We clearly see that all the levels coming from the first band appear equally spaced (except the two levels of the extremes that are a little more separated). This structure is precisely the WSL predicted by Wannier [6]. According to Wannier, the nearest-neighbor energy level spacing ΔE is equal to pf. However, due to our systems being finite, the WSL are not perfect. So, the levels of the ladders are not exactly equally spaced. This is frequently more evident with the extreme levels of the ladders, as occurs with the first ladder of Fig. 2 at $f=0.55.$ If one neglects these two levels, the rest of the levels have a quite reasonable behavior.

A superficial analysis of Fig. 2 could yield to the conclusion that the second WSL comes from the second band. However, this is not true. Indeed, a detailed analysis of the lines shows that the fifth level of the first band is bending at $f=0.44,$ giving rise to the first level of the second ladder, etc. However, because a fast view of the lines induce to consider that the $n-$th ladder is generated by the $n-$th band, and in order to make the discussion of figures easier, we are taking this consideration valid.

On the other hand, it is well known [12] that, for the case $f=0,$ the level density in each band is not uniform. In contrast, when f is large enough and the WSL are well established, the level density is uniform for all values of f greater than a certain minimum value. As a consequence, the trajectories that the eigenvalues follow, as f increases, are slightly curved lines in the region of small values of f, as can be verified with a detailed analysis of each trajectory.

In the following, we analyze the effects of disorder. We show in the insets of Fig. 3 six configurations of potentials for the case $f=0.$ The inset of Fig. 3a shows a finite periodic potential with 8 wide cells and 8 thin cells distributed as

$$C_wC_t\,C_wC_t\,C_wC_t\,C_wC_t\,C_wC_t\,C_wC_t\,C_wC_t\,C_wC_t \qquad (4)$$

where C_w represents a wide cell of length l_w and C_t, a thin cell of length l_t. We are taking $l_w=2,\ \ l_t=1.$ Therefore, the period p is equal to 3 and the number of periods is equal to 8. The above sequence of cells can be constructed by assigning the sequence of blocks AAB with the cells C_w and the sequence AB with the cells C_t. So, the block sequence

$$AABAB\,AABAB\,AABAB\,AABAB\,AABAB\,AABAB\,AABAB\,AABAB \qquad (5)$$

is equivalent to the sequence of cells (4).

We now transform step by step the above periodic system into the system S_8, given by expression (2). In the inset of Fig. 3b, we have moved the eight thin cells to the right. For brevity, the corresponding configurations of cells and blocks are not written here.

In the inset of Fig. 3c, we have dropped three thin cells and in the inset (d), we have moved one of the thin cells to the place that it must have in a Fibonacci sequence of blocks. In the inset (e), we have moved a second thin cell to the place that it had in a Fibonacci sequence. At the end of this process, we obtain the inset of Fig. 3f, which corresponds with the configuration of blocks given by the sequence S_8 of expression (2).

The spectra associated with the insets of Fig. 3 are shown in the whole figures, respectively. The set of points at the left ends of the lines (at $f=0$) form the electronic

 ISBN: 978-1-61208-303-2

spectra associated with the potentials of the insets. The other points of the lines show, as before, the evolution of the energy levels as a function of f.

On the left of Fig. 3a, we see at least two groups of levels which evolve into a complex structure when the intensity f, is increased. Since the system has a total amount of 16 cells, each band must have 16 levels. However, because each period has an internal structure consisting of the two cells C_w and C_t, each band must have an internal structure consisting of two sub-bands, each of them having 8 levels. The 8 levels of lower energy shown in Fig. 3a are just the levels of the first sub-band of the first band $\mathbf{B_1}$. The other 8 levels forming the second sub-band of $\mathbf{B_1}$ are in the same zone as the first sub-band of the second band. The second sub-band of $\mathbf{B_2}$ is not shown in the figure. The first sub-band must be associated with the wide cells, and the second sub-band with the thin cells. The first sub-band of $\mathbf{B_1}$ generates the WSL shown by means of gross points on the right of the figure.

As mentioned, at $f = 0$, the second sub-band of $\mathbf{B_1}$ overlaps with the first sub-band of $\mathbf{B_2}$. In particular, one obtains that the upper level E_2^w of the second band of a periodic system formed uniquely of wide cells is equal to the upper level E_1^t of the first band of a periodic system formed uniquely of thin cells. Their value is $E_1^t = E_2^w = 4.934$, as can be seen on the left of Fig. 3a. However, the 16 levels of this group evolve to form two different Stark ladders. One of them is due to the thin cells and the other to the wide cells. We have attached crosses at the right ends of the levels forming one of these Stark ladders, and arrows to the levels forming the other WSL. We observe that each level associated with a cross is always beside a level associated with an arrow. So, we have a composed ladder in which each of its rungs are indeed coupled closely together. The most important point here, according with the objectives of this work, is to observe that this distribution of levels is similar to the distribution of the cells, that is, a wide cell is always beside a thin cell.

This last effect is shown more clearly in Fig. 3b, where we have put the 8 wide cells together and the 8 thin cells together, as depicted in the inset. On the right of this figure, we see a first WSL generated by the first band of the wide cells, with a nearest-neighbour level spacing of the order of 1.1 at $f = 0.55$. However, for higher energies, we observe a more complicated structure. It consists in two WSL separated at distance ΔS and each of them having 8 levels and 7 spaces. One can understand this characteristic if one observes that now the local period associated with the wide cells is equal to 2, and therefore, the levels associated with these cells must be separated a distance of the order of 1.1 at $f = 0.55$. Similarly, the local period associated with the thin cells is equal to 1, and therefore, their levels must be separated a distance of the order of .55 at $f = 0.55$. These two WSL ladders are separated one from each other because the cells are also distributed in that way.

When one continues moving the other thin cells to the place that they have in the final sequence S_8, one gets the corresponding spectrum shown in Fig. 3f. This figure shows a rather complex structure, which appears as chaotic. However, by using the reasoning above discussed, it is easy to deduce the configuration of the cells produced by these spectra.

IV. CONCLUSION

We have shown that an external electric field can be used as a tool to establish a close correlation between the spectrum of a small one-dimensional disordered quantum system and its geometric configuration. We have taken advantage of the capability of the electric field to produce sets of equally spaced levels in the spectrum of a periodic system, that is, the WSL. This property allows us to analyze the evolution of the energy levels as the system becomes gradually disordered. In this way, we were able to explain why the levels acquire the observed arrangement in the disordered systems. The use of Fibonacci sequences, as a particular case of non-periodic structure, was not crucial and one can analyze any other type of disordered sequences, provided the amount of disorder is large enough. Since the WSL have been observed in three dimensional systems [14], the use of an electric field to analyze the effect of disorder in real three dimensional systems could be a real possibility.

 ISBN: 978-1-61208-303-2

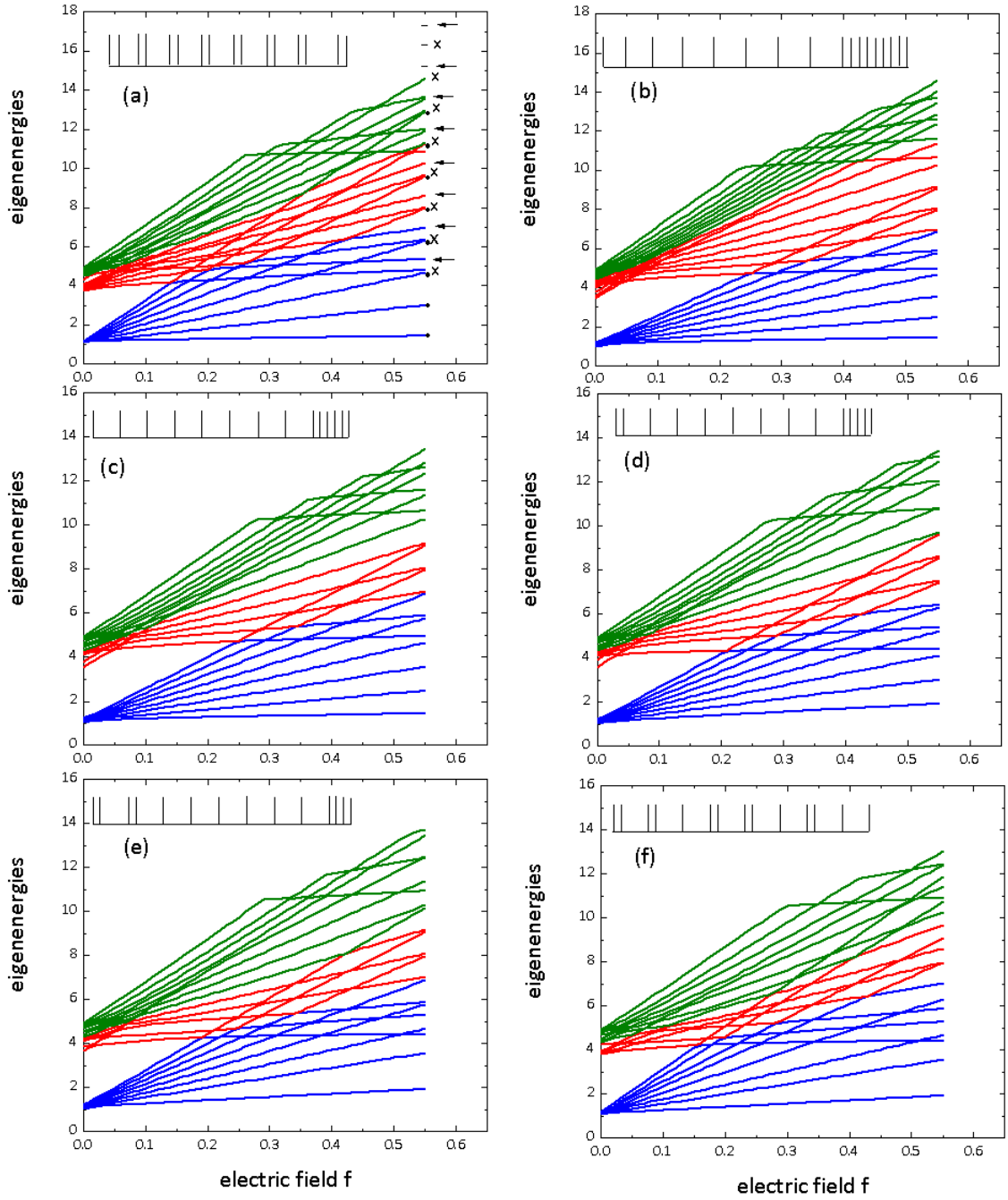

Figure 3. Effect of disorder on the electronic spectra of finite structures as functions of the electric field intensity. The structures are schematically shown in the insets.

REFERENCES

[1] A. Lagendijk, B. van Tiggelen, and D. S. Wiersma, “Fifty years of Anderson localization”, Phys. Today, vol. 62, pp. 24-29, August 2009.

[2] R. Merlin, K. Bajema, R. Clarke, F.-Y. Juang, and P.K. Bhattacharya, “Quasiperiodic GaAs-AlAs heterostructures”, Phys. Rev. Lett. , vol. 55, pp. 1768-1770, October 1985.

 ISBN: 978-1-61208-303-2

[3] Z. Cheng, R. Savit, and R. Merlin, “Structure and electronic properties of Thue-Morse lattices”, Phys. Rev. B, vol. 37, pp. 4375-4382, March 1988.

[4] S. Aubry, C. Godreche, and J. M. Luck, “A structure intermediate between quasi-periodic and random”, Europhys. Lett., vol. 4, pp. 639-643, September 1987.

[5] Q. Niu and F. Nori, “Spectral splitting and wave-function scaling in quasicristalline and hierarchical structures”, Phys. Rev. B, vol. 42, pp. 10329-10341, December 1990.

[6] Y. Liu and R. Riklund, “Electronic properties of perfect and nonperfect one-dimensional quasicrystals”, Phys. Rev. B, vol. 35, pp. 6034-6042, April 1987.

[7] M. Fujita and K. Machida, “Electrons in one-dimensional quasi-lattices”, Solid State Commun., vol. 59, pp. 61-65, July 1986.

[8] B. N. Zahariev and V. M. Chabanov, “New situation in quantum mechanics (wonderful potentials from the inverse problem)”, Inverse Problems, vol. 13, pp. R47-R79, December 1997.

[9] G. H. Wannier, “Dynamics of band electrons in electric and magnetic fields”, Rev. Mod. Phys., vol. 34, pp. 645-655, October 1962.

[10] Arfken, G., Mathematical Methods for Physicists, 3rd ed., Orlando, FL: Academic Press, 1985, pp. 481-485.

[11] A. Rabinovitch, “Stark ladders in finite crystals!”, Phys. Lett. A, vol. 59, pp. 475-477, January 1977.

[12] R. de L. Kronig and W. G. Penney, “Quantum mechanics of electrons in crystal lattices”, Proc. Roy. Soc. (London), vol. 130, pp. 499-513, February 1931.

[13] E. Cota, J. Flores and G. Monsivais, “A simple way to understand the origin of the electron band structure”, Am. J. Phys., vol. 56, pp. 366-372, April 1988.

[14] E. E. Méndez, F. Agulló-Rueda and J. M. Hong, “Stark localization in GaAs-GaAlAs superlattices under an electric field”, Phys. Rev. Lett., vol. 60, pp. 2426-2429, June 1988.

 ISBN: 978-1-61208-303-2

Nano Fabrication of Oxide Patterns Using Atomic Force Microscopy on Titanium: Towards the Development of Nano Devices

N. Guillaume, E. Puyoo, M. Le Berre, D. Albertini, N. Baboux, B. Gautier, F. Calmon
Lyon Institute of Nanotechnology (INL), UMR 5270
INSA de Lyon, Université de Lyon, Villeurbanne, France
e-mail: martine.leberre@insa-lyon.fr

***Abstract*—In this paper related to the field of nano technologies, we report on nano lithography for the fabrication of oxide patterns on titanium thin film using Atomic Force Microscopy (AFM). The patterns consist of lines, dots, and surfaces. Their morphology is assessed in terms of width and height as a function of the growth conditions, e.g., for lines, bias voltage and sweep velocity, and for dots bias voltage and duration of application of the bias voltage. We show that the results present a satisfactorily reproducibility. This opens the way to further developments: nano devices among which simple and double junctions are currently in development, the final goal being the development of single electron devices (SETs).**

Keywords-Atomic force microscope; Nano lithography; Ti/TiOx, Nano devices

I. INTRODUCTION

For more than 4 decades, Complementary Metal Oxide Semiconductor (CMOS) technology has enabled a tenfold increase in computing performance every 5 years. Throughout that period, this trend has mainly been achieved by scaling down MOS devices. Nowadays it is threatened by ever increasing power dissipation of integrated circuits. Among competing emerging research devices, we can find "the one electron electronics" in which the elementary block is the Single Electron Transistor (SET), which features particularly low power consumption [1]. The SET is a three terminal switching device which conveys electrons through successive tunnel events between two electrodes separated with one conductor island (Figure 1). Because its way of working lies in the controlled transport of electrons one by one, the SET is the great winner in terms of electrical consumption comparatively to the others emergent devices.

The realization of an island in such devices brings the necessity of creating tunnel junctions. For electron tunneling to occur in a controlled manner, it is crucial to control distances at a nanometer scale. This has been carried out using various techniques such as break junctions [2], electromigration [3], electrodeposition [4], scanning tunneling microscopy [5], electron beam lithography/shadow evaporation (alone or associated with other techniques like Chemical-Mechanical Planarization) [6][7], nanoparticle positioning [8] and nanoscale oxidation [9][10][11][12]. However, to our knowledge, no systematic study enabling systematic parameter study and derivation have been completed using the latter process when applied to the fabrication of components. Moreover, this technology, which enables "drawing" the mono-electronic component on a thin metal layer, presents the advantage of high flexibility in terms of dimension variability.

This AFM direct writing technique enables the processing of electronic components of increasing complexity (nanowires, nanojunctions, monoelectronic components like SETs), with a possibility of varying the geometry. However this flexible technology involves many parameters (nature of the AFM tip as well as voltage applied, duration, humidity, temperature) which need to be assessed. This is the goal of the present work.

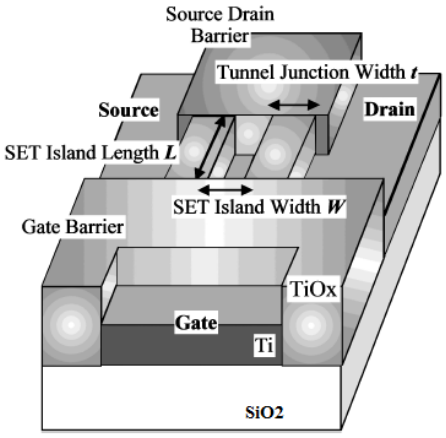

Figure 1. Illustration of the topography of a SET [10].

This paper will be divided in three parts, the first one will be related to the protocol and the equipment used at the laboratory to obtain our results, the second one will show our work on oxide characterization using three main parameters like height of the oxide, width of the oxide and the reproducibility of the method. In the last part, we will discuss of our results and the future perspectives of our work.

 ISBN: 978-1-61208-303-2

II. PROTOCOL AND EQUIPMENTS

All measurements reported in this paper were made using an Atomic Force Microscope NT-MDT Integra. The tips used were conductive tips Nanosensor PPP-EFM Silicon coated with 25 nm of PtIr. The force constant was about 2.8 N/m and the resonance frequency is comprised between 45 and 115 kHz. The resonance frequency is very important in this case because all the experiments were made using the semi-contact mode of the AFM.

In order to regulate the humidity in the microscope chamber, we used two channels of nitrogen. One goes through a water bubbler in order to add some humidity to the nitrogen introduced in the microscope chamber, the other not. Thanks to this set-up the humidity rate was constantly maintained at 55%.

The samples studied were originally silicon substrates with a thermal oxide layer of thickness 520 nm. Then we deposited 5 nm of Ti using e-beam assisted evaporation. As the samples were stored in an ambient environment, a native oxide layer of about 2 nm arose on the Ti layer (as measured by ellipsometry). The roughness parameter Rq or RMS after the Ti deposition reached 0.2 nm.

III. OXIDE CHARACTERIZATION

The working principle of the method implemented here to fabricate nano devices relies on the oxidation using AFM, works as follows.

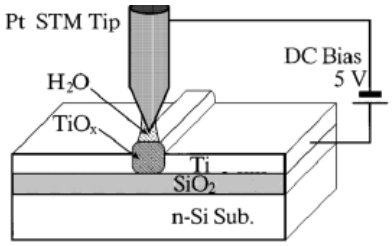

Figure 2. Schematic of the oxidation process with an AFM tip [9].

In ambient environment we can find a thin layer of water on every surface due to humidity contained in the air. When the tip of the AFM approaches the surface, a meniscus of water is formed around the tip. Then, if a bias voltage is applied to the tip, a current carried by the oxyanions comes up, which leads to an oxido-reduction reaction between the oxyanions and the metallic surfaces and proceed to the growth of TiO_x as shown on the Figure 2.

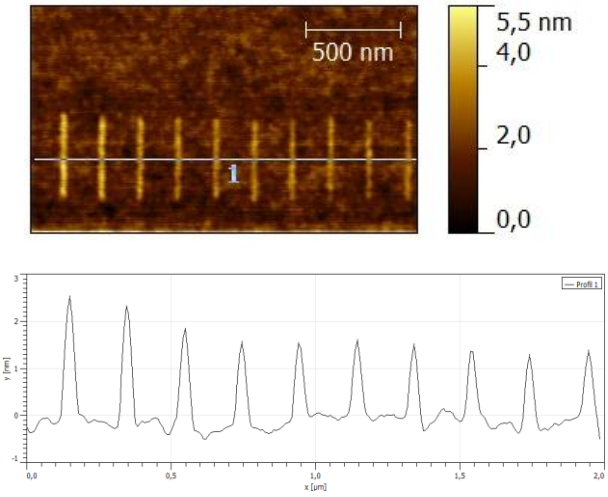

Figure 3. AFM image and corresponding line scan showing oxides lines fabricated using different sweep velocities (0.4µm/s->2.0µm/s per step of 0.4µm/s every two lines) with a bias voltage of -6V.

First, we evaluated the geometrical properties of oxide lines by measuring their height and protrusion width (FWMH), as this method takes into account the topology of the AFM tip. These parameters have been extracted using the average of the profile of the oxide lines as shown on the Figure 3. The evolution of these parameters is assessed as function of the bias voltage applied on the tip and the sweep speed of the tip, or the time per dots in the case of the oxidation of table of dots.

A. Characterization of the oxide height

The experimental height of the oxide lines measured as a function of the bias voltage of the AFM tip is reported in Figure 4. This graph displays also the dependency of the oxide height on the sweep velocity of the AFM probe. The tendencies observed here are in agreement with those of the literature [11]: the oxide height decreases sharply with the absolute value of the bias voltage and also, but to a lesser extent, for increasing sweep velocity.

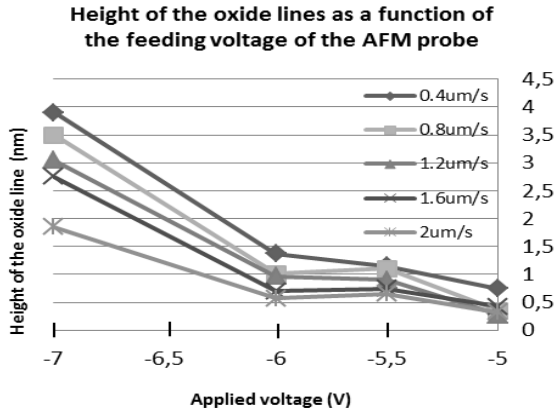

Figure 4. Experimental height of the oxide lines as a function of the bias voltage (comprised between -5V and -7V).

B. *Characterization of the oxide width*

Figure 5 shows how the full width at half maximum (FWHM) of the lines varies depending on the bias voltage and on the sweep velocity.

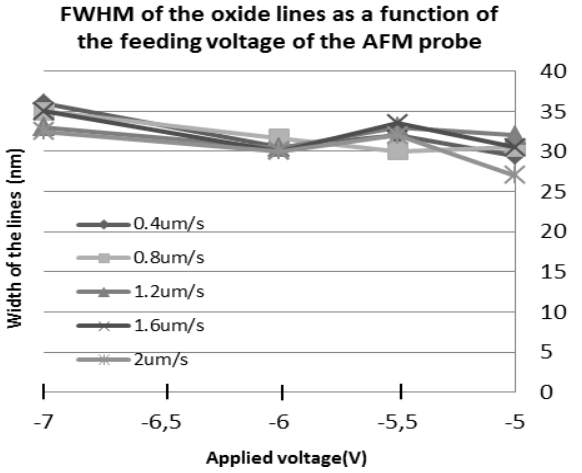

Figure 5. Experimental FWHM of the oxide lines as a function of the bias voltage (comprised between 5V and -7V).

The line width is found to remain roughly constant over the whole span of parameters tested here. The small discrepancies measured belong indeed to the experimental uncertainty which is estimated to ± 8 nm, the image resolution being 256 pixels × 256 pixels for a scan length reaching 2 µm.

C. *Process reproducibility*

The process reproducibility has been assessed by generating arrays of 36 oxide dots. For the results shown in Figure 6, the voltage applied was respectively -6V and -7V. In both cases the duration of the applied voltage reached 200 ms/point. For comparison, the oxide lines considered in the preceding paragraph were performed with scanning velocities ranging between 2 µm/s and 0.4 µm/s, which correspond to a duration of applied voltage ranging from 4 ms/point to 20 ms/point.

Table 1 summarizes the measured height and FWHM of the dots. The standard deviation for either the dot height or FWHM remains very low. This attests for a good reproducibility of the oxidation process.

TABLE I. EXPERIMENTAL HEIGHT AND FWHM OF OXIDE DOTS

Voltage applied	FWHM (nm)		Height (nm)	
	Average	Standard deviation	Average	Standard deviation
-7V	42.5	3.7	4.5	0.5
-6V	36	3.2	2.4	0.5

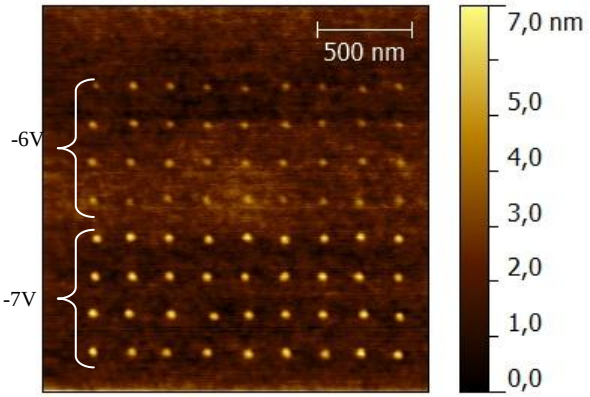

Figure 6. Arrays of oxide dots performed at a bias voltage of -7V and -6V respectively. The duration of the applied voltage is 200 ms/point.

Note that the averaged values reported for the height are slightly exceeding those reported in the figures 4 and 5 and confirm the tendency of increasing the oxide height with the oxidation time.

IV. CONCLUSION AND FUTURE WORK

In this work dedicated to nano lithography, we evaluated the influence of the applied voltage and of the sweep velocity when fabricating oxide patterns using AFM. The oxide patterns consist in lines, dots, and surfaces. Their width and height, which depend on the growth conditions, were assessed as well as the process reproducibility. The height of the lines increases with the absolute value of the bias voltage and with decreasing sweep velocity for lines (or increasing duration of the voltage applied per point for dots). On the other hand, the line width is not parameter-sensitive in the range evaluated.

The immediate outlook of this study is the processing of nano devices of increasing complexity, among which nanowires, simple junctions, double junctions, the final goal being the development of single electron devices (SETs). As a first example of nano device, Figure 7 illustrates a nanowire-type structure. A Ti-nanowire, having a width of 20 nm arises between 2 surfaces of µm-size of locally anodized Ti.

 ISBN: 978-1-61208-303-2

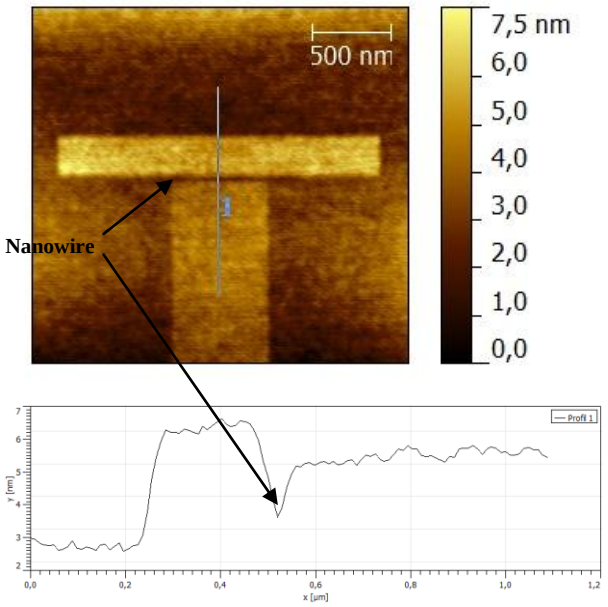

Figure 7. Example of a nano-wire processed by local anodization.

This first demonstration opens the way to more sophisticated devices which will be further developed in the oral talk.

V. ACKNOWLEDGMENTS

Deposition of the titanium films occurred on the Nanolyon Platform. We are particularly indebted to K. Ayadi, J. Grégoire and R. Perrin for their technical support.

REFERENCES

[1] The International Technology Roadmap for Semiconductors - 2007 Edition, Emerging Research Devices, Online:http://www.itrs.net/Links/2007ITRS/2007_Chapters/2007_ERD.

[2] J.J. Parks, A.R. Champagne, G.R. Hutchison, S. Flores-Torres, H.D. Abruna and D.C. Ralph, “Tuning the kondo effect with a mechanically controllable break junction”, Phys. Rev. Lett., Vol. 99, 2007, pp 0266011.

[3] K. I. Bolotin, F. Kuemmeth, A. N. Pasupathy, D. C. Ralph, “Metal-nanoparticle single-electron transistors fabricated using electromigration”, Appl. Phys. Lett., Vol. 84, 2004, pp. 3154-3156.

[4] M.M. Deshmukh, A.L. Prieto, Q. Gu, H. Park, “Fabrication of asymmetric electrode pairs with nanometer separation made of two distinct metals”, Nano Lett., Vol. 3, 2003, pp. 1383-1385.

[5] C. A. Nijhuis, N. Oncel, J. Huskens, H.J.W. Zandvliet, B.J. Ravoo, B. Poelsema and D.N. Reinhoudt, « Room-temperature single-electron tunnelling in dendrimer-stabilized gold nanoparticles anchored at a molecular printboard”, Small, Vol. 2, 2006, pp. 1422-1426.

[6] Y. A. Pashkin, Y. Nakamura, and J. S. Tsai, “Room-temperature Al single-electron transistor made by electron-beam lithography”, Appl. Phys. Lett., Vol. 76, 2000, pp. 2256-2258.

[7] C. Dubuc, J. Beauvais, D. Drouin, “A nanodamascene process for advanced single-electron transistor fabrication”, IEEE Transactions on Technology, Vol. 7(1), 2008, pp. 68-73.

[8] V. Ray, R. Subramanian, P. Bhadrachalam, L.-C. Ma, C.-U. Kim, and S. J. Koh, “CMOS-compatible fabrication of room-temperature single-electron devices”, Nat. Nano., Vol. 3, 2008, pp. 603-608.

[9] K. Matsumoto, M. Ishii, K. Segawa Y. Oka, B. J. Vartanian, J. S. Harris, “Room temperature operation of a single electron transistor made by the scanning tunneling microscope nanooxidation process for the TiOx/Ti system”, Appl. Phys. Lett., Vol 69, 1996, pp. 34-36.

[10] Y. Gotoh, K. Matsumoto and V. Bubanja, “Experimental and Simulated Results of Room Temperature Single Electron Transistor Formed by Atomic Force Microscopy Nano-Oxidation Process”, Jpn. J. of Appl. Phys, Vol 39, 2000, pp. 2334-2337.

[11] C. Huh and S.J. Park, “Atomic force microscope tip-induced anodization of titanium film for nanofabrication of oxide patterns”, J. Vac. Sci. and Technol. B, Vol. 18, 2000, pp. 55-59.

[12] J. Martinez, R.V. Martinez and R. Garcia, “Silicon Nanowire Transistors with a Channel Width of 4 nm Fabricated by Atomic Force Microscope Nanolithography”, Nano Letters, Vol 8(11), 2008, pp. 3636-3639.

 ISBN: 978-1-61208-303-2

Design of Biosensors with Extended Linear Response and Binary-Type Sigmoid Output Using Multiple Enzymes

Oleksandr Zavalov, Sergii Domanskyi,
Vladimir Privman
Department of Physics, Clarkson University
Potsdam, NY 13699, USA
privman@clarkson.edu

Aleksandr Simonian
Materials Research and Education Center
Auburn University
Auburn, AL 36849, USA
als@eng.auburn.edu

Abstract — **We review results on theoretical modeling of biochemical systems in support of the studies of several types of biosensors and systems for "biocomputing" information processing. The developed theoretical techniques have been utilized to investigate performance and optimize a novel approach to biosensors with extended linear response for lysine detection and also to study a "binary" response of a metabolic "branch point effect" system for detection of glucose. We study the experimental data for the flow-injection amperometric biosensor based on the action of Lysine-2-monooxygenase and L-Lysine-alpha-Oxidase. Lysine is a homotropic substrate for both enzymes. Parameter values are identified for an extended linear range of response. For a "branch point effect" system, we demonstrate that an "intensity filter" mechanism can yield a sigmoid response useful in biochemical signal processing and enzyme-based biosensing applications.**

Keywords *– enzyme biosensor; linear response; differential sensitivity; intensity filter*

I. INTRODUCTION

We report our recent results in the field of biosensing and biocomputing aimed at investigating the control of several types of biochemical responses for lysine [1], Section II, and glucose detection [2], Section III. These investigations have been motivated by interest in novel diagnostic applications [3-8] involving sensing, information and signal processing in chemical [9-11] and biochemical [12-15] systems, including those based on enzyme-catalyzed reactions [16-18]. Such systems use enzyme-catalyzed reaction cascades with properties optimized for the information/signal processing in biocomputing systems [19-24] and for controlling the input/output signal response to improve detection in biosensors of different types [8,25-28]. New applications have been considered for the multi-enzyme biosensors with response/actuation of the threshold-type, "digital" nature [1,25,28,29].

A key requirement in design of biocomputing systems has been the avoidance of noise amplification by biochemical processes used as network elements [7,30]. In this regard, the most promising approach has been to transform a typical convex shape signal in a biocatalytic process to a sigmoid-shape response, similar to natural systems [31,32]. Such transformation of the response can yield "biomolecular filters." These filters are usually based on different mechanisms such as self-promoter enzyme properties [33], pH control by buffering [23,34], redox transformations [35], or utilization of competing enzymatic processes [28]. Their action is based on realizing a sigmoid response of the output as a function of the input [2,7,22-24,36-38]. This can be achieved, for instance, by designing systems with "intensity filtering" in which a fraction of the output signal is neutralized by adding an additional (bio)chemical process [7,20,28,35]. When the added filtering reaction practically stops (once the added reactant is consumed), the intensity of the output signal increases, resulting in a sigmoid shape of the response [22-24,36]. Such a response allows a clear differentiation of the levels of the "binary" logic-**0** and logic-**1** output signal levels, as well as avoids noise amplification from the input signal to the output. We consider an example of such a system in Section III.

However, in many biosensor applications the level of the output signal must be approximately proportional to the concentration of the detected "input-signal" substance [27,39-42]. This enables easy calibration in response to the variations of the enzyme activity from batch to batch and during the extended times of biosensor use. Optimization of such biochemical sensing systems should be aimed at achieving a high degree of linearity [1]. We illustrate design of biosensors with extended linear response, by utilizing a combined function of more than a single enzyme, in Section II.

II. BIOSENSORS WITH EXTENDED LINEAR RESPONSE

The experimental study and analysis of the systems for lysine detection have shown that a typical enzymatic process can have a good linear sensitivity only at lower concentrations of lysine [27,40-42]. Another allosteric enzymatic process has an approximately linear response to the same substrate, but only for a range of larger input concentration. Incorporation of this allosteric enzyme in the biochemical system leads to the effect of increasing the linear range of the signal [1,40], but also in some cases to a certain decrease in its intensity. Control of the proportions of the two enzymes in the system can optimize the linearity of this bi-enzymatic biosensor signal [1,39-42]. Many experimental studies of bi-enzymatic biosensors have been recently reported [8,43-46]. Therefore, theoretical analysis of

 ISBN: 978-1-61208-303-2

their performance optimization is warranted [1]. We consider a particular system for detection of lysine that was measured amperometrically by oxygen consumption in a flow-through analyzer [1,27,40-42].

The first enzymatic process is catalyzed by L-Lysine-alpha-Oxidase (LO):

$$\text{L-Lysine} + O_2 \xrightarrow{\text{LO}} \text{α-keto-ε-aminocaproate} + H_2O_2 + NH_3 \quad (1)$$

The output signal of this enzymatic process was measured by the consumption of oxygen. Its shape is linear in a small range of input lysine concentration [27], and it saturates for larger concentrations. The second, allosteric enzymatic process was catalyzed by Lysine-2-monooxygenase (LMO):

$$\text{L-Lysine} + O_2 \xrightarrow{\text{LMO}} \text{δ-aminovaleramide} + CO_2 + H_2O \quad (2)$$

The shape of the output signal for this process is not linear for small inputs. It has a self-promoter sigmoid form (homotropic response) [27,40]. However, when both enzymes LO and LMO are present then the resulting response signal can be made linear with a good degree of linearity. LMO was added approximately in multiples of the LO concentration. With the proper choice of the process parameters, the linearity of the signal will be considerably extended without significantly reducing the output signal intensity [1,27,40-42].

For this biosensor system we propose a modeling approach [1] to quantify the sensitivity and degree of linearity of the resulting signal. It is not always possible to model a system's response in detail, because kinetic equations for biochemical processes involve many pathways and rates. Therefore, our numerical modeling has focused on few key parameters sufficient to quantify the signal processing. The reason for this has been that the available experimental data are usually limited and frequently very noisy.

Most enzymes have mechanisms of action that are quite complex, with many pathways, involving a lot of adjustable rate parameters. These rate constants are normally enzyme-batch dependent and typically change considerably with the chemical and physical conditions of the system. Therefore, we use a simplified kinetic consideration for few key processes in terms of rate constants. This approach allows finding an approximate representation of the shape of the system's response curve or surface with few adjustable rate parameters.

For the first, non-allosteric enzyme, LO, we use the standard Michaelis-Menten (MM) description:

$$E_1 + S \underset{k_{-1}}{\overset{k_1}{\rightleftarrows}} C_1 \quad (3)$$

$$C_1 \xrightarrow{k_2} E_1 + P \quad (4)$$

The first enzyme, LO, of concentration E_1, consumes the substrate (L-Lysine), the concentration of which is denoted as S, and produces the complex, C_1. This complex later transforms to the product, P, while restoring the enzyme E_1. All the concentrations here are time dependent. The first step of the reaction is naturally reversible. For biosensor and information processing applications this system is typically driven by the forward reaction. Thus, we assume that $k_{-1} \approx 0$. Therefore, there are only two adjustable parameters, $k_{1,2}$, for an approximate description of the LO-catalyzed kinetics.

Note that the real experimental data for this biosensor were obtained for flow systems at certain "measurement time," $t = t_m$, here $t_m = 120$ sec [27,40], as function of the input concentration, S. Since both enzymatic processes (LO and LMO) were in their steady states, we can use a representative product concentration, $P(t)$, calculated as a function of time, ignoring spatial variation of the product concentration along the flow.

The actual measurements [27,40-42] were made amperometrically. Therefore, the signal measured, to be denoted V, is not one of the concentrations of the product chemicals, but is rather proportional to the oxygen consumption rate in the system. The conversion factor of the product concentration P to the actually measured signal V is not known, and it can depend on the chemical conditions, specifically, the pH [40], and on the enzyme batch. Thus, the conversion factor, γ, was taken as another adjustable parameter:

$$V = \gamma P(t_m) \quad (5)$$

It is now possible to write down a set of differential rate equations and carry out numerical simulations to analyze the available experimental data. These equations are shown below, once the second enzyme, LMO, kinetics is included. Figure 1 illustrates the results of such modeling. The data for the LO-only experiment were fitted assuming the initial values $E_1(0) = 0.26$ μM, and $S(0)$ varying from 0 up to 60 mM. The parameters were $k_1 = 2.1 \times 10^{-3}$ $\text{mM}^{-1}\text{sec}^{-1}$, $k_2 = 1.0 \times 10^{-5}$ sec^{-1}, $\gamma = 145$ mV/mM.

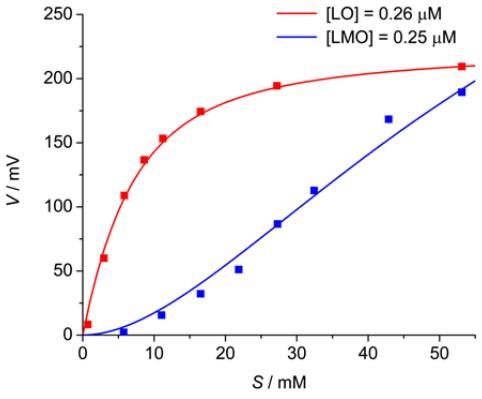

Figure 1. Illustration of data fitting [1] for the LO-only (red) and LMO-only (blue) experiments [40].

 ISBN: 978-1-61208-303-2

For the second added enzyme (LMO), $E_2(t)$, we should take into account the fact that L-Lysine has a self-promoter substrate property (Figure 1). Apparently, LMO is an allosteric enzyme, but the detailed scheme of its functioning has not been studied in the literature. We apply a simplified version of the model [1,47-49] of conventional self-promoter allostericity, which explains sigmoid properties:

$$E_2 + S \underset{k_{-3}}{\overset{k_3}{\rightleftarrows}} E_2^a \tag{6}$$

$$E_2^a + S \underset{k_{-4}}{\overset{k_4}{\rightleftarrows}} C_2 \tag{7}$$

$$C_2 \xrightarrow{k_5} E_2^a + P \tag{8}$$

For this scheme, we assume that some amount of substrate is used to transform LMO into a more active form, E_2^a, where this active form of enzyme works according to the MM scheme similar to Eq. (3-4). This description ignores many possible kinetic pathways connecting them into effective single steps allowing to limit the number of adjustable parameters, and assuming that the conversion factor, γ, is the same. Note the product of the reaction (8) differs from that in (4), for LO. We can use the notation *P* in both cases, because the two processes consume oxygen—which is the actual measured signal—identically. The initial value was $E_2(0) = 0.25$ μM, and the fitted constants were $k_3 = 0.39 \times 10^{-3}$ mM^{-1}sec^{-1}, $k_4 = 0.47 \times 10^{-3}$ mM^{-1}sec^{-1}, $k_5 = 1.2 \times 10^{-3}$ sec^{-1}. The results of our modeling for an LMO-only system are shown in the Figure 1.

Figure 2 illustrates the data vs. model with the two enzymes, with a good degree of consistency for all the initial LMO:LO ratios [1,27,40-42]. The functioning of the enzymes is interconnected via the substrate concentration, which enters in the rate equations:

$$\frac{dE_1(t)}{dt} = -k_1 S E_1 + k_2 C_1 \tag{9}$$

$$\frac{dS(t)}{dt} = -k_1 S E_1 - k_3 S E_2 - k_4 S E_2^a \tag{10}$$

$$\frac{dE_2(t)}{dt} = -k_3 S E_2 \tag{11}$$

$$\frac{dE_2^a(t)}{dt} = k_3 S E_2 - k_4 S E_2^a + k_5 C_2 \tag{12}$$

$$\frac{dV(t)}{dt} = \gamma(k_2 C_1 + k_5 C_2) \tag{13}$$

where $V(t)$ is the measured signal at time $t = t_m$.

The initial values were $E_1(0)$ = 0.29 μM for LO, and $E_2(0) = r \times 0.26$ μM for LMO, with $r = 1, 8, 12, 29$. These parameters were obtained for the data from the original experimental works [27,40]. For $r = 1$, the amounts of the enzymes per unit mass of the gel on which they were immobilized were identical [42].

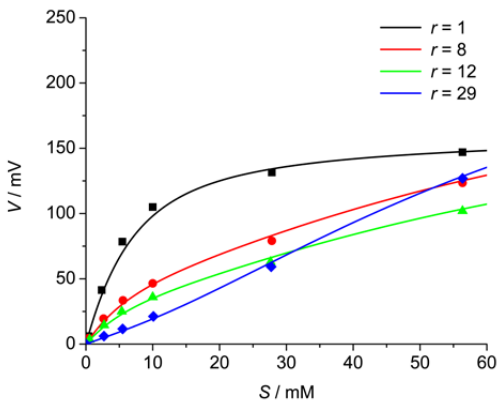

Figure 2. Data fitting [1] for LMO:LO initially present at ratios $r = 1, 8, 12, 29$, see [1,40].

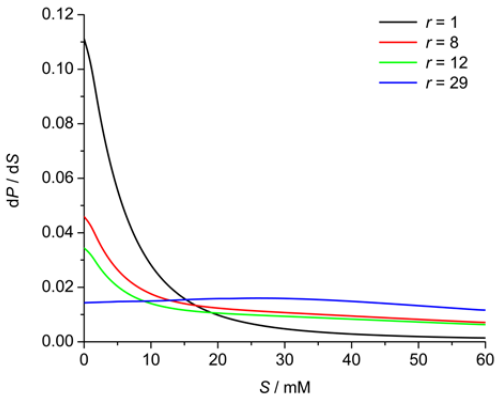

Figure 3. Differential sensitivity calculated over the desired input range, 0 to 60 mM, for various values of the ratio, *r*.

The bi-enzymatic biosensor can be optimized by selection of the parameters, here exemplified by *r*, to get an approximately linear response in the desired input regime. In order to evaluate the properties of the output signal we use the differential sensitivity of the system over the input range, *S*(0) = 0 to 60 mM, see Figure 3:

$$\frac{dP}{dS} = \frac{dP(t_m)}{dS(0)} \tag{14}$$

We aim at finding parameters minimizing this function over the desired input range. Figure 1 shows that for $r = 0$, LO-only, gives us an almost linear signal only for the range of inputs between 0 and 5 mM. However, when $r = 29$ (Figure 2), the response has an approximately linear shape in the extended input range from *S*(0) = 0 to 60 mM, as confirmed by the differential sensitivity plotted in Figure 3.

However, the overall biosensor sensitivity drops due to such modifications. Therefore, other quality measures must be also defined and considered, in addition to "linearity," as detailed in [1], but not reviewed here. Each of such quality measures can be formally defined and modeled. For example, the linearity of the response can be characterized

 ISBN: 978-1-61208-303-2

by a measure of the deviation of the differential sensitivity over the input signal range from the average slope:

$$\Delta = \frac{\left(\int_0^{S_{max}} \left[\frac{dP(S)}{dS} - \frac{P(S_{max}) - P(0)}{S_{max}} \right]^2 dS \right)^{\frac{1}{2}}}{\frac{|P(S_{max}) - P(0)|}{S_{max}}} \qquad (15)$$

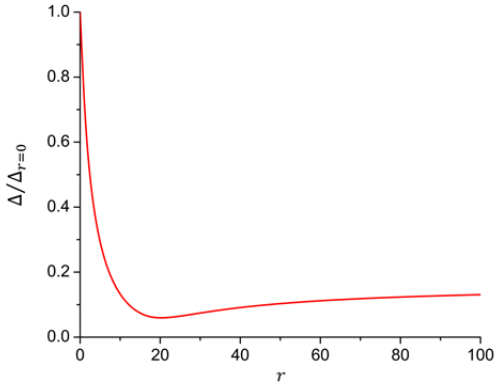

Figure 4. A measure of the response linearity for various values of *r*.

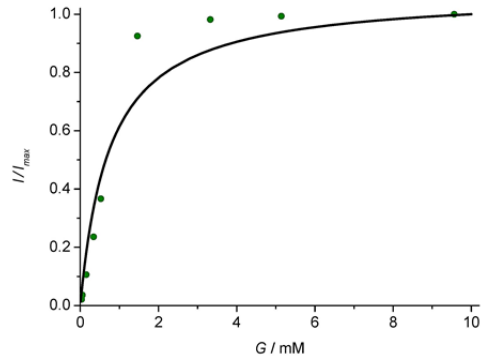

Figure 5. Experimental data [28] (circles) for the normalized current and numerical model [2] (line) without the filtering process.

For the best quality of response's linearity we have to minimize $\Delta/\Delta_{r=0}$, plotted as a function of r in Figure 4,which indicates that values from 14 to 32 represent an optimal range for the parameter *r* selection based on the "linearity" criterion. The actual minimum of the linearity measure (Figure 4) is close to r = 20, consistent with the experimental results [40].

III. BIOSENSORS WITH BINARY-TYPE SIGMOID RESPONSE

We consider an enzymatic biosensor with the binary-type sigmoid response [2,28]. The input in this system is glucose, G, with the initial concentration from 0 mM to 10 mM. These values are assumed as logic-**0** and logic-**1** respectively used to define the YES/NO signals. Electrode-immobilized glucose oxidase (GOx) consumes glucose [2,28]. The output signal $I(t_g)$ was measured at the "gate time" $t_g = 180$ sec as the current due to transfer of two elementary units of charge per reaction cycle [28]. The usual response shape for such biocatalytic reactions is convex, see Figure 5. However, for "binary" information processing it is useful to have a signal of a sigmoid shape [37]. This was accomplished [28] by consuming a fraction of the input (glucose) directly in solution, by a competing enzymatic process. The second enzyme, hexokinase (HK), H, has been added, consuming glucose and adenosine triphosphate (ATP), A, resulting in a biochemical "filtering" effect, see Figure 6.

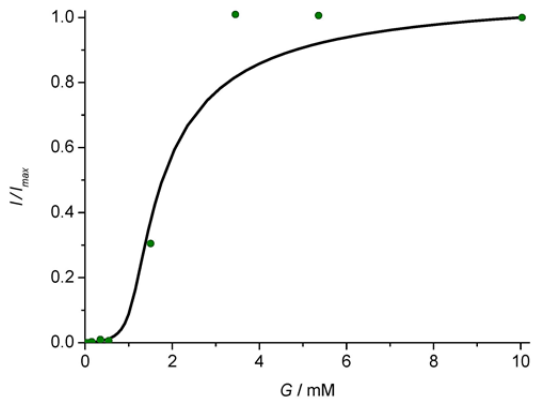

Figure 6. Experimental data [28] (circles) for the normalized current and numerical model [2] (line) with the "filter" process.

We developed a model [2] based on a rate-equation modeling of the key steps of the enzymatic processes in this biosensor system, using a limited number of adjustable parameters. The GOx enzymatic process is modeled as:

$$E + G \overset{k_1}{\rightarrow} C \overset{k_2}{\rightarrow} E + \cdots \qquad (16)$$

The intermediate complex C is gluconolactone, for the kinetics of which we have:

$$\frac{dC(t)}{dt} = k_1 G(t) E(t) - k_2 C(t) \qquad (17)$$

The current $I(t)$ is proportional to the rate of the second reaction in Eq. (16); $I(t_g) \propto k_2 C(t_g)$. Assuming that the oxygen concentration was constant, it was absorbed in k_2. Equation (17) is exactly solvable:

$$C(t) = \frac{k_1 E(0) G}{k_1 G + k_2} \left[1 - e^{-(k_1 G + k_2)t} \right] \qquad (18)$$

The input G has value from 0 to G_{max} = 10 mM. Without the filtering process, least-squares fit of experimental data from [28] gives us the estimates $k_1 \cong 80$ mM^{-1}s^{-1}, $k_2 \cong 60$ s^{-1}.

With the added filtering process, we consider the pathway of the HK biocatalytic process in which glucose transforms into the complex *D*:

$$H + G \overset{k_3}{\rightarrow} D + \cdots \qquad (19)$$

 ISBN: 978-1-61208-303-2

$$D + A \overset{k_4}{\rightarrow} H + \cdots \quad (20)$$

This approach uses two adjustable parameters, $k_{3,4}$:

$$\frac{dG}{dt} = -k_3 HG \quad (21)$$

$$\frac{dH}{dt} = -k_3 HG + k_4 DA \quad (22)$$

$$\frac{dD}{dt} = k_3 HG - k_4 DA \quad (23)$$

$$\frac{dA}{dt} = -k_4 DA \quad (24)$$

The results of a numerical solution and fitting of the available data (see Figure 6) allow us to estimate $k_3 = 14.3 \pm 0.7 \text{mM}^{-1}\text{s}^{-1}$, $k_4 = 8.1 \pm 0.4\ \text{mM}^{-1}\text{s}^{-1}$ [2].

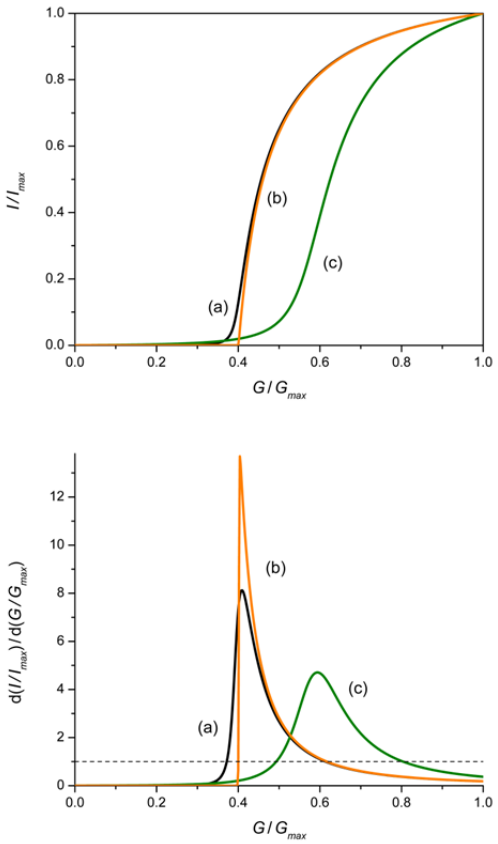

Figure 7. Examples of sigmoid curves (top panel) and their derivatives (bottom panel) for three different selections of the parameters used to control the response: (a) HK = 4 μM and ATP = 4 mM; (b) HK = 8 μM and ATP = 4 mM; (c) HK = 3 μM and ATP = 6 mM.

In order to minimize noise amplification in the output signal, the biosensor parameters must be chosen properly. There are usually several sources of noise. The main is the fluctuations in the input signal and the transmission of this noise from input to output. This transmission could amplify or suppress the noise [3,7,37]. Avoiding this "analog noise" amplification during signal processing is paramount for network stabilization [9,30]. Noise reduction can be achieved by modifying the system's response to sigmoid [2,22-24,34-38,50,51].

Note that a sigmoid curve has a peaked derivative. In order to achieve the response curve as symmetric as possible we consider the position and width of this peak, aiming at finding parameter values for which it is narrow and centrally located. Examples are given in Figure 7, and details of the optimization for the present system are presented in [2].

IV. CONCLUSION

In summary, we reported approaches [1,2] allowing optimization of biosensors based on functioning of multiple enzymes with different kinetics, yielding a binary-type sigmoid or an extended linear response. Kinetic modeling allowed us to evaluate the effects of varying system parameters that can be adjusted to control the response.

V. ACKNOWLEDGEMENT

We wish to thank Prof. E. Katz and Dr. J. Halámek for helpful input and discussions. The team at Clarkson University acknowledges support by the National Science Foundation (grants CBET-1066397 and CCF-1015983). The team at Auburn University acknowledges support from the USDA-CSREES (grant 2006-34394-16953).

REFERENCES

[1] V. Privman, O. Zavalov, and A. Simonian, "Extended Linear Response for Bioanalytical Applications Using Multiple Enzymes," Anal. Chem. vol. 85, 2013, pp. 2027–2031.

[2] S. Domanskyi and V. Privman, "Design of Digital Response in Enzyme-Based Bioanalytical Systems for Information Processing Applications," J. Phys. Chem. B, vol. 116, 2012, pp. 13690–13695.

[3] E. Katz, (Ed.), Molecular and Supramolecular Information Processing. From Molecular Switches to Logic Systems, Willey-VCH, Weinheim, 2012.

[4] E. Katz, (Ed.), Biomolecular Information Processing. From Logic Systems to Smart Sensors and Actuators, Willey-VCH, Weinheim, 2012.

[5] A. P. de Silva and S. Uchiyama, "Molecular logic and computing," Nature Nanotech. vol. 2, 2007, pp. 399–410.

[6] G. Ashkenazi, D. R. Ripoll, N. Lotan, and H. A. Scheraga, "A molecular switch for biochemical logic gates: conformational studies," Biosens. Bioelectron. vol. 12, 1997, pp. 85–95.

[7] V. Privman, G. Strack, D. Solenov, M. Pita, and E. Katz, "Optimization of Enzymatic Biochemical Logic for Noise Reduction and Scalability: How Many Biocomputing Gates Can Be Interconnected in a Circuit?" J. Phys. Chem. B, vol. 112, 2008, pp. 11777–11784.

[8] J. Chen, Z. Fang, P. Lie, and L. Zeng, "Computational Lateral Flow Biosensor for Proteins and Small Molecules: A New Class of Strip Logic Gates," Analyt. Chem. vol. 84, 2012, pp. 6321–6325.

[9] A. Credi, "Molecules That Make Decisions", Angew. Chem. Int. Ed. vol. 46, 2007, pp. 5472–5475.

[10] U. Pischel, "Chemical approaches to molecular logic elements for addition and subtraction," Angew. Chem. Int. Ed. vol. 46, 2007, pp. 4026–4040.

[11] K. Szacilowski, "Digital information processing in molecular systems," Chem. Rev. vol. 108, 2008, pp. 3481–3548.

 ISBN: 978-1-61208-303-2

[12] X. G. Shao, H. Y. Jiang, and W. S. Cai, "Advances in Biomolecular Computing," Prog. Chem. vol. 14, 2002, pp. 37–46.

[13] Z. Ezziane, "DNA computing: applications and challenges," Nanotechnology, vol. 17, 2006, R27–R39.

[14] R. Unger and J. Moult, "Towards computing with proteins," Proteins, vol. 63, 2006, pp. 53–64.

[15] V. Bocharova, et al. "A Biochemical Logic Approach to Biomarker-Activated Drug Release," J. Mater. Chem. vol. 22, 2012, pp. 19709–19717.

[16] S. Sivan, S. Tuchman, and N. Lotan, "A biochemical logic gate using an enzyme and its inhibitor. Part II: The logic gate," Biosystems, vol. 70, 2003, pp. 21–33.

[17] R. Baron, O. Lioubashevski, E. Katz, T. Niazov, and I. Willner, "Logic gates and elementary computing by enzymes," J. Phys. Chem. A, vol. 110, 2006, pp. 8548–8553.

[18] G. Strack, M. Pita, M. Ornatska, and E. Katz, "Boolean logic gates that use enzymes as input signals," ChemBioChem, vol. 9, 2008, pp. 1260–1266.

[19] T. Niazov, R. Baron, E. Katz, O. Lioubashevski, and I. Willner, "Concatenated logic gates using four coupled biocatalysts operating in series," Proc. Natl. Acad. Sci. USA, vol. 103, 2006, pp. 17160–17163.

[20] G. Strack, M. Ornatska, M. Pita, and E. Katz, "Biocomputing security system: concatenated enzyme-based logic gates operating as a biomolecular keypad lock," J. Am. Chem. Soc. vol. 130, 2008, pp. 4234–4235.

[21] S. Sivan and N. Lotan, "A biochemical logic gate using an enzyme and its inhibitor. Part I: The inhibitor as switching element," Biotech. Prog. vol. 15, 1999, pp. 964–970.

[22] J. Halamek, O. Zavalov, L. Halamkova, S. Korkmaz, V. Privman, and E. Katz, "Enzyme-Based Logic Analysis of Biomarkers at Physiological Concentrations: AND Gate with Double-Sigmoid "Filter" Response," J. Phys. Chem. B, vol. 116, 2012, pp. 4457–4464.

[23] O. Zavalov, V. Bocharova, V. Privman, and E. Katz, "Enzyme-Based Logic: OR Gate with Double-Sigmoid Filter Response," J. Phys. Chem. B, vol. 116, 2012, pp. 9683–9689.

[24] O. Zavalov, et al. "Two-Input Enzymatic Logic Gates Made Sigmoid by Modifications of the Biocatalytic Reaction Cascades," Int. J. Unconv. Comput. vol. 8, 2013, pp. 347–365.

[25] K. M. Manesh, et al. "Enzyme logic gates for the digital analysis of physiological level upon injury," Biosens. Bioelectron. vol. 24, 2009, pp. 3569–3574.

[26] D. Margulies, and A. D. Hamilton, "Digital analysis of protein properties by an ensemble of DNA quadruplexes," J. Am. Chem. Soc. vol. 131, 2009, pp. 9142–9143.

[27] A. L. Simonian, I. E. Badalian, I. P. Smirnova, and T. T. Berezov, Biochemical Engineering-Stuttgart. Editor M.Reuss. G. Fisher Pub., Stuttgart-New York. 344, 1991.

[28] S. P. Rafael, A. Vallée-Bélisle, E. Fabregas, K. Plaxco, G. Palleschi, and F. Ricci, "Employing the metabolic 'branch point effect' to generate an all-or-none, digital-like response in enzymatic outputs and enzyme-based sensors," Anal. Chem. vol. 84, 2012, pp. 1076–1082.

[29] M. Pita, J. Zhou, K. M. Manesh, J. Halamek, E. Katz, and J. Wang, "Enzyme logic gates for assessing physiological conditions during an injury: Towards digital sensors and actuators," Sens. Actuat. B, vol. 139, 2009, pp. 631–636.

[30] V. Privman, "Control of Noise in Chemical and Biochemical Information Processing," Israel J. Chem. vol. 51, 2011, pp. 118–131.

[31] Y. Setty, A. E. Mayo, M. G. Surette, and U. Alon, "Detailed map of a cis-regulatory input function," Proc. Natl. Acad. Sci. USA, vol. 100, 2003, pp. 7702–7707.

[32] N. E. Buchler, U. Gerland, and T. Hwa, "Nonlinear protein degradation and the function of genetic circuits," Proc. Natl. Acad. Sci. USA, vol. 102, 2005, pp. 9559–9564.

[33] V. Privman, V. Pedrosa, D. Melnikov, M. Pita, A Simonian, and E. Katz, "Enzymatic AND-Gate Based on Electrode-Immobilized Glucose-6-Phosphate Dehydrogenase: Towards Digital Biosensors and Biochemical Logic Systems with Low Noise," Biosens. Bioelectron. vol. 25, 2009, pp. 695–701.

[34] M. Pita, et al. "Towards Biochemical Filter with Sigmoid Response to pH Changes: Buffered Biocatalytic Signal Transduction," Phys. Chem. Chem. Phys. vol. 13, 2011, pp. 4507–4513.

[35] V. Privman, et al. "Biochemical Filter with Sigmoid Response: Increasing the Complexity of Biomolecular Logic," J. Phys. Chem. B, vol. 114, 2010, pp. 14103–14109.

[36] V. Privman, M. A. Arugula, J. Halamek, M. Pita, and E. Katz, "Network Analysis of Biochemical Logic for Noise Reduction and Stability: A System of Three Coupled Enzymatic AND Gates," J. Phys. Chem. B, vol. 113, 2009, pp. 5301–5310.

[37] D. Melnikov, G. Strack, M. Pita, V. Privman, and E. Katz, "Analog Noise Reduction in Enzymatic Logic Gates," J. Phys. Chem. B, vol. 113, 2009, pp. 10472–10479.

[38] E. Katz and V. Privman, "Enzyme-Based Logic Systems for Information Processing," Chem. Soc. Rev. vol. 39, 2010, pp. 1835–1857.

[39] O. Nikitina, et al. "Bi-enzyme biosensor based on NAD^+- and glutathione-dependent recombinant formaldehyde dehydrogenase and diaphorase for formaldehyde assay," Sensors and Actuators B, vol. 125, 2007, pp. 1–9.

[40] A. L. Simonian, G. E. Khachatrian, S. Sh. Tatikian, Ts. M. Avakian, and I. E. Badalian, "A Flow-Through Enzyme Analyzer for Determination of L-Lysine Concentration," Biosens. Bioelectron. vol. 6, 1991, pp. 93–99.

[41] A. Simonian, "Flow-injection biosensors based on immobilized enzymes and cells," Doctor of Science, Bioengineering, Dissertation, Moscow Institute of Applied Biochemistry, Moscow, 1993.

[42] A. L. Simonian, et al. "Flow-Injection Amperometric Biosensor Based on Immobilized L-Lysineoxidase for L-Lysine determination," Anal. Lett. vol. 21, 1994, pp. 2849–2860.

[43] L. Coche-Guerente, S. Cosnier, and P. Labbe, "Sol-gel derived composite materials for the construction of oxidase/peroxidase mediatorless biosensors," Chem. Mater. vol. 9, 1997, pp. 1348– 1352.

[44] G. E. De Benedetto, F. Palmisano, and P. G. Zambonin, "One-Step Fabrication of a Bienzyme Glucose Sensor Based on Glucose Oxidase and Peroxidase Immobilized Onto a Poly(pyrrole) Modified Glassy Carbon Electrode," Biosens. Bioelectron. vol. 11, 1996, pp. 1001–1008.

[45] M. Delvaux, A. Walcarius, and S. Demoustier-Champagne, "Bienzyme HRP–GOx-modified gold nanoelectrodes for the sensitive amperometric detection of glucose at low overpotentials," Biosens. Bioelectron. vol. 20, 2005, pp. 1587–1594.

[46] T. Ferri, S. Maida, A. Poscia, and R. Santucci, "A Glucose Biosensor Based on Electro - Enzyme Catalyzed Oxidation of Glucose Using a HRP - GOD Layered Assembly," Electroanalysis, vol. 13, 2001, pp. 1198–1202.

[47] J. Monod, J. Wyman, and J.-P. Changeux, "On the nature of allosteric transitions: a plausible model," J. Mol. Biol. vol. 12, 1965, pp. 88–118.

[48] J. Wyman, "Possible allosteric effects in extended biological systems," J. Mol Biol. vol. 14, 1969, pp. 523–538.

[49] J.-P. Changeux, "Allosteric interactions interpreted in terms of quaternary structure," Brookhaven Symposia in Biology, vol. 17, 1964, pp. 232–249.

[50] D. Melnikov, et al. "Enzymatic AND Logic Gates Operated Under Conditions Characteristic of Biomedical Applications," J. Phys. Chem. B, vol. 114, 2010, pp. 12166–12174.

[51] J. Halamek, et al. "Biomolecular Filters for Improved Separation of Output Signals in Enzyme Logic Systems Applied to Biomedical Analysis," Analyt. Chem. vol. 83, 2011, pp. 8383–8386.

 ISBN: 978-1-61208-303-2

The Provision of Mass Calibrations for Micro/Nano Force Measurements

Adriana Vâlcu / National Institute of Metrology
Mass Laboratory
INM
Bucharest, Romania
e-mail: adivaro@yahoo.com

Fănel Iacobescu/Romanian Bureau of Legal Metrology
BRML
Bucharest, Romania
e-mail: iacobescufanel@yahoo.com

Abstract — **The accurate force measurement is a problem of a great importance in industry, research and society because of extremely wide range of force relating applications. Over the last decade, increasing attention has been paid among the National Institutes of Metrology (NMIs) worldwide in measurement of small forces, which play a more important role in micro or nanotechnology and other significant areas (medicine, energy, environment). The equipments used to make such measurements must have metrological traceability to a realization of SI unit of force, within the required uncertainty. In this respect, the NMIs have started to study methods for completing a hierarchy of SI-traceable force metrology at low force level. As it is known, one of the ways to achieve traceability route to SI units for force measurements is through the definition of mass, length and time. For this purpose, the known method for force calibrations or measurements is the use of deadweight machines, based on masses suspended in the Earth's gravitational field (force generated by a known mass in a known gravitational field). Another way for measuring small forces is based on the comparison of a force transducer with the indication of a balance, which works on the Electromagnetic Force Compensation (EMFC) mode. Starting from these two methods, the Mass laboratory of National Institute of Metrology (INM) from Romania considered it necessary to extend the dissemination of mass unit below 1 mg, in order to meet current needs in the field of small forces measurements. In this respect, the article deals with the provision of mass calibrations for low force measurements, consisting in (1) calibration of micromass standards having nominal values between (100…500) µg, corresponding to approx. (1....5) µN, and (2) metrological characterization of a weighing instrument that works on the principle mentioned above and has a resolution of 0.1 µg (corresponding to approx. 1nN).**

Keywords – ***micromasses; low forces measurement; deadweight machines; mass comparator; traceability.***

I. INTRODUCTION

Accurate measurements play a key role in all industrial activities, from research - development to the marketing of a product, being able to say with certainty that what cannot be measured, cannot be produced.

That is the reason why "the metrologists" are continuously involved in the development of new measurement standards, new technical methods of measurement, to conceive new tools and procedures to meet the growing demands in improving accuracy, increasing trust and speed of measurements.

In this time of flourishing nanotechnology research, the measurement of micro/nano forces becomes more significant in industry, research and society because of extremely wide range of force relating applications.

Given that some tests in different fields need to measure low forces, relevant test systems must be traceable to the masses smaller than a milligram.

In this respect, the development of the technique for micro-mass measuring is highly vital for MEMS (Micro-Electro-Mechanical Systems) and NEMS (Nano-Electro-mechanical Systems) applications and also, for providing traceability to the SI units (International System of Units, international abbreviation SI) for such measurements.

The extension of dissemination of mass scale below this limit represents the basis of micro/nano force measurements being required by industries such as pharmaceutical, defense, environmental monitoring, energy production and transportation, etc.

The calibration of these micromasses was carried out for the first time in Romania, at INM.

In a first stage, were calibrated two sets of micromass standards belonging to INM (having foil shape) and after that, in a second stage, these weights were used as check standards for calibration of other micromass weights having wire shape. In the paper, only the second stage of this calibration is presented.

The article is divided into six sections as follows: introduction, a short description of the methods used for force measurements, equipments and micromass standards used in calibrations, evaluation of standard uncertainty in the calibration of the weights, assessment of ultra-microbalance used for low force measurements, and conclusions.

II. METHODS USED FOR FORCE MEASUREMENTS. A SHORT DESCRIPTION

Currently, there are three main methods used for the force measurement [1]:

a) **Mass balance**, where the unknown force is balanced against a known mass using a digital weighing instrument.

The gravimetric calibration by using mass standards is much more accurate (with two orders of magnitude) than by using force measurements based on the dependence of some electric, magnetic, acoustic or optical parameters variation with the applied load;

b) **Force balance**, i.e., balancing force via a magnet-coil arrangement, called electromagnetic force compensation, or by means of Electrostatic Force Balance (EFB);

 ISBN: 978-1-61208-303-2

c) **Deflection type transducers** measuring the specific deformation of an elastic element, e.g., piezoresistive cantilever as portable microforce calibration standard.

By tradition, the traceability route for force measurement is the force generated by a known mass in a known gravitational field [2]. This force is referred to by the term deadweight. Thus, a deadweight force is traceable if a mass artifact (corresponding to the deadweight) is available.

For this purpose are used deadweight force machines (considered primary force standards), based on masses suspended in the Earth's gravitational field. The traceability is established from a traceable mass artifact combined with an accurate determination of the local gravity.

Another way for developing primary standards based on deadweights is to use a balance. This principle is based on the comparison of a force transducer with the indication of an EMFC balance. The force transducer is pressed in a controlled way against the balance and, according to Newton's principle (action equals reaction), the force equivalent mass indication on the balance is taken as the reference [3]. This way, the mechanical forces applied to the transducer can be compared indirectly with the deadweights.

III. DESCRIPTION OF THE EQUIPMENTS AND MICROMASS STANDARDS USED IN CALIBRATION

A. *Weighing instrument*

There are two ways to use a weighing instrument:

- As a mass comparator whose measurable properties are its sensitivity and/or the mass value of the smallest scale interval, measurement repeatability results (determined according to measurement cycle used, ABBA or ABA [4]) and, if necessary, the effect of the loads eccentrically placed (eccentricity).

In this case, the mass comparators allow only differential weighing (the mass comparator gives the difference of mass values between the two weights, mass standard and test weight); mass comparators are used only in the dissemination of mass unit starting from national mass standard (with values derived from the International Prototype of the kilogram) to the standards of the lowest accuracy.

- As a direct weighing instrument (a common balance) whose measurable properties are repeatability of indications, the whole range of display scale, built-in weights and, if necessary, the effect of the loads eccentrically placed (eccentricity)

In this case, the balance can be used both for differential and for proportional weighing (the balance indicates the mass of the body placed on its pan, without having recourse to mass standards) [5].

The weighing instrument used in our research is an UMX 5 balance (Mettler fabrication), presented in Figure 1, which operates in an electro-magnetic force compensation (EMFC) mode, namely the mass of a sample (weighed object) is determined by measuring the force that is exerted by the sample on its support in the gravitational field of the Earth [6].

Figure 1. UMX 5 Mass comparator [7]

As was shown, the UMX 5 can be used as mass comparator (for the calibration of the weights), whereas for the next stage, in the low force measurements can be used as a direct weighing instrument.

The weighing instrument has the following specifications:

- maximum capacity: 5.1 g;
- readability: 0.0001 mg.

B. *Air Density Measurement Equipment*

The mass of an object is obtained by weighing in air.

Because the weighing instrument indicates a value that is proportional to the gravitational force on the object reduced by the buoyancy of air, the instrument's indication in general has to be corrected for the buoyancy effect. The value of this correction depends on the density of the object (depending on the material that is made) and the density of the air [8].

A schematic representation of the air buoyancy is presented in Figure 2.

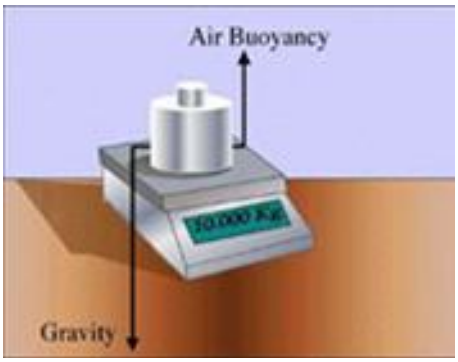

Figure 2. Representation of the air buoyancy [9]

The usual method of determining air density is to measure temperature, pressure and humidity and calculate air density using the equation recommended by the Comité International des Poids et Mesures, modified in 2007 [10]. The mass laboratory is located in a basement and the air conditions are controlled.

For accurate determination of the air density an environmental monitoring system is used, consisting in a precise "climate station", having the following technical parameters:

 ISBN: 978-1-61208-303-2

- temperature:	readability:	0.001°C;
	U (k=2):	0.03°C;
- dew point:	resolution:	0.01°C;
	U (k=2):	0.05°C;
- barometric pressure:	resolution:	0.01 hPa;
	U (k=2):	0.03 hPa

C. Description of the micromasses

The unknown weights to be calibrated are wire shaped, Figure 3, being kept in a protection box, along with a handling tool, Figure 4.

The microstandards have the nominal value between (500…100) µg with a classical sequence of (5; 2; 2; 1).

All the weights are made of aluminum alloy. At this moment, this limits the minimum mass of the standard to about 100 µg, any smaller mass being difficult to handle.

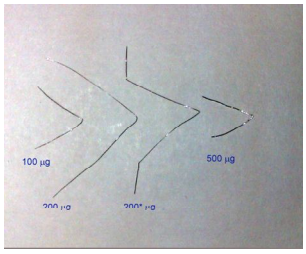

Figure 3. Micromass wire shape

Figure 4. Box containing wires shape

Micromass standards belonging to INM are foil shaped, Figure 5, being kept in a protection box, with a (5; 2; 1) sequence.

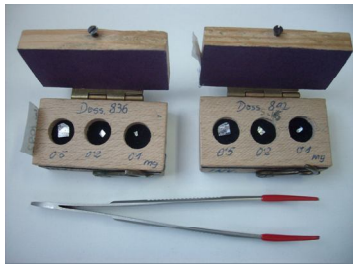

Figure 5. Boxes containing micromass foil shape

D. Measurement model

In the calibration of mass standards, when the highest accuracy is required, the comparison by subdivision method is mainly used. In short, the comparison consists of comparing groups of the same nominal value. These groups are performed in several variants, which have the same nominal value, variants that are compared between them, allowing a control for all the achieved measurements.

With this method, only one reference weight is used; the number of weighing equations should be larger than the number of unknown weights and an appropriate adjustment calculation should be performed in order to avoid propagating errors. In the matrix design, although all the micromass are considered unknown, in the interpretation of the results, the micromass foil shape belonging to INM, constitute also, check standards for the measurement.

As is defined in [4], a check standard is used in a statistical control process to provide a "check" to ensure that standards, measurement processes and results are within acceptable statistical limits. A check standard is usually a weight, which is included in the weighing design as an 'unknown' weight. The control procedure works best with weighing designs where the check standard can easily be incorporated into the design as an unknown weight [4].

Using as reference standard a mass of 1 mg, made of aluminum alloy, seven micromass standards are calibrated arranging them in ten possible pairs; in the design, as check standards are used: 1 mg $_{INM}$, 0.5 mg $_{INM}$ and 0.1mg $_{INM}$.

The calibration data used are obtained from weighing cycles ABBA for each y_i (which is the weighing comparison according to design matrix "X").

The comparison scheme can be represented in matrix form as follow:

$$Y = X\beta + e \tag{1}$$

where

Y $(n,1)$ is the vector of the n observations (including buoyancy corrections);

β $(k, 1)$ vector of the k mass values of the standards to be determined;

X (n, k) design matrix (entries of the design matrix are +1, –1, and 0, according to the role played by each of the parameters (from the vector β) in each comparison;

e $(n,1)$ vector of the deviations ;

s_i $(n,1)$ is the vector containing standard deviation of the mean value of each mass difference.

$$X = \begin{bmatrix} -1 & 1 & 0 & 0 & 0 & 0 & 0 & 0 \\ -1 & 0 & 1 & 1 & 0 & 0 & 0 & 0 \\ 0 & -1 & 1 & 1 & 0 & 0 & 0 & 0 \\ 0 & 0 & -1 & 1 & 0 & 0 & 0 & 0 \\ 0 & 0 & -1 & 0 & 1 & 1 & 1 & 0 \\ 0 & 0 & 0 & -1 & 1 & 1 & 0 & 1 \\ 0 & 0 & 0 & 0 & 1 & -1 & 0 & 0 \\ 0 & 0 & 0 & 0 & 1 & 0 & -1 & -1 \\ 0 & 0 & 0 & 0 & 0 & 1 & -1 & -1 \\ 0 & 0 & 0 & 0 & 0 & 0 & 1 & -1 \end{bmatrix} \quad Y = \begin{bmatrix} y_1 \\ y_2 \\ y_3 \\ y_4 \\ y_5 \\ y_6 \\ y_7 \\ y_8 \\ y_9 \\ y_{10} \end{bmatrix} = \begin{bmatrix} -0.00087 \\ 0.01727 \\ 0.01786 \\ -0.01825 \\ -0.0232 \\ 0.00116 \\ 0.00042 \\ 0.00768 \\ 0.00723 \\ -0.00634 \end{bmatrix} \tag{2}$$

$$s_i = \begin{bmatrix} 0.00018 \\ 0.00029 \\ 0.00048 \\ 0.00021 \\ 0.00043 \\ 0.00031 \\ 0.00009 \\ 0.00006 \\ 0.00017 \\ 0.00039 \end{bmatrix} mg \quad \beta = \begin{bmatrix} 1_{Ref} \\ 1_{INM} \\ 0.5_{INM} \\ 0.5 \\ 0.2 \\ 0.2* \\ 0.1_{INM} \\ 0.1 \end{bmatrix} \tag{3}$$

 ISBN: 978-1-61208-303-2

The general mathematical model for "y", corrected for air buoyancy is:

$$y = \Delta m + (\rho_a - \rho_0)(V_1 - V_2) \quad (4)$$

with:

Δm difference of balance readings between two weights;

ρ_o 1.2 kg m^{-3} the reference air density;

ρ_a air density at the time of the weighing;

V_1, V_2 volumes of the weights (or the total volume of each group of weights) involved in a measurement.

To estimate the unknown masses of the weights, the least square method was used [5] [11].

The design matrix "X" and the vector "Y" are transformed in X' and Y' respectively. This transformation is usually performed when the observations are of unequal accuracy (to render them of equal variance). Taking into account that such tiny micromass standards are calibrated and the scale division of the comparator is very small (0.1 µg), any influence, which can affect the results should be considered:

$$X' = G \cdot X \text{ and } Y' = G \cdot Y \quad (5)$$

G is a diagonal matrix containing the diagonal elements:

$$g_{ii} = (\sigma_0/s_i)^2 , \quad i = 1 \ldots n \quad (6)$$

and σ_0 a normalization factor defined by [5]:

$$\sigma_0^2 = 1/\Sigma(1/s_i^2) , i = 1 \ldots n, \quad (7)$$

The estimates of the unknown masses are calculated, giving the next results:

$$\langle \beta \rangle = \left(X'^T X' \right)^{-1} X'^T Y' = \begin{bmatrix} 0.0013 \\ 0.0005 \\ 0.0184 \\ 0.0001 \\ 0.0010 \\ 0.0006 \\ -0.0065 \\ -0.0002 \end{bmatrix} mg \quad (8)$$

IV. EVALUATING STANDARD UNCERTAINTY IN THE CALIBRATION OF THE WEIGHTS

In evaluating standard uncertainty associated with the results of calibration, the following contributions must be taken into account:

- type A uncertainty: evaluation of uncertainty method by statistical analysis of series of repeated observations;

- type B uncertainty is evaluated by scientific judgment based on all of the available information on the possible variability of an input quantity that has not been obtained from repeated observations.

A. Type A evaluation of standard uncertainty. Uncertainty u_A of the weighing process

The standard deviation (uncertainty of type A) of a particular unknown weight is given by:

$$U_{A(\beta_j)} = s\sqrt{c_{ij}} \quad (9)$$

where:

c_{ij} are the diagonal elements of the matrix $(X'^T \cdot X')^{-1}$;

s is the group standard deviation calculated as follows [5]:

$$s^2 = \{ \Sigma[s_i^2 (n_i - 1) \cdot g_{ii} + \langle e_i' \rangle^2] \} / f \quad (10)$$

f are "the degrees of freedom," being equal to :

$$f = (\Sigma n_i) - M \quad (11)$$

n is the number of weighing equations;

M is the total number of the weights.

If $\langle y' \rangle = X' \langle \beta \rangle$ are the estimates of the weighted weighing results, the vector of the weighted residuals, <e'>, can be obtained from:

$$\langle e' \rangle = y' - \langle y' \rangle \quad (12)$$

B. Type B evaluation of standard uncertainty

The components of type B uncertainty are:

- Reference standard, u_r;
- Resolution of the weighing instrument, u_{res};
- Sensitivity of the weighing instrument, u_s;
- Effect of the air buoyancy, u_b;
- Effect of the load eccentric placed, u_{ecc};
- Magnetic proprieties of the weights, u_{ma};
- Convection effects, u_{conv}.

All these components are calculated in the same manner as in [11] [12].

C. Combined standard uncertainty, u_c

The combined standard uncertainty of the weight β_j is given by [4]:

$$u_{c(\beta j)} = [(u_A^2(\beta_j) + u_r^2(\beta_j) + u_b^2(\beta_j) + u_s^2 + u^2_{res} + u^2_{ecc} + u^2_{ma} + u^2_{conv}]^{1/2} \quad (13)$$

D. Expanded uncertainty

The expanded uncertainty "U" of the weights β_j is given by:

$$U_{(\beta_j)} = 2 \cdot u_{c(\beta_j)} = 2 \cdot \begin{bmatrix} 0.00060 \\ 0.00033 \\ 0.00033 \\ 0.00019 \\ 0.00020 \\ 0.00017 \\ 0.00017 \end{bmatrix} = \begin{bmatrix} 0.0012 \\ 0.0007 \\ 0.0007 \\ 0.0004 \\ 0.0004 \\ 0.0003 \\ 0.0003 \end{bmatrix} mg \quad (14)$$

V. ASSESSMENT OF ULTRA - MICROBALANCE

The balance was characterized only in the range 100 µg to 1 mg corresponding to the nominal mass of the calibrated micro standards.

A. Tests performed for the calibration of ultra-microbalance

The calibration of the weighing instrument consisted in [13]:

- applying test loads to the instrument under specified conditions;

- determining the errors of the indication and uncertainty of measurement attributed to the results.

For a load j applied on the pan in an ascending, descending, or in combination way, the error of indication was calculated as follows:

 ISBN: 978-1-61208-303-2

$$E_j = I_j - m_{mmj} \quad (15)$$

where I_j is the indication of the balance and m_{mmj} is the mass value of the micromass from the calibration certificate. The errors of indication were determined at the next loads: 1 mg, 900 µg, 700 µg, 600 µg, 500 µg, 300 µg, 200 µg and 100 µg;

- repeatability test consisted in loading the balance with the same load under repeatability conditions, namely: the same measurement procedure, same operator, same measuring system, same operating conditions and same location and replicate measurements on the same or similar objects over a short period of time [14]. Repeatability of indication was determined at the next loads: 1 mg, 0.5 mg, 0.2 mg and 0.1 mg.

- determining the effect of the loads eccentrically placed: the load L_{ecc} was applied in an arbitrary order on the pan in the positions indicated in Figure 6 (A, B, C, D, E) in order to check the influence of eccentrically placed weights on the measurement. The eccentricity was performed at 200 µg.

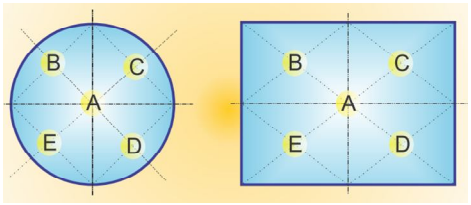

Figure 6. Positions of the load on the pan

From the indications I_i obtained for different positions of the load, is calculated the difference ΔI_{ecci}:

$$\Delta I_{ecci} = I_i - I_A \quad (16)$$

B. Standard uncertainty of the error of indication

Starting from the equation (15) it can be obtained the standard uncertainty of the error:

$$u(E) = \sqrt{u^2(I) + u^2(m_{mm})} \quad (17)$$

where:

$u(E)$ is standard uncertainty of the error of indication;

$u(I)$ is standard uncertainty of the indication;

$u(m_{mm})$ is standard uncertainty of the micromass used.

The expanded uncertainty of the error was calculated as follows [13, 15]:

$$U(E) = 2u(E) = 2\sqrt{d_0^2/12 + d_L^2/12 + s^2(I) + \hat{w}^2(\delta I_{ecc})I^2 + u^2(m_{mm})} \quad (18)$$

where:

- d_0 is the resolution of the balance at no-load indication;
- d_L the resolution of the balance at load ;
- $s(I)$ uncertainty due to repeatability of the indication, given by standard deviation of several weighing results;

$$u(\delta I_{rep}) = s(I_j) = \sqrt{\frac{\sum_{i=1}^{n}(I_{ji} - \overline{I_j})^2}{n-1}} \quad (19)$$

- $\hat{w}(\delta I_{ecc})$ is uncertainty associated to the effect of the load eccentrically placed:

$$\hat{w}(\delta I_{ecc}) = \frac{|\Delta I_{ecc,i}|_{max}}{2\sqrt{3}L_{ecc}} \quad (20)$$

- $u(m_{mm})$ is standard uncertainty of the micromass, given by expended uncertainty from the calibration certificate, U, combined with uncertainty due to instability of the micromass, u_{instab} (or drift D).

$$u(m_{mm}) = \sqrt{\left(\frac{U}{k}\right)^2 + u_{instab}^2} = \sqrt{\left(\frac{U}{k}\right)^2 + \left(\frac{D}{2\sqrt{3}}\right)^2} \quad (21)$$

All the uncertainty components can be graphically represented in an Ishikawa (Fishbone) diagram, as shown in Figure 7.

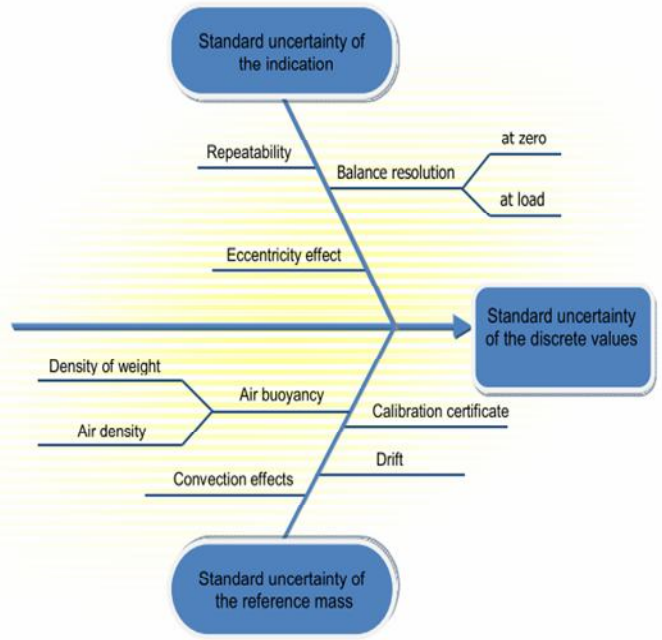

Figure 7. Ishikawa diagram of uncertainty components in the calibration of the balance

TABLE I. CENTRALIZATION OF THE RESULTS OBTAINED IN THE ULTRA-MICROBALANCE CALIBRATION

Quantity of Influence			Results							
Indication		in µg	100,1	200,1	300,3	500,4	600,2	701,4	901,3	1001,4
Error		in µg	-0,3	0,5	0,49	-0,26	-0,2	-0,27	0,4	-0,1
Repeatability		in µg	0,0710	0,0707	0,0707	0,0833	0,0833	0,0833	0,0833	0,0823
Digitalisat'n	$d_0/\sqrt{12}$	in µg	0,0289	0,0289	0,0289	0,0289	0,0289	0,0289	0,0289	0,0289
Digitalisat'n	$d_1/\sqrt{12}$	in µg	0,0289	0,0289	0,0289	0,0289	0,0289	0,0289	0,0289	0,0289
Eccentricity	$\tilde{w}_{ecc}(I)$	in µg	0							
$u(I)$		in µg	0,0819	0,0816	0,0816	0,0928	0,0928	0,0928	0,0928	0,0919
Uncertainty of reference standard		in µg	0,350	0,390	0,740	0,660	1,010	1,050	1,440	1,200
Test loads m_N		in µg	100	200	300	500	600	700	900	1000
$u(\delta m_c)=U_{mc}/2$		in µg	0,1750	0,1950	0,3700	0,3300	0,5050	0,5250	0,7200	0,6000
$u(\delta m_D)=D/\sqrt{3}=U_{mc}/\sqrt{3}$		in µg	0,1010	0,1126	0,2136	0,1905	0,2916	0,3031	0,4157	0,3464
$u(\delta m_{conv})$		in µg	0							
Uncertainty of the error u(E)		in µg	0,2180	0,2395	0,4350	0,3922	0,5905	0,6133	0,8365	0,6989
k			2							
U(E)=ku(E)		in µg	0,44	0,48	0,87	0,78	1,18	1,23	1,67	1,40

Table I contains a centralization of results obtained in the calibration of the microbalance in the corresponding range of calibrated micromasses.

VI. CONCLUSION AND FUTURE WORK

The aim of the work described here is to provide mass calibrations for force measurements below 10 µN by extending the mass scale below 1 mg.

Thus, traceable force can be obtained using mass artifacts ranging from (100…500) µg to create appropriate deadweight loads.

Other applications of micromasses are in improving uncertainty in determining the indication error and sensitivity error of weighing instruments of special accuracy (micro and ultra-microbalances).

In the future, these microweights will become essential for providing traceability for new areas such as biotechnology and to meet the current requirements of various sectors of health and defense.

The paper focused on the calibration of weights below 1mg, carried out for the first time in Romania, at INM.

Also, a balance with special accuracy (ultra-micro) was characterized in a metrological manner for the first time in the low range 1 mg … 100 µg using micromass standards.

Thus, the balance can be used as was described at the Section II.

Measurement procedures and associated uncertainty obtained in the calibrations of the microweights and of the balance were presented.

Currently, the smallest mass standard used in metrology is 1 mg. Although in OIML recommendation [4], the traceability of microweights to SI units is not identified (some referring being made only in the description of the subdivision method), their calibration gives the possibility to extend the dissemination of mass scale below this limit.

REFERENCES

[1] D.M. Ştefănescu, "Handbook of Force Transducers. Principles and Components," Hardcover, Springer-Verlag, 2011, pp. 293-299.

[2] R. K. Leach and C. W. Jones, "Towards a Traceable Infrastructure for Low Force Measurements," International Federation for Information Processing, vol. 260, 2008, pp. 307-314.

[3] C. Schlegel, O. Slanina and R. Kumme, "Construction of a standard force machine for the range of 100 µN – 200 mN," Proceedings of IMEKO TC3, TC5 and TC22 Conferences, 2010, pp. 33-36.

[4] OIML, International Recommendation No 111, "Weights of classes E1, E2, F1, F2, M1, M2, M3," 2004, pp. 5-71.

[5] R. Schwartz, "Guide to mass determination with high accuracy," PTB MA-40, 1995, p. 3 and pp. 54-58.

[6] R. Nater, A. Reichmuth, R. Schwartz, M.Borys and P.Zervos, "Dictionary of weighing terms," 2009, pp.85-86.

[7] Mettler Toledo, "Mass comparator Catalogue," unpublished, p. 13.

[8] International Document OIML D 28, "Conventional value of the result of weighing in air," 2004, pp. 4-8.

[9] http://www.oregon.gov/ODA/MSD/pages/mass.aspx

[10] A. Picard, R. S. Davis, M. Glaser and K. Fujii, "Revised formula for the density of moist air," (CIPM-2007), Metrologia 45, 2008, pp. 149–155.

[11] A. Valcu, "Test procedures for class E1 weights at the Romanian National Institute of Metrology. Calibration of mass standards by subdivision of the kilogram," Bulletin OIML, vol. XLII, no. 3, July 2001, pp. 11-16.

 ISBN: 978-1-61208-303-2

[12] A. Valcu, "Improvement of the Calibration Process for Class E1 Weights Using an Adaptive Subdivision Method," Proceeding of IARIA-ADAPTIVE Conference, 2012, pp. 51-56.

[13] EURAMET cg-18 Guide, "Guidelines on the Calibration of Non-Automatic Weighing Instruments," 2011, pp. 11-24

[14] OIML, International Vocabulary of Metrology, "Basic and General Concepts and Associated Terms (VIM)," 2012, pp. 22-23.

[15] A. Vâlcu and S. Baicu, "Analysis of the results obtained in the calibration of electronic analytical balances," Proc. IEEE Electrical and Power Engineering International Conference and Exposition, (EPE), oct. 2012, pp. 861–866, doi: 10.1109/ICEPE.2012.6463825

 ISBN: 978-1-61208-303-2

Carbon Nanotube Emitters in Sensoric Application

Jan Pekarek, Radimir Vrba, Martin Magát, Jana Chomoucka, Jan Prasek, Jaromir Hubalek
Department of Microelectronics, Faculty of Electrical Engineering and Communication
Brno University of Technology
Brno, Czech Republic
e-mail: pekarek@feec.vutbr.cz

Ondrej Jasek, Lenka Zajickova
Department of Physical Electronics, Faculty of Science
Masaryk University
Brno, Czech Republic

***Abstract*—A contemporary approach to study the emission properties of carbon nanotubes (CNTs) in low distances between two electrodes is described in this paper. The method could be used in modern MEMS pressure sensor applications. The field emission works on the principle that the field emission current is correlated with the electrical field intensity, i.e., the anode-emitter distance when the applied voltage is fixed. This means that the CNTs array serves as the emitter source of electrons between the cathode and the anode in the electric field. The measurement of emission current density flowing through the electrodes is carried out in a vacuum chamber pumped by a turbomolecular pump. The vacuum chamber is equipped with a linear nano-motion drive SmarAct that enables precise changes of the distance between two electrodes inside the vacuum chamber (step width from 50 nm to 1000 nm, sub-nanometer resolution). For this experiment, CNTs are deposited using a thermal chemical vapour deposition.**

Keywords-carbon nanotubes; emission properies; thermal chemical vapour deposition; microwave torch deposition.

I. INTRODUCTION

Carbon nanotubes (CNTs) are molecular-scale tubes of graphitic carbon with outstanding properties. They are among the stiffest and strongest fibres known, and have remarkable electronic properties and many other unique characteristics. The diameter of a nanotube is on the order of a few nanometers (approximately 50 000 times smaller than the width of a human hair), while they can be up to several millimeters in length [1] [2]. For these reasons, they have attracted huge academic and industrial interest, with thousands of papers on nanotubes being published every year.

Field emission involves the extraction of electrons from a solid by tunnelling through the surface potential barrier. The emitted current depends directly on the local electric field at the emitting surface E, and on its work function, ϕ. Fowler-Nordheim model [3] shows that the dependence of the emitted current on the local electric field E and the work function ϕ, is exponential like. As a consequence, a small variation of the slope or surrounding of the emitter and/or the chemical state of the surface has a strong impact on the emitted current. The small diameter of carbon nanotubes is very favourable for field emission. The device emits electrons when an electric field or voltage is applied [4] [5].

Several techniques have been developed to produce nanotubes in sizeable quantities, including arc discharge, laser ablation, high pressure carbon monoxide and chemical vapour deposition (CVD). Most of these processes take place in vacuum or with process gases. Large quantities of nanotubes can be synthesized by CVD methods; advances in catalysis and continuous growth processes are making CNTs more commercially viable [6-8].

This paper is structured as follows: The field emission mechanism is described in Section II. In Section III, we describe the sample preparation and measurement setup. A short discussion about the obtained results and the method for possible packaging of emission pressure sensor is described in Section IV. Section V concludes the paper.

II. THEORY - EMISSION MECHANISM

Large field amplification factor, arising from the small radius of curvature of the nanotube tips, is partly responsible for the good emission characteristics. It is however still unclear whether the sharpness of the nanotubes is their only advantage over other emitters, or if intrinsic properties also influence the emission performances.

If the nanotubes seem to follow the Fowler-Nordheim law, they can be thought of as metallic emitters. Nanotube emissions deviate from Fowler-Nordheim model. Such deviations are usually attributed to space-charge effects, which induce a diminution of the F-N slope at high fields. Thus nanotubes cannot be considered as usual metallic emitters [3].

Theory of emission mechanism is shown in Fig. 1. Field emission involves the extraction of electrons from a solid by tunnelling through the surface potential barrier. The emitted current (I_E) depends directly on the local electric field at the emitting surface E, and on its work function, ϕ. If the applied voltage is fixed, the emitted current depends directly on emitter distance x. The variable E_F represents Fermi level.

 ISBN: 978-1-61208-303-2

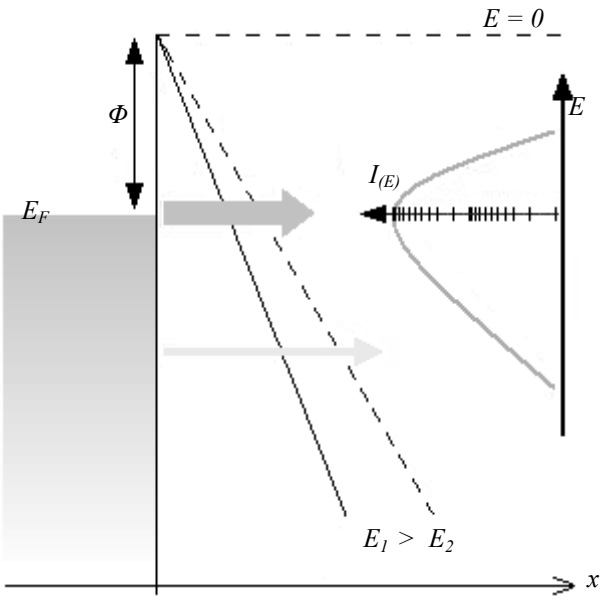

Figure 1. Theory of emission mechanism (Fowler-Nordheim law) [3]

Also, for nanotubes, electrons are not emitted from a metallic continuum as in usual metallic emitters, but rather from well-defined energy levels of ~0.3 eV half width corresponding to localized states at the tip. The energy spread of nanotubes is typically half of the metallic emitters (~0.2). The shape of the energy distribution suggests that the electrons are emitted from narrow energy levels. The greatest part of the emitted current comes from occupied states with a large density of states near the Fermi level, but the other deeper levels also contribute to the field emission. The position of these levels with respect to the Fermi level, which depends primarily on the tip geometry (i.e., tube chirality, diameter and the eventual presence of defects), would be, together with the tip radius the major factors that determine the field emission properties of the tube. Finally, it is worth noting that the presence of localized states influences the emission behaviour greatly. Local density of states at the tip reaches values at least 30 times higher than in the cylindrical part of tube increasing the carrier density for strong emission.

III. EXPERIMENTAL

A contemporary approach to study the emission properties of carbon nanotubes in low distances between two electrodes was used in this paper. Each electrode consists of high doped silicon substrate. The field emission works on the principle that the field emission current is correlated with the electrical field intensity, i.e., the anode-emitter distance when the applied voltage is fixed. This means that the CNTs array serves as the emitter source of electrons between the cathode and the anode in the electric field. The measurements were five times repeated and the same results were obtained.

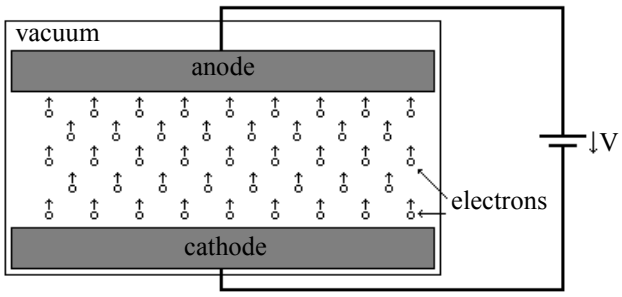

Figure 2. Schematic illustration and principle of measuring the emission properties.

The measurement of emission current density flowing through the electrodes was carried out in a chamber pumped by a turbomolecular pump and equipped with feedthroughs for voltage application and current measurement. The vacuum chamber was equipped with a new vacuum compatible linear nano-motion drive SmarAct that enables precise changes of the distance between two electrodes inside the vacuum chamber (step width from 50 nm to 1000 nm, sub-nanometer resolution). Special software, enabling to set up the step size, number of the steps and speed of the motion, was developed for its control. Additionally, a measurement control unit and the software were prepared for an automatic electrical measurement.

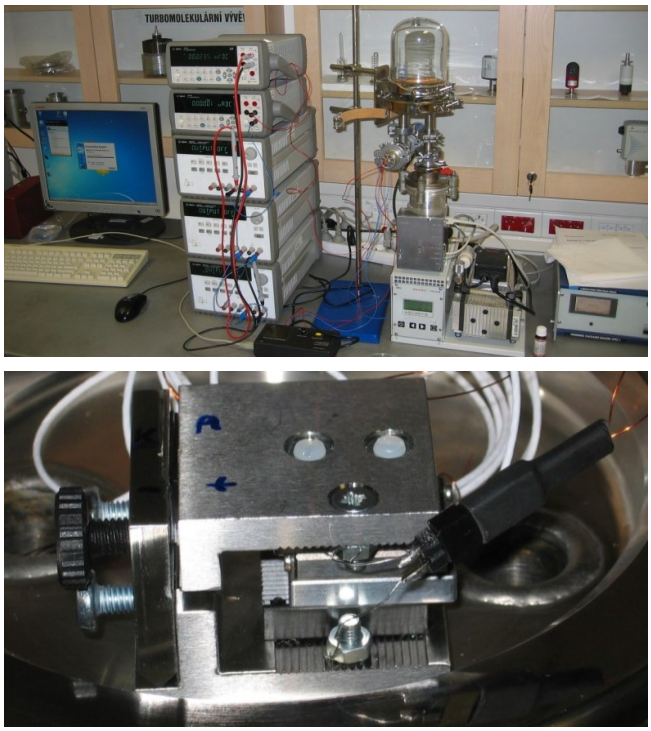

Figure 3. The workplace for emission measuring (up) and the detail of nano-motion drive SmarAct (down).

Electrode substrates on silicon wafer were fabricated using lithography and standard thin-film technology. The base for silicon electrodes is monocrystalline N-type 4” Si wafer with <100> orientation and the thickness of 525 μm (ON Semiconductor). Wafer is doped with antimony and its

resistivity is 0.005 Ω.cm. On the places where the MWCNTs should grow, the 300 nm thick layer of Ti/Ta were sputtered to ensure better adhesion of lately deposited MWCNTs. Then on the tantalum layer was evaporated 5 nm thick catalyst layer of iron. Prepared substrates were then cut to separate microelectrodes and used as the substrate for grown of vertically aligned MWCNTs.

For this experiment, carbon nanotubes were deposited using a thermal chemical vapour deposition. Typical deposition process was as follows. The substrate was placed in quartz boat and put in the centre of horizontal furnace equipped with quartz glass tube (1000 mm long) terminated with flanges as it is schematically shown in the Fig. 4.

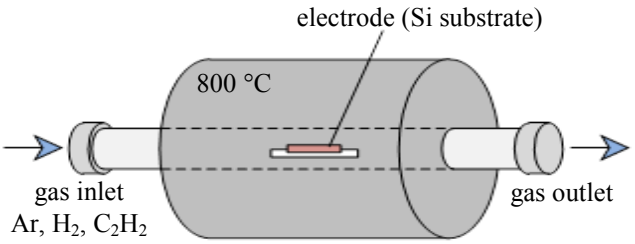

Figure 4. Scheme of thermal CVD furnace.

Gas flow rates were controlled by electronic flow controllers. The inner diameter of quartz glass tube is 45 mm and hot zone length is 150 mm. The furnace deposition temperature was measured by K type thermocouple. The substrate was heated under mixture of Ar, flow rate 2800 sccm, and H_2, flow rate 500 sccm, to 800 °C with ramp rate of 25 °C.min^{-1}. The CNTs were grown at 800 °C under mixture of Ar (1400 sccm) and C_2H_2 (30 sccm). Deposition time was 20 minutes. After the deposition the substrate cooled down under Ar flow (1400 sccm). A detailed study of the deposition of CNTs and their characterization were published in [9] [10].

IV. RESULTS AND DISCUSSION

Successfully fabricated electrodes with deposited MWCNTs were analysed optically using SEM (TESCAN, Czech Republic). SEM micrographs of fabricated electrode with different scale are shown in Fig. 5.

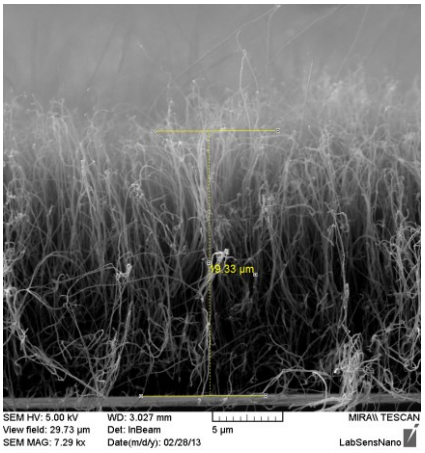

Figure 5. SEM analysis of the CNTs.

Measurements were performed at pressure of 10^{-4} Pa for ten electrode distances – from 84 µm to 100 µm. For these ten distances, the same results were obtained for multiple times. The emission current in dependence on the applied voltage was measures as basic results. Graphs of these dependences are shown in Figs. 6 and 7.

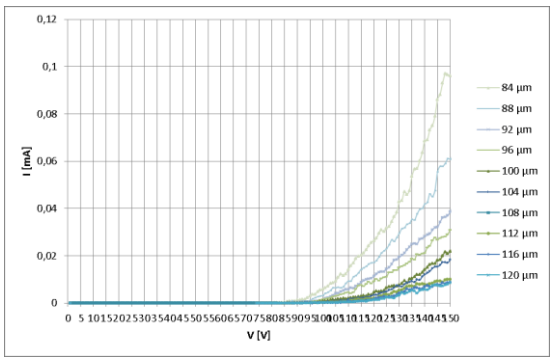

Figure 6. Result of measured emission current in dependence on the applied voltage.

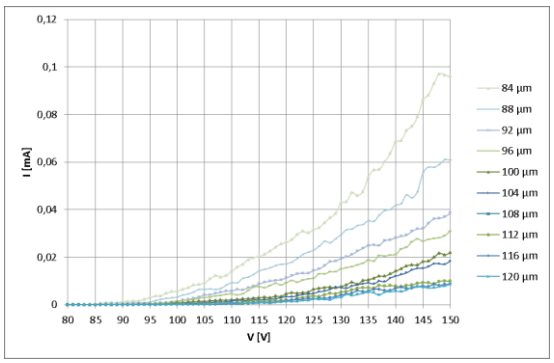

Figure 7. The detail result of measured emission current in dependence on the applied voltage for higher voltages.

In the set of experiments on the array with CNTs with dimension of 4x4mm, the field emission results show that in the small electrode distance, there is the low turn-on field (smaller than 1 V/µm) and there is achieved a high current density at 1,8 V/µm.

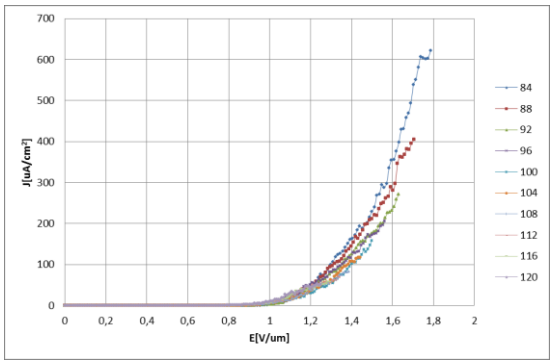

Figure 8. Results of current density in dependence on intensity for ten electrode distances.

 ISBN: 978-1-61208-303-2

The measured results follow the Fowler-Nordheim law as expected. For smaller electrode distances, it is expected a higher current density for same applied voltages or vice versa, the same current density at lower applied voltages.

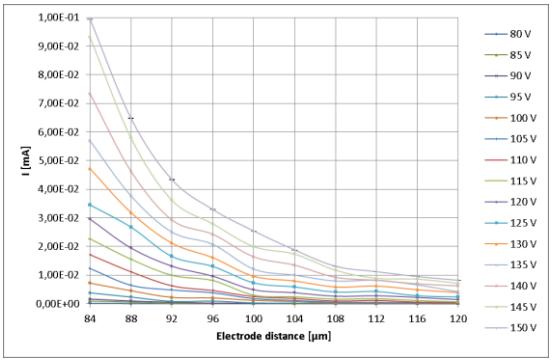

Figure 9. Results of emission current in dependence on the electrode distance for applied voltage from 80 to 150 V.

The curves in Fig. 9 show, that the emission current depends on electrode distance when the applied voltage is fixed. This could be a confirmation of the proposed solution and CNTs could be used as emitters in a pressure sensor.

A method for packaging emission pressure sensor was also invented so the emission could exist outside the laboratory vacuum chamber. The entire sensor could be encapsulated in the housing known from the production of vacuum tubes (Fig. 10).

Figure 10. Possible package for emitter made from carbon nanotubes.

Two conductive silicon electrodes are bonded together. The cathode is with carbon nanotubes, the anode is flexible. The pressure from external inlet causes the bend of anode, i.e., the emission current (electrode distance) is changing when the applied voltage is fixed.

The zirconium getter should be inside the tube to maintain vacuum for long-term activities. Getter is used for disposal of residual gases and mainly for moisture absorption.

V. CONCLUSION

In conclusion, we successfully fabricated vertically aligned carbon nanotubes using CVD method. The tips of nanotubes serve the electrons. The emission current is dependent on electrode distance. The measured dependencies show that the CNTs are stable and low noise. If one of the electrodes will be flexible (membrane), this system could be used for pressure sensing. We also introduced the method for packaging emission pressure sensor for application outside the laboratory vacuum chamber.

ACKNOWLEDGMENT

This research was supported by the Grant Agency of the Czech Republic under 205/10/1374 project, by the project Prospective applications of new sensor technologies, No. FEKT-S-11-16, and by the project Research4Industry, the registration number CZ.1.07/2.4.00/17.0006.

The described research was performed in laboratories supported by the SIX project; the registration number CZ.1.05/2.1.00/03.0072, the operational program Research and Development for Innovation.

REFERENCES

[1] M. de Volder, D. O. Vidaud, E. R. Meshot, S. Tawfick, and A. J. Hartet, “Self-similar organization of arrays of individual carbon nanotubes and carbon nanotube micropillars”, Microelectronic Engineering, vol. 87, no. 5-8, 2010, pp. 1233-1238.

[2] M Meyyappan, “Carbon Nanotubes: Science and Application”, 1st ed. Boca Raton, Florida: CRC Press, 2005. 304 p. ISBN 978-0849321115.

[3] D. Tomanek and R. J. Enbody, “Science and application of nanotubes”. New York: Kluwer Academic Publisher, 2002. 398 p.

[4] M. Magat, J. Pekárek, and R. Vrba, “Characterization and field emission properties of fields of nanotubes”, 3rd International Conference on Nanocon, 2011, pp. 696-700.

[5] K.R. Izrael’yants, A.L. Musatov, A.B. Ormont, E.G. Chirkova, and E.F. Kukovitsky, “Emission characteristics of planar field electron emitters containing carbon nanotubes operating in the high current density mode”, Carbon, 2010, vol. 48, 2010, pp. 1889-1896.

[6] D. Vairavapandian, P. Vichchulada, and M. Lay, “Preparation and modification of carbon nanotubes: Review of recent advances and applications in catalysis and sensing”, Anal. Chim. Acta, vol. 626, pp. 119-129.

[7] J. Prasek, et al., “Electrochemical properties of CNT's modified microelectrodes”, 3rd International Conference on Nanocon, 2011, pp. 497-502.

[8] J. Pekarek, R. Ficek, R. Vrba, and M. Magát, “Electrodes Modified by Carbon Nanotubes for Pressure Measuring”, 32nd International Spring Seminar on Electronics Technology, 2009, pp. 629-633.

[9] J. Pekarek, R. Vrba, M. Magát, and P. Kulha, “Possible applications of freestanding carbon nanotubes in MEMS technology”, 3rd International Conference on Nanocon, 2011, pp. 491-496.

[10] L. Zajickova et al., “Synthesis of carbon nanotubes by plasma enhanced chemical vapor deposition in an atmospheric-pressure microwave torch”, Pure and Applied Chemistry, vol. 82, no. 6, pp. 1259-1272.

 ISBN: 978-1-61208-303-2

Experimental Evaluation of Optical Feedback for Nanopositioning of Piezo Actuator Stage

Piotr Skupin, Mieczyslaw Metzger, Dariusz Choinski
Faculty of Automatic Control, Electronics and Informatics
Silesian University of Technology
Gliwice, Poland
{piotr.skupin, mieczyslaw.metzger, dariusz.choinski}@polsl.pl

***Abstract*—The paper presents the realization of the nanopositioning control of activated sludge samples observed under the microscope. To achieve the desired control goals, the most typical and cheapest components of the positioning system were used. It has been shown both experimentally and numerically that one of the simplest control algorithms (in this case the PI controller) can provide satisfactory good results in positioning control systems. Moreover, based on the simplified description of the microactuator, analytical stability conditions of the closed-loop system have been given. Then, it was possible to find the analytical and experimental stability regions on the controller parameter plane and to compare them against each other.**

Keywords-microactuator; nanopositioning control; hysteresis; stability analysis

I. INTRODUCTION

Nanopositioning control is a very essential issue in various fields of science and technology [1], [2]. A basic device, which allows for very precise and accurate positioning is a piezoelectric actuator (microactuator) using piezoceramic element that undergoes the phenomenon of reverse piezoelectric effect. In most cases, the typical operating range for positioning purposes is 20 to 30 micrometers, and depending on the accuracy of the position measurement, the device allows for positioning with accuracy within a several nanometers. Hence, the piezoceramic actuators are often used in the positioning control of mirrors on the optical table, in microscopes, digital cameras, etc.

Among the many areas, in which microactuators are widely used, broadly defined biotechnology offers a strong application potential of such devices and the typical example is the in-vitro fertilization. The second important field of application of microactuators is the precise positioning of mechanical parts in the laboratory equipment used for a proper conduction of micro-scale processes. In our case, we will focus on the design of positioning control system, which can be used for precise positioning of samples of activated sludge observed under the microscope. However, the key issue in the design of the positioning control system is to provide a precise and accurate measurement of the microactuator stage position.

An interesting paper addressing this problem is the survey paper by Fleming published in Sensors & Actuators A: Physical [3]. This paper describes and compares the following sensors: piezoelectric and piezoresistive strain sensors, resistive and capacitive sensors, electrothermal sensors, eddy current sensors, linear variable displacement transformers, interferometers and linear encoders. The quick reference on the sensors used for nanopositioning control in biotechnology can be found in [4].

In the literature, laser sensors are the most frequently described sensors for nanopositioning purposes (see, e.g., [5-9]). In turn, the application of optical encoder for delay-varying repetitive control of walking piezoactuator can be found in [10]. In [11], the strain gauge sensor was used for hysteresis analysis of the piezostack actuator. These studies were performed for displacements in the range of several micrometers. In turn, the induction coil sensor can be used for positioning in the micro- (but not nano-) scale [12].

In principle, for microscopic observations, it is more convenient to use the same microscope to measure the position of the microactuator stage. Moreover, the microscope can also be used for calibration of position sensors for microactuators, because it can provide a sufficiently high precision in position determination during microscopic observations. More precise positioning is hardly observable be the experimenter, hence, in many cases is not necessary. The application of microscope for positioning control is also described in the literature. For instance, in in-vitro fertilization, two coaxial microactuator stages are used for appropriate positioning of the needle observed under the microscope [13]. This paper also gives a short survey of various positioning sensors used in the in-vitro fertilization equipment. In turn, the paper [14] describes the application of microscope to provide visual feedback in positioning control on the XY plane. It should be emphasized that some papers describing advanced control algorithms (see, e.g., [15], [16]), provide only limited information on the position sensor or measurement technique. Probably, their authors were mainly focused on the presentation of their results assuming that the position measurements are precise and accurate; hence, the measurement errors are negligible.

But, the main reason for which nanopositioning is an interesting control problem is the nonlinear nature of the plant (microactuator), which manifests itself as hysteresis in the relation between position of the microactuator stage and

 ISBN: 978-1-61208-303-2

the control voltage. As a result, it is necessary to implement closed-loop control system, for which accuracy and precision of positioning is only dependent on the applied measurement sensor. Although the application of microscope is an expensive and complex solution (image processing is required), only the image from microscope can provide an accurate position of the microactuator stage. On the other hand, other types of sensors provide indirect information on the actual position of the microactuator stage.

Among the papers dealing with the influence of hysteresis on the quality of positioning control, it is worth mentioning earlier studies (e.g., [17], [18]), which describe piezoelectric actuators. It should be emphasized that the general properties of the closed-loop control systems (e.g., stability or quality of transients) for plants with hysteresis nonlinearity, have been well-known in the field of control theory since the 1950s of the past century. In majority of papers concerning nanopositioning control problem, the hysteresis phenomenon is often taken into account. For instance, the latest attempts to model the hysteresis behavior can be found in [4], [11], [19] and [20].

Among various control algorithms that can be used for positioning purposes, the simplest and historically the first is the classical PI (or PID) control algorithm. These algorithms are frequently applied in the combination with feedforward [13], fuzzy logic [15] or artificial neural networks [21]. The last cited paper [21] describes sliding mode control (SMC) algorithm showing its advantages over the classical PID controller. But, the improvement of the control quality achieved for the SMC is insignificant in comparison to the results for the PID controller. Hence, it leads us to the conclusion that the simple PID algorithm is the better option. For instance, the in-vitro fertilization system described in [13] uses two piezoactuators controlled by two independent PID controllers. Moreover, many authors consider the piezostack actuator to be an interesting nonlinear plant, which can serve as a benchmark system for testing new control algorithms. At this point, it is worth mentioning the advanced delay-varying repetitive control (DVRC) [10] or repetitive control algorithm with feedforward [16].

In this paper, we present an experimental set-up for analysis and calibration of piezostack actuators. The optical microscope is used to obtain the direct measurement of position of the microactuator stage. We will show that the classical PI controller is sufficient to obtain the acceptable control quality. The remainder of the paper is organized as follows. Section II provides details on the laboratory setup and describes a way to obtain information on the stage position, which is then used to manipulate the activated sludge samples during microscopic observations. Section III describes the control algorithm, which is based on the optical feedback provided by the microscope. Finally, Section IV discusses the main results.

II. EXPERIMENTAL SET-UP FOR NANOPOSITIONING CONTROL

The general schema of the measurement set-up is shown in Fig. 1. The presented system uses the microactuator, which allows for positioning in the range up to 25 micrometers, with an accuracy of several nanometers. In order to measure a position of the movable stage of the microactuator, the digital camera coupled with the optical microscope is used.

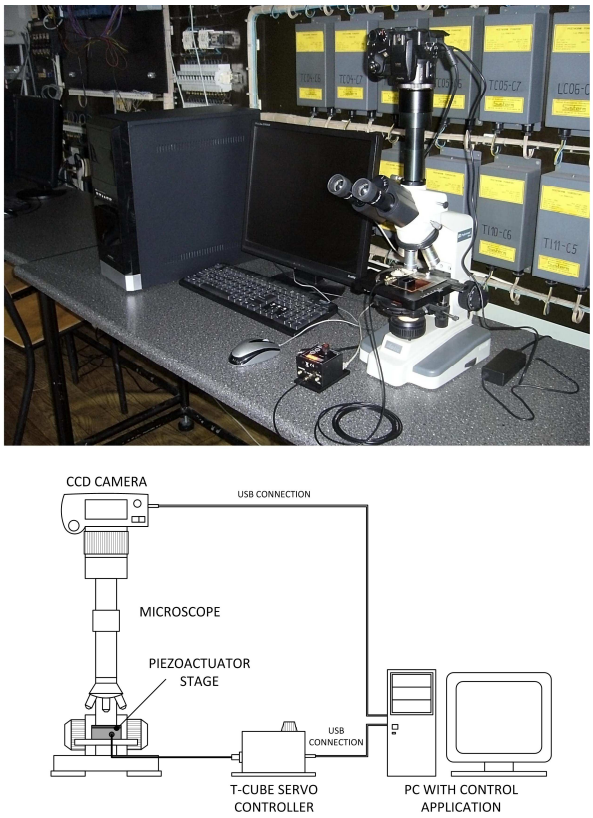

Figure 1. The general scheme of the experimental set-up.

Fig. 2 explains how to receive information on the stage position. A small glass plate, on which the analyzed sample is placed, has been mounted to the microactuator stage. But, to measure the stage position, a piece of tape has been attached to the top surface of the glass plate. This piece of tape is a graphical indicator used to determine the stage position with reference to the microscope stage. The shape of the indicator should be sufficiently large to obtain the stage position in the whole range of displacement and sufficiently small to maximize the field of view during microscopic observations. Then, the microscopic image of 320x240 pixels is recorded by the digital camera and sent to the computer via USB port. In the control application, created in LabVIEW environment, the captured image is processed by the threshold image segmentation method, which is performed on-line. As a result, a 320x240 matrix corresponding to the processed image is filled with ones and zeros. Because, the range of displacement is 25 micrometers, which is equal to 88 pixels, hence, one pixel corresponds to about 284 nanometers for total magnification of 400x (40x objective and 10x ocular). Since the diameter of a single sludge flock varies between 10 and 100 micrometers, the accuracy to 284 nanometers is sufficient for our purposes.

 ISBN: 978-1-61208-303-2

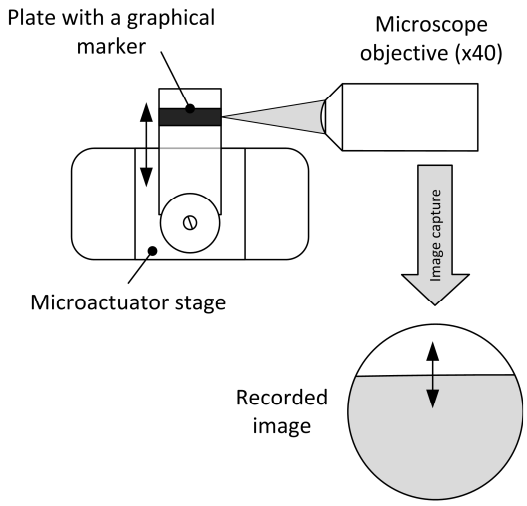

Figure 2. The idea of position measurement of the microactuator stage.

Information on the stage position can be then used by any control algorithm responsible for precise positioning of the microactuator stage. In turn, a single-channel T-Cube servo controller connected to the computer via USB port provides a source of control voltage. The control voltage (0-75[V]) changes the position of the microactuator stage and it can be generated either manually, i.e., in the T-Cube servo controller or indirectly in the control application, which is based on ActiveX components. The possibility of using ActiveX components facilitates the control system design process, which is described in the next section.

III. DESIGN OF POSITION CONTROLLER

Determination and analysis of the static characteristics of the controlled plant (microactuator) is a very important stage in the controller designing process. In the considered case, the static characteristics presents the relation between the stage position in micrometers and the input voltage. These characteristics were obtained by cyclic changes of the input voltage in steps of 2 volts. The obtained characteristics are shown in Fig. 3. Irrespective of the range of input voltage, a hysteresis effect was observed. The hysteresis is a typical phenomenon for piezoceramic materials and it is also noticeable in Fig. 4, which shows the step responses of microactuator stage. The analysis of these responses will help us to determine the dynamical properties of the controlled plant. It can be easily noticed that the same levels of the input voltage correspond to different stage positions. Moreover, the step changes in the input voltage cause instantaneous changes in the microactuator stage position (Fig. 4). Because, in our case, the microactuator stage will be applied for positioning of samples under the microscope, hence, at sampling rate of 10Hz (the sample time T=100[ms]), the much faster dynamics of the microactuator is negligible. In other words, it is assumed that the microactuator is a static element and can be described by the following equation:

$$y = k \cdot u \quad (1)$$

where: y – is the position of the microactuator stage in [μm], u – is the input voltage [V], k=1/3 [μm/V] – is the gain of the plant. It also means that the dynamical properties of the closed-loop system will be entirely determined by the dynamics of the controller. In other situations, it may prove necessary to take into account the dynamical properties of the controlled plant (microactuator system), especially, when the input voltage changes at high frequency. Unfortunately, due to the time needed to process the captured image, it was not possible to set the sample time less than 100 milliseconds. Hence, it was not possible to analyze the behavior of the microactuator stage immediately after the step change in the control voltage. It is worth noting that the problem of control of a static system (without dynamics) is rare and untypical, but can be quite complex, especially when the controlled plant is highly nonlinear.

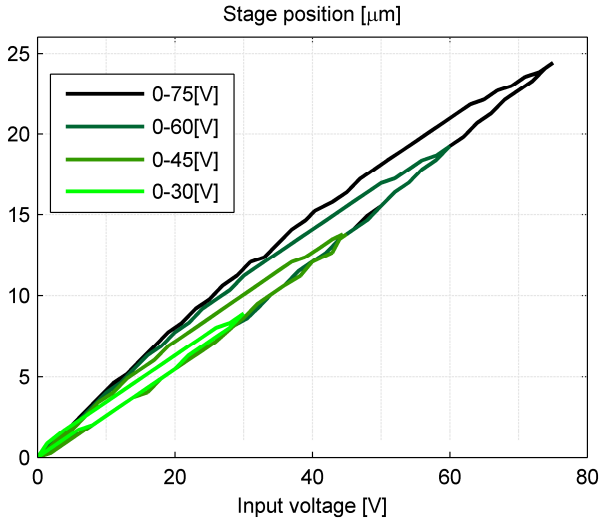

Figure 3. Static characteristics of the controlled plant.

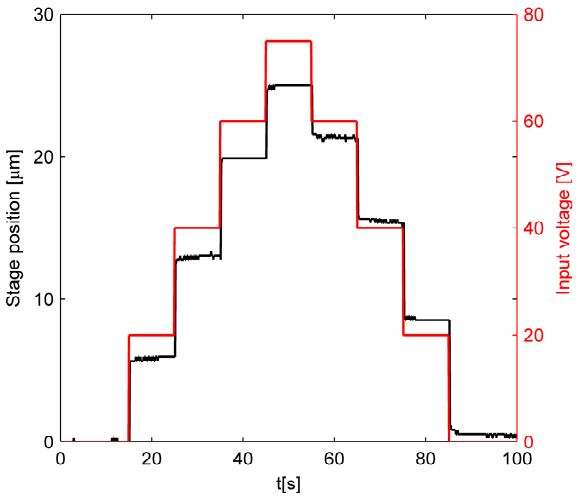

Figure 4. Step responses (black) to step changes in input voltage (red).

 ISBN: 978-1-61208-303-2

The simplified model of the microactuator (1) does not also include the hysteresis behavior, but it will simplify the controller design process. However, to take into account the hysteresis effect, a well-known Preisach model [22], [23] can be applied. Other models proposed in the literature are based, for instance, on artificial neural networks [24].

For positioning purposes, the classical PID controller can be used and its transfer function is as follows:

$$K(s) = k_p\left(1+\frac{1}{sT_i}+\frac{sT_d}{sT_b+1}\right) \quad (2)$$

where: k_p – the proportional gain, T_i – the integral time, T_d – the derivative time, T_b – the time constant in the derivative part (D) of the controller.

Based on the equations (1) and (2), a simulator of the closed-loop control system was created in LabVIEW environment. The simulator allowed for appropriate choice of the controller structure and for tuning its parameters. Based on the simulation runs, sufficiently good results, i.e., short settling time and no control error, were obtained for the PI (T_d=0) controller with the following parameters: k_p=0.5 and T_i=0.5[s]. A more detailed analysis of the closed-loop system described by (1) and (2) will allow to derive necessary and sufficient conditions for stability of the system. But, in order to determine the stability conditions, at first, it is necessary to find a discrete time description of the closed-loop system. In our case, the input-output description of the closed-loop system is as follows:

$$y(z)\cdot\left(z+k_pk\left(\frac{T}{T_i}\cdot\frac{z}{z-1}+1\right)\right) = w(z)\cdot k_pk\left(\frac{T}{T_i}\cdot\frac{z}{z-1}+1\right) \quad (3)$$

where: y(z), w(z) – are z-transforms of the actual and set point stage position, respectively, k_p – the proportional gain of the controller, T_i – the integral time, k – the gain of the plant and T – the sample time.

Hence, the characteristic equation of the closed-loop system (3) has the following form:

$$z^2\cdot T_i + z\cdot(k_pk\cdot T + k_pk\cdot T_i - T_i) - k_pk\cdot T = 0 \quad (4)$$

The above equation can be easily transformed to Laplace domain by using the well-known relation z:=(s+1)/(s–1). Then, by using the Routh-Hurwitz criterion, the necessary and sufficient condition for stability of (3) is as follows:

$$0 < k_p < \frac{2T_i}{T+2T_i}\cdot\frac{1}{k} \quad (5)$$

The proposed control algorithm was implemented in the control application written in G language in LabVIEW and its front panel is shown in Fig. 5. Owing to the application of ActiveX components provided by the manufacturer of the microactuator, the communication process between the microactuator and the control application is simplified. The information on the microactuator stage position is obtained from the segmented image according to the algorithm described in Section II.

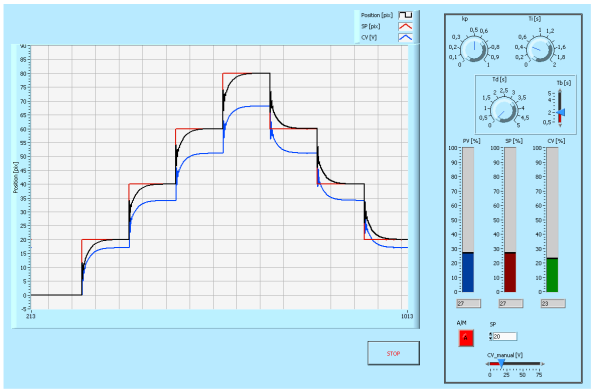

Figure 5. Front panel of the control application in LabVIEW.

Moreover, the implemented algorithm includes the bumpless switching between the automatic and manual modes of operation and the anti-reset windup, i.e., the integral part of the controller is disabled when the upper or lower bound is reached by the control voltage (the controller output signal).

IV. Experimental Results and Concluding Remarks

Fig. 6 presents step responses of the positioning control system for the previously determined structure and parameter values of the PI controller (k_p=0.5, T_i=0.5[s]). The obtained results were compared with step responses of the simulated closed-loop system described by equations (1) and (2) for the same controller parameters.

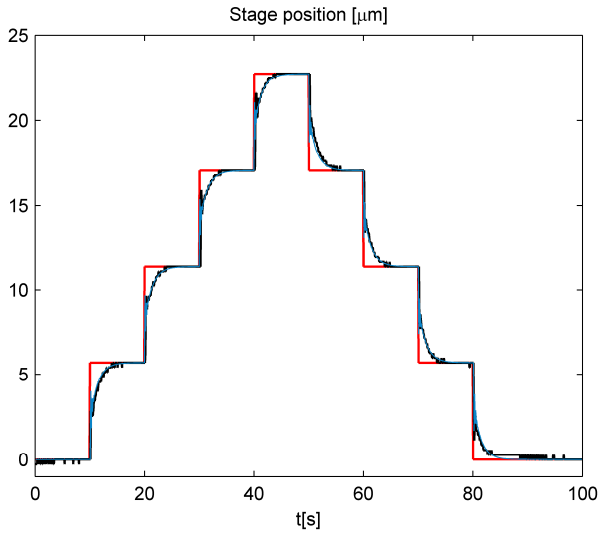

Figure 6. Comparison of the real (black) and simulated (blue) step responses of the closed-loop system. Red line represents changes in the set point position.

Although, there is a good conformity between experimental and simulated positions of the microactuator stage, the

visible differences occur in the transients of control voltages (Fig. 7). Most probably, this is due to the hysteresis effect, which is not included in the description of the simulated plant (1). It is also easy to notice that the hysteresis has an influence on the plant gain, which is dependent on the actual and previous values of the control voltage (Fig. 3).

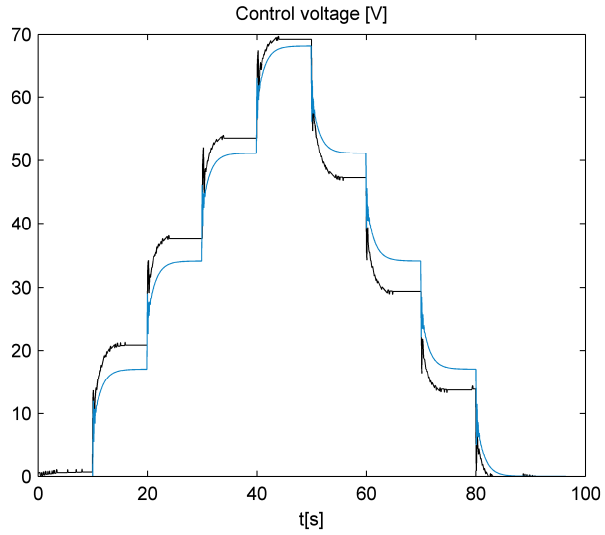

Figure 7. Control voltage in real (black) and simulated (blue) closed-loop control system.

On the other hand, it should be emphasized that the proposed controller ensures a complete elimination of the hysteresis behavior in the relation between the actual and set point stage positions (Fig. 8), which is one of the well-known properties of the closed-loop system.

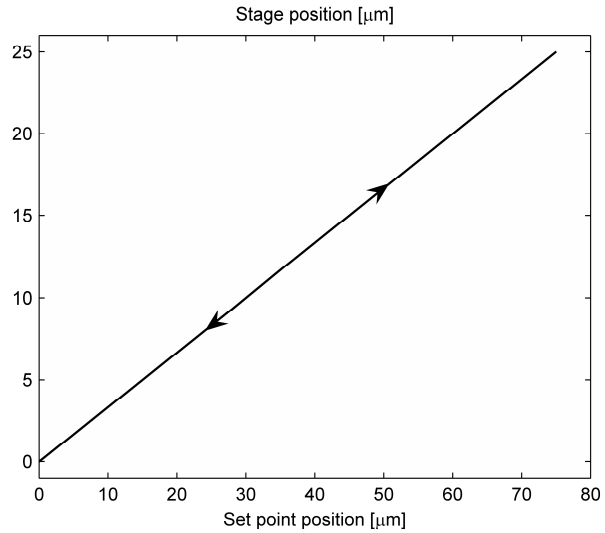

Figure 8. Steady state position in the closed-loop system.

Now, it remains to verify the stability condition (5), which was derived in the previous section for the simplified system (1)-(2). This can be achieved by analyzing the behavior of the positioning control system for large values of the proportional gain k_p (closed to critical values of k_p determined from inequality (5)) and for fixed integral times T_i in the controller. Fig. 9 presents the obtained results on the controller parameter plane (k_p,T_i) and compares the stability regions obtained experimentally and analytically based on the condition (5). In this case, the set point values were changed by 5 to 10 micrometers to cover the whole range of possible displacements of the microactuator stage.

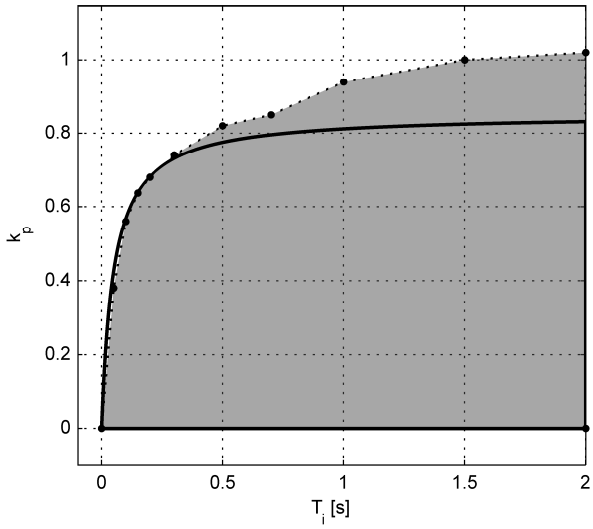

Figure 9. Stability regions of the closed-loop system. Black thick line is a boundary of stability region computed from eqation (5) and black dotted line from experimental results.

The experimental stability region turned out to be larger, than the region resulting from inequality (5). Most probably, the reason for this behavior is due to the hysteresis effect, which is not included in (5). Near the marginal stability boundary, the control voltage changes very rapidly and, as a result, the stage platform moves back and forth at very high frequency. Hence, it is highly probable that the hysteresis plays an important role in the behavior of the positioning control system. However, this should be verified by more detailed analysis. It should also be emphasized that the analytical determination of the stability region is not an easy task for plants, which exhibit hysteresis behavior. On the other hand, if the controller parameters satisfy inequality (5), then the positioning control system is stable.

In conclusion, the presented system allows for positioning of the observed samples with an accuracy of one pixel (several nanometers). It means that the accuracy is dependent on both the resolution of captured image and the total magnification of the optical microscope. At larger magnifications, the graphical indicator will be displaced by a distance of more pixels; hence, one pixel will be corresponding to a smaller distance in nanometers. Similarly, for a fixed magnification, but for a digital camera providing images of higher resolution, there will be more pixels corresponding to the entire range of stage displacement. In effect, the accuracy of positioning will be mainly limited by the current magnification of the optical microscope. The greater the total magnification, the better accuracy of

 ISBN: 978-1-61208-303-2

positioning can be achieved. In the case of using different types of position sensor (e.g., capacitive or strain gauge sensor), the accuracy of positioning control is limited by the accuracy of the applied sensor. Another important issue that must be taken into account in the further development of the system is the speed of positioning of the microactuator stage. In the presented case, acceptable results were obtained by using the classical PI controller. However, to increase the speed of positioning, it is necessary either to tune the controller parameters again without violating the stability condition (5) or to change the structure of controller.

ACKNOWLEDGMENT

This work was supported by the National Science Centre under grant No. 2012/05/B/ST7/00096 and by the Ministry of Science and Higher Education under grant BK-UiUA.

REFERENCES

[1] A. Sinno, P. Ruaux, L. Chassagne, S. Topcu, Y. Alalyli, G. Lerondel, S. Blaize, A. Bruyant, and P. Royer, "Enlarged Sample Holder For Optical AFM Imaging: Millimeter Scanning With High Resolution," First International Conference on Sensor Device Technologies and Applications (SENSORDEVICES 2010), Venice/Mestre, Italy, July 2010, pp. 190–194.

[2] D. Zhang, Z. Gao, M. Malosio, and G. Coppola, "A Novel Flexure Parallel Micromanipulator Based on Multi-Level Displacement Amplifier", The Third International Conference on Sensor Device Technologies and Applications (SENSORDEVICES 2012), Rome, Italy, August 2012, pp. 31–37.

[3] A.J. Fleming, "A review of nanometer resolution position sensors: Operation and performance," Sensor. Actuat. A-Phys., vol. 190, February 2013, pp. 106–126.

[4] S.C. Jordan and P.C. Anthony, "Design Considerations for Micro- and Nanopositioning: Leveraging the Latest for Biophysical Applications," Curr. Pharm. Biotechnol., vol. 10, August 2009, pp. 515–521.

[5] Y-M. Han, S-M. Choi, S-B. Choi, and H-G. Lee, "Design and control of a hybrid mount featuring a magnetorheological fluid and a piezostack," Smart Mater. Struct., vol. 20, July 2011, pp. 1–13.

[6] P-B. Nguyen and S-B Choi, "Micro-position Control of a Piezostack Actuator Using Rate-Dependent Hysteretic Compensator," Int. J. Prec. Eng. Man., vol. 12, October 2011, pp. 885–891.

[7] H.G. Kim, "Nano positioning control for dual stage using minimum order observer," J. Mech. Sci. Technol., vol. 26, March 2012, pp. 941–947.

[8] S.B. Choi, S.R. Hong, and Y.M. Han, "Dynamic characteristics of inertial actuator featuring piezoelectric materials: Experimental verification," J. Sound Vibration, vol. 302, May 2007, pp. 1048–1056.

[9] S.B. Choi, S.S. Han, Y.M. Han, and B.S. Thompson, "A magnification device for precision mechanisms featuring piezoactuators and flexure hinges: Design and experimental validation," Mech. Mach. Theory, vol. 42, September 2007, pp. 1184–1198.

[10] R.J.E. Merry, D.J. Kessels,W.P.M.H. Heemels, M.J.G. van de Molengraft, and M. Steinbuch, "Delay-varying repetitive control with application to a walking piezo actuator," Automatica, vol. 47, August 2011, pp. 1737–1743.

[11] P-B. Nguyen and S-B Choi, "A novel rate-independent hysteresis model of a piezostack actuator using the congruency property," Smart Mater. Struct., vol. 20, May 2011, pp 1–10.

[12] M. De Volder, J. Coosemans, R. Puers, and D. Reynaerts, "Characterization and control of a pneumatic microactuator with an integrated inductive position sensor," Sensor. Actuat. A-Phys., vol. 141, January 2008, pp. 192–200.

[13] P.R. Ouyang, W.J. Zhang, Madan M. Gupta, and W. Zhao, "Overview of the development of a visual based automated bio-micromanipulation system," Mechatronics, vol. 17, December 2007, pp. 578–588.

[14] J. Cas, G. Skorc, and R. Safaric, "Neural network position control of XY piezo actuator stage by visual feedback," Neural. Comput. Applic., vol. 19, October 2010, pp. 1043–1055.

[15] K. Abidi and A. Sabanovic, "Sliding-Mode Control for High-Precision Motion of a Piezostage," IEEE T. Ind. Electron., vol. 54, February 2007, pp. 629–637.

[16] C-Y. Lin and P-Y. Chen, "Precision tracking control of a biaxial piezo stage using repetitive control and double-feedforward compensation," Mechatronics, vol. 21, February 2011, pp. 239–249.

[17] P. Ge and M. Jouaneh, "Modeling hysteresis in piezoceramic actuators," Prec. Eng., vol. 17, July 1995, pp. 211–221.

[18] D. Hughes and J.T.Wen, "Preisach modeling of piezoceramic and shape memory alloy hysteresis," Smart Mater. Struct., vol. 6, June 1997, pp. 287–300.

[19] S.R. Viswamurthy and R. Ganguli, "Modeling and compensation of piezoceramic actuator hysteresis for helicopter vibration control," Sensor. Actuat. A-Phys., vol. 135, April 2007, pp. 801–810.

[20] L. Deng and Y. Tan, "Modeling hysteresis in piezoelectric actuators using NARMAX models," Sensor. Actuat. A-Phys., vol. 149, January 2009, pp. 106–112.

[21] M. Kinouchi, I. Hayashi, N. Iwatsuki, K. Morikawa, J. Shibata, and K. Suzuki, "Application of Fuzzy PI control to improve the positioning accuracy of a rotary-linear motor driven by two-dimensional ultrasonic actuators," Microprocess. Microsyst., vol. 24, April 2000, pp. 105–112.

[22] F. Preisach, "Über die magnetische Nachwirkung," Z. Phys., vol. 94, May 1935, pp. 277–302.

[23] I.D. Mayergoyz and G. Friedman, "Generalized Preisach model of hysteresis". IEEE T. Magn., vol. 24, January 1988, pp. 212–217.

[24] L. Chuntaoa and T. Yonghong, "A neural networks model for hysteresis nonlinearity", Sensor. Actuat. A-Phys., vol. 112, April 2004, pp. 49–54.

 ISBN: 978-1-61208-303-2

Theoretical Study of Micro Flow Instability by Orr-Sommerfeld Equation in Micro Canal

Brahim Dennai, Toufik Chekifi
Department of mechanics, ENERGARID laboratory
E-mail: dennai.univ@yahoo.fr, khelfaouidz@yahoo.fr

Rachid Khelfaoui, Asma Abdenbi
Bechar University, Algeria
chtoufiklmd@gmail.com, abdbiol.univ@yahoo.fr

***Abstract*— Due to interfacial effects that concerns micro channel jets, Plateau-Rayleigh is a well-known instability. In micro fluidics context, the gravity is negligible and surface tension phenomena are predominant. Over the past decade, there has been extensive research into the design of microfluidic systems for chemical analysis. All previous works provided an overview of instabilities that lead to a rich variety of different flow regimes that can be obtained in a micro channel. We survey advancement over ten years in the development of micro scale devices for instability gaseous micro flow. A parametric instability study was systematically conducted with varying system pressure, heat flux, and channel size with and without inlet restrictor. This paper describes various works for micro channel instability flow in gaseous micro fluidic devices. The main objective of this work is the mathematical resolution of the Orr-Sommerfeld equation, and then used this solution to create perturbations in the flow by varying the pressure. The instability of physics is explored using previous theoretical and numerical analyses, as well as experimental observations. The difficulty of the analytical resolution of the Orr-Sommerfeld equation for a velocity profiles for the perturbation has always been a problem; that is why we are going to try to get it numerically.**

Keywords-Gaseous instability; micro canal; microfluidics simulation; experimentation; gaseous flow.

I. INTRODUCTION

Microfluidics is the science and technology of the manipulation of fluids in small channels. The development of the microfluidics science has been seen in the mid of the 70th. The current micro fabrication technology has allowed its rapid expansion from the middle of the 80th [1]. The interest in this science has led to a major development, particularly in the field of chemistry and biology. This growing interest is reflected in several publications.

Drazin and Reid [2] define hydrodynamic instability as a branch of hydrodynamics, which is concerned with "when and how laminar flows break down, their subsequent development and their eventual transition to turbulence." Fluid instabilities may be broadly divided into two classes: convective instability and dynamic instability.

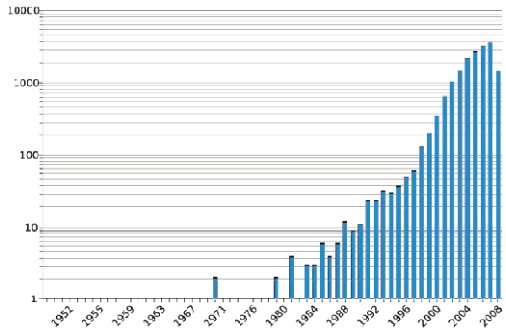

Figure 1. Growth in the number of publications on microfluidics in recent decades [1].

While the convective instabilities can be understood rather easily in terms of forces acting on displaced parcels of fluid, the dynamic one are more varied and more challenging to understand.

When thin cylinders of liquid tend to break up into droplets in the presence of large surface tension; this phenomenon is known as Rayleigh-Plateau instability [2], and it is caused by a positive feedback loop between the decreased cylinder radius and increased tension forces.

As a result, liquid jets and spindles along the boundary of a liquid sheet will reliably break apart as soon as they become thin enough for the surface tension forces to dominate the inertia forces [3] [4]. For applications, we can use coaxial cylinders to create jets, or to generate droplets in order to obtain some micromixers [5]. The classical Rayleigh-Plateau instability is described as a phenomenon in which the velocity inside the jet is constant; the same kind of analysis is done in a more general setting using a long wave approximation [6]. The numerical linear instability is done in the context of a shear flow [7]. K.C Sahu, et al., use the same strategy of Colin and Tancogne [8] in order to study the stability of a coflow composed by a newtonian fluid and a non-newtonian one. The spatial responses of the film to inlet controlled periodic perturbations which have been characterized when the Rayleigh-Plateau is relevant [9].

 ISBN: 978-1-61208-303-2

The emphasis has been put on the linear and nonlinear development of the primary wave train. S. Shabahang et al. [10], present the observation of the Rayleigh-Plateau capillary instability in a multi-material fiber at the core cladding interface.

The Plateau–Rayleigh instability, often just called the Rayleigh instability that is responsible for the phenomenon of the break-up of a jet. Fonade [11] gave some principles of such study focusing primarily on the flow type "jets". The method that is used is similar to the harmonic analysis of a system: in a given mean flow, we add a perturbation which is characterized by velocity and pressure. These characteristics are sinusoidal functions.

The frequency is kept as a parameter; we study how the flow is modified by the perturbation. If the system is nonlinear the answer will depend on the amplitude of the perturbation; therefore, we take low amplitude, which permits linearizing equations.

We consider a parallel of two dimensional flow which defined by $\left[\overrightarrow{U}(y), \overline{p}(x, y)\right]$ in which we superpose a perturbation which defined by $\left[\overrightarrow{U}'(x, y), \overline{p}'(x, y)\right]$.

It is supposed that the mean flow $\left[\overrightarrow{U}, \overline{p}\right]$ and the global flow $\left[(\overrightarrow{U} + \overrightarrow{U}'), (\overline{p} + \overline{p}')\right]$ separately verify the continuity equation and Navier-Stokes equations.

A stream function of the perturbation which is periodic with respect to time, verifies the continuity equation and Navier-Stokes equations. This function is written with the following complex notation:

$$\psi(x, y, t) = \phi(y) e^{i\alpha_1 (x - c_1 t_1)} \quad (1)$$

$\phi(y) = \phi_r + i\phi_i$: The amplitude functions of the perturbation.

α_1 and c_1: constants that are generally complex [Only the real part of the stream function has a physical sense].

When we replace adimensional quantities in the relation (1):

$$\psi = \psi . U_0 L$$
$$x = X . L$$
$$c_1 = c . U_0 = (c_r + i c_i) U_0$$
$$\phi = \phi . U_0 L$$
$$\alpha_1 = \alpha / L = \alpha_r + i\alpha_i \qquad t_1 = tL / U_0$$

The relation (1) becomes:

$$\psi = \phi . e^{[-\alpha_i x + (\alpha_i c_r + \alpha_r c_i) t_1] + i[\alpha_r x - (\alpha_r c_r + \alpha_i c_i) t_1]} \quad (2)$$

The relation (1) is used to calculate the components (u ', v') of the perturbation velocity. Medium flows and global verify the Navier-Stokes equations in which the pressure between these two equations is eliminated, to obtain the equation that is known as "Orr-Sommerfeld" [12].

$$\left(\frac{U}{U_0} - c\right)\left(\frac{d^2\phi}{dY^2} - \alpha^2\phi\right) - \phi\frac{d^2(U/U_0)}{dY^2} = -\frac{i}{\alpha R}\left[\frac{d^4\phi}{dY^4} - 2\alpha^2\frac{d^2\phi}{dY^2} + \alpha^4\phi\right] \quad (3)$$

R : the Reynolds number $R = \frac{U_0 L}{v}$; U : mean flow.

In this equation we must add the boundary conditions that are written to a jet:

- v' = 0 whether $\phi = d\emptyset/dy = 0$ for $Y \to \pm\infty$
- v' = 0 whether $\phi = 0$ for Y = 0 when we consider a change of a symmetrical perturbation relative to the axis of the jet.
- u = 0 whether $d\emptyset/dy = 0$

(4)

For Y = 0, when we consider an antisymmetric perturbation.

The stability study is to find the eigenvalues of the constants α and c; such as, the solution $\emptyset$ of equation (3) which verifies the boundary conditions.

In addition to the mean flow U, and the Reynolds number R, we have three parameters $(\alpha_r = \alpha, c_i, c_r)$ in equation (4). $\propto$ is undetermined parameter $(\alpha = 2\pi/\lambda)$ in which λ is the wavelength of the perturbation.

The association between the equation (2) and the boundary conditions (4) provides a solution $\emptyset(y)$ and a pair of values c_r, c_i that are dependent on the Reynolds number R and $\propto$. The perturbation will be amplified when $c_i > 0$ and it will be amortized when $c_i < 0$. The perturbation will be neutral or indifferent when $c_i = 0$.

The condition $c_i = 0$ provides the neutral stability curve $f(\alpha, R) = 0$ that can be represented in the plan(α, R).

II. A METHOD OF OBTAINING AN EXACT SOLUTION

We develop a method to obtain an exact solution of Orr-Sommerfeld equation by reducing, the resolution of this differential equation solving a Volterra integral equation.

We observe that:

$$(U - c)(\varphi'' + \alpha^2\varphi) - U''\varphi = -\frac{i}{\alpha R}(\varphi'''' - 2\alpha^2\varphi'' + \alpha^4\varphi) \quad (5)$$
$$(\varphi'''' - 2\alpha^2\varphi'' + \alpha^4\varphi) = (\varphi'' + \alpha^2\varphi)' - \alpha^2(\varphi'' + \alpha^2\varphi)$$

We introduce the function f by the differential equation:

$$\varphi''-\alpha^2\varphi = f \qquad \text{(Change of variable)}$$
$$r^2-\alpha^2=0 \quad ; \quad r_1=\alpha \ , r_2=-\alpha$$

The solution of the differential equation

$$\varphi''-\alpha^2\varphi=0$$

is:

$$\varphi(p)=C_1(p)e^{\alpha p}+C_2(p)e^{-\alpha p}$$

where p is the parameter of integration

$$\begin{cases} C'_1(p)e^{\alpha p}+C'_2(p)e^{-\alpha p}=0 \\ \alpha C'_1(p)\left(e^{\alpha p}\right)'-\alpha C'_2(p)\left(e^{-\alpha p}\right)'=f(p) \end{cases}$$

$$\Rightarrow \varphi(y)=\frac{1}{\alpha}\int_0^y f(p)\sinh\alpha(y-p)dp+c_1^*e^{\alpha y}-c_2^*e^{-\alpha y}$$

$$\Rightarrow \varphi(y)=\frac{1}{\alpha}\int_0^y f(p)\left(\frac{e^{\alpha(y-p)}-e^{-\alpha(y-p)}}{2}\right)dp+C_1\cosh\alpha y+C_2\sinh\alpha y$$

$$\Rightarrow \varphi(y)=\left(\frac{1}{\alpha}\int_0^y\frac{1}{2}f(p)e^{-\alpha p}dp\right)e^{\alpha y}-\left(\frac{1}{\alpha}\int_0^y\frac{1}{2}f(p)e^{\alpha p}dp\right)e^{-\alpha y}+$$
$$\left(c_1^*+c_2^*\right)\cosh\alpha y+\left(c_1^*-c_2^*\right)\sinh\alpha y$$

$$\Rightarrow \varphi(y)=\frac{1}{\alpha}\int_0^y f(p)\sinh\alpha(y-p)dp+C_1\cosh\alpha y+C_2\sinh\alpha y \quad (6)$$

Using the boundary condition in (6) $\varphi(0)=\varphi'(0)=0$

$$\varphi'(y)=\frac{1}{\alpha}f(p)\sinh\alpha(y-y)+\alpha C_1e^{\alpha y}+\alpha C_2e^{-\alpha y}$$

$$\begin{cases} \varphi(0)=C_1-C_2=0 \\ \varphi'(0)=\alpha C_1+\alpha C_2=0 \end{cases}$$

$$\begin{cases} C_1-C_2=0 \\ C_1+C_2=0 \end{cases} \Rightarrow C_1=C_2=0$$

Then the equation (3):

$$(1)\Rightarrow (U-c)f-U''\frac{1}{\alpha}\int f(p)\sinh\alpha(y-p)dp=-\frac{i}{\alpha\,\mathrm{Re}}(f''-\alpha^2f) \quad (7)$$

A new function ϕ is introduced by the equation $f''-\alpha^2 f=\phi$ (change of variable)

With the same steps we obtain the following solution:

$$f(y)=\frac{1}{\alpha}\int_0^y\phi(p)\sinh\alpha(y-p)dp+A\cosh\alpha y+B\sinh\alpha y \quad (8)$$

If we replace f in the equation (7) we obtain:

$$[(U-c)\frac{1}{\propto}\emptyset(p)sinh\propto(y-p)dp+Acosh\propto y-$$

$$U''\frac{1}{\propto}\int_0^y f(p)sinh\propto(y-p)dp=-\frac{i}{\propto Re}\emptyset(y)].i\propto Re$$

$$\Rightarrow \phi(y)-i\,\mathrm{Re}(U-c)\int_0^y\phi(p)\sinh\alpha(y-p)dp+$$

$$i\,\mathrm{Re}\,U''\int_0^y f(p)\sinh\alpha(y-p)dp=i\alpha\,\mathrm{Re}\left(A\cosh\alpha y+B\sinh\alpha y\right)$$

If we replace $f(p)$ by the expression (8), we obtain:

$$\phi(y)-i\mathrm{Re}\int_0^y\left(\frac{U''}{\alpha\phi(p)}\int\phi(s)\sinh\alpha(y-s)ds-(U-c)\right).$$
$$.\sinh\alpha(y-p)\phi(p)dp=i(i\alpha\,\mathrm{Re}\left(A\cosh\alpha y+B\sinh\alpha y\right)- \quad (9)$$
$$-\alpha\,\mathrm{Re}\int_0^y\left(A\cosh\alpha y+B\sinh\alpha y\right)\sinh\alpha(y-p)dp)$$

and if we pose :

$$i\alpha\,\mathrm{Re}\left(A\cosh\alpha y+B\sinh\alpha y\right)-\alpha\,\mathrm{Re}\int_0^y\left(A\cosh\alpha y+B\sinh\alpha y\right)$$
$$\sinh\alpha(y-p)dp=F(y)$$

We obtained:

$$\phi(y)-i\mathrm{Re}\int_0^y\left(\frac{U''}{\alpha\phi(p)}\int_0^p\phi(s)\sinh\alpha(y-s)ds-(U-c)\right)\sinh\alpha(y-p)\phi(p)dp=iF(y) \quad (10)$$

Posing:

$$K(y,p)=\int_0^y\left(\frac{U''}{\alpha\phi(p)}\int_0^p\phi(s)\sinh\alpha(y-s)ds-(U-c)\right)\sinh\alpha(y-p)$$

We obtain:

$$\phi(y)+i\,\mathrm{Re}\int_0^y K(y,p)\phi(p)dp=-iF(y) \quad (11)$$

As a result, by the complex integral equation of the Volterra type of the second species, we can obtain the solution of the differential equation φ(y) of the Orr-Sommerfeld equation by a simple quadrature.

$$\varphi=\frac{1}{2\alpha^2}\int_0^y[(y-p)cosh\alpha(y-p)-\frac{1}{\alpha}sinh\alpha(y-p)]x$$
$$\emptyset(p)dp+\frac{1}{2\alpha}ysinh\propto y+$$
$$+\frac{B}{2\alpha}\left(ycosh\propto y-\frac{1}{\alpha}sinh\propto y\right) \quad (12)$$

III. SIMULATION OF MICROCHANEL T JONCTION GEOMETRIES

The boundary condition: P_{inlet1}= 2 bars, P_{inlet2}= 2.3, 2.5, 3 bars and P_{outlet} = 1 bar.

The descriptions of the simulated geometry with its dimensions are shown in Figure 2.

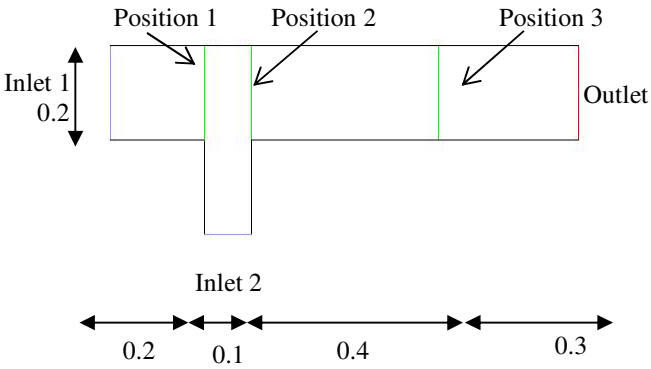

Figure 2. Description of schematic geometry (mm).

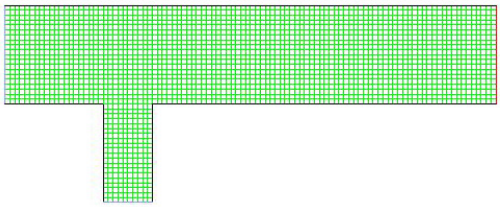

Figure 3. Meshing geometry of simulation.

IV INTERPRETATION OF RESULTS AND PERSPECTIVES

The following results represent the velocity profiles in different positions 1, 2 and 3 for different pressures a, b and c (Figure 4).

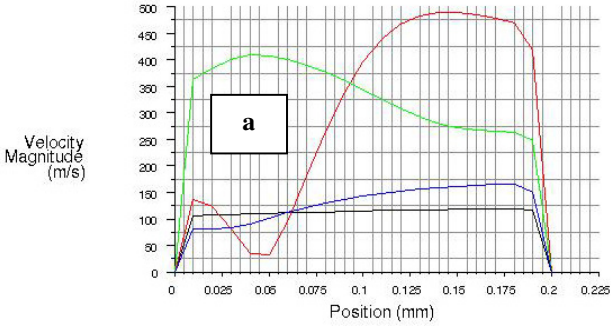

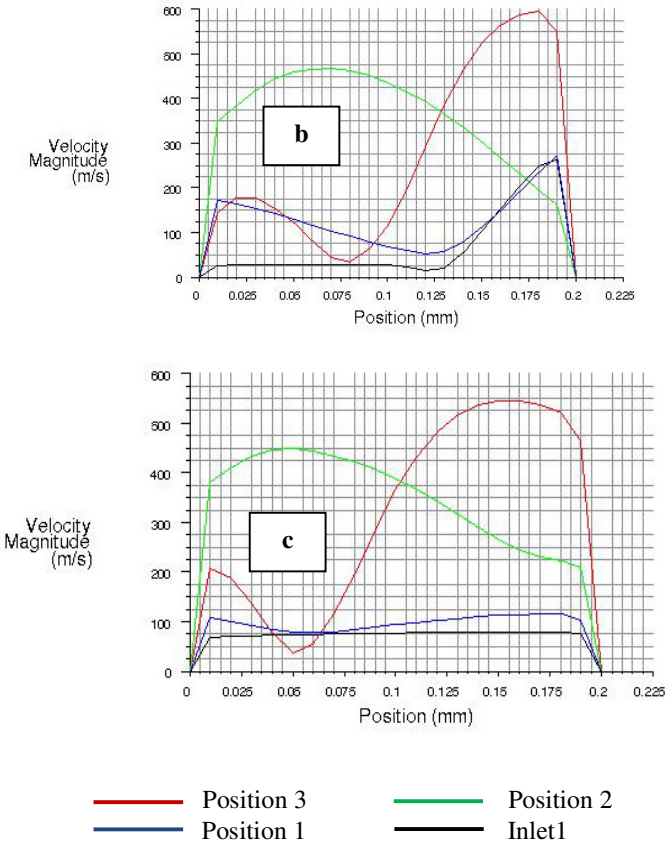

Figure 4. The velocity (m/s).
a: P_{Inlet2}=2.3 bars, b: P_{Inlet2}=2.5 bars, c: P_{Inlet2}=3 bars

With the variation of the entry pressure (P Inlet2), the velocities to the wall equals: zero (Figure 4: a, b, c).

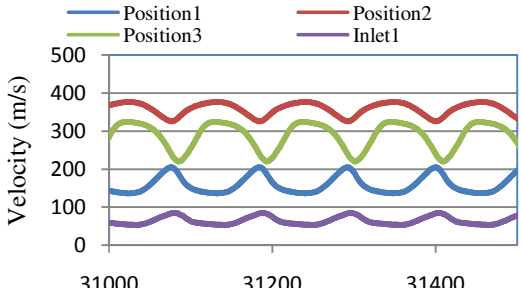

Figure 5: Velocity (m/s) in different position (PInlet2 = 3 bars)

In table 1, the disruption caused a variation (increase) of the velocity is shown.

TABLE1. THE MAXIMAL TRANSVERSAL VELOCITY (m/s) IN DIFFERENT POSITIONS FOR DIFFERENT PRESSURES INLET2.

Pressure Inlet2 (bars)		2.3	2.5	3
maximal transversal Velocity (m/s)	Inlet1	113,69	77,72	61.024105
	position1	140,36	118,02	136.13811
	position2	329,42	342,59	399.43102
	position3	309,67	325,83	382.96531

We note that the transversal velocity at a position 2 is always maximum comparing at others positions with any pressure inlet 2 and it increases when the pressure inlet 2 increases.

V. CONCLUSION

Microfluidics deals fluid flow, single or multiphase systems in very small dimensions in the micrometer range. In this paper, we present a study of jet created by a perturbation as different pressures.

Our research team is in the process of developing a new line of research in our laboratory, the study of the hydrodynamic instability of gas flow.

The equation of the perturbation is known by the Orr Sommerfeld equation. The difficulty of the analytical resolution of this equation is always a problem for obtained a velocity profiles for the perturbation we try to obtain it numerically.

The first result consist a manipulation of all step of mathematical resolution of Sommerfeld equation. Really the difficulty is located on resolution of Voletra equation.

The numerical results were presented. The velocity profile at different position of geometry indicates the sensibility of pressures. We conclude the perturbation of principal flow is directly influenced by the size of elementary channel and pressures.

ACKNOWLEDGEMENTS

Many thanks to all the team ISC (ENERGARID laboratory) for their help and motivation.

REFERENCES

[1] L. Tanguy, « Actionnements électriques de fluides dédiés aux microsystèmes », PhD Thesis, Toulouse university, 2009.

[2] P. G. Drazin and W. H. Reid,"Hydrodynamic stability", Cambridge University Press, second edition, United Kingdom, 1981.

[3] P. G. Gennes, F. B. Wyart and D. Quéré, "Capillarity and wetting phenomena: drops, bubbles, pearls, waves", ISBN 978-0-387-21656-0 (eBook), Springer Verlag, 2004.

[4] L. De Luca and M. Costa, "Instability of a spatially developing liquid sheet", journal of Fluid Mechanics, 2009, 331, 127–144.

[5] F. Sarrazin, et al., "Micro-drops approach in micro-reactors: mixing characterization", La Houille Blanche, N◦3 (Mai-Juin 2006), pp. 50-55 DOI:10.1051/lhb:200603007.

[6] F. Charru, " Instabilités hydrodynamiques", EDP Sciences, ISBN CNRS Éditions 978-2-271-06565-0, 2007.

[7] Y. Renardy, Instability at the interface between two shearing fluids in a channel, journal: Physics of Fluids, 28, 3441 (1985); http://dx.doi.org/10.1063/1.865346.

[8] K. C. Sahu, et al., "Linear instability of pressure-driven channel flow of a Newtonian and a Herschel-Bulkley fluid", journal: Physics of Fluids, 19, 122101 (2007); http://dx.doi.org/10.1063/1.2814385.

[9] C. Duprata, C. Ruyer-Quil, and F. Giorgiutti-Dauphiné, "Experimental study of the instability of a film flowing down a vertical fiber" Eur. Phys. J. Special Topics 166, 63–66 (2009)

[10] S. Shabahang, J. J. Kaufman D. S. Dengn, and A. F. Abou raddy, " Observation of the Plateau-Rayleigh capillary instability in multi-material optical fibers", Appl. Phys. Lett. 99, 161909 (2011); http://dx.doi.org/10.1063/1.3653247

[11] J. Dat and C. Fonade, "Jet Flow Similitude", La Houille Blanche, no. 6, pp. 435-442, (Septembre 1978), DOI: 10.1051/lhb/1978036.

[12] M. Miklavcic, "Eigenvalues of the Orr-Sommerfeld equation", Differential and Integral Equation, International Journal for Theory & Applications, vol. 4, no. 4, pp. 731 – 737, July 1991.

 ISBN: 978-1-61208-303-2

Measurement of Optical Properties of Nanofluids and its Effects in Near-wall Flow Evaluation

Kanjirakat Anoop and Reza Sadr
Micro Scale Thermo Fluids (MSTF) Laboratory
Texas A&M University at Qatar
e-mail: anoop.baby@qatar.tamu.edu
email: reza.sadr@qatar.tamu.edu

Abstract—**There have been several ongoing researches in nanofluids (suspensions of nanoparticles in a basefluid) due to the anomalous heat transfer enhancement that were reported earlier. Exploration of the near-wall flow region using Particle Image Velocimetry (PIV) technique could bring more insights for reasons behind such enhancements. However, such measurement techniques are extremely depended on the optical properties of the fluid under study. Hence prior measurements of the optical properties are necessary for estimating velocity values while implementing these fluids. In present study, optical properties of SiO_2 – water nanofluids at various particle concentrations are investigated. Measurements of refractive indices and the optical transmittance of nanofluids, which are directly related to the depth of penetration and visible depth in nPIV (nano PIV) measurements, are carried out. Further, near-wall velocities of water and nanofluids are measured using nPIV technique as a case study.**

Keywords-Refractive index, transmittivity, nPIV

I. INTRODUCTION

Cooling of components still remains as one of the major challenges faced by electronic industries. Many modes of cooling techniques were tried in the past. Improving the heat transfer capacity of the cooling liquid by suspending solid particles was one among them. Suspending micron-sized particles however resulted in effects such as particle sedimentation, higher pumping power requirement, and erosion of heat exchanger surfaces. Suspending nano-sized particles seemed to be a better option, hence introducing of new class of cooling fluid known as nanofluids. Nanofluids**,** are engineered colloidal suspensions of nano-sized particles in a heat transfer fluid, and have received considerable attention; due to the anomalous thermal properties reported earlier [1,2]. However, in recent times, many contradicting results with respect to thermal performance of nanofluids are being reported. Main reason for such contradicting observation is due to the unclear understanding of the phenomenon behind the thermal enhancements. Non-intrusive near-wall velocity measurements are expected to bring insights explaining reasons for the anomalous thermal enhancements. However, any non-intrusive optical flow measurement techniques would be highly dependent on the optical properties of the medium. As nanofluids are fluids with suspended nan-sized particles, estimation of optical properties based on classical theories may be unreliable. Hence, detailed investigations of its optical properties are required before implementing them in measurements. In present work optical properties of nanofluids are measured, and a case study analysis is carried out on its effects in near-wall flow measurements.

Initial attempt to measure near-wall flow fields of nanofluids was made by Walsh et al. [3] by using a Micro Particle Image Velocimetry (μPIV) technique. They obtained velocity profiles of nanofluids flowing inside a microchannel. However, the spatial resolution of their work was limited to several microns and could not capture details of velocity field very close to the walls. To surpass this limitation and to achieve a detailed flow field evaluation at near-wall region, efforts were made by Anoop and Sadr [4] to conduct nPIV (nano Particle Image Velocimetry) measurements while using nanofluids. nPIV is an extension of μPIV working on evanescent-wave illumination generated by total internal reflection (TIR) of a laser beam at the fluid-solid interface between the flow and the wall [5]. The effects of errors in measured velocity values in nPIV measurements as a result of particle mismatch of tracers was investigated by Sadr et al. [6]. This was further expanded by including the effects of Brownian motion, light penetration profiles, surface forces such as van der Waals, and electrostatic forces, and the velocity gradient on the near-wall measurements using a traditional PIV cross-correlation method [7].

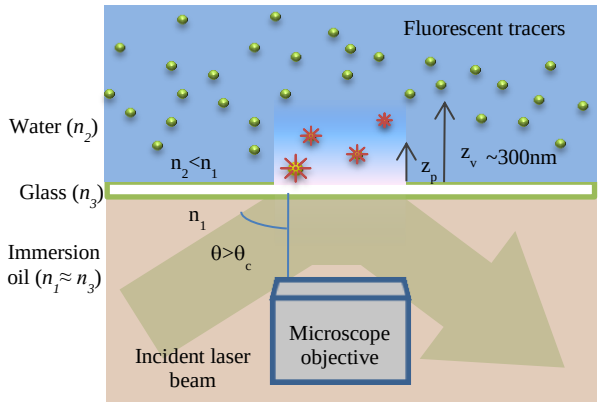

Figure 1. Schematic showing nPIV measurement principle.

The working principle behind the nPIV measurement technique is described next. When a light beam travels through a medium with a refractive index n_1, into another transparent medium with a lower refractive index of n_2 at

 ISBN: 978-1-61208-303-2

an angle exceeding the critical angle, $\theta_c=sin^{-1}(n_2/n_1)$, it gets totally reflected at the interface (Fig.1). However, the electromagnetic field penetrates into the lower refractive index region and propagates for a small distance parallel to the interface, creating what is known an evanescent wave. This evanescent wave is capable of exciting fluorescent particles in this region while the large numbers of particles farther away in the bulk liquid remain unexcited. Evanescent wave intensity, *I*, in the direction normal to the interface decays exponentially with distance, *z*:

$$I = I_0 \exp(-z/z_p) \quad (1)$$

where I_0 is the maximum intensity at the wall and z_p is the penetration depth.

$$z_p = \frac{\lambda_0}{4\pi n_1}\left(sin^2\theta - (n_2/n_1)\right)^{-1/2} \quad (2)$$

λ_0 is the wavelength of the light and θ is the incident angle. For visible light at a glass water interface, z_p is on the order of O (100nm). Figure 1 shows the schematic of a general TIRF setup used in an nPIV experiment where only the near-wall fluorescent particles in the fluid are excited and viewed from the bottom of the microscope plate [6]. The emission intensity of the tracer particles in this region is an exponential function of the distance from the wall with a decaying trend as stated by (1) [7]. It can be noted that the penetration depth is depended on refractive index of the medium (2). When nanofluids are used as the medium their refractive index values of the medium will change with respect to particle loading. Hence, prior knowledge of refractive index values of nanofluid would be crucial while implementing them in nPIV measurements.

For an evanescent wave, z_p is the penetration depth, however, the actual depth that could be imaged would be larger than it and is defined as visible depth (z_v). Depending on the optical characteristics of the imaging system, this depth of visible region, z_v, changes with the intensity of the incident laser beam, transmission of light through the medium, fluorescent particle characteristics, camera and the background noise of the imaging system. In short, z_v represents actual visible depth in the captured image. Another point to be noted is the opaque nature of nanofluids. From visual observation of nanofluids, it can be noted that the opacity of medium is increased with particle addition. This in-turn could reduce the visible depth. Hence, it would be important to see the effect of light transmittivity in nanofluids also while implementing them in nPIV measurements. It is assumed that any reduction in transmittivity due to use of nanofluids would reduce visible depth.

Even though nPIV measurements were made earlier for nanofluids [4], the optical characterisation of nanofluids were not carried out and were estimated on theoretical studies alone. No experimental efforts were made to investigate the optical properties of them. Thus, in present study, the optical properties of nanofluids are measured and their influence on nPIV measurements are analysed. Refractive index value and transmittivity values are measured to obtain their influence on penetration depth (z_p) and visible depth (z_v). Nanoparticle concentrations are varied from 0 to 6% by mass. Further, nPIV measurements are conducted with nanofluids to see the effect of nanoparticles in the near-wall flow region.

II. MEASURMENT OF OPTICAL PROPERTIES

Before detailing the measurements of nanofluids optical properties, a brief description on preparation of nanofluids is given. SiO_2-water nanofluids are used in the present study. Nanofluids are prepared by a top down approach in which commercially bought nanoparticles are mechanically dispersed in a basefluid (in present case water). Appropriate amounts of SiO_2 nanoparticles (~ 20nm average diameter, Sigma Aldrich, #637238) are dispersed in de-ionized water using an ultrasonic bath (VWR ultrasonic cleaner, 35 kHz) for 30 minutes. Further, the colloidal suspension is subjected to intensified ultrasonication by immersing a probe type sonicator (QSonica S-4000, 20 kHz). Cyclic ultrasonic pulses for about 45 minutes are given to the suspension so as to achieve maximum possible de-agglomeration of particles. Particle concentrations varying from 0 to 6% by mass (henceforth represented as %wt) are considered for present investigation.

In present work, refractive indices of nanofluids are measured using a laboratory refractometer (RE40D, Mettler Teldo), which measure reflective index values based on total internal reflection principle. Light from a LED light source gets partially reflected to an optical CCD sensor at the surface of sapphire prism and sample interface. Measurement from the sensor is used in evaluation of refractive index values. The equipment had a measurement range of refractive index values from 1.32 to 1.7, which matches with the measurement requirements of the nanofluids. Prior to actual measurements, the refractometer was calibrated with standard distilled water at ambient conditions.

To acquire information of transmission of visible light through the nanofluid sample, experiments are conducted to determine the transmittance using a spectrometer. Percentage transmittance of the nanofluid samples are measured using a Perkin Elmer Lamda 950 spectrometer in the visible region. The spectrometer consists of a light source, a mono-chromator, a wave length selector, a sample holder having a specified path length, and a detector. Light at a desired wavelength is passed through the sample and the transmitted light through the medium is measured by the detector. The sample path lengths can be varied using different sizes of cuvettes. During experimentation, initial baseline readings are obtained by placing the basefluid (water) in the spectrometer and are later compared with the nanofluid samples. Percentage transmittance is measured for the sample at wavelengths in the visible region. In present work, experiments were

 ISBN: 978-1-61208-303-2

conducted with two path lengths, 10mm and 1mm (Starna Cells Inc.).

III. NANO-PIV MEASUREMENTS

After measuring the optical properties of nanofluids, near-wall velocity measurements of nanofluids are performed using nPIV technique. An objective based TIR method is used in present study. The microchannel flow cell (Translume Inc) used in the experiment is fabricated in quartz and has a rectangular cross section (300µm width and 100µm Height). The bottom quartz plate is customized to have a thickness of 0.12mm in order to have a clear TIR falling on the objective of the microscope. During the experiment, different flow rates ranging from 0.005ml/min (±0.1%) to 0.06ml/min is maintained in the micro channel using a syringe pump (KDS200, KD Scientific) along with a 2.5 ml gas-tight glass syringe (Hamilton). The excitation light in the near-wall region was provided by an Argon-Ion CW laser beam with a wave length of 488 nm (Spectra Physics BeamLok 2060). Images were obtained using an EMCCD camera (ProEM 512, Princeton Instruments) attached to an inverted epi-fluorescence microscope (Leica DMI6000B) via a 63x 1.47NA oil immersion objective. The pixel resolution for the images obtained from this imaging set up was 4×10^6 (pixel/meter). The nPIV seeding particles used were 100nm (±5%) diameter polystyrene fluorescent particles (F8803, Invitrogen) having peak excitation and emission wavelengths of 505nm and 515nm, respectively.

In all the experimental runs, the fluorescent particle concentration was maintained at a constant volume concentration of 0.017%. When nanofluid samples were prepared, the fluorescent particles were added to the nanofluids suspension and sonicated thoroughly, keeping the same fluorescent particle concentration. Thus, the nanofluids sample contained both SiO_2 nanoparticles as well as the fluorescent particles suspended in it. However, when visualizing the flow it was observed that fluorescent particles were alone getting excited. The SiO_2 nanoparticles were seen not self-illuminating or creating a background illumination. The angle of incidence of light in the water-quartz interface was evaluated to be 65^o, based on the numerical aperture value of the objective lens and refractive indices at the interface. This yielded a penetration depth of $z_p \cong 90$nm (2). The depth of visible region (z_v) is then estimated to be 350±20nm for the basefluid, based on the penetration depth and the intensity value of the background noise in captured images.

IV. RESULTS AND DISCUSSION

Initially, the optical properties of nanofluids are discussed. Figure 2 shows the effective refractive index values of nanofluids measured for various concentrations. Measurements show a rapid increase in refractive index values at lower particle loadings (from 0 to 1wt%) and a gradual increase after that up to 6wt%. A careful observation, however, would reveal that the total percentage increase in refractive index values were below 1% even while particle loading were increased by 6wt%. Similar orders of refractive index values were reported in earlier studies for other nanofluids [8, 9].

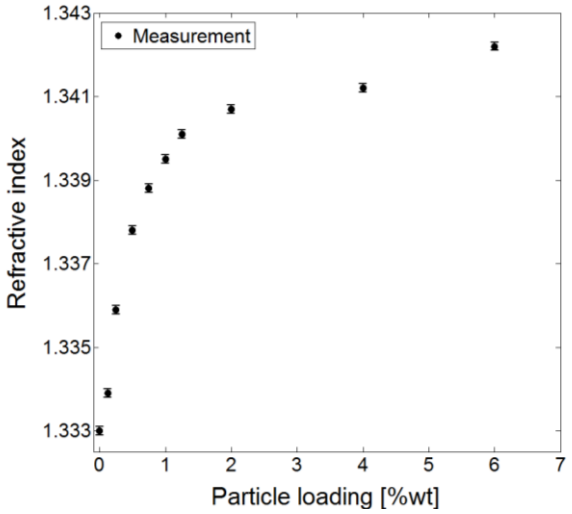

Figure 2: Refractive index values of nanofluids.

Even though the increases in refractive index values were low, their effect in increasing penetration depth (z_p) needs to be considered. The penetration depth is evaluated using (2) and is plotted in Fig. 3.

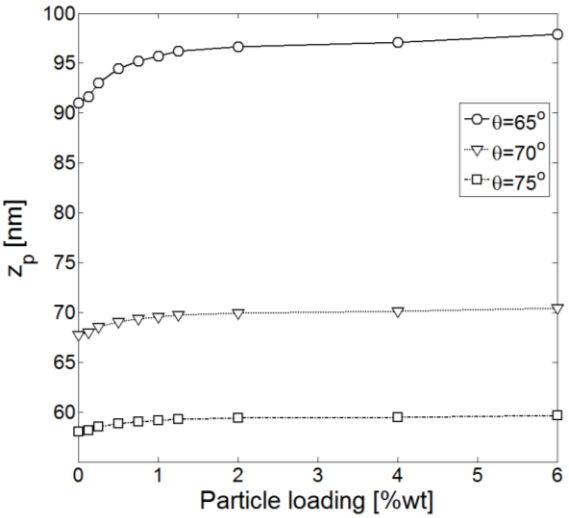

Figure 3: Effect refractive index of nanofluids on penetration depth

Effects of three incident angles which are above critical angles are plotted. Only a minimal increase in penetration depth is observed while using nanofluids. It is observed that penetration depth has increased by about

 ISBN: 978-1-61208-303-2

7nm for 6wt% nanofluid when compared with that of water.

Effect of opacity of nanofluids and its influence on transmission of visible light is examined next. Figures 4 and 5 show the percentage transmittance of nanofluid samples measured using 10mm and 1 mm path length respectively. Percentage transmission at a wavelength of 488nm (wavelength of incident light in nPIV measurements) is chosen for estimation. Inset figure shows the transmittance spectrum of all the samples in the entire visible region wavelengths. Photograph of the cuvette used in the measurement is also given in the figure.

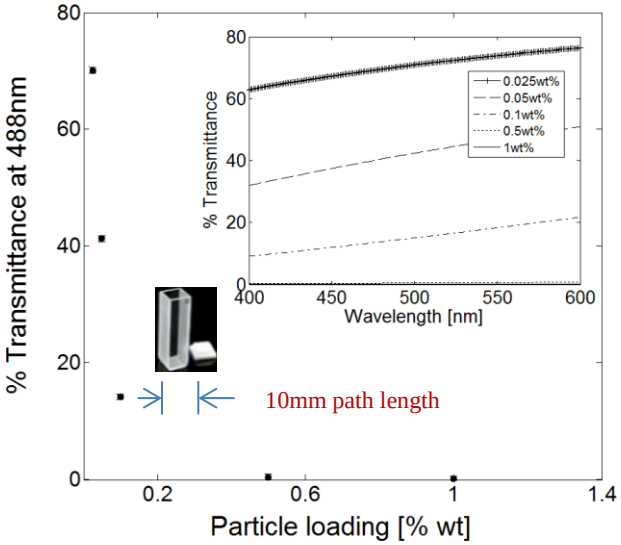

Figure 4: Percentage transmittance for nanofluids measured with 10mm path length.

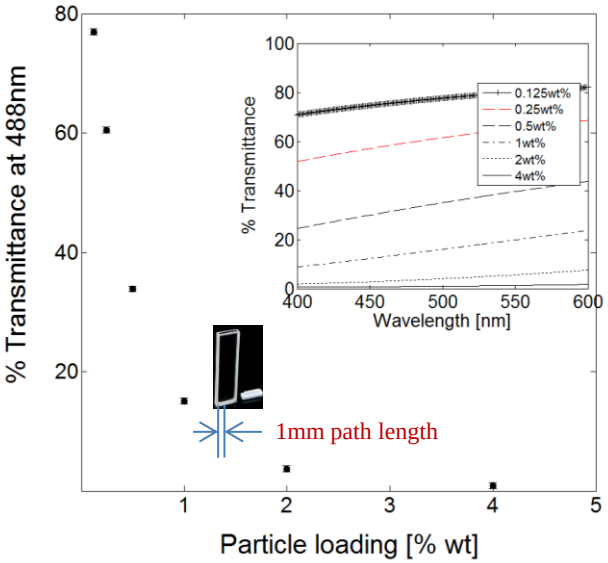

Figure 5: Percentage transmittance for nanofluids measured with 1mm path length.

It is observed that adding nanoparticle in the basefluid has increased the opacity of the solution. With 10mm path length, percentage transmittance became almost zero when the particle loading has reached 1wt%. Further measurements were not possible with this path length. However, percentage transmittance measurements were possible at higher particle loadings while using 1mm path length cuvette. Measurements up to 4 wt% were possible with 1mm path length as shown in Fig. 5. A maximum of ±2% uncertainty is observed in all the measurements.

Following Beer-Lambert law, transmittance (T) is related to path length (l) and absorption coefficient (α) of the liquid as given below [10].

$$T = 10^{-\alpha l} \quad (3)$$

In order to combine the results of 1mm path length and 10mm path length, variation of absorption coefficient with that of particle loading is plotted in Fig. 6.

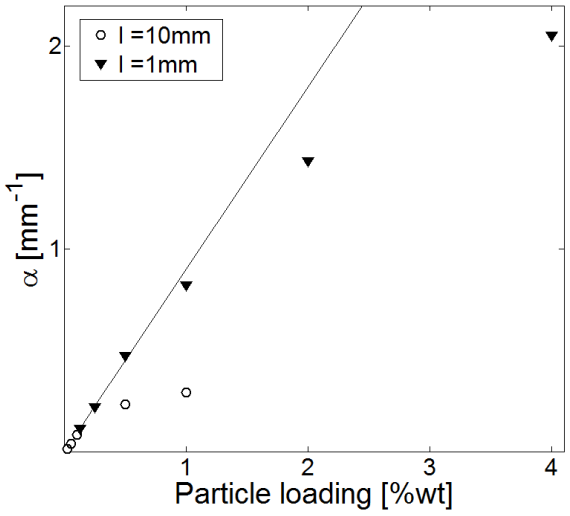

Figure 6: Variation of absorption coefficient with particle concentration

Ideally, absorption coefficient for a suspension needs to be constant for a particular loading even while measuring with varying path lengths. However, present measurements did not show considerable matching beyond 0.5 wt% particle loading. One reason for this could be the fact that the sensor in the spectrometer was not getting sufficient signals to evaluate transmittivity beyond particle loading of 0.5wt% (Note from Figure 4 that the percentage transmission was below 1% above 0.5% particle loading for 10 mm path length measurements). At 1wt% the percentage transmittance measurement was 0.122%, which would be highly unreliable. Similarly for 1mm path length experiments beyond 2 wt% seems unreliable. Further examination of Fig. 6 shows that, the linear trend of absorption coefficient with respect to concentration for nanofluids was true only below 2 wt% particle loading. Thus, it would be judicious to consider only measurements with

 ISBN: 978-1-61208-303-2

1mm path length below 2wt% concentration in our further analysis. A linear fit in this region is made and is estimated to be,

$$\alpha = 89.\phi \quad (4)$$

where, ϕ, is the particle loading by mass. Using equations 3 and 4, transmittivity at any given path length could be evaluated. The maximum focal depth in nPIV measurements is of magnitude 500nm. For a path length of 500nm and particle loading of 6wt%, the percentage reduction in transmittivity could be evaluated to be less than 1%. In other words, percentage reduction in transmittivity in a depth of 500nm for nanofluids would be very minimal.

Thus, from the measurement and analysis of optical properties of nanofluids it is clear that the changes due to refractive index values and opacity would not influence nPIV measurements in the measurement depth. To evaluate the effect of nanofluids on nPIV measurements, preliminary near-wall velocity measurements using water and nanofluids at various particle concentrations are made. The flow rates are varied from 0.005ml/min to 0.06ml/min and near-wall images are captured. For each experiment, 1500 nPIV image pairs of 256x80 pixels were acquired with a inter frame time delay of 0.6 ms. The images were then post–processed using a standard FFT-based cross correlation program that uses a 3D Gaussian peak finding algorithm based on a Gaussian surface fit to determine the tracer particles' displacements and velocities[4]. In nPIV measurements, the focal depth of the objective lens is larger than the penetration depth of the evanescence wave, therefore, all the particles in the image are in focus and there would be no back-ground light. Figure 7 shows the near-wall velocities measured for nanofluid and water at a visible depth of 350nm.

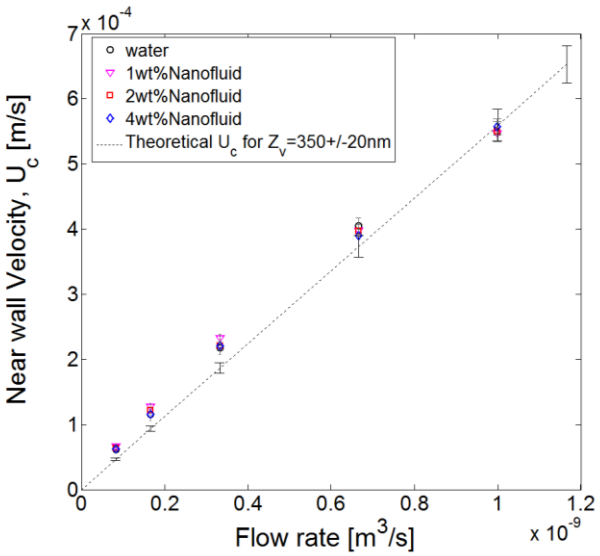

Figure 7. Near-wall velocity of nanofluids measured using nPIV technique.

It is observed from the figure that there is not much noticeable variation in near-wall velocity values measured for nanofluids even after considerable amount nanoparticles loading. The velocity variations measured for each flow rates are all falling within the experimental uncertainty values [11].The plot shows that even after increasing the particle loading by one order of magnitude, the near-wall velocity behaves the same. This indicates that nanofluids behaves as a homogeneous mixture and have Newtonian flow characteristics. Similar observation was made in earlier studies with nanofluids also [3, 4].

It should be kept in mind that, in present study, visible depth (z_v) variation while using nanofluids were estimated qualitatively from the transmittivity values. Their actual effect in nPIV measurements may be different owing to their effect on background and increasing noise levels. More efforts to measure z_v quantitatively and to include them in the near-wall velocities are being currently undertaken at our laboratory.

V. CONCLUSIONS

The present work investigates the effect of optical properties of SiO_2-water nanofluids on near-wall flow measurements. Particle concentrations were varied from 0 to 6wt%. Refractive index values of nanofluids, which affect penetration depth of the evanescent wave (z_p) were measured. Less than one percent increase in refractive index values were observed for nanofluids. Transmittivity, which would indirectly influence visible depth (z_v) were measured using a spectrometer. Analysis showed that transmittivity of light or opacity, in a depth of 500nm was not much affected by the use of nanofluids. No significant variation in near-wall velocities were recorded for nanofluids in comparison with that of water. nPIV measurements vindicated the homogeneous and Newtonian nature of the nanofluids.

ACKNOWLEDGMENT

This publication was made possible by NPRP grant # 08-574-2-239 from the Qatar National Research Fund (a member of Qatar Foundation). The statements made herein are solely the responsibility of the authors.

REFERENCES

[1] S. K. Das, S. U. S Choi, W. Yu and T. Pradeep, "Nanofluids Science and Technology," John Wiley, New York, 2008.

[2] W.Yu and H.Xie, "A review of nanofluids: Preparation, Stability mechanisms, and applications," Journal of Nanomaterials, 435873, 2012, doi:10.1155/2012/435873.

[3] P. A. Walsh, V. M. Egan and E. J. Walsh, "Novel micro-PIV study enables a greater understanding of nanoparticle suspension flows: nanofluids," Microfluid Nanofluid, 8, June 2010, pp.837–842, doi:10.1007/s10404-009-0553-z.

[4] K. Anoop and R. Sadr, "nPIV Velocity Measurement of Nanofluids in the Near-Wall Region of a Microchannel," Nanoscale Research Letters, vol. 7, May 2012, 284, doi: 10.1186/1556-276X-7-284.

 ISBN: 978-1-61208-303-2

[5] C. M. Zettner and M. Yoda, "Particle velocity field measurements in a near-wall flow using evanescent wave illumination," Experiments in Fluids, vol. 34, Jan 2003, pp. 115-121,doi: 10.1007/s00348-002-0541-5.

[6] R. Sadr, H. Li and M. Yoda, "Impact of hindered brownian diffusion on the accuracy of particle-image velocimetry using evanescent-wave illumination," Experiments in Fluids, vol. 38 (1), 2005, pp. 90-98, doi: 10.1007/s00348-004-0895-y

[7] R. Sadr, K. Anoop and R. Khader, " Effects of surface forces and non-uniform out-of plane illumination on the accuracy of nPIV velocimetry," Measurement Science and Technology, vol. 23, 2012, 055303, doi:10.1088/0957-0233/23/5/055303.

[8] R. A. Taylor, P. E. Phelan, T.P. Otanicar, R. Adrian and R. Prasher, "Nanofluid optical property characterization: towards efficient direct absorption solar collectors," Nanoscale Research Letters, 6:225,2011, doi:10.1186/1556-276X-6-225.

[9] I. Kim and K. D. Kihm,"Measuring near-field nanoparticles concentration profiles by correlating surface Plasmon resonance reflectance with effective refractive index of nanofluids," Optics Letters, 35(3), 2010, pp. 393-395, doi: 10.1364/OL.35.000393.

[10] Handbook of Chemistry and Physics, 56thEdition, Weast, R.C., CRC Press, Cleveland, 1975.

[11] L. H. Benedict and R. D. Gould, " Towards better uncertainty estimates for turbulence statistics," Experiments in Fluids, vol. 22,1997, pp. 129-136.

 ISBN: 978-1-61208-303-2